A Thesis Entitled

A SPECTROMETER FOR THE INVESTIGATION OF BACKSCATTERING OF 10 - 20 keV ELECTRONS

by

RICHARD SEBASTIAN SHORTER, B.Sc., A.R.C.S.

Submitted for the Degree of Doctor of Philosophy of the University of London

Imperial College of Science and Technology

London

1979

ABSTRACT

RICHARD SEBASTIAN SHORTER

A SPECTROMETER FOR THE INVESTIGATION OF BACKSCATTERING OF 10 - 20 keV ELECTRONS

An electron spectrometer is described for the investigation of backscattering in the energy range 10 - 20 keV. The design specifications, which have been met, were for a spectrometer with a resolution of 1 part in 10^4 in energy at a count rate of 100 electrons per second. The energy analyser has an acceptance angle of 3.4×10^{-6} sterad and is capable of alignment without the use of a monochromatic reference beam.

The reason for the choice of a retarding field, "high pass", energy analyser are discussed, together with a comparison of various such analysers previously used. The design of a simple retarding mesh filter and the inherent limitations of such filters are discussed.

The analyser, despite being designed for use at potentials in excess of 30 kV, suffered from field emission noise from the retarding electrode at potentials greater than 16 kV. The reason for this emission and a successful method for its limitation in the range 16 - 30 kV are given.

Two dimensional computer predictions of the field intensity distribution in the immediate vicinity of the mesh were made in conjunction with Mr. K.W. Jones (Physics Dept., I.C.S.T.) and these were used to provide a qualitative comparison with the experimentally determined properties of the mesh system.

Data presented include backscattered spectra at an angle of scatter of 150° from C, Al, Cu, Au and Pb. Also shown are spectra over the energy loss range 0 - 20 eV, in which the quasi-elastic peak (energy loss > 7 eV) is clearly resolved for specimens with atomic no. greater than 45.

A comparison is made between this data, previous experimental work and recent scattering theory.

The spectra are used to predict the width of KIKUCHI bands, on the basis of a simple convolution of band shape with energy. The predicted widths of the bands are compared with those experimentally observed.

CONTENTS

CHAPTER 1 INTRODUCTION

Page

CHAPTER 2 APPARATUS

CHAPTER 3 ELECTRON ENERGY ANALYSERS

Page

CHAPTER 5 THE ANALYSER PERFORMANCE

CHAPTER 6 ELECTRON BACKSCATTERING SPECTRA

APPENDIX 5 Ray tracing

APPENDIX 6 Program

APPENDIX 7 Calculation

FIGURES AND TABLES

Chapter 1

Chapter 2

Chapter 3

Chapter 4

Chapter 5

Chapter 6

Chapter 7

Chapter 8

Appendix 1

Appendix 2

Appendix 3

Appendix 4

Appendix 5

Appendix 6

Appendix 7

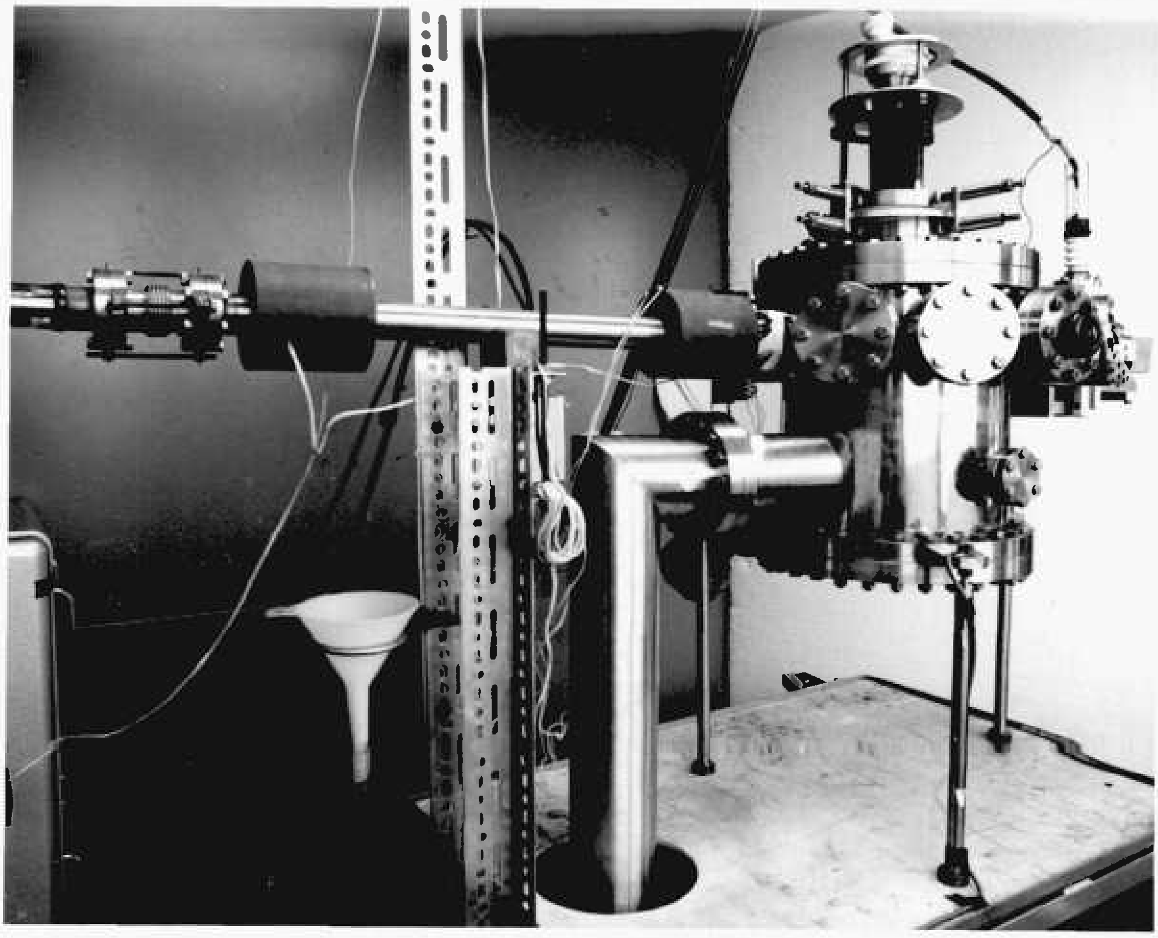

Frontispiece: The electron spectrometer.

The main chamber, pumping line and electron gun can be seen. The analyser is positioned opposite the gun.

CHAPTER 1

INTRODUCTION

1.1 Aim

This work is primarily concerned with attempting to link theories of Kikuchi bands produced in the backscattered direction (Alam, 1952; Alam et al, 1954; Venables et al, 1973) with recent experimental observations of the energy spectra of electrons backscattered from polycrystalline metal surfaces (Darlington, 1971; 1975).

1.2 Kikuchi bands

Kikuchi bands are seen when electrons pass through thick perfect crystals. They are the result of diffraction of the electrons at the crystal planes, but are seen at greater thickness of crystal and higher angles of scatter than is normally associated with electron spot or streak patterns.

The bands have been the subject of much research, both experimental (Kikuchi, 1928;Gjonnes, 1966; Gjonnes and Watanabe, 1966) and theoretical (Kainuma, 1955; Okamoto et al, 1971; Shamamoto et al, 1972, etc.). The common feature of all Kikuchi patterns is that their geometry is dependent solely on the crystal position, and not on the incident beam direction. The relative intensity of various parts of a pattern, however, are dependent on beam direction. The pattern and the theory of formation are discussed in Chapters 7 and 8.

The apparent problem with Kikuchi patterns produced in the backscattered direction (Fig. 1.1) is that they are visible at all. Several workers (Alam, 1952; Alam et al, 1954; Venables et al. 1973) have observed such patterns, though none have been able to explain them in terms of the energy spectrum of the electrons backscattered from the crystal. The presence of Kikuchi patterns is not confined to crystals of high atomic number, but has even been observed in the backscattered direction with Li F (Alam, 1952).

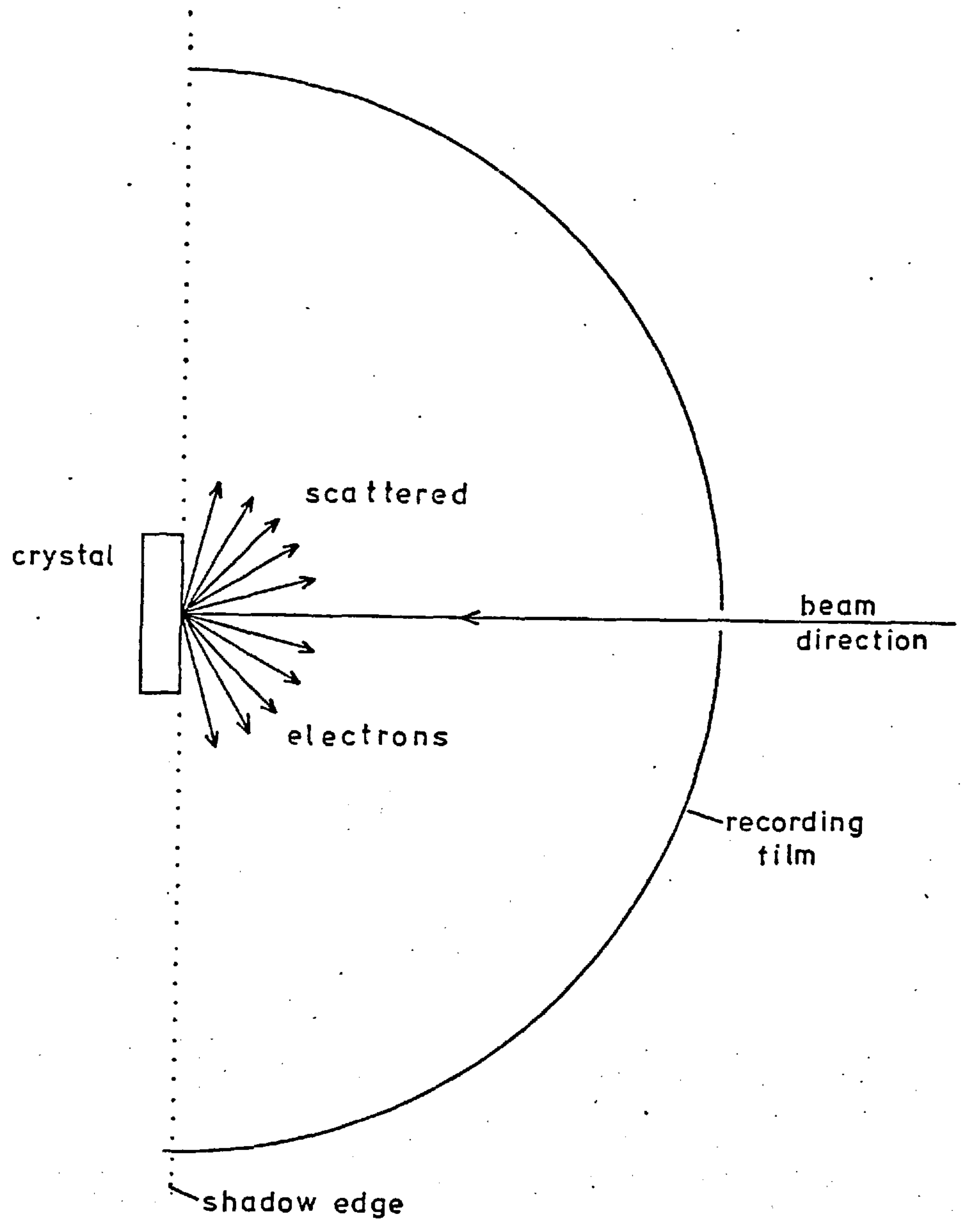

Fig 1.1 Orientation of electron beam, crystal and film for the recording of high angle Kikuchi bands.

The electrons involved in most other diffraction patterns (Bragg spots, etc.) are assumed to be phase linked to the incident electron wave. The wave is elastically scattered by the periodic crystal potential, but suffers no change in energy or relative phase. Any electron involved in a process which includes a substantial loss in energy is assumed to constitute part of the incoherent background of the diffraction pattern.

It has long been appreciated that Kikuchi patterns were part of this background, being the result of further diffraction of the already scattered electrons (Thomson and Cochrane, 1939). It has, however, usually been assumed by experimentalists that these electrons had an energy fairly close to that of the original beam, and it is assumed in theories such as those of Okamoto et al (1971) that losses of more than 1% in energy do not occur. The problem raised by the work of Alam et al (1954) is that the patterns are seen in the backscattered direction apparently with a width corresponding to that produced by elastic electrons, yet in a region where elastic and low-loss electrons ($<1\%$) form only a small fraction of the electron flux (Kanter, 1957).

Alam (1952) assumed that the crystal produced sufficient elastic scattering to produce the pattern. Kanter's work cast doubt on this as he showed a wide range in the energy spectrum from polycrystalline specimens. Kryn'ko et al (1965) showed that there was no gross difference between the spectra produced by single crystals and polycrystalline specimens. Thus, the bands seen by Alam et al must have been the product of diffraction of electrons with a very wide spectrum of energies.

No experiments have been performed with sufficient resolution to establish this point beyond doubt. Even when this is done it is far from obvious why the measured width of the pattern corresponds not to a mean electron energy, but to the extreme end of the range.

Electron spectrum

One possible solution to the problem may be that elastic and low-loss electrons constitute a larger part of the spectrum than has previously been reported. Most observed spectra in the energy range 5 - 30 keV have been recorded on spectrometers with minimum resolution of 50 eV or more. The elastic electrons might well constitute a large proportion of the spectra which has not yet been separately resolved.

1.3 Experimental work

The aim of the experimental work described here was to produce an electron spectrometer capable of resolving 5 eV at a primary electron energy of at least 15 keV. The object of this was to investigate the elastic and quasi-elastic region of the spectrum to determine what proportion of the total spectrum it constituted.

The spectrometer and its design are described in Chapters 2, 3 and 4, and its operation and use in Chapters 5 and 6 and their associated appendices.

1.4 Mechanism of Kikuchi band production

The assumptions about Kikuchi band production proposed above may not prove correct. If electrons of all energies can be shown to produce diffraction patterns and they can be shown to add to a finite value, rather than forming a continuous background, the appearance of Kikuchi bands at high angle would not be surprising. The proposition that inelastically scattered electrons of all energies can form Kikuchi bands is discussed in Chapters 7 and 8.

1.5 The mechanism of electron backscattering and energy loss in solids

The discussion of Kikuchi bands requires an understanding of the mechanisms leading to the angular scattering and energy loss which energetic electrons undergo when they pass through solids. The subjects have recently been reviewed by Darlington (1971) and Wells et al (1974) from which much of this brief discussion is drawn.

1.6 Cross-section and mean free path

It is convenient to describe the probability of particular interactions between atoms and energetic electrons in terms either of mean free path (L) or scattering cross section (σ). These are related mathematically

$$L = (n \sigma)^{-1} \qquad 1.1$$

where n = no. of atoms per unit volume.

1.7 Total scattering cross section σ , m^2

This is an effective area normal to the initial incident electron trajectory. Electrons passing through this area will be involved in an interaction process of the particular type considered.

1.8 Scattering cross section $\sigma (> \varphi) \, m^2$, as a function of scattering angle φ

This is the effective area of the atom normal to the electron trajectory for all interactions of the specified kind involving scattering through an angle greater than φ .

1.9 Differential scattering cross section $d\sigma / d\Omega$, m^2/(atom). (sterad)

This is the effective area of the atom for scattering events of the specified kind through an angle φ into unit solid angle (Fig. 1.2).

The azimuthal angle, ϑ , has been ignored as all the interactions under consideration are, to a first approximation, isotropic in ϑ (Fig. 1.2).

1.10 Relation between cross sections

The cross sections are related as follows :

$$\frac{d\sigma}{d\Omega} = \frac{d\sigma}{d\varphi} \cdot \frac{d\varphi}{d\Omega} \qquad 1.2$$

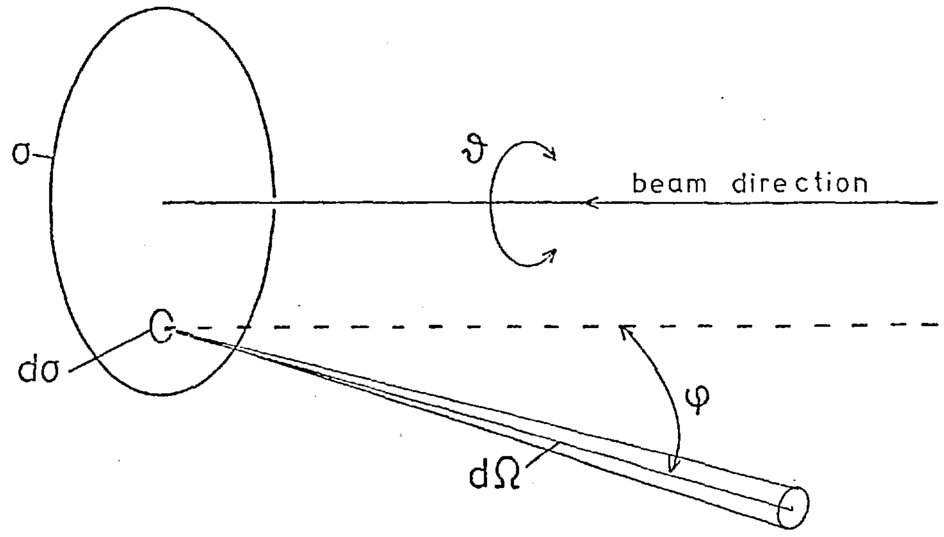

Fig 1.2 Scattering cross section parameters

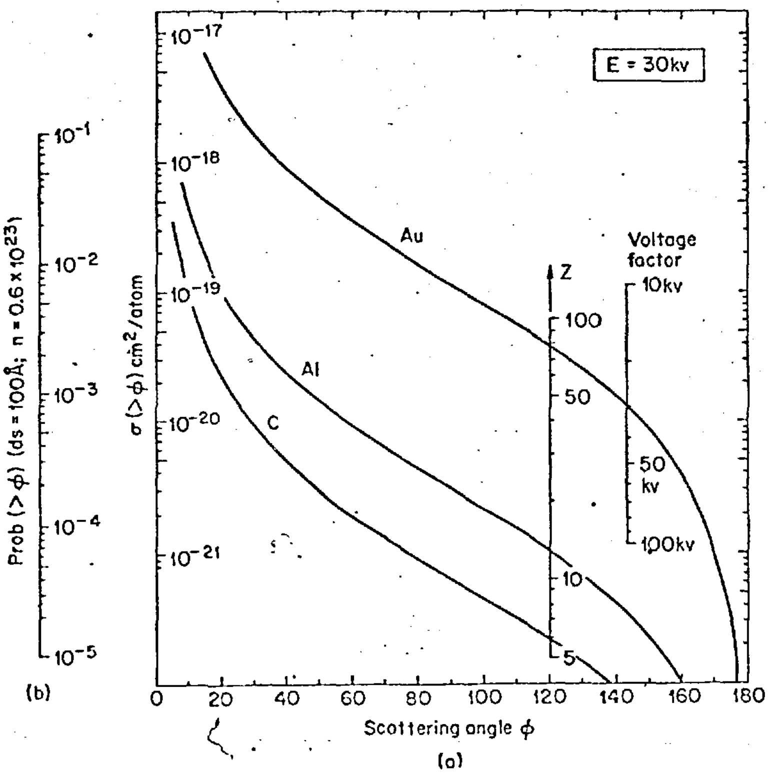

FIG. 3.1 (*a*) Total Rutherford scattering cross section for C, Al, and Au at 30 kv; (*b*) probability of a Rutherford scattering event through an angle $> \phi$ for a path element of length 100 Å.

Fig 1.3 Total Rutherford cross sections.
(Wells et al, 1974)

but

$$\Omega = 2\pi(1 - \cos\varphi) \qquad 1.3$$

$$\therefore \frac{d\sigma}{d\Omega} = \frac{1}{2\pi \sin\varphi} \cdot \frac{d\sigma(>\varphi)}{d\varphi} \qquad 1.4$$

The probability of a scattering event involving a deflection through an angle greater than φ is

$$\text{Prob}(>\varphi) = n\ \sigma(>\varphi)\, ds \qquad 1.5$$

where n is the number of atoms m^{-3}, and ds is the thickness considered.

The mean distance (free path), L, between events is given by :

$$L = \frac{1}{n\ \sigma} \qquad 1.1$$

1.11 Separate processes

It is convenient to divide the processes into those which change the direction of the electrons and those which produce loss in their energy.

1.12 Wide angle scattering

The most efficient process for the high angle scattering of electrons (scattering angle $\gg 5^{\circ}$) is the electrostatic interaction between the atomic nucleus and the electron (Rutherford, 1911). Following Evans (1955), the differential Rutherford scattering cross section is

$$\frac{d\sigma}{d\Omega} = \frac{d}{16} \csc^4 \frac{\varphi}{2} \qquad 1.6$$

d is the distance of closest approach between the nucleus and the electron. Thus,

$$\frac{d\sigma}{d\Omega} \approx 1\cdot3 \times 10^{-19} \frac{Z^2}{E^2} \csc^4 \frac{\varphi}{2} \qquad 1.7$$

where E is in electron volts. This does not account for the screening of the nucleus by its surrounding electrons. Taking this into consideration, the cross section becomes:

$$\frac{d\sigma}{d\Omega} = \frac{d^2}{16}\left(\sin^2\frac{\varphi}{2} + \frac{\varphi_1}{4}\right)^{-2} \qquad 1.8$$

where

$$\varphi_1 = 3.69\,\frac{Z^{1/3}}{E^{1/2}} \qquad 1.9$$

These are shown in fig. 1.3a. Fig. 1.3b shows the probability of a Rutherford scattering event through an angle greater than φ for a path element of length 10 nm.

It can be seen that the probability of scattering through angles of between 10° and 20° is relatively high, even for elements of low atomic number such as carbon.

Fig. 1.4 gives the differential cross-section which gives a better indication of the intensity observed in any particular direction. From this it is evident that elastic electron scattering through angles of greater than 90° is probable, particularly for high atomic weight elements.

1.13 Energy loss produced by elastic scattering

The energy loss associated with a Rutherford type collision is given by :

$$\Delta E = \frac{2mE}{M}(1 - \cos\varphi) \qquad 1.10$$

where m = mass of electron

M = mass of nucleus

φ = deflection angle

Thus, for a scattering of 150° from gold at 20 keV, the energy loss is 0.21 eV. The same scattering from carbon would produce an energy loss 3.37 eV, and from aluminium 1.50 eV. Boersch (1971) has argued that this loss will only occur if the phonon excitation energy is less than the predicted value for ΔE.

The formulae presented here are classical approximations. More accurate results for the scattering cross sections can be obtained by a quantum mechanical treatment (Motz, Olsen and Koch, 1964). The results so obtained are, however, in numerical rather than analytic form, and offer little more insight into electron scattering in the energy range (15 - 20 keV) under consideration.

1.14 Energy loss processes

In general, processes producing large energy loss are concerned with electron-electron interactions. The incident electron may ionize an atom, may cause an inter-band transition or may produce a collective excitation of all the electrons in a crystal (a plasmon).

The cross sections of the individual processes are discussed in detail by Green and Leckey (1976) and are shown for Aluminium in the range 0 - 20 keV in Fig. 1.5. From this it can be seen that the plasmon cross section is considerably higher than those for either ionization or individual electron excitations. The three processes, however, contribute almost equally to the total energy loss rate for any electron. This is because of the relative losses produced by each process. The plasmon loss is usually in the range 6 - 15 eV, whereas the other losses tend to be 40 – 50 eV. The probable energy loss per unit path length due to either process is sufficiently similar for an approximation to be used, which does not distinguish between the two types of process. This leads to the Bethe energy loss law, which relates the energy loss of an electron to the length of its path through a solid and also to the Thomson -Whiddington law, which obtains a similar relationship empirically (Cosslett and Thomas, 1964c).

1.15 Models for electron penetration

Most models for electron penetration into a solid have used a Rutherford cross section to predict the angular deflection of the electrons followed by a continuous loss approximation of either Bethe or Thomson - Whiddington to describe the energy loss within the solid. The models fall into two distinct classes, diffusion models and single or multiple - event backscattering models.

1.16 Diffusion models

Bethe, Rose and Smith (1938); Archard (1961); and Tomlin (1963) all produce models which describe electron scattering in terms of diffusion from a mean depth below the surface of the specimen. These predict the correct relative energy distribution, though with too low a value for the mean energy, and as with any model based on a continuous loss law, it ignores the possibility of electrons being backscattered with almost no loss in energy.

1.17 Single event backscattering model

Everhart (1960) proposed a model for backscattering in which the electron was assumed to travel in a straight line until either it lost all energy, or was scattered out of the crystal by a Rutherford scattering event involving an angle greater than 90°. Again this did not take account of the probability of electrons losing energy at a different rate from the mean, and thus did not predict an elastic component in the backscattered direction.

This model was extended to include two scattering events by Archard (1961), and is discussed in detail by Cosslett and Thomas (1965).

1.18 Monte Carlo method

In a Monte Carlo calculation the paths of individual electrons are traced on the basis of a random number selection of their possible scattering events. This is extensively discussed by Shimizu et al (1975 and 1976). Assuming that sufficient trajectories are used, a very accurate picture can be built up of the scattering within a solid.

A limitation of this method is that a vast number of trajectories must be

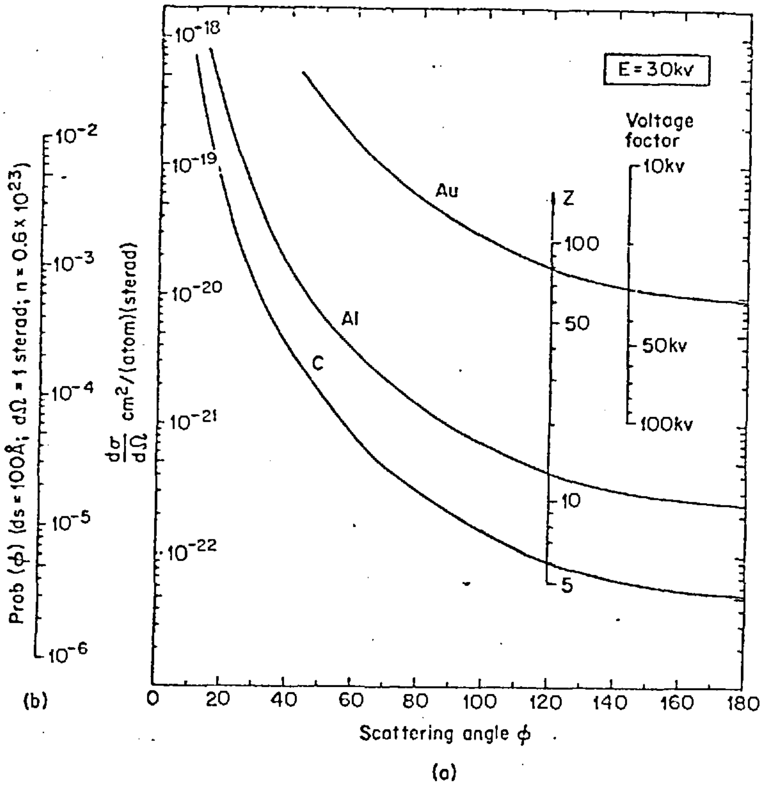

FIG. 3.2 (*a*) Differential Rutherford scattering cross section for C, Al, and Au at 30 kv; (*b*) Probability of a Rutherford scattering event through an angle ϕ into a collection solid angle of 1 sterad for a path element of length 100 Å.

Fig 1.4 Differential Rutherford scattering cross sections. (Wells et al,1974)

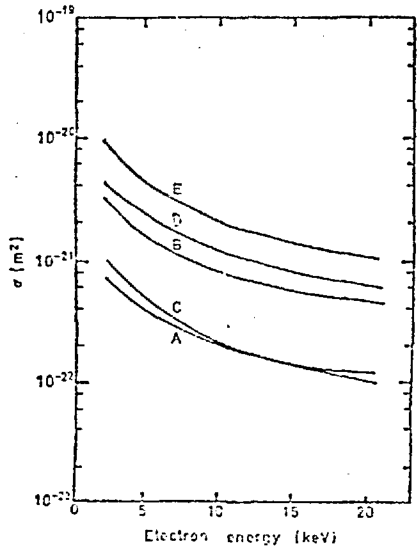

Figure 4. Contributions to the total cross-section for electron scattering per atom in Al. A, inner shell ionization; B, plasmon scattering; C, individual conduction electron excitation; D, total inelastic scattering; E, elastic scattering.

Fig 1.5 Contribution of the separate processes to the total scattering cross section for Al. (Green and Leckey, 1976) calculated to produce a statistically accurate result. This has led to the use of the continuous loss approximation in all calculations of backscattering coefficients or energy loss spectra, e.g. Bishop (1966), Budal (1970), Dashen (1964), Verdier and Arnal (1969), and Arnal, Verdier et al (1969).

In Monte Carlo calculations to predict forward scattering spectra, it has been possible to use accurate cross sections to describe the scattering processes, Green and Leckey (1976), Shimizu et al (1975 and 1976). In these cases elastic scattering can be predicted, though in no case has sufficient energy resolution been used to verify it.

1.19 Conclusion

There is, as yet, no calculation which gives an accurate picture of elastic scattering to high angles. This is because the continuous energy loss process has always been assumed. Therefore no theoretical comparison can be made with the experimental results obtained in Chapter 6.

The problem of computation seems at first glance relatively trivial. However, the vast number of trajectories involved for high resolution require a large investment of computer time. A rough estimate gives a minimum requirement of 10^7 trajectories to produce an accurate picture of the backscattering of 20 keV electrons from gold. The computer time needed for this would be in excess of 400 hours if the program operates at a similar speed to that of Green and Leckey (1976).

Such studies are at the moment possible, though a specific study of the elastic component (Chapter 6) in the spectrum seems the only calculation which would be of sufficient interest to be worthwhile.

CHAPTER 2

APPARATUS

2.1 Introduction

The apparatus, designed and constructed by Dr. P.N.J. Dennis, is described below. The major reconstruction of the apparatus done by the author is described in Chapter 4. One exception to this is the minor rearrangement of the pumping line made by the author, described below.

2.2 Overall design of the vacuum tank

The initial design concept for the apparatus was of an electron spectrometer having a set of electron energy analysers ranged around a central scattering specimen. The apparatus would thus be able to record the energy spectra of initially monochromatic electrons scattered by a specimen, in several directions simultaneously.

The chamber (frontispiece) was constructed as a right cylinder 350mm deep and 300mm internal diameter. All seals on the chamber were standard knife edge with copper gaskets, except for the top and bottom plates of the main chamber, which used gold wire seals. The chamber itself was built to ultra high vacuum standards (Ward and Bunn, 1967; Readhead et al, 1968; Green, 1968; Robinson, 1968) of stainless steel (EN58B) internally arc welded.

Six 115 mm diameter ports were spaced at 30° intervals around the chamber in one plane about the central axis. A 70 mm diameter port for an electron gun and two 150 mm diameter viewing ports were fitted in the same plane. The chamber was also equipped with two ports for evaporators inclined at 45° to the specimen axis and directed at the specimen, together with one for an ion guage near the base of the chamber. A Vacuum Generators UMD 2 specimen manipulator was fitted to the top plate so that the specimen could be situated at the centre of the chamber in the plane

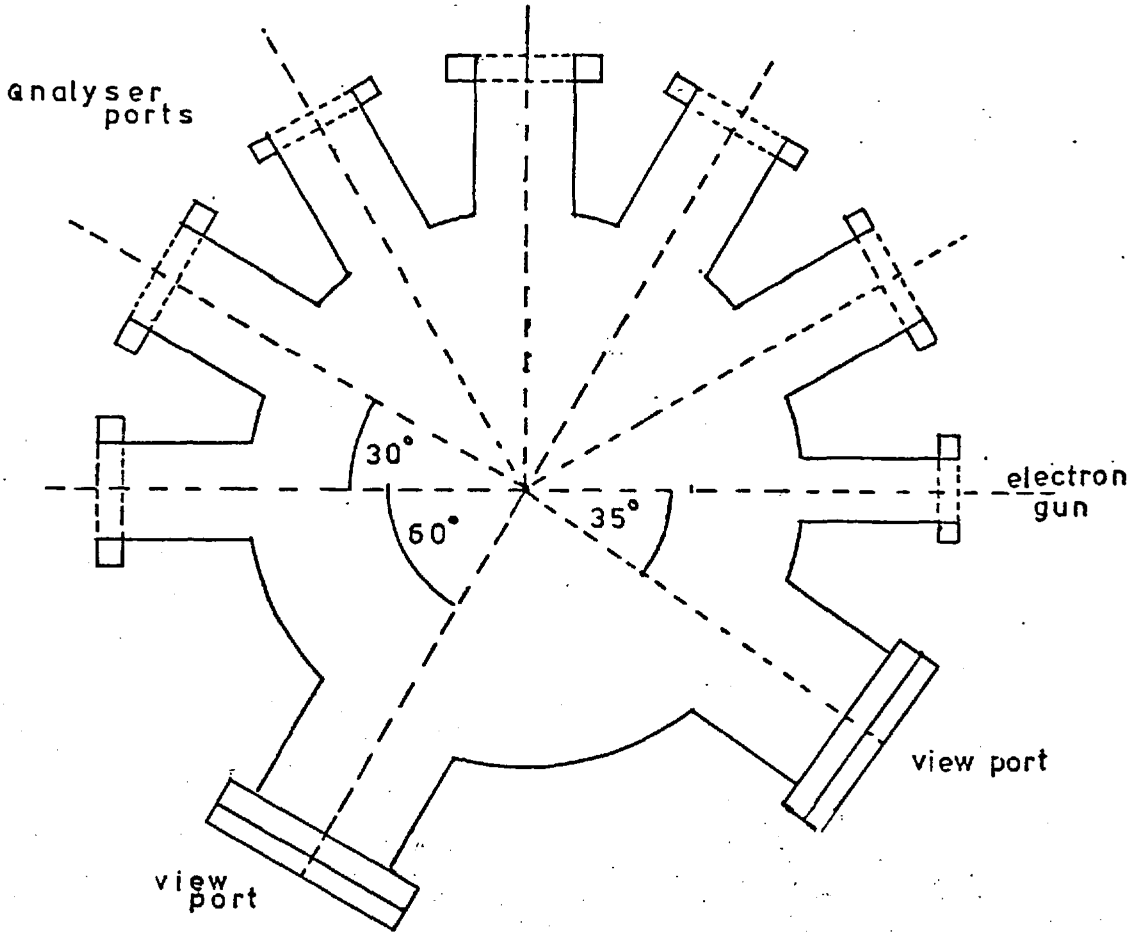

Fig. 2.1 Spectrometer main chamber, horizontal section.

of the analyser ports. The manipulator provided three rotational and three translational degrees of freedom.

2.3 The pumping system

The main chamber was linked to the pumping system (Fig. 2.2) via a 460 mm long L bend of 150 mm diameter steel tubing (frontispiece). The reason for this rather curious arrangement was so that the base of the chamber was left free for the addition of a camera similar to that of Alam (1952).

The pumping system consisted of an Edwards High Vacuum EO4 diffusion pump using polyphenyl ether pumping fluid ('Santovac 5', manufactured by Monsanto Co.) This was backed by an Edwards ES200 two stage rotary pump connected to it by a magnetic valve and gauze filter. The filter was initially mounted horizontally. (Fig. 2.2 solid line). A water cooled baffle and liquid nitrogen trap were fitted above the diffusion pump.

The system had no roughing line as such. Rough pumping to 1 Pa was done through the diffusion pump whilst it was cold. It was thus necessary to allow the diffusion pump to cool down before the chamber could be let up to atmospheric pressure. In practice this did not prove a nuisance and saved considerably in the cost and complexity of the backing line. The pumping system and base unit were constructed by Vaughn and Cameron Ltd.

Considerable contamination of the chamber by burned rotary pump oil was noticed after the system had been in use for about two years. It was found that, despite the gauze filter, rotary pump oil had been backstreaming to the diffusion pump. It was found that the manufacturers' specification was that the filter should only be used in the vertical position, and this explained the contamination.

The backing line was altered (broken line, Fig. 2.2) to include a bakeable zeolite oil trap. The gauze filter was repositioned as shown, and a 1" hand valve

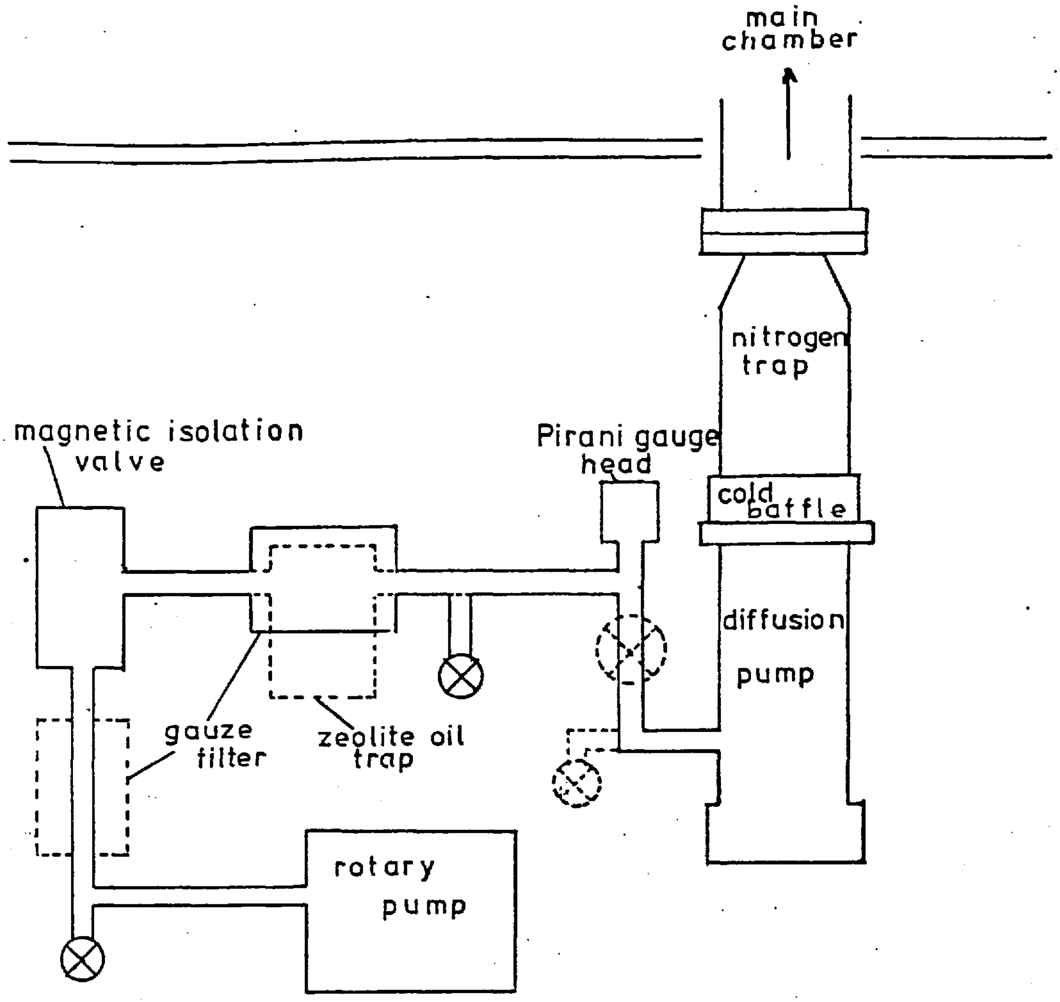

Fig. 2.2 The pumping system. The original system is shown, solid line, together with later additions, pecked line.

was fitted between the trap and the diffusion pump.

The system was originally compatible with U.H.V. This restraint was relaxed to save the large number of copper gaskets used. These were replaced by flat viton, which, though more expensive than copper, have an indefinite life if used with care. The base pressure of a viton sealed system is generally of the order of 1×10^{-6}Pa , which was well below the required pressure of 2×10^{-5}Pa at which the system was usually operated.

The system was never completely baked, though both the gun and analyser were locally baked to 100°C after each time they were let up to atmospheric pressure. This local heating was done using asbestos covered electrical heating tape loosely wrapped around the component and removed after use. Small internal components were heated using an elliptical mirror and heating lamp of the type used by Unvala and Maries (1974). When local heating was used, the temperature was not raised by more than 100°C to avoid damage to the viton rings used to seal the flanges.

2.4 The electron gun

The spectrometer had one electron gun mounted, with its lens, on the 70 mm port of the main chamber (Fig. 2.1). Several electron guns, all originally designed for cathode ray tubes, were tried by Dr. Dennis. The final one (Fig. 2.3) (designed for the G.E.C. T490 series of tubes) was of the conventional triode type (Klemperer and Barnett, 1971, Fig. 4.23) having grid, anode and cathode rigidly mounted on three ceramic bars. The indirectly heated cathode was oxide coated to increase electron emission.

The gun was insulated from the chamber by a pyrex tube and was connected to the external high voltage supply by tungsten lead-throughs in the re-entrant glass to metal seal. The anode had sliding spring contacts with the vacuum tube wall.

A coil of 400 turns was used to focus the beam (Fig. 2.3). A pair of

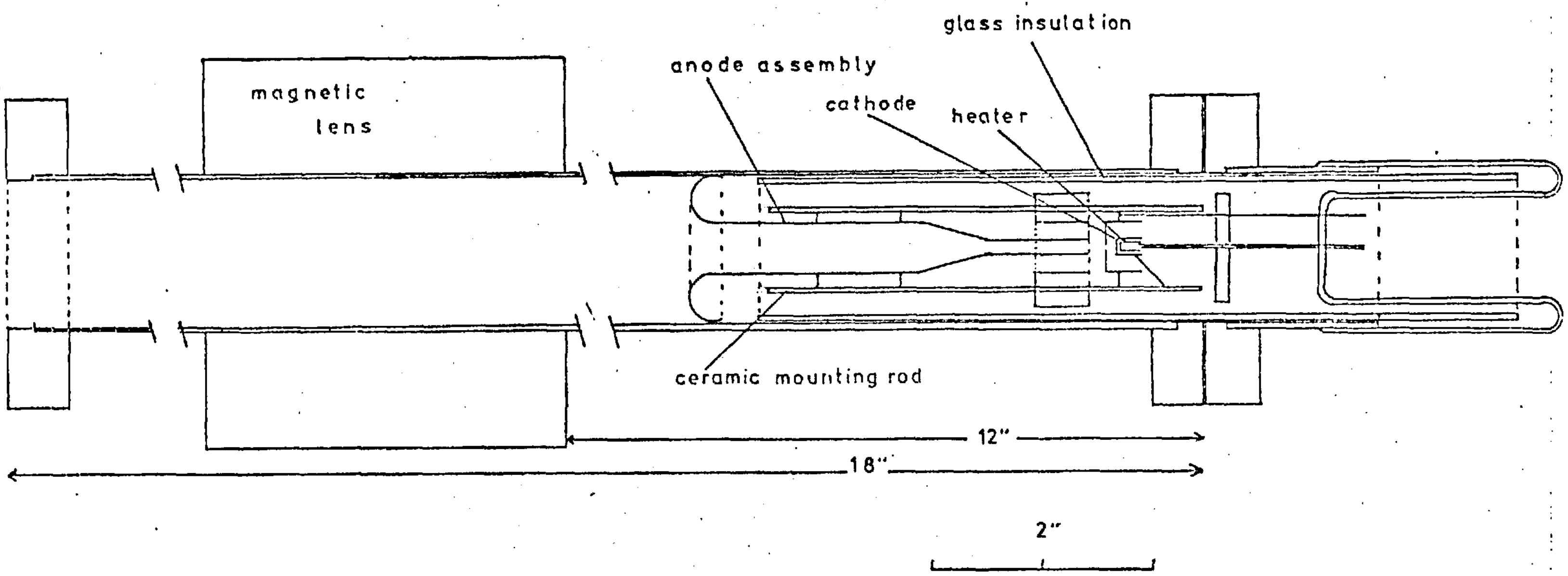

<u>Fig.2.3</u> Electron gun (for G.E.C. T490 series of tubes)

deflection coils were fitted to the tube between the lens and the main chamber.

The gun and lens combination typically gave a beam current of 5×10^{-8}A at 20 keV into a spot 2 mm in diameter.

2.5 The electron energy analyser

The analyser chosen by Dr. Dennis was a simple retarding field using a mesh filter (the details of the operation of this type of analyser are discussed in Chapter 4). The analyser chamber was in the form of a 'T' piece (Fig. 2.4) rigidly fixed to one of the analyser ports (Fig. 2.1). Electrons entered the analyser via two collimating apertures. The apertures were each 100 μm diameter holes in 3 mm molybdenum discs designed for use in an electron microscope. The discs were held by tungsten springs in two holders separated by 20mm. The holders were fixed together and mounted on three adjusting screws at the front of the analyser. This arrangement allowed free pumping of the analyser chamber, whilst preventing electrons entering it by any route other than the defining apertures.

A Willemite (Zn_2 SiO_4 or $2ZnO$-SiO_2) phosphor was laid on the aperture holder facing into the main chamber. This could be seen through one or other of the viewing ports. The arm of the main chamber onto which the analyser was attached was fitted with a pair of deflection coils to align the electron beam relative to the apertures.

The retarding electrode (Fig. 2.5) consisted of a short stainless steel tube rigidly suspended from a 50 kV ceramic insulator attached to the 70 mm diameter flange of the 'T' piece. The outer surfaces of the tube were rounded and polished to 20 μm using alumina paste, to reduce field emission between the electrode and the walls of the analyser.

The outer tube contained a second, divided tube, which acted as support for a wire mesh. The 60 lines per mm mesh was mounted by stretching a small piece over one half of the tube and cementing it in place with conducting 'Araldite'. The

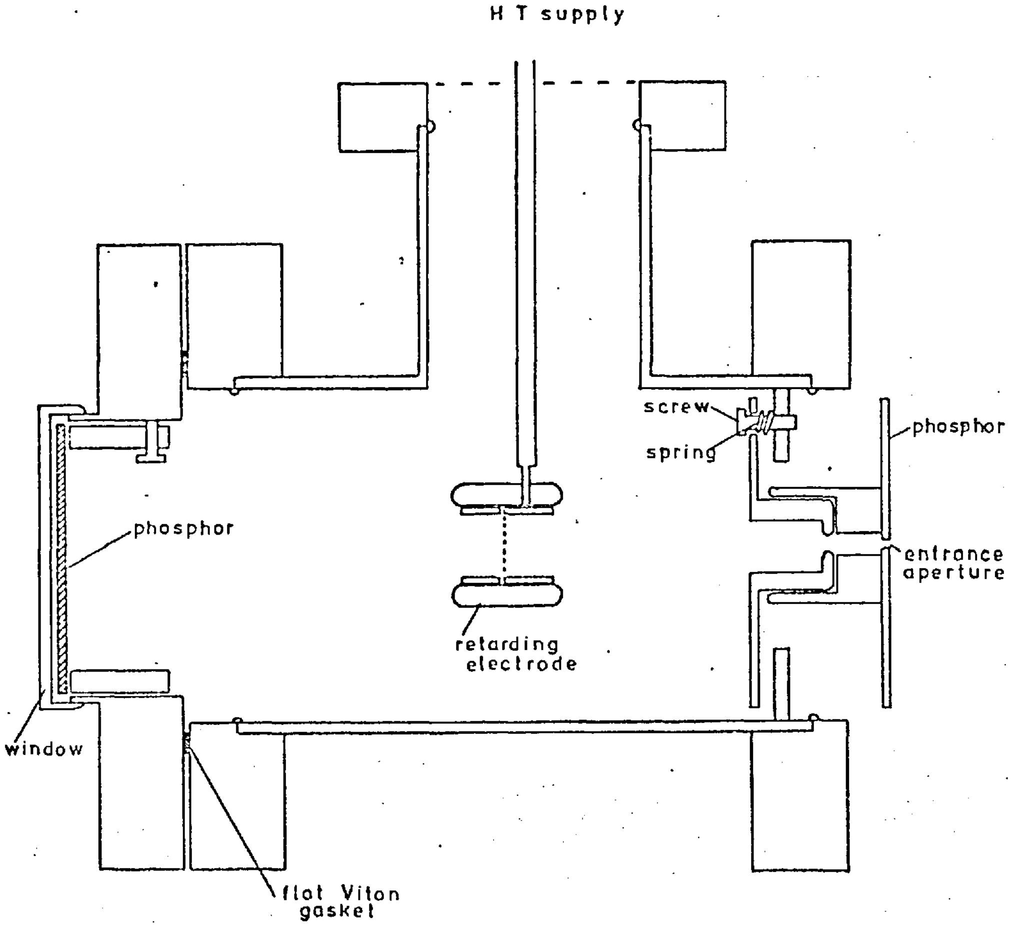

Fig. 2.4 The original analyser, vertical section. The 30kV insulating seal between the analyser chamber and the electrode is not shown.

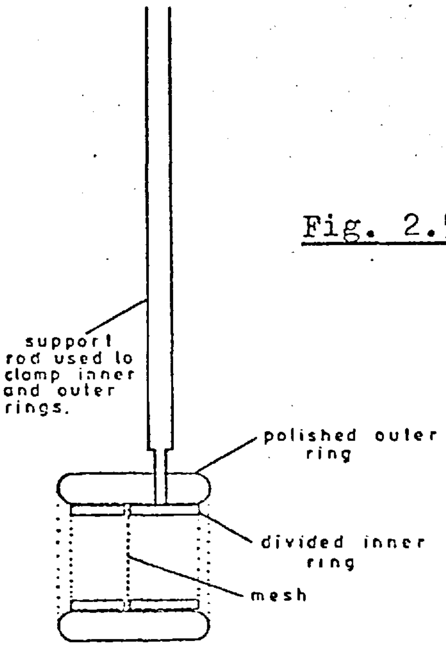

Fig. 2.5 The analyser electrode.

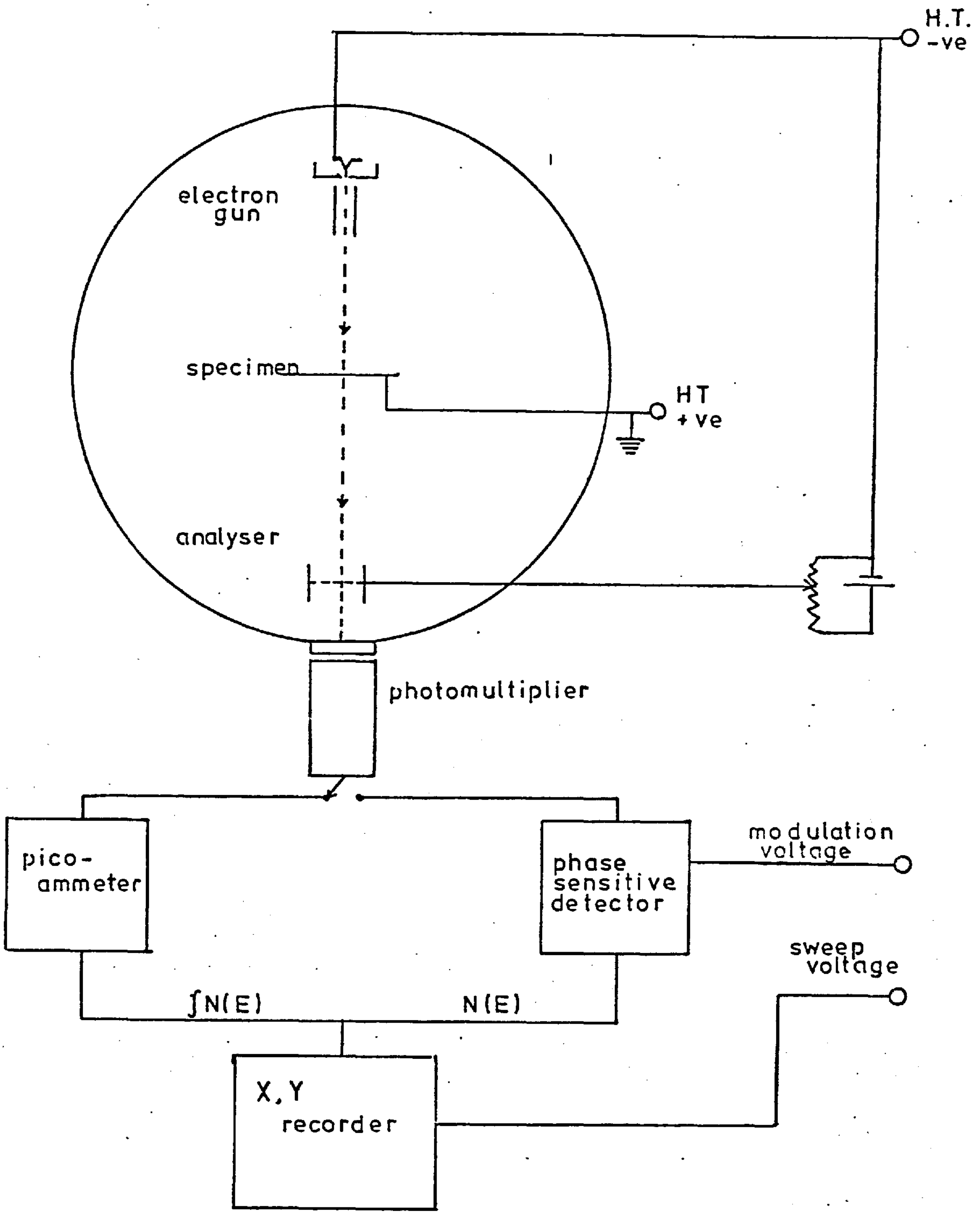

Fig. 2.6 Schematic diagram of the electron detection and recording system.

The output of the photomultiplier could either be recorded directly as $\int N(E)dE$ vs E or differentiated and recorded as N(E)dE vs E.

two halves of the tube were then cemented together and slid into the outer tube, where it was clamped by the end of the copper supporting rod which screwed through the outer tube.

Despite considerable care, the mesh was never planar and usually showed deviations of between one and three degrees over a large proportion of the area of the mesh.

The mesh electrode acted as a high pass filter or potential step. Those electrons with sufficient energy to surmount the potential barrier were accelerated back to earth potential and detected using the phosphor and photomultiplier shown schematically in Fig. 2.6.

The output of the photomultiplier could either be used by direct measurement with a picoammeter to give a record of $\int N(E)$, or by electrical differentiation, using a phase sensitive detector, to give N(E) directly (Fig. 2.6). The method of differentiation has been discussed by Leder and Simpson (1958), Denbigh and Grigson (1965), Curtis and Ferrier (1970), and others. In the context of this experiment it is further discussed in Chapters 4 and 5, and Appendix 4.

2.6 Electrode potential modulation

The high tension supply was reconstructed by the author and is described in Chapter 4. The reason for this was that the H.T. had been the subject of continual development, and the boxes housing it needed rebuilding to reduce the number of breakdowns. The only feature altered was the means of supplying the small alternating voltage to the retarding electrode necessary for electrical differentiation of the output signal from the photomultiplier.

The system developed by Dr. Dennis was the optical link shown schematically in Fig. 2.7. The main elements of the link were the matched photodiode (TIL32) and phototransistor (TIL78) combination.

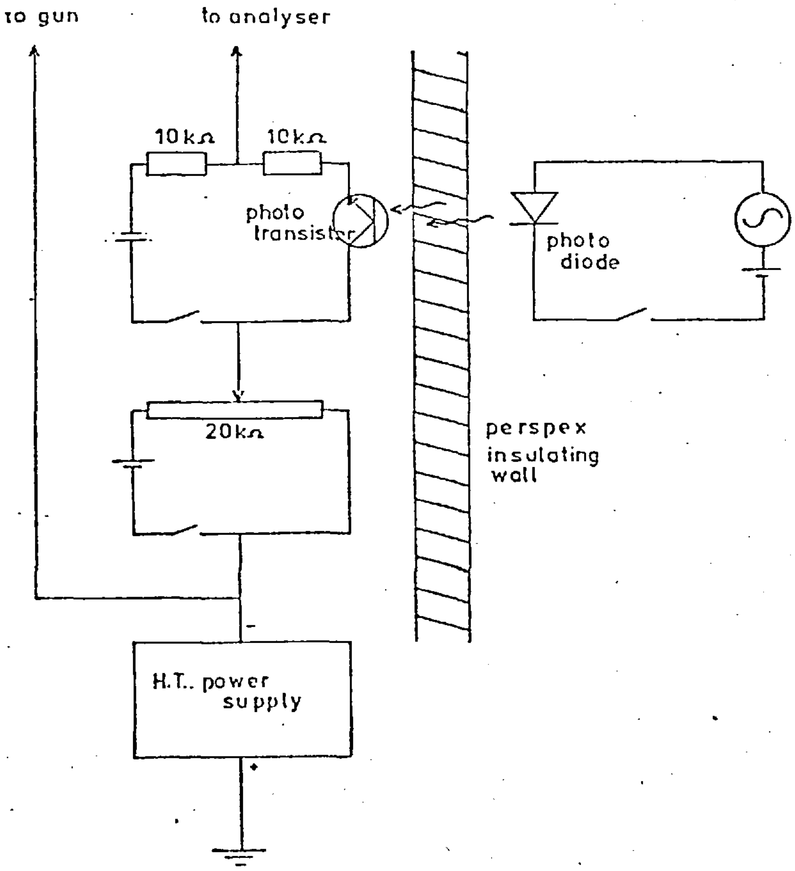

Fig. 2.7 Method of modulation of the H.T. supply be means of a photo-diode and photo - transistor.

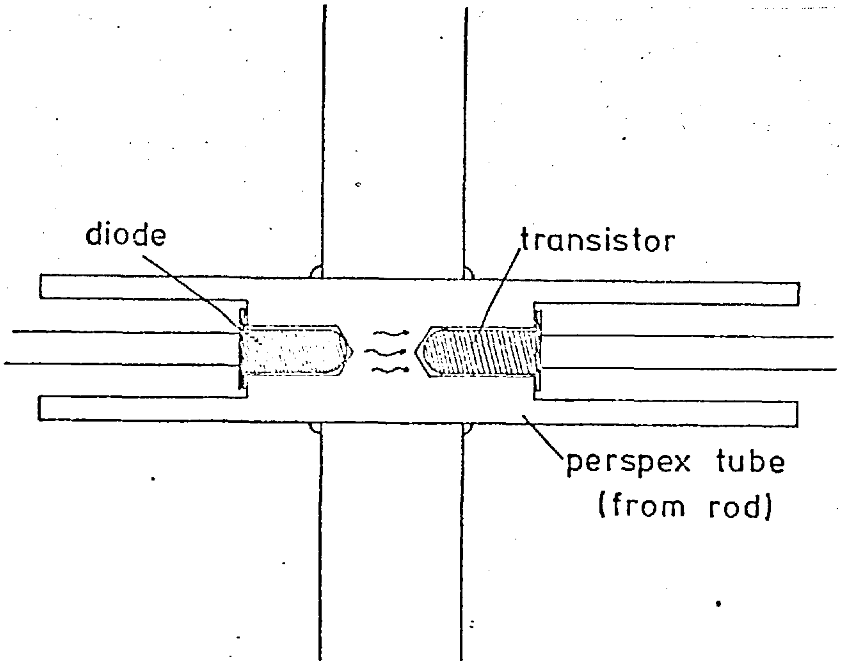

Fig. 2.8 Detail of mounting of photo- diode and photo-transistor in a perspex rod to provide maximum optical coupling and electrical insulation across the wall of the H.T. box.

The photodiode was modulated by a signal generator in the frequency range 5 Hz – 2 kHz, which also provided the reference for the phase sensitive detector (PSD). The light from the photodiode was used to modulate the output of the phototransistor in the simple circuit shown. Initially the circuit produced 0.2 V RMS modulation at the retard electrode. This was not sufficient modulation, and so a system (Fig. 2.8) for closer coupling of the phototransistor and photodiode was devised by the author. The two were mounted in a drilled perspex rod, so that they were separated by 2 mm and well aligned with respect to each other, yet were well insulated, having 150 mm track length between them. Stray light was excluded by painting the outer surface of the rod. This essentially produced a 50 kV opto-isolator. The system provided 0.5 V RMS modulation, which was sufficient until that part of the system was rebuilt. The opto-isolator was later replaced with a capacitor link (Chapter 4). The reason for this was the opto-isolator was easily damaged by H.T. discharges which did not affect the more robust capacitor. Given a more stable H.T. system, the small modulating voltage obtained by the opto-isolator could easily have been amplified (Curtis and Ferrier, 1970) to provide suitable amplitude for modulation of the H.T. voltage.

2.7 System performance

The spectrum, N(E), in the energy range E_o to E_o-60eV for electrons transmitted through a specimen of polycrystalline aluminium on amorphous carbon is shown (Fig. 2.9). This was not reproducible, and the apparent features of the curve indicated must be severely doubted in the light of the width of the 'elastic' peak in relation to that of the main loss peaks. This was regarded as a particularly good result. The more usual state of the system may be appreciated from the integral ($\int N(E)$) spectra shown in Fig. 2.10. This shows the spectra for different values of the analyser deflection coil current for a carbon specimen. Remembering that N(E) is always

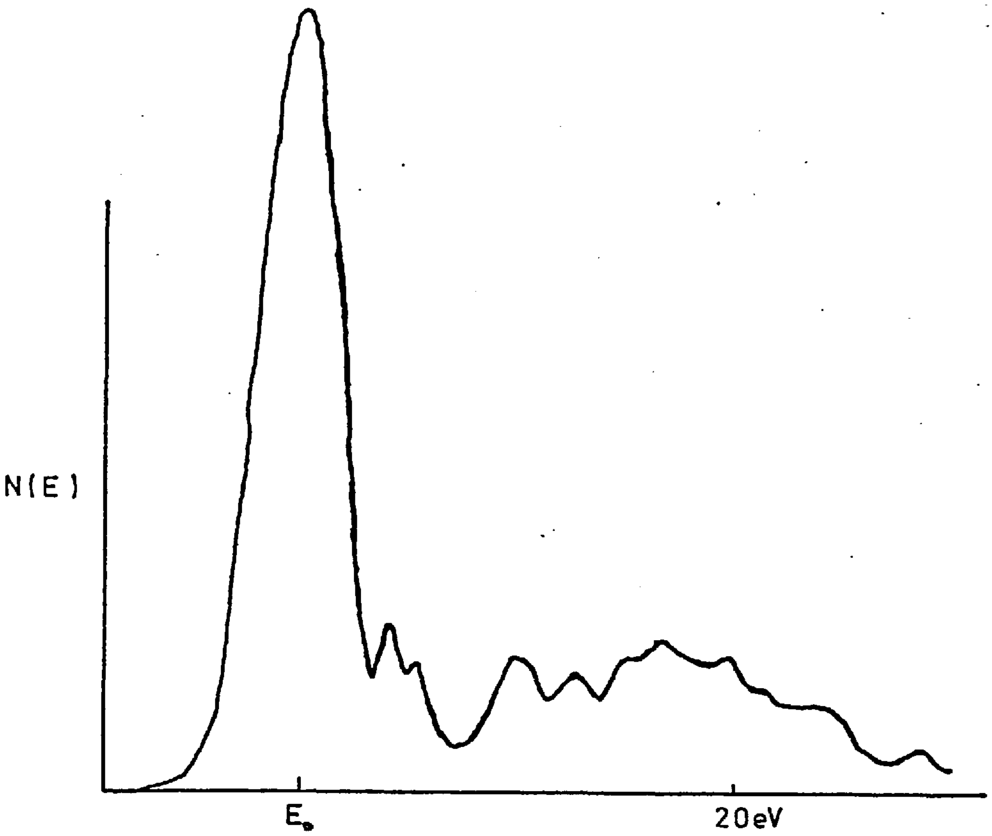

Fig. 2.9 Differential transmission spectrum taken from a thin carbon film using a beam energy of 20 keV.

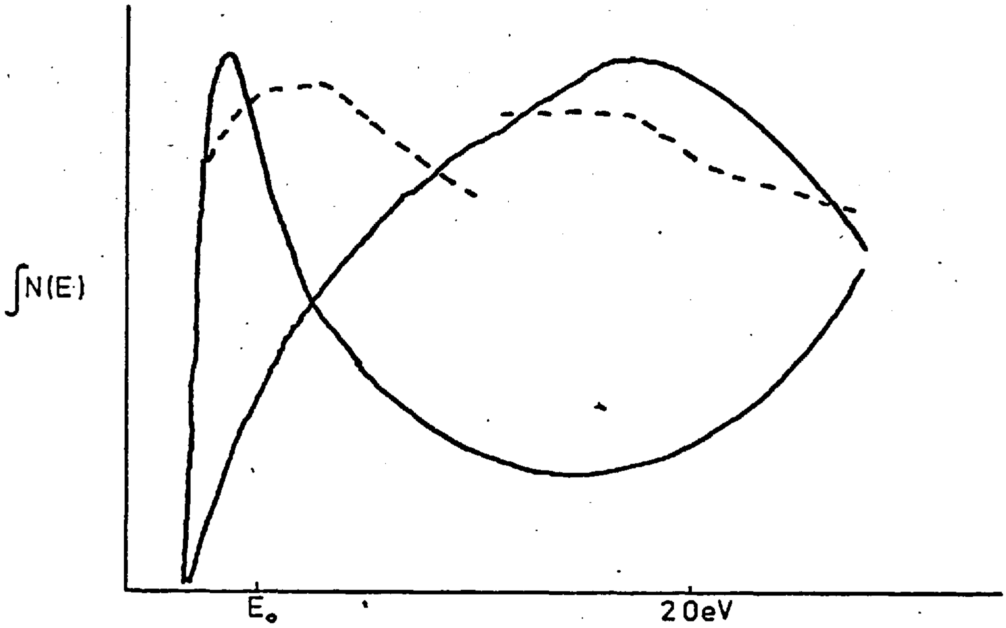

Fig. 2.10 Integral transmission spectra taken from a thin carbon film using a beam energy of 20 keV.

The various lines show the effect of different settings of the coils used to direct the beam into the entrance aperture of the analyser.

greater than, or equal to, zero, it must be concluded that the system was not functioning correctly. These results were obtained by Dr. Dennis in June 1974.

CHAPTER 3

ELECTRON ENERGY ANALYSERS

3.1 The choice of an analyser

The choice of electron energy analyser was reviewed when it was found that the original analyser was unsatisfactory and required entire reconstruction. For completeness this review has been extended to include analysers covering the energy ranges between 0 and 100 keV.

Charged particle energy analysers are conveniently classified as dispersive or non-dispersive, though hybrids do exist ie. dispersive analysers used with retarding fields.

The dispersive analysers usually spread an electron beam in angle according to the electron energy. Measurements are obtained either by recording the complete spectrum with, for example, a photographic plate, or by varying the power of the dispersive element of the spectrometer and scanning the spectrum over a detection aperture.

The advantage of this type of spectrometer is that the signal output, f(N(E), E). dE, can usually be directly interpreted as being the energy spectrum, N(E).dE. Here N(E).dE represents the number of electrons with energy in the range E to E + dE and f(N(E), E).dE is a function of N(E) and E. In practice, the instrumental transfer function, g(E), is made independent of N(E), thus the output signal, f(N(E), E).dE becomes g(E).N(E).dE. If g(E) is constant, the signal is, with suitable scaling, N(E).dE, where dE is the resolution of the instrument.

The non-dispersive analysers are high pass filters allowing high energy electrons to pass while rejecting low energy ones. The resolution of the system depends on the convergence of the electron beam at the analyser and the uniformity of the potential step. The output of a non-dispersive system is usually $\int_{E_o}^{\infty} N(E).g(E).dE$, where E_o

is the energy to which the filter is set. The main advantage of this type of system is its simplicity of concept and construction.

3.2 Signal to noise ratio

The signal to noise ratio of a dispersive analyser is always better than that of a non-dispersive one. The required spectrum is, in either case, N(E).dE. The noise signal, (I_n), produced by Shot noise, is given by the square root of the total signal (Taylor, 1972). The non-dispersive analyser thus has a signal to noise ratio (I_s/I_n) given by $N(E).dE / (\int_{E_o}^{\infty} N(E).dE)^{\frac{1}{2}}$, whereas the dispersive analyser gives a ratio $I_s/I_n = N(E).dE / (N(E).dE)^{\frac{1}{2}}$. It is clear from this that for Shot noise, which is the basic and unavoidable type, a dispersive analyser will always give a better separation of signal and noise than a non-dispersive analyser of the same resolution, dE.

This has been discussed by several authors, notably Taylor (1969 and 1972) and Chang (1971). Both authors compare 127° dispersive analysers with low energy electron diffraction (LEED) hemispherical retarding potential analysers (RPA); however, their comments are generally applicable.

3.3 Requirements

The analyser for this work had to meet several different requirements, some of which were in strong conflict. The vacuum chamber could not be altered appreciably, thus the analyser had to operate 200mm from the specimen and be mounted on a 112 mm diameter copper-sealed flange. Workshop and technical facilities and time were limited, and thus the analyser design had to be such that it could be constructed simply and without outside help.

The analyser was required to give a resolution (E/dE) greater than 1000, preferably 10 000. (This is equivalent to 20 eV and 2 eV respectively with a beam energy of 20 keV). The analyser was expected to operate over the energy range

5 keV to 30 keV, allowing scans of ± 50 eV at maximum resolution. It also had to be capable of low resolution (c 100) scans over the complete range from 5 keV to 30 keV. To the resolution requirements was added the need to be able to align the analyser without a reference beam and for considerable tolerance in the specimen position.

3.4 Order of focus

In the following discussion the terms "first order focus" and "second order focus" are used in describing the properties of analysers. It is useful to explain the meaning of these terms by considering the first order focus produced by a simple magnetic analyser. Consider the magnetic analyser (Fig. 3.1) referred to a rectangular set of coordinates. All electrons of velocity v entering the analyser at the entrance aperture (0,0) will follow a circular path of radius $r = \frac{v}{B} \cdot \frac{m}{e}$ where

v = velocity

B = field strength

e/m = charge to mass ratio of electron

The position of the centre of this circle will depend on the angle ϑ that the incident electron makes with the y axis (see Fig. 3.1). The analytic equation of the path of any electron is thus

$$x^2 - 2ax\cos\vartheta + y^2 - 2ay\sin\vartheta = 0$$

from which it can be seen that the electron crosses the x axis at the point $x = 2a\cos\vartheta$ Now for small $x = 2a\left(1 - \vartheta^2/2\right)$, thus the crossing point is independent of θ though it does depend on ϑ^2. This crossing point is thus the first order focus of all electrons leaving (0,0) at small angles to the y axis (Fig. 3.2). In some analyser geometrics, second and even third order foci can be obtained where the position of the focus is independent not only of ϑ but of ϑ^2 and ϑ^3 respectively.

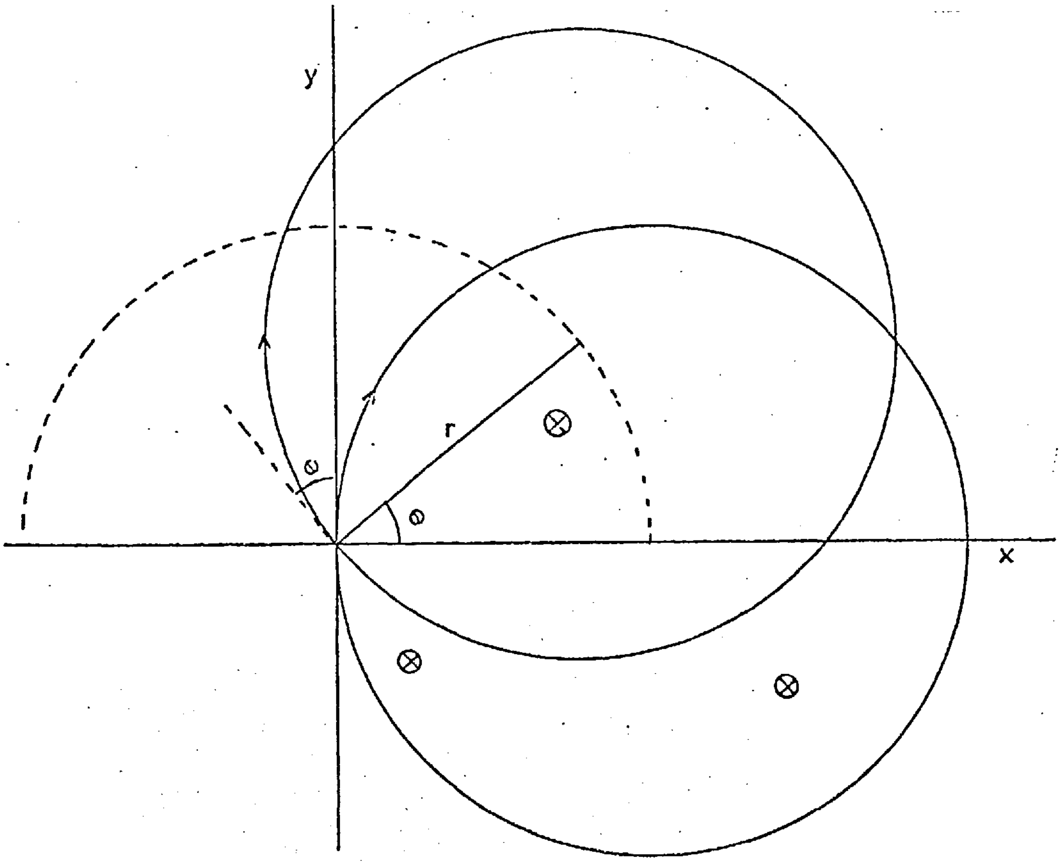

Fig.3.1 Paths of electrons in a uniform magnetic field.

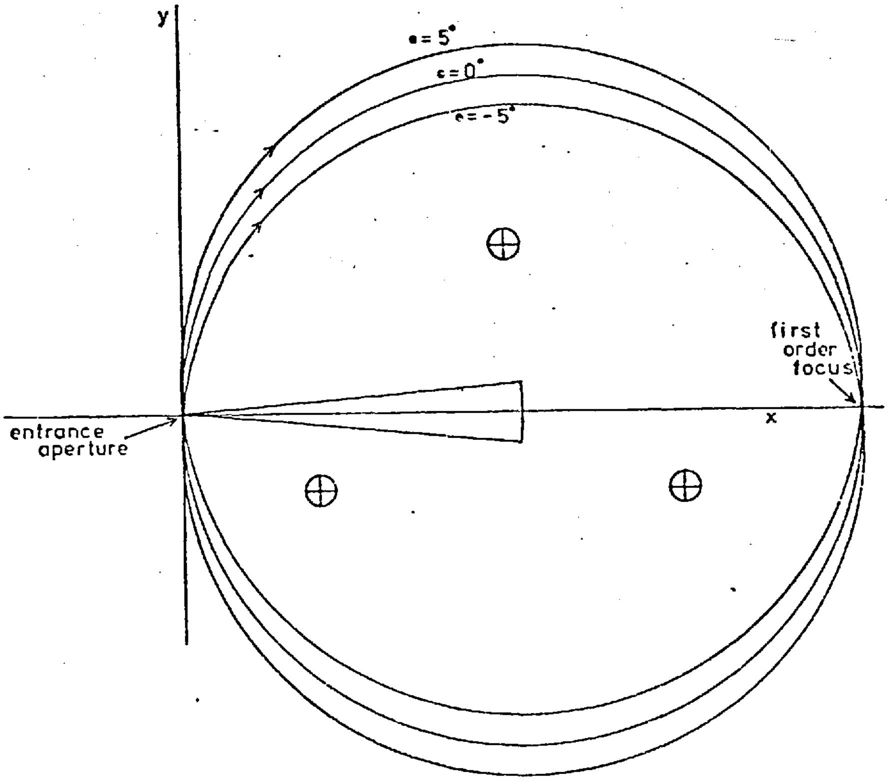

Fig.3.2 Paths of mono-energetic electrons in a uniform magnetic field showing a first order focus in ϑ .

3.5 Magnetic analysers

Magnetic analysers for electrons in the energy range 5 - 30 keV have been described by several authors (reviewed in detail by Sevier, 1972). They are generally complex in structure and involve careful design of the field around the entrance and exit apertures or the use of very small angular acceptance to obtain the desired resolution. (Klemperer and Shepherd , 1963 , Cole and Jennings, 1971). The design parameters are well known (Sevier, 1972), thus, despite their complexity they have been widely used.

Magnetic analysers have the following virtues :

i) Parasitic magnetic fields (e.g. Earth field) are of minor importance as electrons are not slowed in their transit through the analyser.

ii) There are no problems with high voltage electrodes (see Chapters 4 and 5) and no problems with field emission (see Chapter 5).

iii) They can be designed to image to any accuracy (the diffraction limit is not a real constraint).

This last property has resulted in the use of magnetic analysers for the improvement of the image contrast from thick specimens in the electron microscope.

Fig. 3.3 shows two examples of asymmetric magnetic analysers, each providing a second order line focus.

3.6 180° Analyser

It has been appreciated by many workers that a first order focus may be obtained by 180° deflection of charged particles in a uniform magnetic field (section 3.3) (Siegbahn, 1965 ; Danysy, 1912, 1913; Castaing et Henry, 1962 and 1964). The symmetry of this system allows two 90° deflections to be used to obtain a spread in

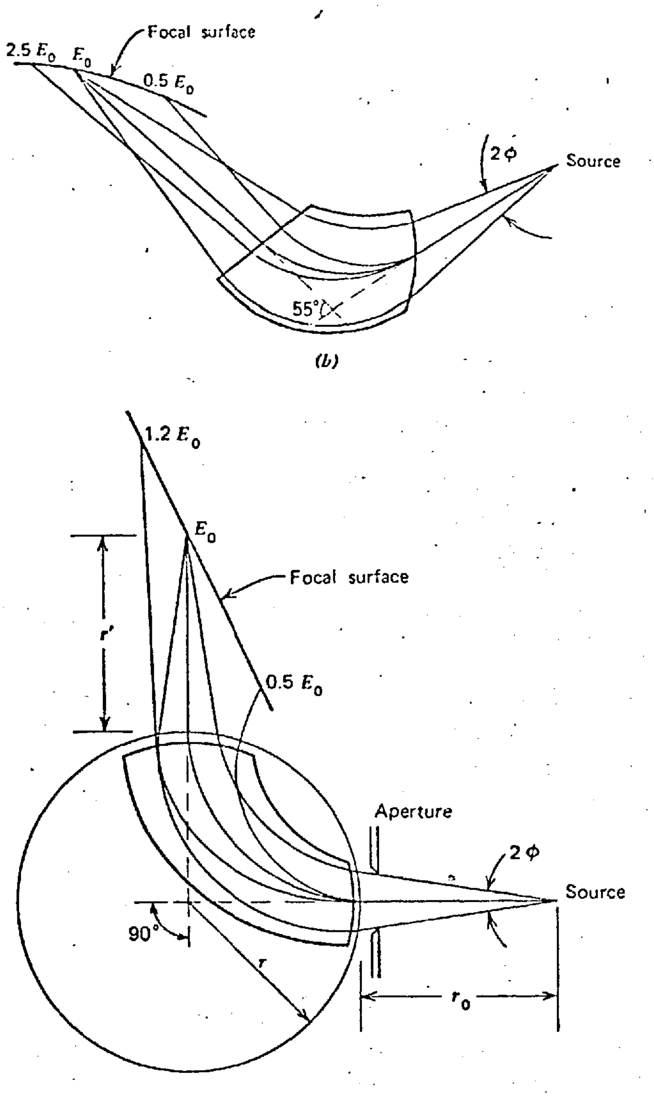

(b)

(c)

Figure 3. (*a*)–(*c*), (*f*)–(*h*) Various instrumental arrangements using a homogeneous magnetic field.

Fig.3.3 Magnetic spectrometers from Sevier (1972) energy and yet maintain the same beam direction. This principle was used by Mme Henry et al (1969). By placing an electrostatic mirror in front of a 90° magnetic prism, she was able to maintain the optical path of the electrons in a microscope while providing high resolution energy selection. This system has been used by several other microscopists, and is discussed in detail by Henkelman and Ottensmeyer (1974), and Egerton et al (1975). Recent versions of this principle, employing four 90° deflections, have been proposed by Rose and Plies (1974), Plies and Rose (1977), and Wollnik et al (1976). In both cases the difficulty is that the optical column of the microscope must be greatly adapted, though much better resolution is theoretically possible.

Devices similar to that developed by Mme Henry have been used as combined energy monochromators and analysers for 180° reflection studies (Verdier, 1969, 1974). In such cases, however, the analyser is only a 90° sector, thus no focusing results, and good collimation is required to maintain resolution.

Another form of magnetic analyser was proposed by Ichinokawa (1968), who altered the symmetry in the intermediate lens of an electron microscope and introduced an off axis source slit below the specimen. The resulting chromatic aberration from the rectangular pole pieces produced a final image of the slit displaced according to the energy of the electrons. This analyser was used by Considine (1970) in the Cambridge high voltage electron microscope, but was replaced by a magnetic prism (Darlington and Sparrow, 1977) beneath the projector lens in order to increase the spatial resolution of the microscope.

Magnetic analysers were ruled out for the present work for two reasons. Firstly, the chamber was not suitably screened to accept it; secondly, the group had no expertise in the manufacture or operation of such an analyser. Neither of these is insuperable, but both would have cost time which was not available. The ideal

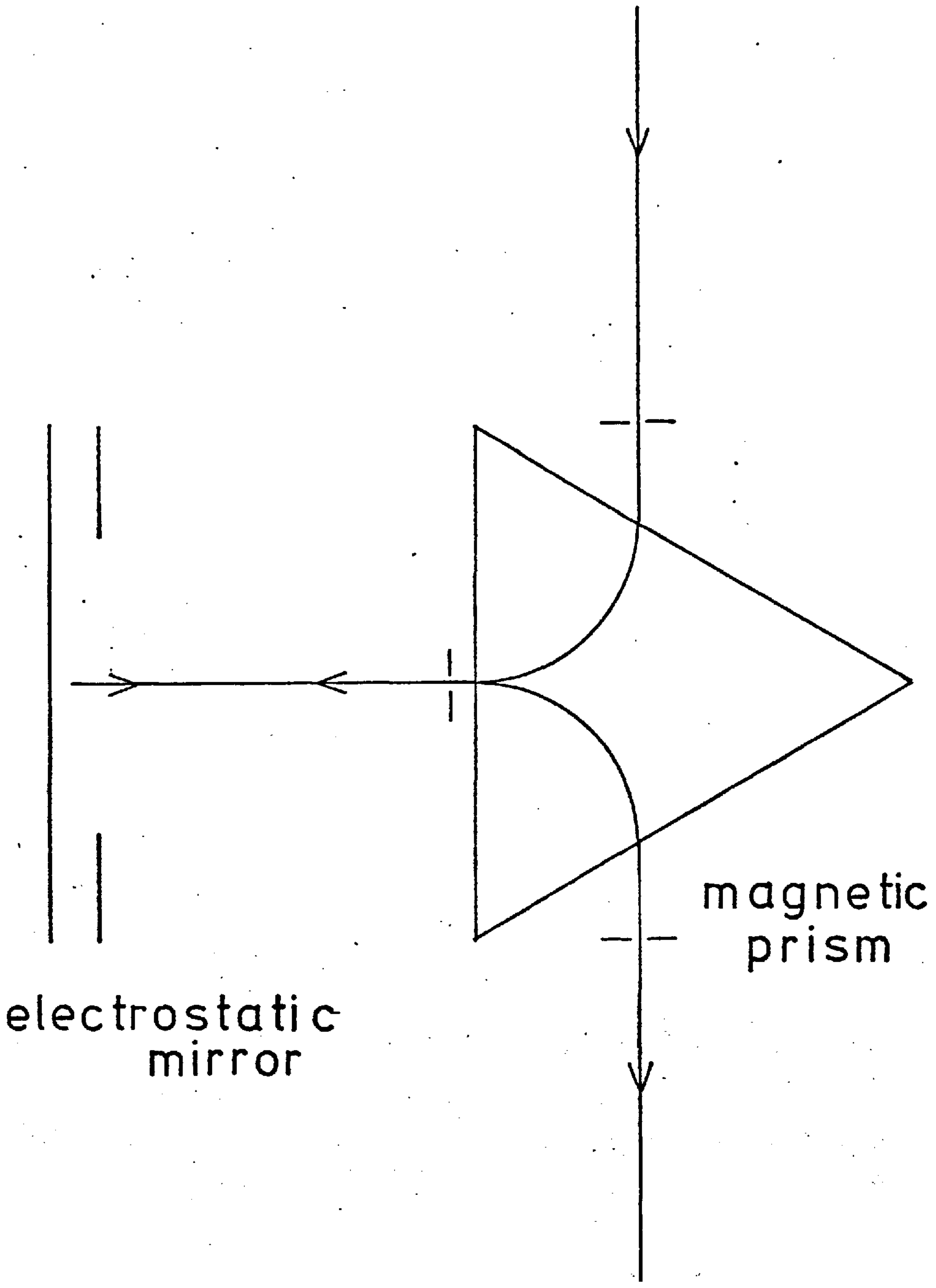

Fig 3.4 Prism-mirror-prism energy filter

analysers for the application might well be the prism-mirror-prism or Wien filter (section 3.7), as in either case the analyser neither screens the entrance aperture nor has a small acceptance angle.

The advantage of magnetic analysers over most electrostatic ones is their ability to analyse the total signal at one time. This is because, in general, the focus conditions apply to electrons of many different energies. This means that the analysed electrons can be projected onto a photographic plate and recorded simultaneously. The need for accurate intensity measurements led to the abandonment of such analysers; however, with the advent of very small recording devices, it is paradoxical that no attempt has been made to combinethe virtues of the magnetic analysers with them.

3.7 Combined electrostatic and magnetic analysers

The use of electrostatic and magnetic fields in opposition to select charged particles of a single velocity was first used by Wien (1897), though the technique had previously been used by J.J. Thomson (1897) to measure the velocity of electrons for his determinations of e/m.

The electrons enter a region of flux density B and field intensity E. Only those electrons with velocity $u = E/B$ will not be deviated. The filter does not image the electrons and thus relies on collimation and beam diameter to govern the resolution; however, its simplicity means that it can easily be combined with other lens systems, such as accelerating and retarding lenses, in order to improve its resolution (fig. 3.5).

Boersch (1954) and Dietrich (1958) both report Wien filters with resolutions better than 2000, with an input beam of semi angle 3×10^{-3} rad. Boersch et al (1964) used a similar filter, together with retarding lenses to provide a resolution of 2×10^{6}.

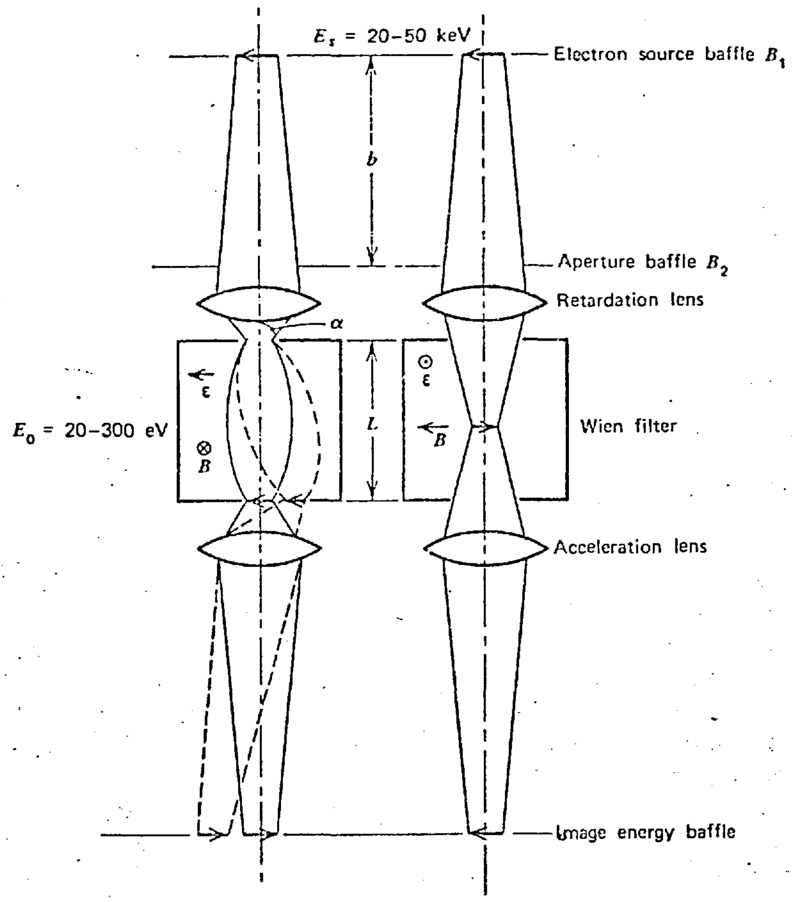

Figure 22. Wien filter analyzer used by Boersch et al.[182]

Fig.3.5 Wien filter used by Boersch et al (1964) (from Sevier, 1972)

The very high resolution of these instruments requires monochromatising the beam, and hence a double filter is often employed (Anderson and Le Poole, 1970). One advantage of the Wien filter, when used in a microscope, is that it does not deviate the beam, hence the microscope adjustments are independent of the filter.

3.8 Electrostatic Analysers

Dispersive analysers

Many forms of electrostatic deflection analysers have been suggested and used. An indication of their popularity is the number of references cited in recent review papers. Rudd (1972, 1962), quoting 100 references, reviews a simple form of each analyser up to 1968, and this has been extended by Afanes'ev and Yavor (1975) (256 references) to include much work, particularly East European, up to 1973. There are currently at least five types of deflection energy analyser.

3.9 Parallel plate analyser

This analyser is the simplest of the deflection analysers. The electrons pass through an entrance slit at an angle ϑ (figs. 3.6 and 3.7) and enter a uniform electrostatic field. They perform a parabolic path and leave again at an angle to the base plate. The analyser has been shown to have first order focusing when $\vartheta = \pi/4$ (Yarnold and Bolton, 1949), and second order focusing when $\vartheta = \pi/6$ (Green and Proca, 1970). The parallel plate analyser cannot produce a focus in the azimuthal angle φ but one solution, suggested by Schmitz and Melhorn, 1972, (figs. 3.8 and 3.9) is to produce an analyser with azimuthal symmetry. This fountain analyser has very good theoretical properties when operated at $\vartheta = \pi/6$, but suffers from its need for a large ring collector for the electrons below the exit aperture.

Other problems with the analyser are the effects of the entrance and exit apertures on the ideal parallel field between the plates. This has been discussed by Green and Proca (1970), from which it is clear that, by use of a narrow beam at

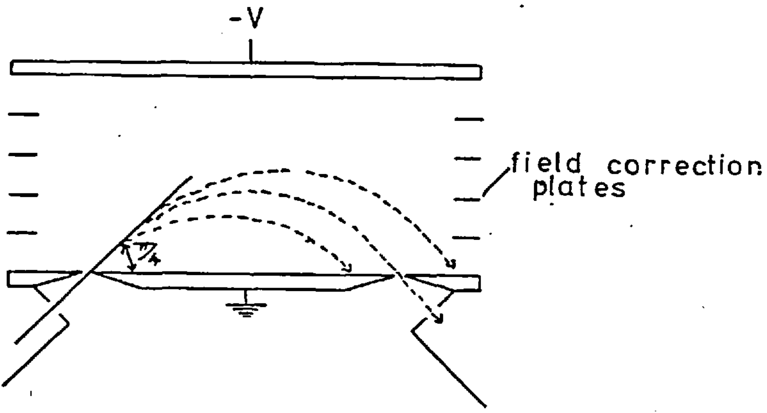

Fig.3.6 Parallel plate analyser, π/4 configuration.

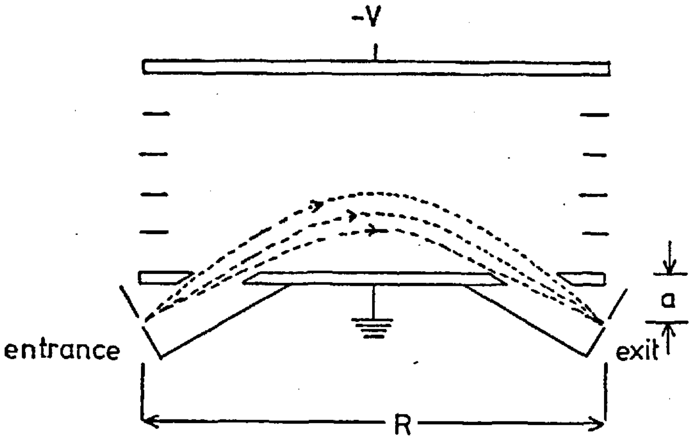

Fig.3.7 Parallel plate analyser, π/6 configuration.

When the entrance and exit apertures are the same distance from the base plate the condition for second order focusing is $R/a = 6\sqrt{3}$

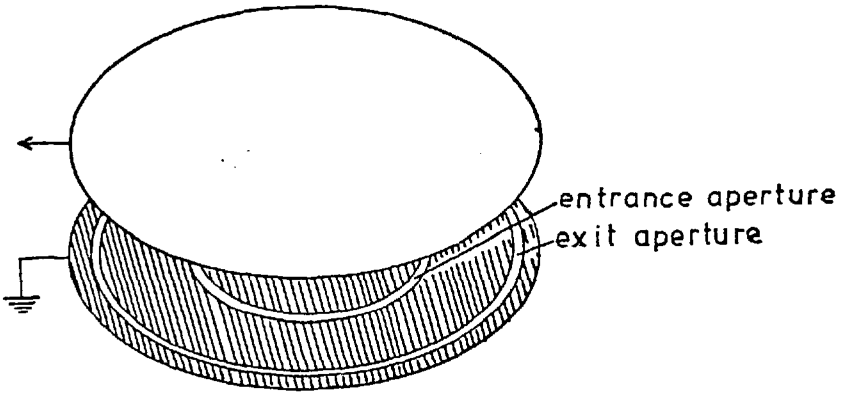

Fig.3.8 Fountain spectrometer (schematic)

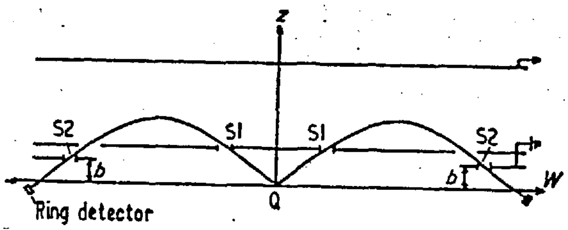

Figure 4 Schematic representation of a modified $\pi/6$-fountain spectrometer

Fig.3.9 Fountain spectrometer from Schmitz and Melhorn (1972).

$\vartheta = \pi/6$, very high resolution ($\sim$ 2000) can be obtained.

3.10 Cylindrical and cylindrical sector analysers

These are the oldest of the electrostatic deflection analysers, being first described by Hughes and Rojansky (1929) and built by Hughes and McMillen (1929). The analyser consists of two concentric cylinders with a potential between them. For electrons incident through an aperture placed between the cylinders, a first order focus is obtained at an exit aperture, making an angle of 127° 17' with the entrance (fig. 3.10 and 3.11). The analyser will operate with the angle between entrance and exit apertures less than 127°, but at some sacrifice to resolution or angular acceptance. Darlington (1971) and Bishop (1965) both used 127° analysers to investigate the backscattering of electrons from metal surfaces.

There is still considerable interest in this analyser. Arnow and Jones (1972) and Arnow (1974) discuss a system which uses two 127° analysers in series to produce an electron beam of very well defined energy, which is used to investigate the interaction between electrons and helium atoms. The resulting electrons are also analysed using a 127° sector analyser.

Arnow (1976) derives the non paraxial beam conditions for cylindrical analysers citing the 127° analyser as a particular case. The resolution of a 127° sector analyser is $\sim$ 75 and can be optimised according to the criteria given by Rudd (1972) to a maximum of about 100. However, the scope of the analyser can be considerably enhanced by use of pre-retardation of the electrons as they enter the analyser (Roy et al, 1975).

The input and output of a sector analyser present problems, as the potential at the entrance is not the same as that on either of the curved plates. One solution is to use a lens to form a virtual source in the same way as with a spherical analyser (q.v.), but it is possible to form a slit which follows the particular potential of the

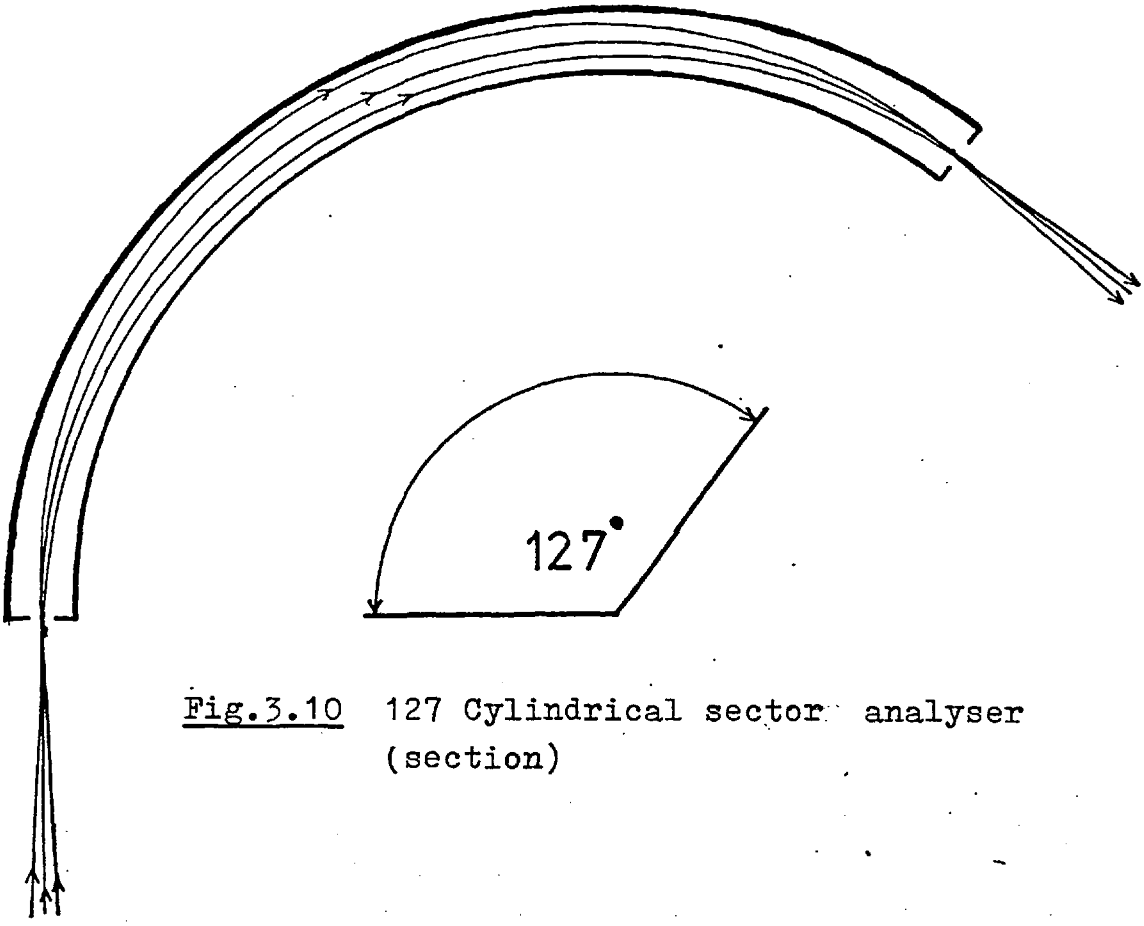

Fig.3.10 127 Cylindrical sector analyser (section)

Fig.3.11
127 Cylindrical sector analyser (projection)

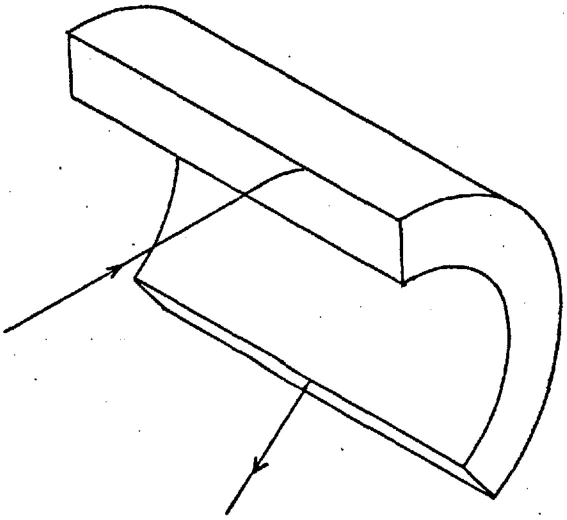

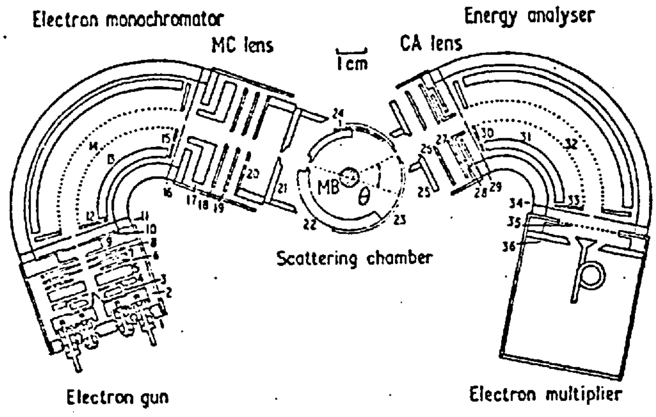

Figure 1 Cross section of the electron spectrometer to scale. The main parts are identified in the figure while the parts identified by a number are described in the text

Fig.3.12 127 Sector analyser from Roy et al, (1972). Fine wire mesh (14 & 32) is used to form the equipotential planes in order to prevent both the scattering of rejected electrons and the formation of secondaries.

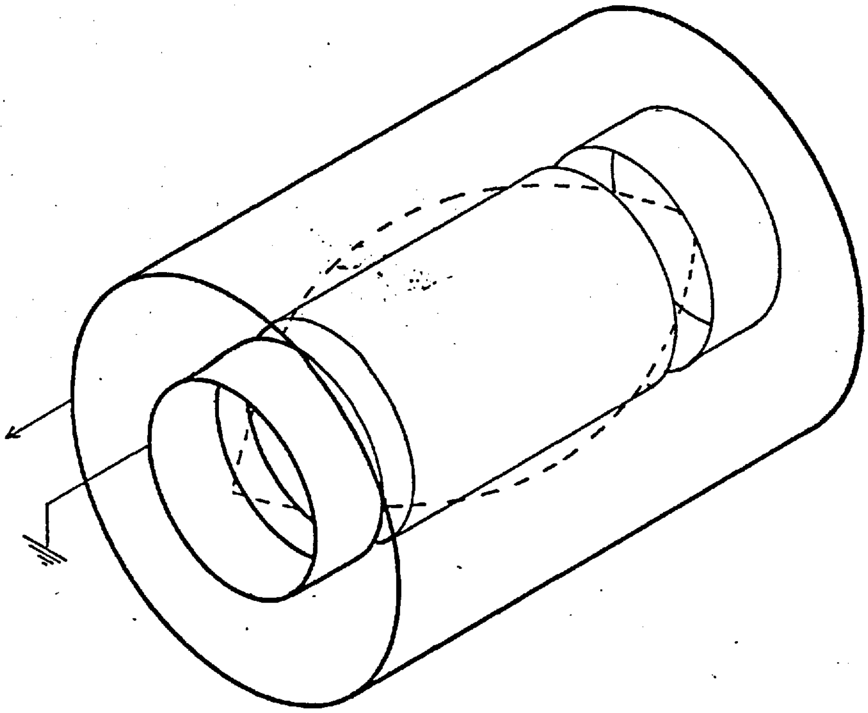

Fig.3.13 Cylindrical mirror analyser, schematic.

entrance point and thus does not disturb the field. Hertzog (1935) shows conditions which reduce the deflection angle to 119° and allow the use of plane slits.

As with all analysers, reduction of the beam size and divergence greatly improves the resolution. Crewe (1977) gives calculations for the resolution of a 90° sector in which he predicts a resolution of 10^{6} at 10 m rad, falling to 5×10^{4} at 50 m rad.

The virtue of the analyser is its simplicity combined with good transmission and/or high resolution.

3.11 The Cylindrical Mirror Analyser (C.M.A.)

The C.M.A., like the sector analysers, relies on the field between two concentric cylinders to separate the energetic electrons. The specimen and focus of the C.M.A. are both on the cylindrical axis (fig. 3.13), rather than the circumference, as with the sector analysers. The C.M.A. is basically a parallel plane analyser rotated about the axis between the specimens and the focus.

The analyser gives second order focusing in ϑ (Aksela, 1970 and 1971). The analyser is very dependent on the width of the entry slit in the inner cylinder. It has been shown (Risley, 1972) that better resolution may be achieved by placing the specimen off the cylindrical axis.

The measured resolution of the analyser is typically 100 (Sar-el, 1967), but, if the fringing fields at the entrance and exit apertures are corrected using fine mesh the resolution can be increased to 200 (Frank, 1976). If the angular acceptance is reduced, the resolution, as with all analysers, is improved substantially; however, the point of the analyser is thus lost, as its main virtue is its good resolution with a very wide azimuthal aperture.

The C.M.A. suffers from the fact that the specimen is inaccessible, thus one standard variant is to use hemi-cylinders so leaving the specimen accessible on one side (Bishop et al, 1972). This variant also allows the use of a parallel input beam (Toburn, 1974). The use of a hemi-cylinder requires careful correction of the fringing fields between the cylinders in order that the field is still apparently due to infinite right cylinders. Correction is also needed on all C.M.A.s at their ends, unless they are substantially longer than the distance between entrance and exit slits.

The analyser is not ideally suited for use with pre-retardation lenses or grids as it is difficult to match the lenses to the curved and angled surface of the inner cylinder, and much of the virtue of the azimuthal symmetry is lost (Hafner et al, 1968). This has been done, however, by Gardner and Samson (1975) and Baker and Williams (1976). In both cases a resolution better than 400 was achieved . Gardner and Samson discuss the effect of the lens system on the collection efficiency.

The analysers discussed here have all been small (~ 10 cm outer diameter) single pass instruments. Resolution may be improved either by increase of size (Citrin et al, 1972) or by using a double pass instrument (two C.M.A.s back to back) (Pianetta and Lindau, 1977). Citrin's instrument, 1 metre in diameter, had a resolution of 1250 and a collection aperture of 0.06 sterad.

A disadvantage of the C.M.A. is that the filter pass energy is not a simple function of the analyser potentials and is a function of specimen position (Risley, 1972). This means that the analyser requires calibration. Sickafus and Holloway (1975) have shown that shifts of up to 2% in energy may be obtained with an analyser of resolution 150 depending on the specimen position.

3.12 The hemispherical analyser

This analyser, which consists of two concentric hemispheres, has first order point focusing in two dimensions and is well matched to a point source of electrons. The system (figs. 3.14 and 3.15) is however not matched to an apertured source, as the entrance does not form part of an equipotential plane. The general solution to

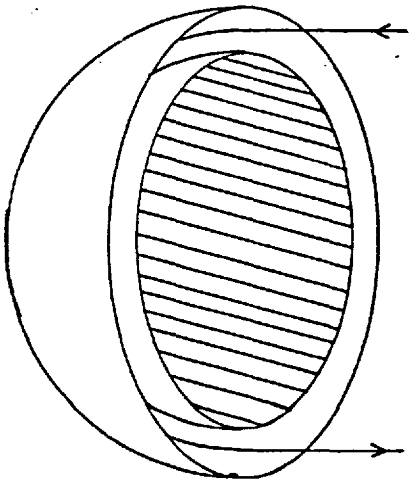

Fig.3.14 Hemispherical analyser, schematic.

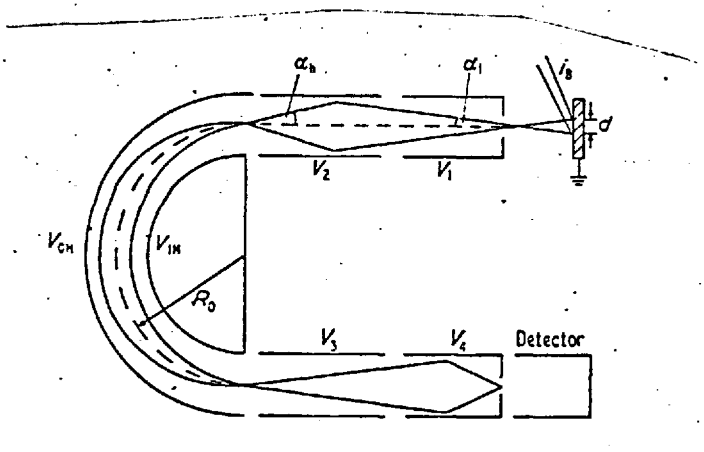

Figure 1 The arrangement of electron optical elements and the definitions of symbols used

Fig.3.15 Hemisherical analyser from Bassett et al (1972) showing lens system used to produce a point source of electrons at the entrance to the hemisphere.

this has been either to collimate a beam with apertures at a distance from the analyser or to use a lens system to form a source point at the entrance to the analyser. The use of a lens system provides scope for pre-retardation of the beam and maintains the useful angular acceptance of the analyser.

Purcell (1938) first demonstrated the use of a spherical sector as an analyser. A sector of less than 180° can be used as an analyser to provide a first order focus external to the sphere. This has the disadvantage of being difficult to construct without causing severe aberrations of parts of the image. An analyser similar to that designed by Purcell was constructed by Franzen and Porter (1975) for the investigation of the energy distribution of thermal electrons emitted by a tungsten tip.

Detailed designs for hemispherical spectrometers have been given by Kuyatt and Simpson (1967), Bassett et al (1972) and Bassett (1974). All the instruments are similar in size, having a principal radius of about 25mm, and give a resolution at the hemispheres of 100 for a point source. The resolution of Bassett's spectrometer has been improved to 10000 by severe collimation of the beam.

Using retarding lenses Noller et al (1975) have demonstrated a spectrometer with a wide aperture and resolution better than 1000. Designs for the lenses have been published by Wannberg et al (1974). Hafner et al (1968) have compared the performance of the hemispherical and cylindrical analysers and have concluded that the latter, despite its lack of analytical field solution, is superior.

3.13 Other electrostatic analysers

Other configurations have been proposed for electrostatic deflection analysers. The most interesting is the 'pill box' or 'Bessel' box, shown in Fig. 3.16. Originally proposed by Allen et al (1972), its design parameters and detailed description of a prototype are given by Allen et al (1976). The analyser was initially reported to have a resolution of 300, but it is claimed that a resolution of 3000 can be

Fig.3.16 Bessel box from Allen et al (1972).

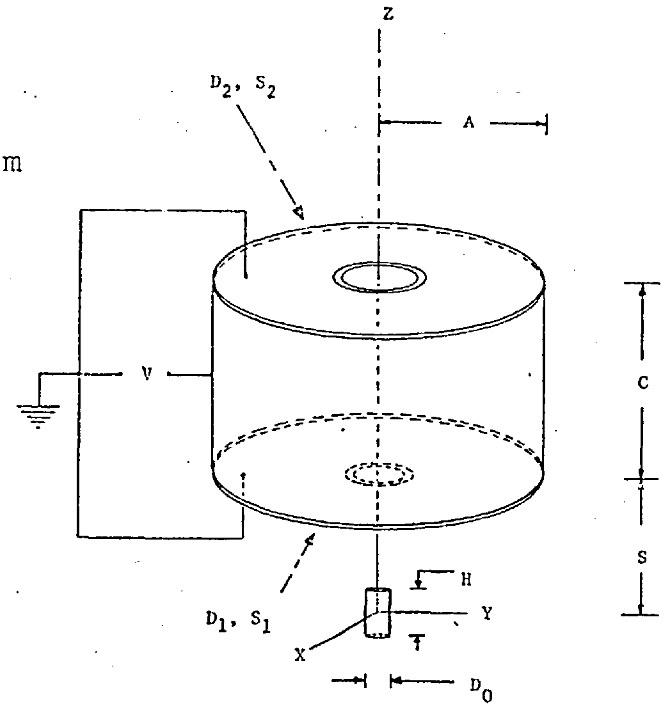

Figure 1. Geometry of the Bessel Box Analyzer.

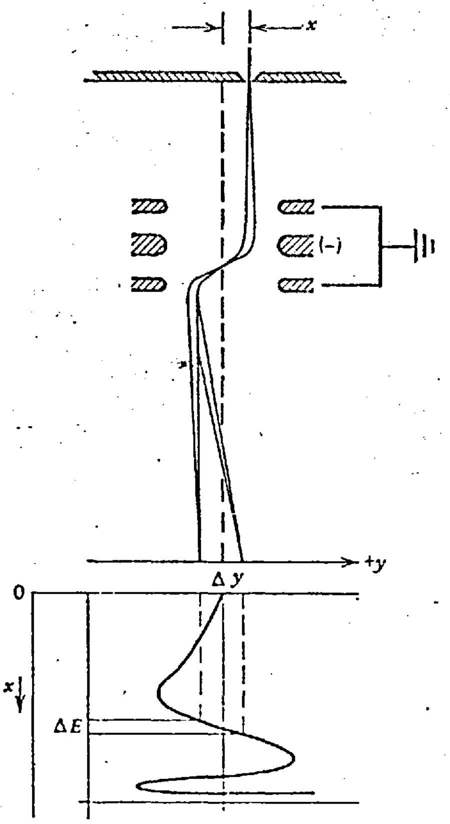

Figure 21. Möllenstedt analyzer.

Fig.3.17 Mölenstedt analyser showing the dependence of the angular deflection Δy on the energy, E, of the electrons and the entrance aperture position x. Sevier, 1972.

obtained by reduction of the size of the entrance and exit apertures. Whilst these figures are very good considering the extreme simplicity of construction of the 'pill box', the system has one major disadvantage, in that the specimen is inaccessible. The analyser is, however, very suitable for the gas phase work for which it was intended.

The Möllenstedt Analyser relies on the chromatic aberration of a three element electrostatic lens to provide separation in energy. In its most usual form, this lens (fig. 3.17) is housed below the projector lens in a microscope column. The system has very high resolution for a narrow angle beam. Möllenstedt (1949) claimed a resolution of 3×10^4, and Gaukler (1963) 5×10^5.

There have been several theoretical descriptions of the analyser (Leonhard, 1954; Williamson, 1966; Metherell and Whelan, 1966), and there is continued interest in it (Wellington, 1974) as it can easily be included in the base of a microscope column. The analyser images a slit onto a photographic plate and can thus be used to obtain information about more than one point at a time. The images formed by electrons from different regions of the spectrum are overlaid on the plate, so the analyser can only be used where energy losses are small compared with the main beam energy.

Bunting (1971a, b and 1972) proposed a similar system using the chromatic aberration of a thick lens with cylindrical symmetry. He gives design details and an analysis of the electron trajectories. The performance is similar to a simple Mollenstedt analyser, though the Bunting analyser can only image a single point. The Bunting analyser is relatively easy to machine on a lathe.

In both Mollenstedt and Bunting analysers the angle of acceptance is small (usually less than 2×10^{-3} rads), but as they are generally used with intense beams this is normally not a problem.

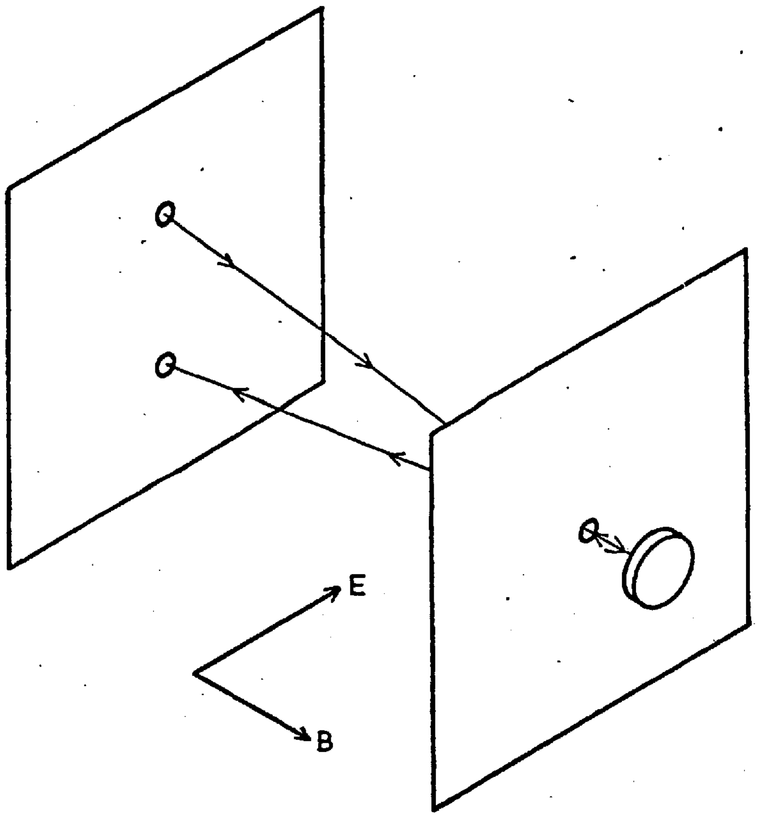

<u>Fig.3.18</u> Trochoidal filter, schematic diagram after Stamatovic and Schulz (1970).

The electrons follow an extreme trochoidal path between the entrance and exit apertures.

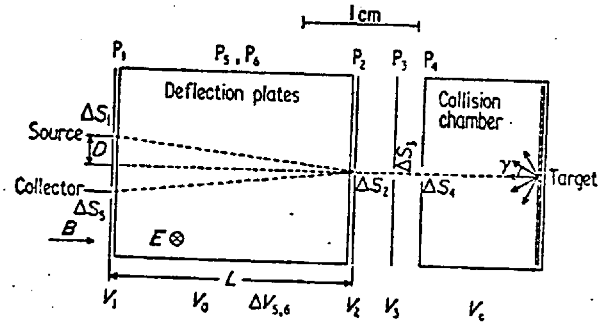

Figure 1 Schematic diagram of the 180° backscattering spectrometer

<u>Fig.3.19</u> Troichoidal filter from Roy and Burrow (1975).

The trochoidal filter

Stamatovic and Schulz (1970) describe an analyser which uses an electrostatic field in conjunction with a magnetic field. The magnetic field is nearly parallel with the beam. The filter (fig. 3.18) both monochromates the incident beam and analyses the returning beam. Roy and Burrow (1975) describe a similar machine and examine the performance (fig. 3.19).

3.14 General comments

All electrostatic deflection analysers suffer from a common failing, which is that the electrons rejected by the analyser can be scattered within the analyser, causing the production of energetic secondary electrons. If these secondary electrons are formed in the right place, they can emerge, forming a spurious and unpredictable part of the signal. This effect has recently been reported by Wendelken and Propst (1976), who used a 127° sector analyser. They overcame the problem by depositing nickel 'soot' on the inner surface of the analyser. This is produced by deposition from a tungsten filament at a pressure of 100 Pa of nitrogen. Gold soot similarly deposited, whilst initially absorbing more electrons, was found to become optically bright when baked during the pumping sequence.

Roy et al (1975) used a wire mesh to form the electrode planes in their 127° sector analyser (fig. 3.12). This is difficult to construct but considerably reduces scattering.

Froitzheim et al (1975) suggest the ribbing of the internal surfaces of analysers so that electrons meet the ribs normally. The electrons would be scattered away from the exit aperture with the production of few secondaries.

The use of at least one of these methods would seem sensible in the construction of any analyser of the types discussed.

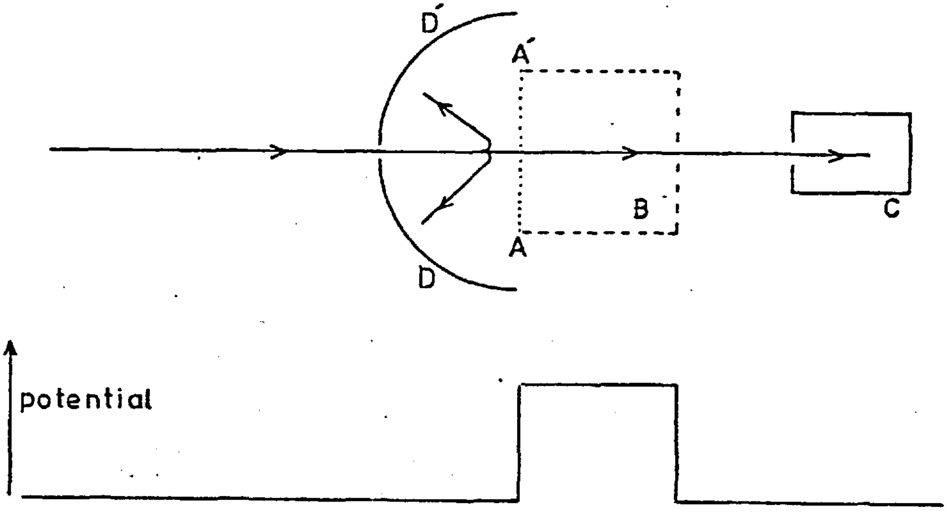

Fig.3.20 Retarding field analyser configurations.

Electrons travelling from left to right meet a potential step, AA' . The electrons passing the step may either be collected at the potential of the step, B, or be re-accelerated to be collected at ground potential, C. A further signal may be obtained by collecting those electrons rejected at the step, DD' .

3.15 Retarding field analysers

The retarding field analyser or potential step is one of the oldest forms of electron velocity analyser (Lenard, 1902) and has been in common use since. The principle of the analyser is simple. The electrons are directed at a sharp potential step (AA' fig. 3.20) of height V volts. Electrons with energy greater than eV pass over the step, those that have less energy are repelled. The signal can be detected in one of three ways, by a detector at either the high or low potential collecting the electrons allowed to pass, or by detecting those electrons rejected (respectively B, C, DD', fig. 3.20).

The parameters of such analysers have been extensively reviewed by Klemperer (1965) and Simpson (1961) and more recently by Huchital and Rigden (1972) and Ward (1976).

3.16 The parallel plane analyser

The simplest form of the retarding field analyser consists of parallel planes, one at the ground potential, and the other at high negative potential (Simpson, 1961) (Fig. 3.21). Electrons are projected from the low potential plane normally. The resolution depends on the semi-angle ϑ of the cone of electrons emitted from the low potential plate. This is, however, only true as long as the electrons come from the surface of the plate. Simpson (1961) points out that the moment a hole is added to introduce electrons into the gap it forms a diverging lens spreading the electrons and reducing the resolution.

It has become the aim of most workers to produce a focus of electrons at the highest useful potential (usually a saddle point), rather than a planar electrode system. The aim is for the electrons to pass through the maximum potential at almost zero velocity at right angles to it.

Boersch (1953) demonstrated a symmetrical einzel lens used as a retarding

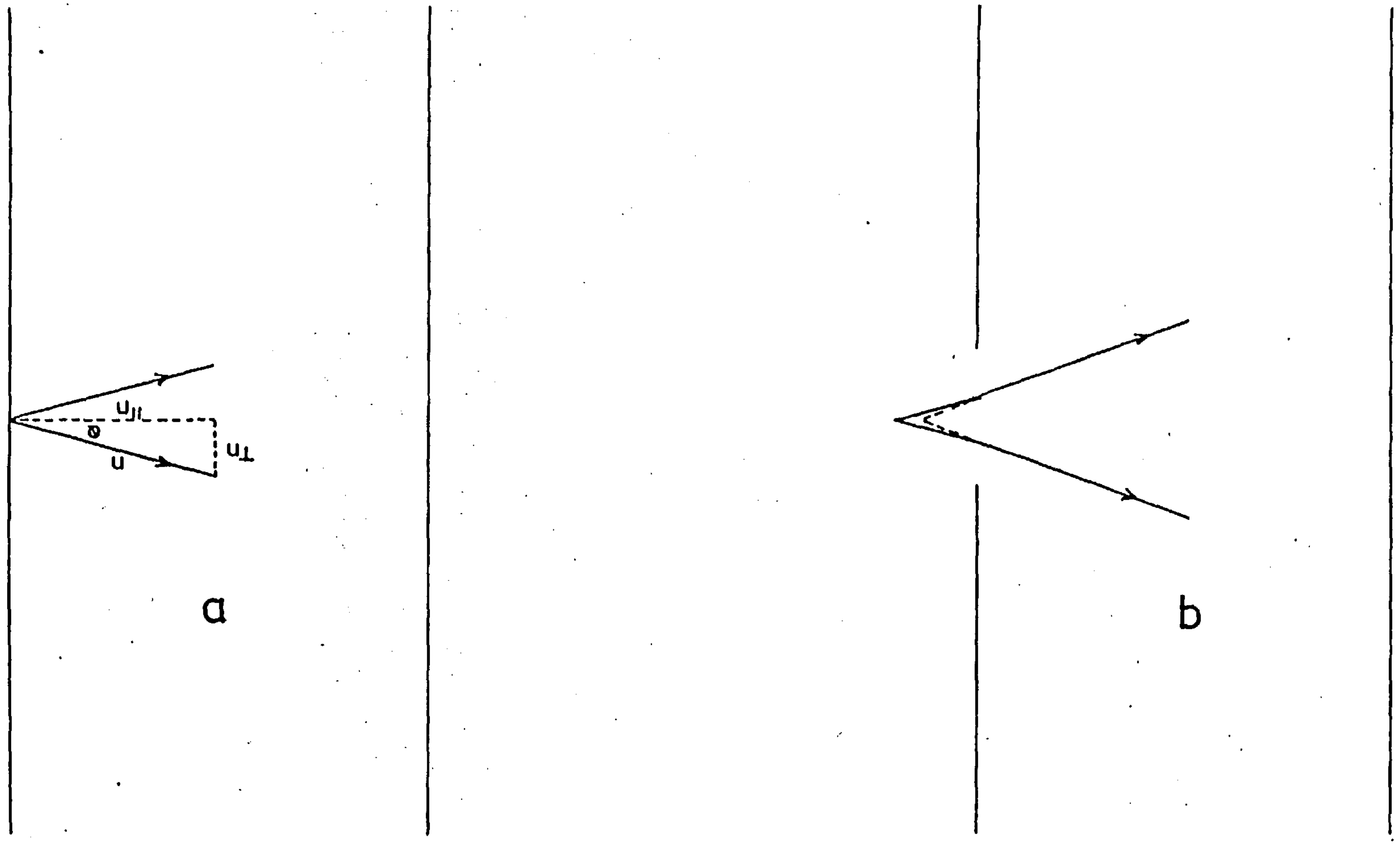

Fig 3.21 Resolution of parallel plane analyser

a ideal $E/E_0 = u_{\perp}^2 / u_{\parallel}^2 = \sin^2\theta$

b increased divergence due to finite aperture filter for narrow beams (fig. 3.22). A similar device was demonstrated by Forst (1958) who also showed the effect on resolution of increasing the beam diameter from 0.02 mm (resolution 5000) to 0.5 mm (resolution 330)(fig. 3.23). These systems require both small radius and divergence as the lenses are not capable of strong aberration-free focusing (cf. Bunting, 1970). However, these are simple systems with moderate resolution and have been widely used where strong well defined beams are available (Beck and Robbie, 1972).

Simpson and Marton (1961) designed a symmetric five element lens system used later by Kessler and Linder (1964). This analyser (figs. 3.24 and 3.25) focused the electron beam onto a small hole in the thin central electrode. After passage through the analyser the beam was remagnified to its original diameter. The system was reported to have a resolution better than 5000 for an electron beam of up to 1 mm in diameter, and is thus one of the best analysers for large beams. The analyser has not found favour because there are two interrelated potentials which must be altered in order to sweep a wide range of energies if the focus conditions are to be maintained. If the range is made too large the lens becomes a rather poor dispersive instrument as the focus conditions only apply to the passband.

Several workers have used coaxial magnetic fields to maintain the collimation of electron beams as they pass through single element analysers with long central electrodes. Boersch and Miessner (1962) and Brack (1962) (fig. 3.26) both produced analysers with resolutions better than 5×10^4 by the use of such external magnetic fields. The fields serve to prevent the very slow electrons in the analyser bore from hitting the walls and being lost because of their residual transverse momentum. It has been commented (Simpson, 1961) that the use of such fields can lead to spurious results because electrons are transmitted which have large transverse momenta. However, this objection can be overcome if the beam is initially collimated so that the

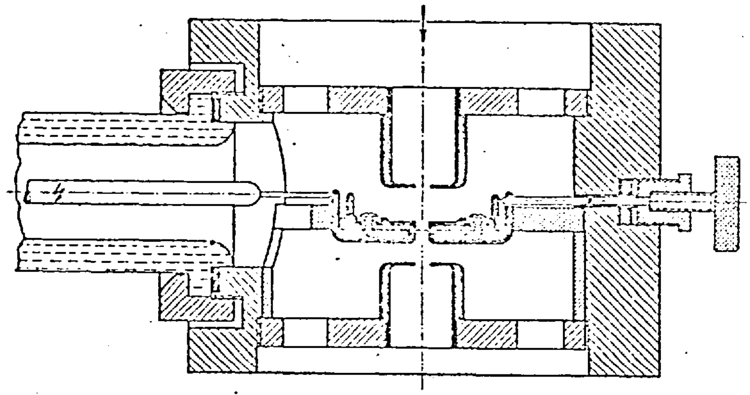

Fig. 4. Linsenfilter mit zentrierbarer Vorblende.

Fig.3.22 Symmetric einzel lens retarding field analyser from Boersch (1952)

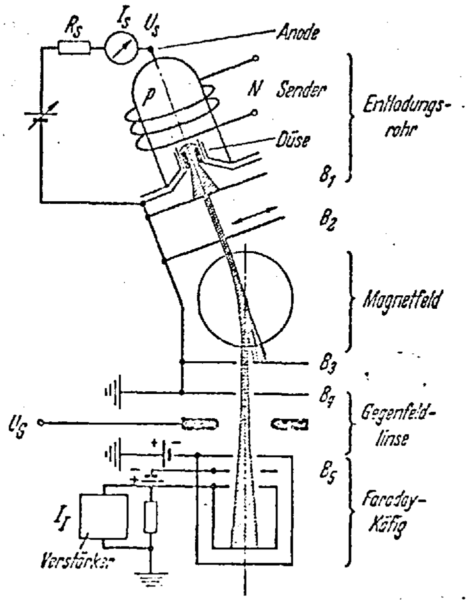

Abb. 1. Schema der Versuchsanordnung

Fig.3.23 Spectrometer using a symmetric einzel lens retarding field analyser, from Forst (1958).

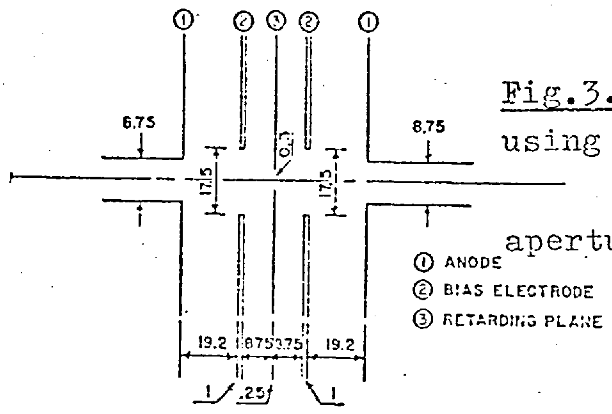

Fig. 1. Electrode configuration for intermediate image filter lens. Dimensions in millimeters. Additional range, at cost of some resolution, may be obtained by increasing retarding plane aperture to 0.6 mm.

Fig.3.24 Retarding field analyser using symmetric lenses to focus the beam through a small aperture in the central plane. Simpson and Marton (1961)

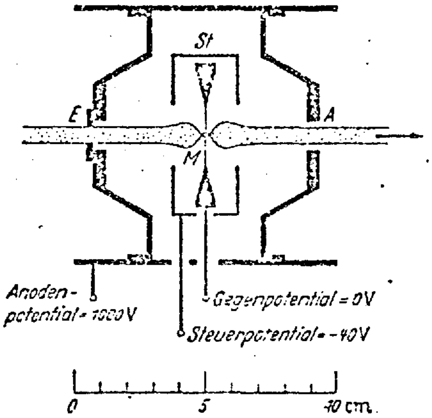

Abb. 1. Maßstäbliche Prinzipskizze der Zwischenbildfilterlinse. Als Beispiel wurden die Spannungswerte für den Fall angeschrieben, daß die Energie der Primärelektronen 1000 eV beträgt

Fig.3.25 Intermediate image filter lens. Kessler and Linder, 1964.

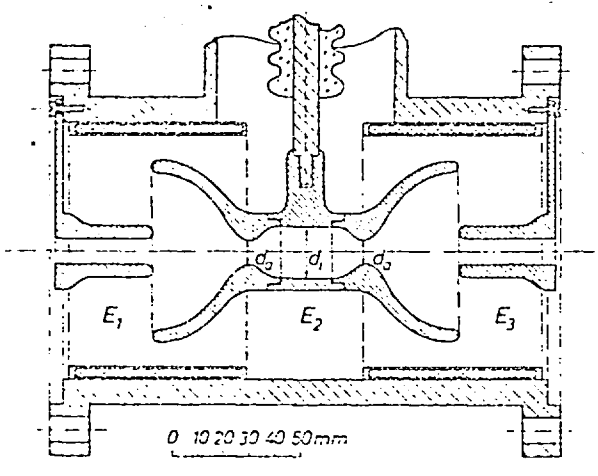

Abb. 2. Längsschnitt der Filterlinse.

Fig.3.26 Analyser with long central electrode and magnetic collimation from Brack (1962).

transverse momentum corresponds with the expected resolution of the analyser. The field will then merely maintain the collimation without degrading the resolution. This assumes that the equipotentials presented to the beam are planar. If they are not, the beam will acquire larger transverse momenta at the expense of the energy resolution of the analyser. The magnetic field must be sufficiently strong to contain the beam within the region where the equipotentials are planar and perpendicular to the mean beam direction.

The analyser reported by Brack used a paraxial field of 9×10^{-3}T and the resolution was 0.4 eV. The maximum transverse velocity of the electrons was thus 3×10^5 ms^{-1}, giving a maximum radius for the helical path of 0.2 mm. Brack ascribes much of the lack of resolution to the thermal energy spread of the beam, thus the radius would be considerably less. Without the magnetic field the beam would have spread to a width of several centimetres which could not have been analysed.

3.17 Electrode size

The main reason for the long electrode in both the analysers reported by Brack (1962) and Boersch et al (1962) was to form a planar equipotential perpendicular to the beam at the saddle point. Another solution has been to use a planar or spherical mesh to form the equipotential surface. The equipotential surface formed by a mesh follows the shape of the mesh to within two mesh spacings of the mesh surface (cf Chapter 5 and Appendices 5 and 6) and can be made a good approximation to the ideal parallel plane analyser. Such analysers have been used by Boersch (1953), Graczyk and Moss (1968), (figs. 3.27 and 3.28) in electron microscopes and by Denbigh (1965), Tompsett (1966), Sheppard (1973) and Ward (1976) in scanning high energy diffraction apparatus (SHEED). As this system was eventually chosen for the present work, a full discussion of it is left to Chapters 4

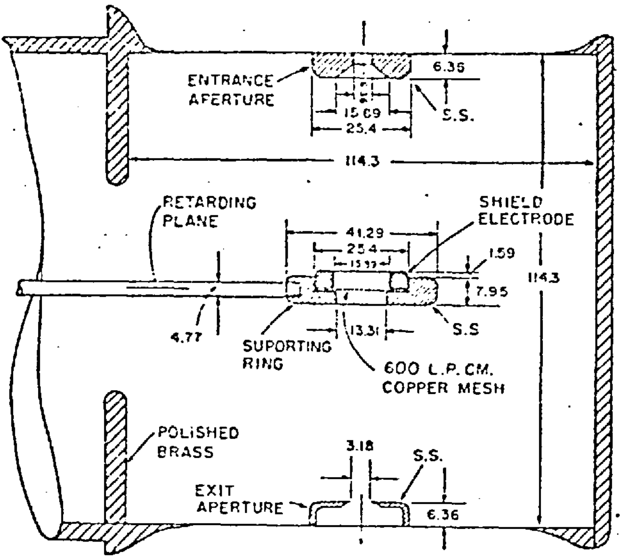

FIG. 2. Cross section of electrostatic electron velocity filter. S.S. is 18-8 polished stainless steel. All dimensions in millimeters.

Fig.3.27 Velocity filter using fine wire mesh. From Graczyk and Moss (1968).

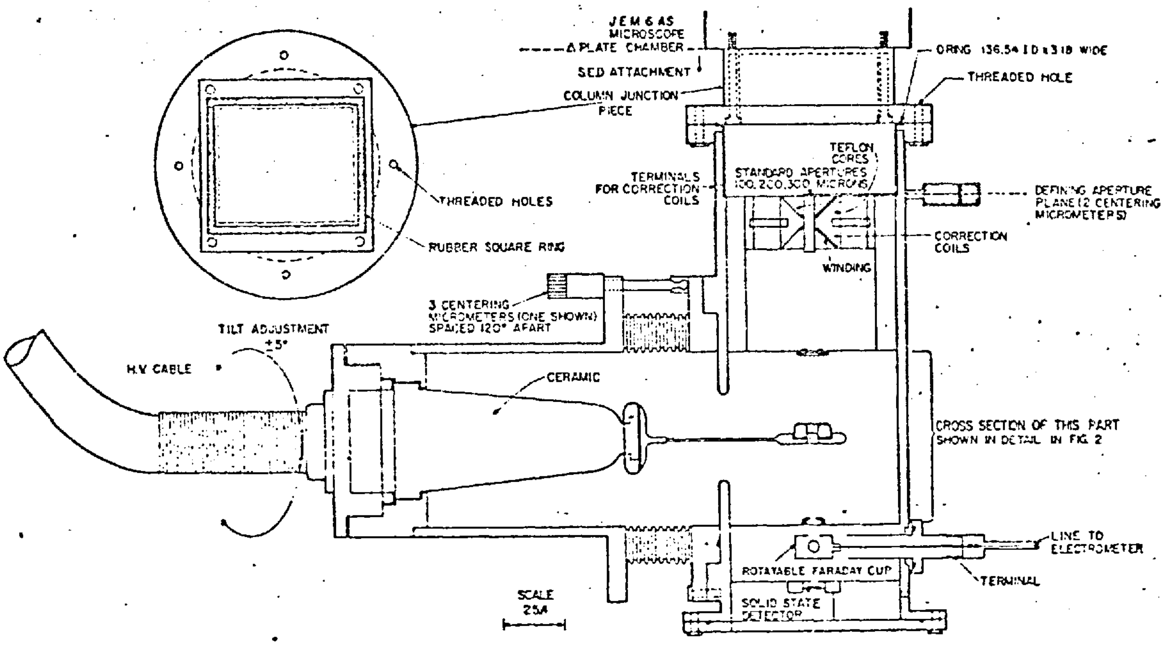

FIG. 3. Cross sectional view of the mechanical column of the SED system. All dimensions in millimeters.

Fig.3.28 Velocity filter from Graczyk and Moss (1968) and 5 and their appendices.

The SHEED workers have all produced instruments having a single planar mesh with a resolution of 4×10^3 or better. Denbigh gives a figure for the resolution of his analyser of 5×10^4 limited to 2×10^4 by the thermal width of the beam used.

3.18 Spherical Geometry

The spherical geometry of retarding mesh analyser has been used by many workers where a large angle of collection is required, both at high energy (Kanter, 1961; Matsukawa et al, 1974) and at low (< 1000 eV) energy (Palmberg, 1967; Taylor, 1969). The ability of such a system (fig. 3.29) to collect over a hemisphere is a unique feature of this type of analyser though the resolution is generally limited (< 100).

The factors affecting this resolution are the object shape and position, the fact that the collecting sphere is never complete and is dogged by fringing field errors. Also the mesh of most systems is woven and relatively coarse, thus degrading the sphericity of the field in the region of the mesh (Huchital and Rigden, 1972; Avery, 1976).

3.19 Electrostatic differential retarding field analysers

Lindau et al (1973) proposed a retarding field analyser with differential output conceptually very similar to the magnetic lens spectrometer proposed by Klemperer (1935) (fig. 3.30). The claimed resolution is 200 and, though it appears complex, it should be simpler to machine than any comparable analyser as the elements are a set of spaced rings. Hartop and Huber (1977) have used an instrument of this type with a resolution of 600 at 10 eV. It is unfortunately limited by the potentials in it to 1000 V, but it could be made larger for high voltage work.

3.20 Faraday cups

Retarding field analysers using high potential collectors have been used over

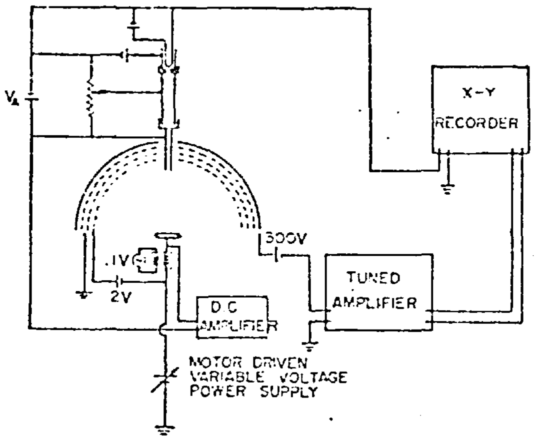

FIG. 3. Circuit for measuring energy distribution of slow secondary electrons.

Fig.3.29 LEED screen geometry from Palmberg (1967)

Fig.3.30 Electrostatic differential analyser from Lindau et al (1973)

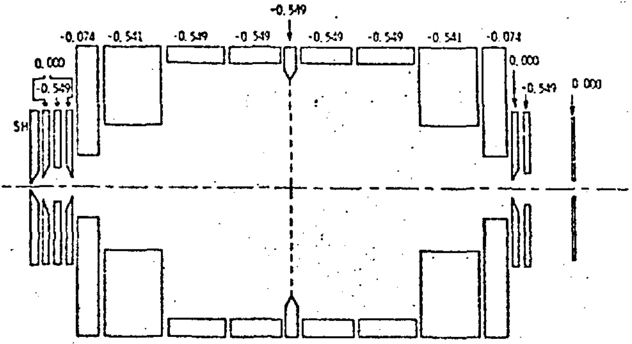

FIG. 2. This figure shows the voltages on different electrodes and lenses used for our computer calculation. All values are given in volts. Electrons with a kinetic energy of $E_{\text{kin}}=h\nu-I$, i.e., 21.216 $-$15.578=5.638 eV are ejected from the sample housing (the first ionization potential of N_2 is studied). The potential on the sample housing, SH, is for the six different cases (see Fig. 4): (a)—43 meV undervoltage, +5.132 V; (b)—24 meV undervoltage, +5.113 V; (c)—3 meV undervoltage, +5.092 V; (d)—7 meV overvoltage, +5.082 V; (e)—17 meV overvoltage, +5.072 V; and (f)—50 meV overvoltage, +5.039 V.

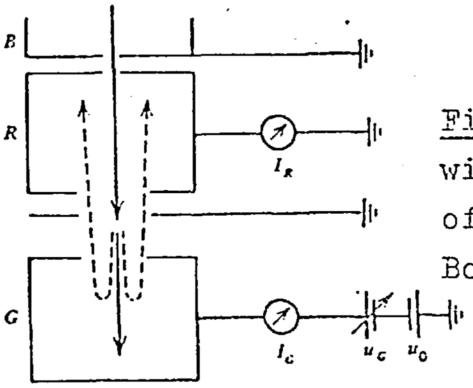

Fig.3.31 Retarding field spectrometer with facility for the collection of rejected electrons used by Boersch and Schweda (1962), from Sevier (1972)

Figure 20. Retarding field analyzer as used by Boersch and Schweda.[155]

a wide range of energies from 45 keV (Haberstroh, 1956) to 10 eV (Burkstrand, 1971). They are essentially similar to previously described analysers except that there is some means of collection of the electrons at the retarding potential. The principal difficulty in the use of such analysers is the requirement that the collector must be floated at high potential whilst a small current from it is measured. Because of this they are now usually only used for low energy work. This form of collector forms part of the analyser described by Boersch and Schweda (1962) (fig. 3.31).

3.21 Rejected electron collection

The inverse retarding field analyser (fig. 3.31) was described by Boersch and Schweda (1962). This instrument, besides using a Faraday cup collector, also collected separately those electrons rejected by the high potential Faraday cup. Ideally, the total number of electrons collected ($I_G + I_R$) is constant. This would be of use in low energy transmission work, where the presence of a large peak at the primary beam energy would swamp I_G, resulting in poor signal to noise ratio for lower energy electrons. The inverse would be true for the signal to noise ratio of I_R.

3.22 Secondary electron production and collection of rejected electrons

The production of secondary electrons has not been reported as introducing spurious signals in any retarding field analysers. This is probably because the secondary electrons produced by collision are formed on the side of the saddle potential away from the exit aperture, and thus are accelerated away from the exit aperture rather than towards it.

Collection of rejected electrons can occur with a suspended SHEED type analyser, but only if the collector is very large. Screening is not difficult and no major problems have been reported.

This is further discussed in Chapter 5.

3.23 Commentary

From the above it is clear that a wide variety of analysers is available, most of which could be adapted to act in the manner required.

The choice fell on the retarding mesh analyser similar to those used by the SHEED analysers. The reasons for this choice were :

1) Its simplicity of manufacture and alignment.
2) No major alteration was needed to the vacuum chamber.
3) Only one high voltage connection was required.

After study of the factors discussed herein, it was felt that the reason for the failure of the original analyser (Chapter 2) was that the central electrode was too long for use without a paraxial magnetic field. Space did not allow field coils to be added, thus the analyser electrode was altered. The new analyser was a plane mesh inset into a mounting ring to provide some focusing. The construction and operation of the analyser are discussed in Chapters 4 and 5.

CHAPTER 4

APPARATUS IMPROVEMENTS

4.1 The electron spectrometer II

This chapter serves to outline the alterations and innovations made to the original spectrometer by the author.

4.2 The electron gun

The gun described in Chapter 2 had two fundamental drawbacks in normal use. It was extremely unstable and it was not sufficiently well insulated, tracking and breakdown of the insulation occurring above 16 kV. Both faults were due to the confined space in which the gun was being used.

The gun was housed (Fig. 2.3) in a glass tube which acted as the insulation from the earthed steel vacuum wall. The insulator was, because of its size, only useful to 30 kV, even when new clean glass was used. This was because the tracking lengths near the cathode were too short. After a few hours use the development of tracks meant that the highest usable voltage was 16 kV.

Several attempts were made to improve the insulation by increasing the length and thickness of the glass insulator. These attempts were successful in lengthening the time between major breakdowns, but these still occurred.

The electron gun was found to be very unstable. A plot of emission current against time (Fig. 4.1a) shows fluctuations of 20% in current over a period of ten seconds. This is believed to have been due to the fact that the open cathode of the gun emitted electrons in all directions, causing severe local charging of the insulator in which it was housed. This charging resulted in variations of the field between the anode and cathode, thus directly influencing the beam current. Charging would not normally happen as, when in use in a cathode ray tube, the gun is housed in a

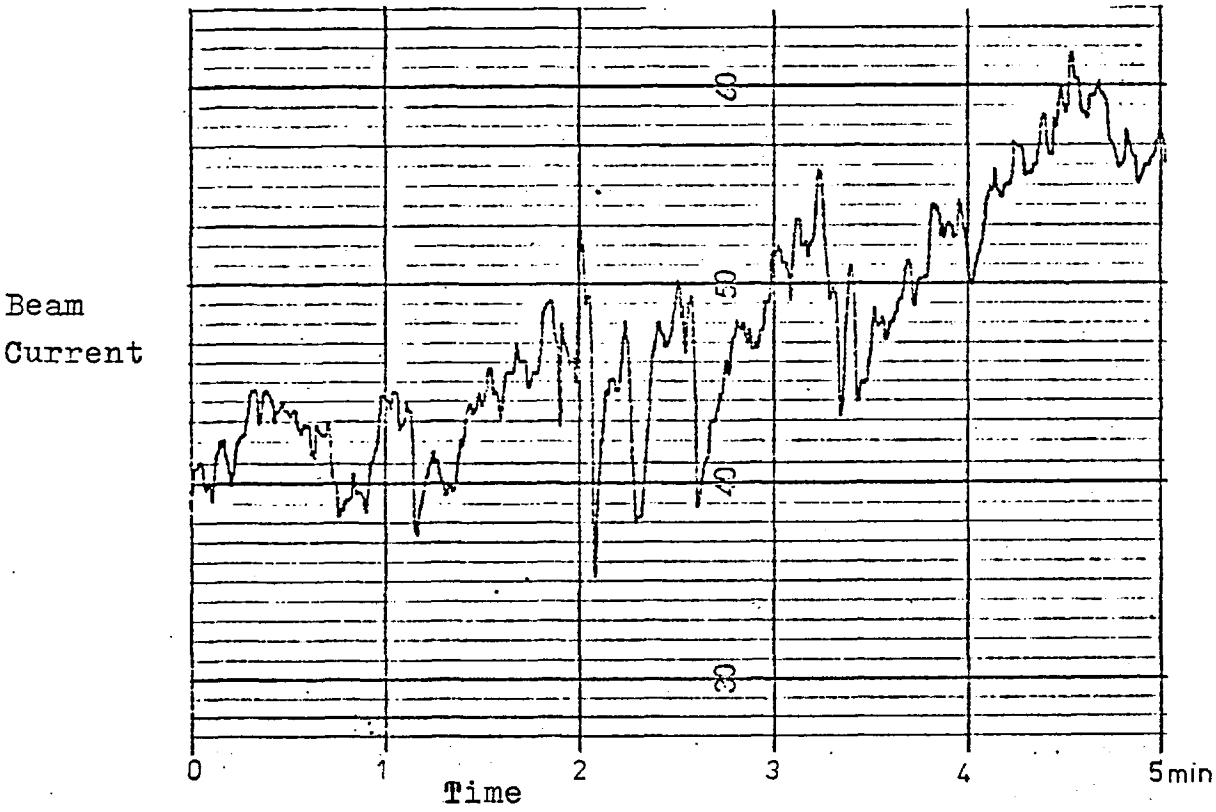

<u>Fig.4.1a</u> Variation of beam current of G.E.C. T490 gun (Fig.2.3) with time.

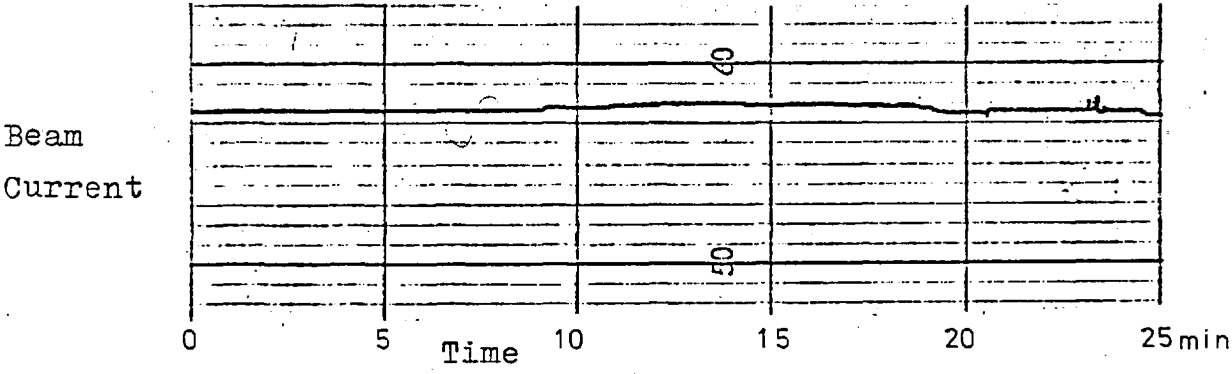

<u>Fig.4.1b</u> Variation of beam current of 'new' gun (Fig.4.2) With time.

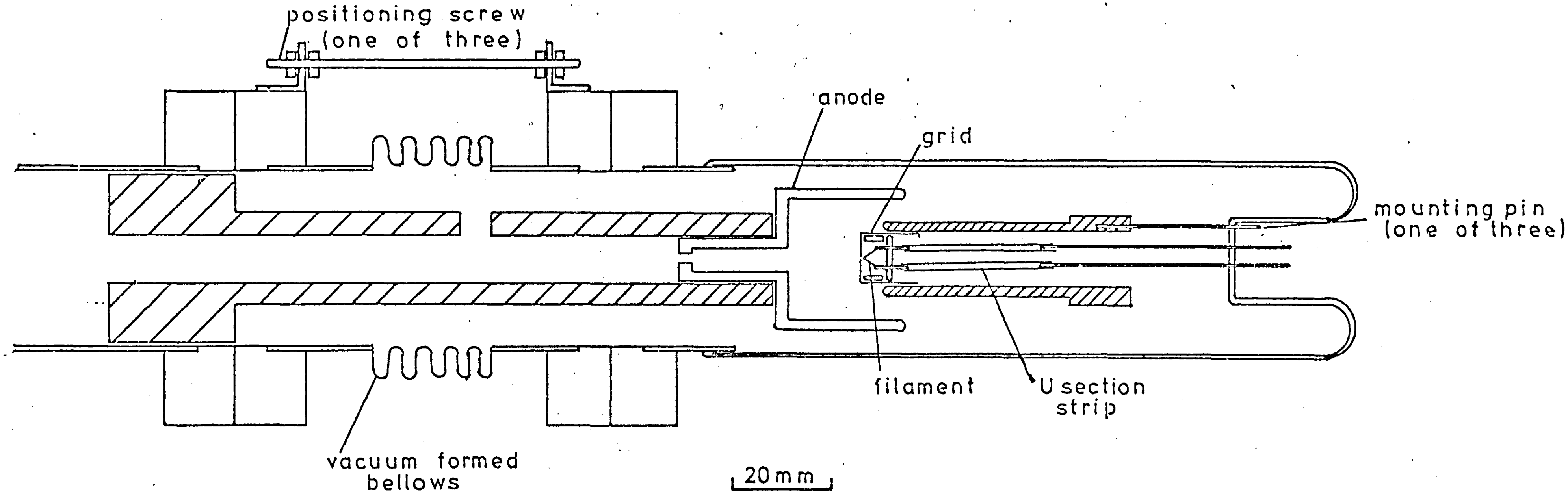

<u>Fig.4.2</u> The 'New' electron gun.

conducting region at cathode potential. Another possible reason for the fluctuations is that the emmission from the oxide coated cathode was not stable under the relatively poor vacuum conditions.

The two problems could have been lessened by increasing the size of the chamber in which the gun was housed, but, as the problems this would have introduced would have been great, it was felt better to build a gun of a rather more conventional microscope type.

4.3 The new gun

The design of the gun was limited by the 70 mm knife edge flange, onto which the gun and lens assembly had to be mounted and by the need to avoid reconstruction of the pumping line to accommodate an enlarged gun chamber.

The gun was of the conventional triode type (Fig. 4.2). The cathode consisted of a polished steel tube mounted on three tungsten pins in a glass envelope, which acted as the high voltage insulation. The filament/grid assemblies (Figs. 4.3 and 4.4) were push fitted into the front of the tube. The grid connections were made via the mounting pins for the tube. Connections to the filament were made by two lengths of nickel sheet bent in U section and spot welded to the pins of the filament. These contacts were slid over two tungsten lead throughs.

The original filament holder (Fig. 4.3) had a ceramic base onto which a filament of 0.1 mm diameter tungsten wire was attached by two stainless steel barrel connectors. This proved unsatisfactory in that the filaments flexed on heating, and the filament to grid distance was arbitrary. These two factors meant that several attempts had to be made to achieve a satisfactory filament change.

The second version of the grid assembly (Fig. 4.4) used an A.E.I. microscope filament mounted in the grid cap. The filament was spaced from the end of the cap by a glass tube. Several lengths of tube were tried, the most satisfactory length being 6.9 mm. This provided the most powerful output, assuming the anode to cathode distance and grid bias were also correctly adjusted.

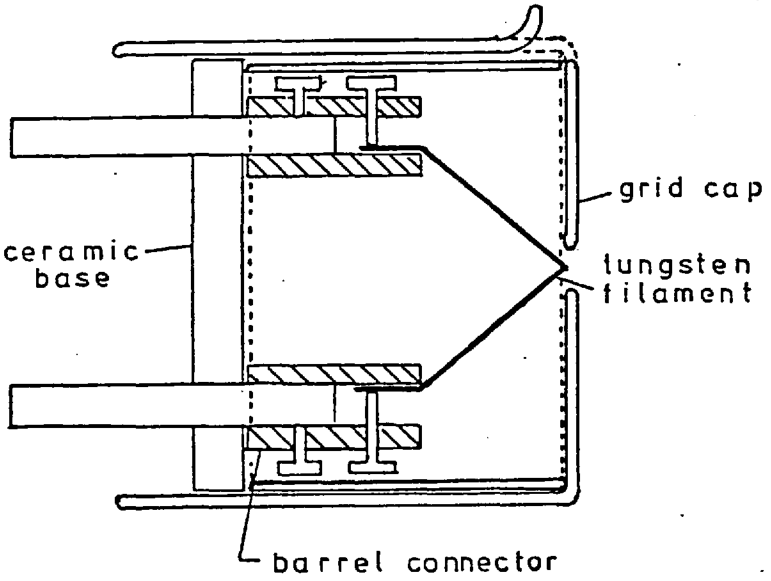

Fig.4.3 Filament / grid assembly for new gun, version I, tungsten wire filament.

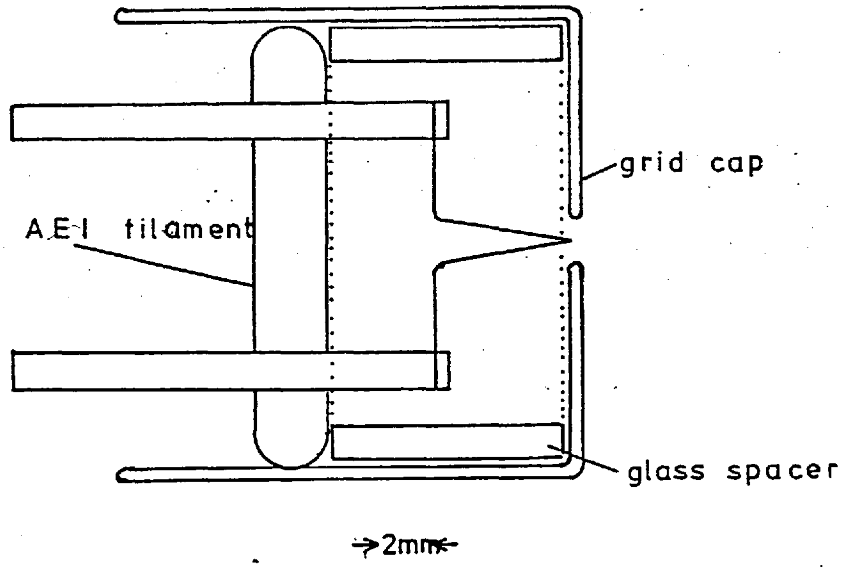

Fig. 4.4 Filament / grid assembly for new gun, version II, A.E.I filament.

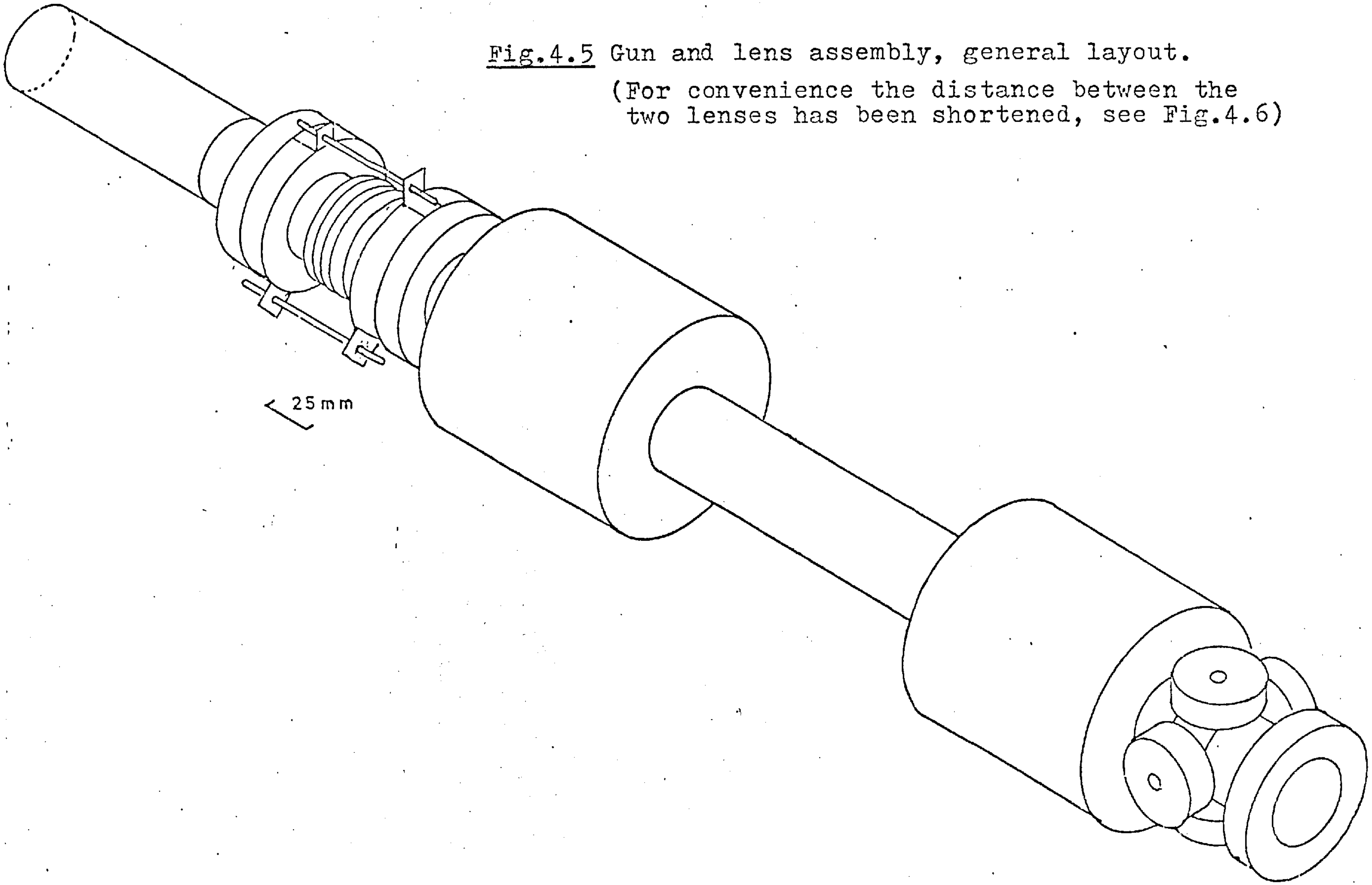

Fig.4.5 Gun and lens assembly, general layout.
(For convenience the distance between the two lenses has been shortened, see Fig.4.6)

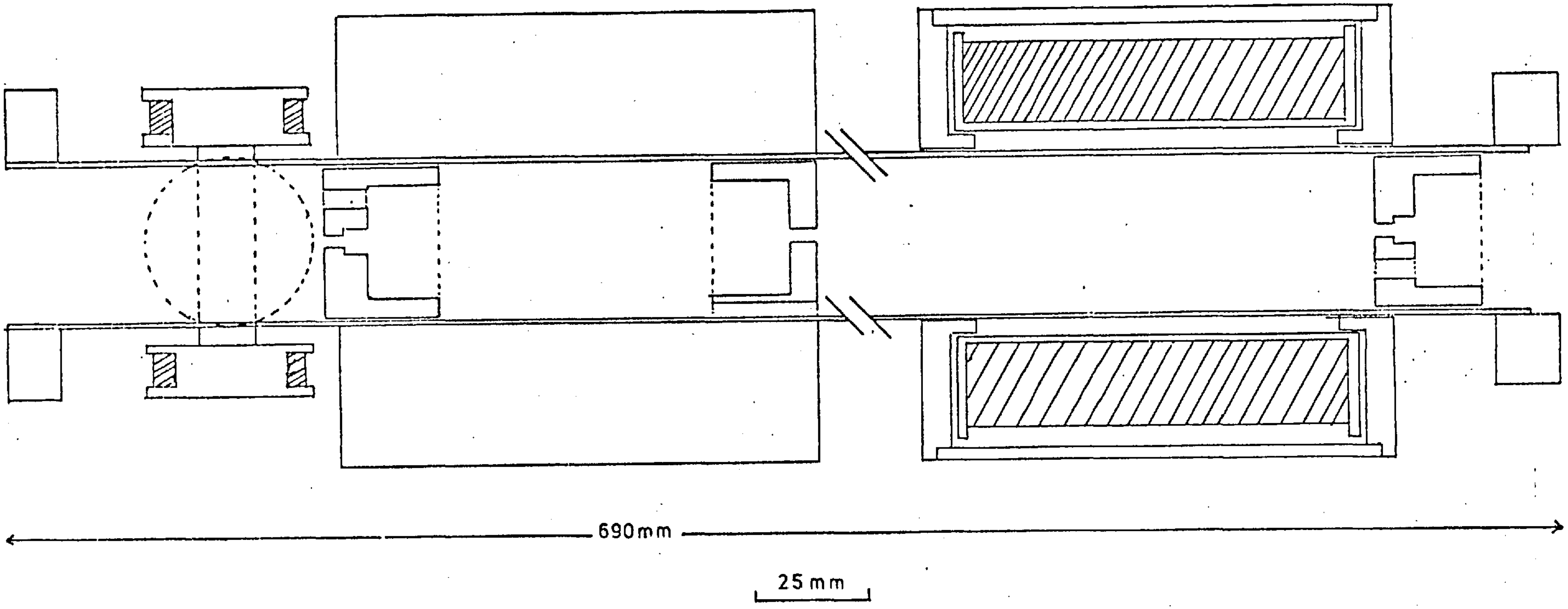

Fig.4.6 Lens assembly, vertical section.

Filament changes involved removing the grid assembly with long nose pliers from the outer tube, welding the nickel U section sheet to the pins of a new filament, then trying to settle both these on the deeply recessed tungsten pins. In practice, filament changes took no longer than on a similar commercial gun using a flat tantalum filament (Gibson, 1973) and the gun had the advantage of being much brighter. (The maximum current obtained was 2×10^{-7}A as opposed to 1×10^{-9}A, reported by Gibson (1973)).

The anode was a push fit into the end of the lens tube (Figs. 4.3 and 4.6) and extended through a set of bellows linking the cathode assembly to the main lens tube. The anode ended in a highly polished cap, which enclosed the grid cap and acted as an X-ray shield.

The cathode could be positioned relative to the anode by means of three brass studs (Fig. 4.2 shows one), the flexibility being provided by the bellows previously mentioned. This allowed ± 3 mm motion in each of the three orthogonal directions, which was sufficient to align the grid centrally with the anode and obtain the correct anode to cathode spacing.

4.4 The lens system

The original lens system consisted of a single unclad coil of 400 turns, which was powered by a Wier 413 power supply. This was not sufficiently versatile for the needs of the spectrometer, as it did not allow any control of the beam current with the lens. A further drawback was the regular damage caused to the power supply by the breakdown of the HT.

The single lens was replaced by two, each of 20 000 turns, powered by a 300 volt regulated power supply (APT model 504). Each lens (Fig. 4.6) was clad on its outer surface with soft iron to increase the strength of the lens and to reduce the extent of the stray fields. This was particularly important as the electron energy analyser was at times operated within 150 mm of the final lens.

Two orthogonal pairs of deflection coils were fitted between the final lens and the main chamber.

Three apertures were placed in the lens bores (Fig. 4.6). Each had a 1mm central aperture and was a tight, sliding fit in the lens bore. Each aperture was vented for more efficient pumping.

4.5 System performance

By suitable use of the condenser lens the following range of beam currents and spot size were obtained :-

At 20 kV

2×10^{-7}A	into	0.5 mm diameter spot
1×10^{-9}A	into	0.1 mm diameter spot

At 2 kV

4×10^{-9}A	into	1 mm diameter spot
1×10^{-10}A	into	0.2 mm diameter spot

The beam currents could be stably reduced to 1×10^{-14}A by reducing the filament current suitably.

The stability of the complete system is shown by Fig. 4.1b for a typical 40 minute run. The minor excursions are due to switching near the apparatus, but only represent a maximum instability of 1% in current.

4.6 Conclusions

It is obvious that the gun and lens system devised were crude in that no provision was made for aligning the lenses and apertures other than centering the cathode. This resulted in quite severe coma in the final spot. In practice, though, this did not matter as the exact shape of the final spot was unimportant.

The system misalignment resulted in movement of the spot when its intensity was altered by use of the condenser lens. In several calibration experiments it was important that the spot should not move, and in these the intensity was controlled by alteration of the filament current.

4.7 The analyser

The original analyser had the major disadvantage that it could not be moved relative to the beam entrance aperture after the system was pumped out. This poor setting of the analyser was the cause of the extraordinary N(E) curves shown in Fig. 2.10.

It has been shown by several authors (Denbigh, 1965; Bunting, 1971; Ward, 1976) that in order to produce accurate N(E) data with a retarding field analyser, motions must be provided to position the analyser, both in angle and linear direction, about the two axes in the mesh plane.

The freedom for such motion was obtained by inserting a set of edge-welded bellows between the main chamber and the analyser assembly previously described (Chapter 2). The final version of the analyser, Fig. 4.7, consisted of the original analyser chamber linked to the main vacuum chamber by the bellows. Passing through the centre of the bellows and fixed relative to the main chamber was a tube. This carried, at the main chamber end, the aperture holder, and at the analyser end, a highly polished electrode with a 2 mm central aperture.

The aperture holder consisted of a dural plate with a central 1 mm hole. A commercial 300 μm microscope aperture in a 3 mm disc was mounted in the hole. It was held in place at the rear of the screen by an oversize tantalum washer. The front surface of the holder was coated with fluorescent material. Initally, difficulty

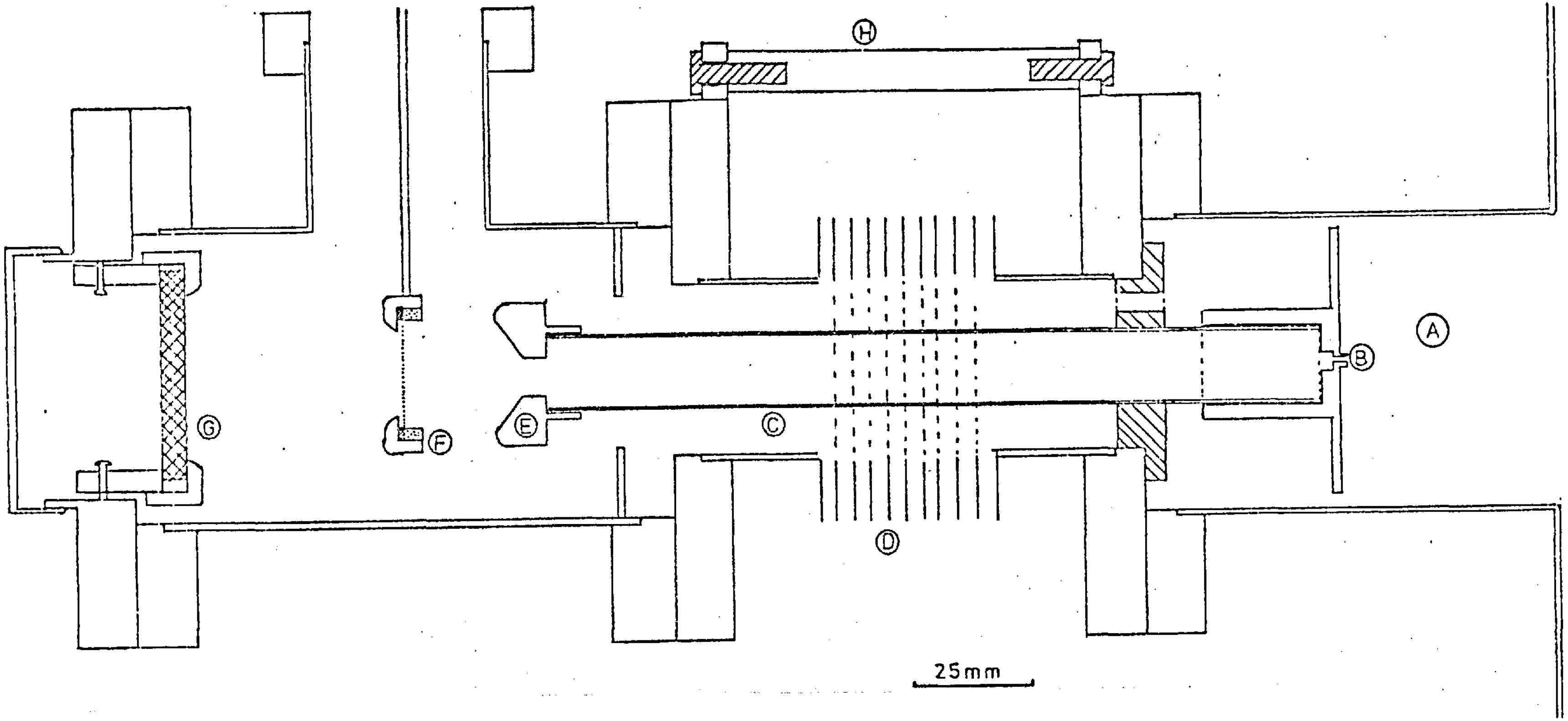

Fig.4.7 Analyser, general layout.

A) Vacuum chamber	E) Polished, stainless steel ring.
B) Entrance aperture.	F) Analyser mesh in mount.
C) Non magnetic Cu-Ni tube	G) Scintillator
D) Edge welded stainless steel bellows.	H) Support rod, one of three used when the chamber was up to air.

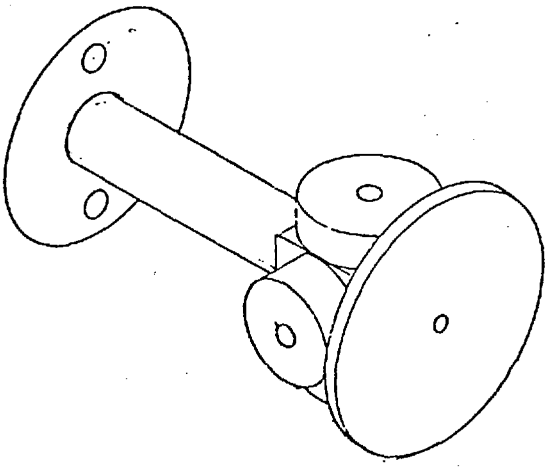

Fig.4.8 Analyser , entrance aperture.

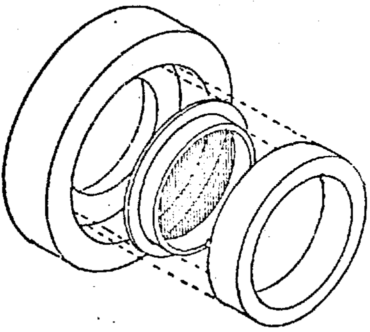

Fig.4.9 Analyser , mesh and mount.

was experienced in getting the phosphor to settle around the central aperture as the surface tension of the amyl-acetate suspension fluid drew the liquid away from the aperture as it dried. This was remedied by leaving a small lip at the edge of the aperture at the end of the last face cut on the plate. The liquid was then drawn towards the aperture and thus slightly thickened the screen in that region as it dried. Mounted behind the screen were two perpendicular pairs of coils, each of 600 turns of 34 gauge coated copper wire. (These are shown in Fig. 4.8 but not in 4.7).

The tube was mounted in a ring which was a push fit in the fixed end of the bellows assembly. The ring was vented to allow pumping of the analyser chamber.

The high voltage electrode was considerably altered from the one described in Chapter 2, as discussed in Chapter 3. The electrode consisted of a 25mm diameter mounted copper mesh of pitch 30 lines per mm. These meshes are used in television camera tubes and are supplied in a pressed nickel mount, L shaped in cross section. The mount was held between two steel rings and suspended from the high voltage lead-through by a steel rod. The rod passed through the outer ring and clamped the inner ring to it without strain on the nickel mount which would otherwise distort the mesh. Both rings were highly polished and mounted as shown (Figs. 4.7 and 4.9).

Fig. 4.7 also shows the mount used to hold a disc of plastic scintillator (NE 102A) in the rear window of the analyser. A tie rod, one of three, is shown, which was used to support the bellows when the system was not under vacuum or the manipulator was not in place.

4.8 The analyser manipulator

The analyser chamber and its associated photomultiplier tube were aligned with respect to the main chamber by means of the manipulator described below. It provided two linear and two rotational motions of ± 5 mm and $\pm 2^{\circ}$ respectively.

The manipulator consisted of three basic sections, shown separated in Fig. 4.10.

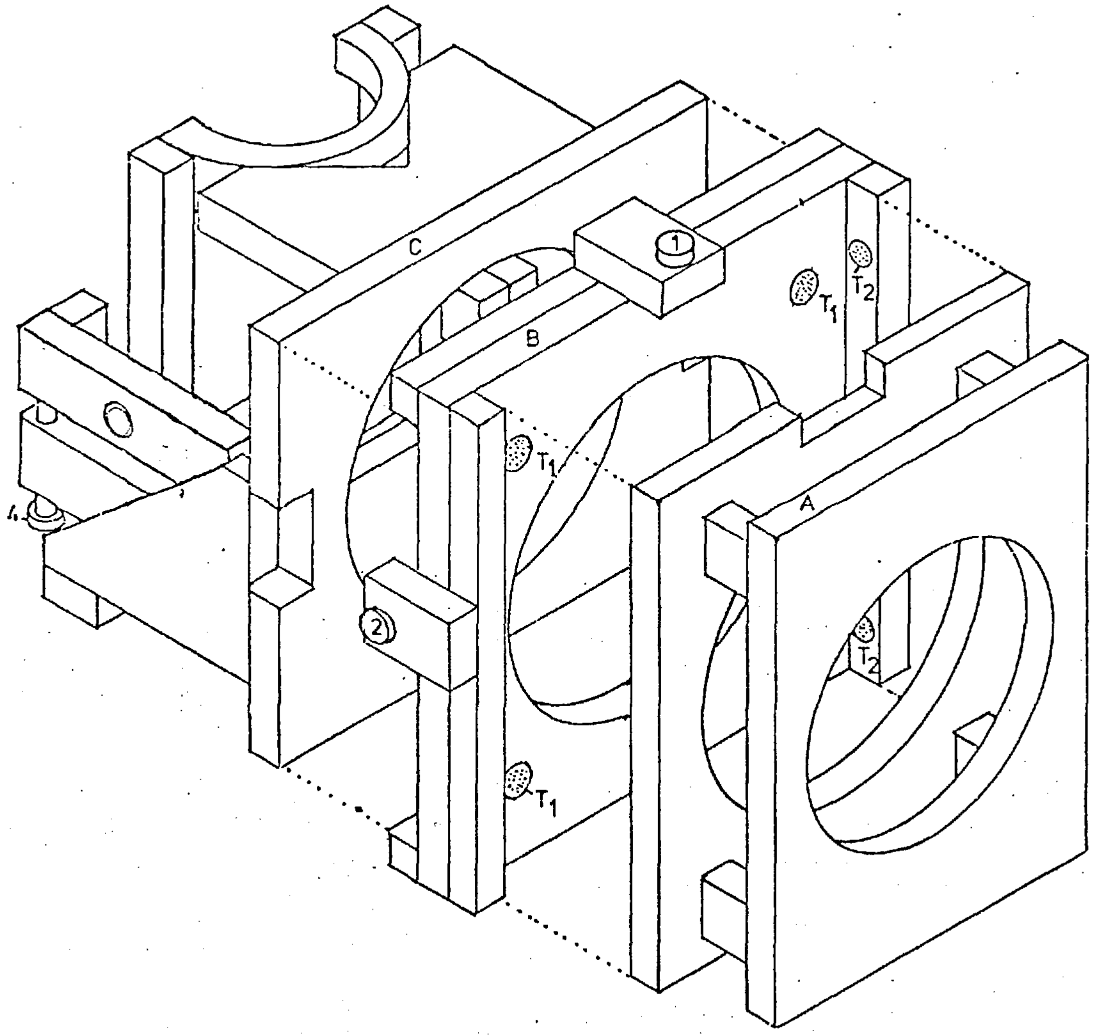

Fig.4.10 Manipulator , front view.

A, Front plate, bolted to main chamber.
B, Centre plate.
C, Rear plate, with trunnion and gimbal.
1, Screw for vertical motion.
2, Screw for horizontal motion.
4, Screw for rotation about horizontal axis.

T1, T2, Teflon pads inset into dural.

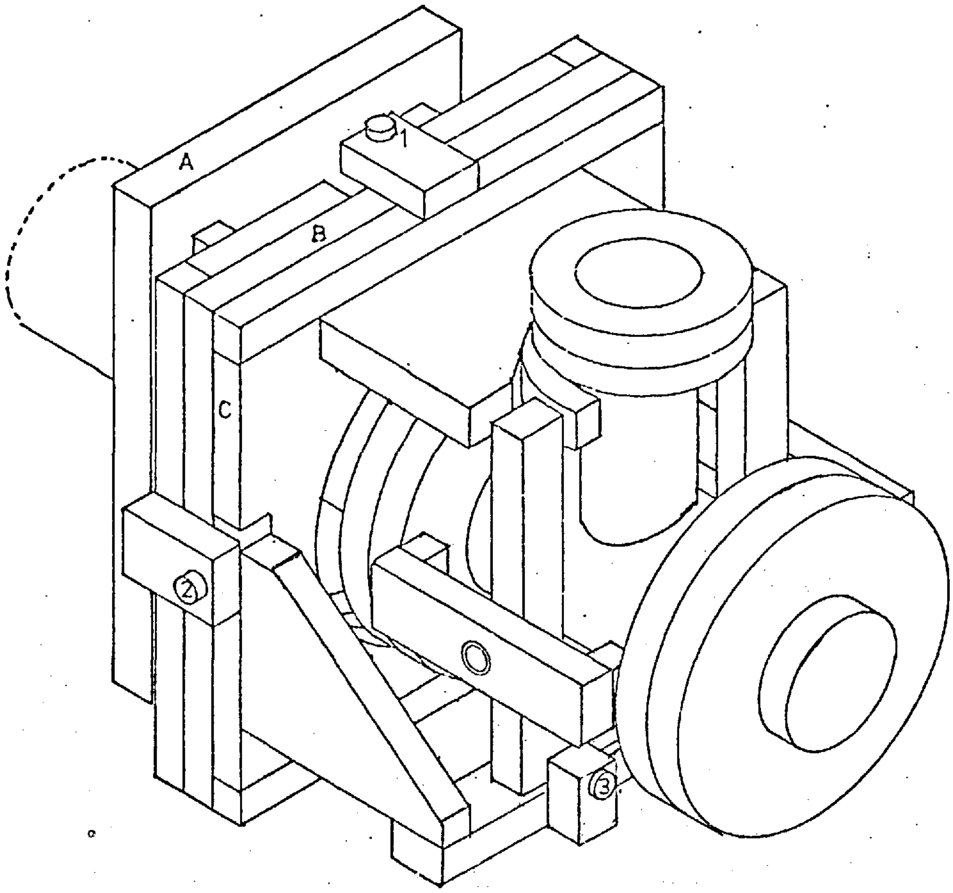

Fig.4.11 Manipulator , rear view, with analyser.

A, Front plate.

B, Centre plate.

C, Rear plate with trunnion and gimbal.

1, Screw for vertical motion.

2, Screw for horizontal motion.

3, Screw for rotation about vertical axis.

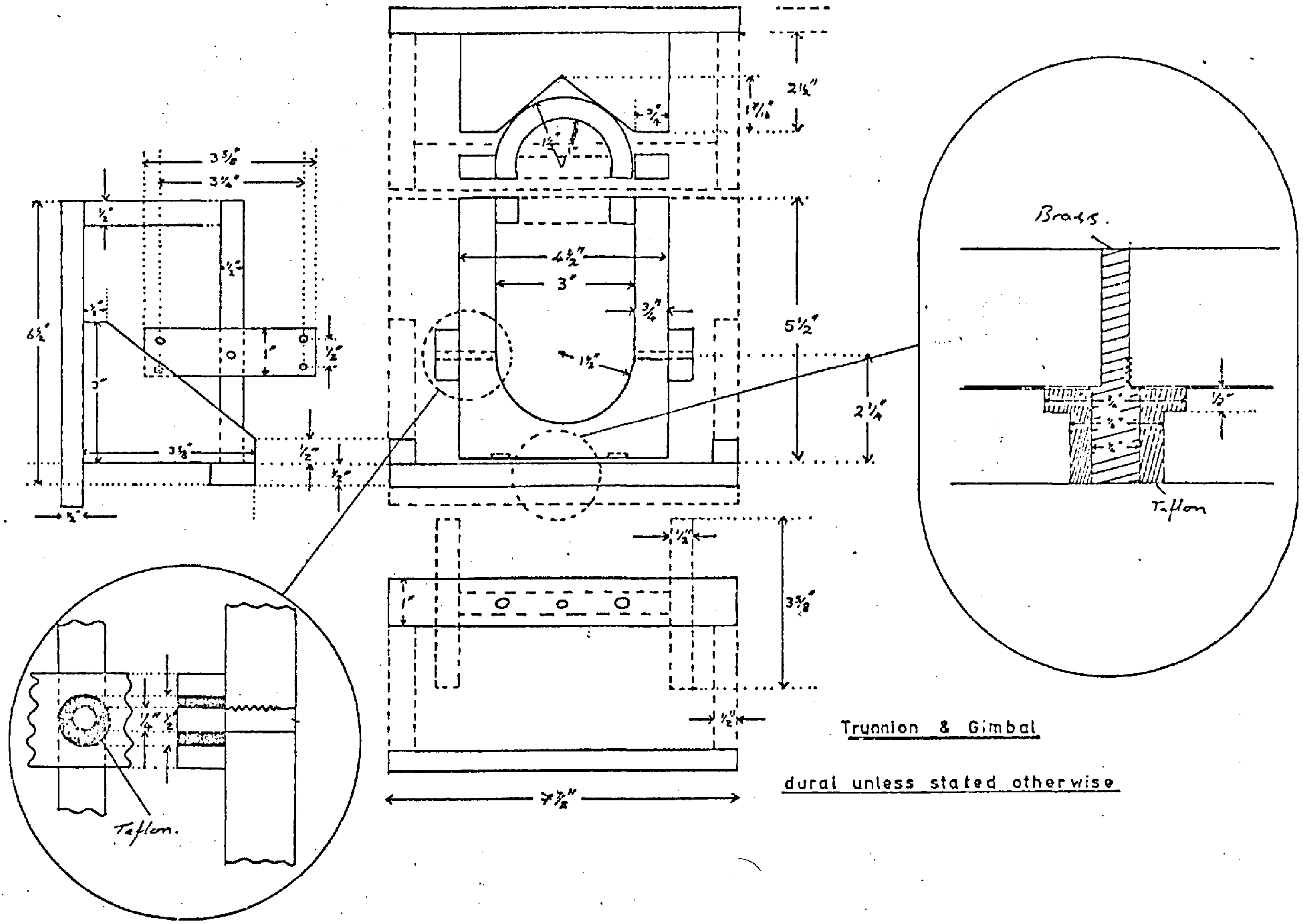

Trunnion & Gimbal

dural unless stated otherwise

Fig.4.12

The front section was rigidly bolted to the flange at the main chamber end of the bellows to provide a reference. The next plate was constrained by two vertical bars to slide in the vertical direction against the front plate. The vertical motion was controlled by a screw (1) bearing on the top of the front plate. Similarly horizontal motion was achieved using a third plate. Two screws (2) were used to drive and also to lock this motion.

The third plate carried a simple trunnion and gimbal arrangement (Figs. 4.11 and 4.12) which held the analyser chamber. Screws were used to control rotation about the horizontal (3) and vertical (4) axes. The arms of the trunnion were bolted to the analyser chamber by lugs included under the flange bolts at each end of the chamber.

There was a support at the top of the gimbal to avoid too great a torque being applied to the lower bearing when the system was evacuated.

The three main plates were not in contact but were separated by four Teflon rods (T1) passing through and projecting on either side of the central plate. Pads of Teflon (T2) projected from the horizontal and vertical slide bars and beneath the gimbal to reduce friction and to provide a smoother motion. The gimbal and trunnion arms were mounted on brass pins in Teflon bearings.

Despite the heavy loadings imposed on the bearings when the system was evacuated, no noticeable wear was produced in two years' use.

4.9 The photomultiplier

A photomultiplier, type RCA 6342A, was mounted on the rear window of the analyser (Fig. 4.13). The tube was enclosed in a 'Vulcathene' housing (commercial drain pipe) which was lined and covered with aluminium foil, the outer layer acting as an earthed screen and the inner providing uniform photocathode potential over the

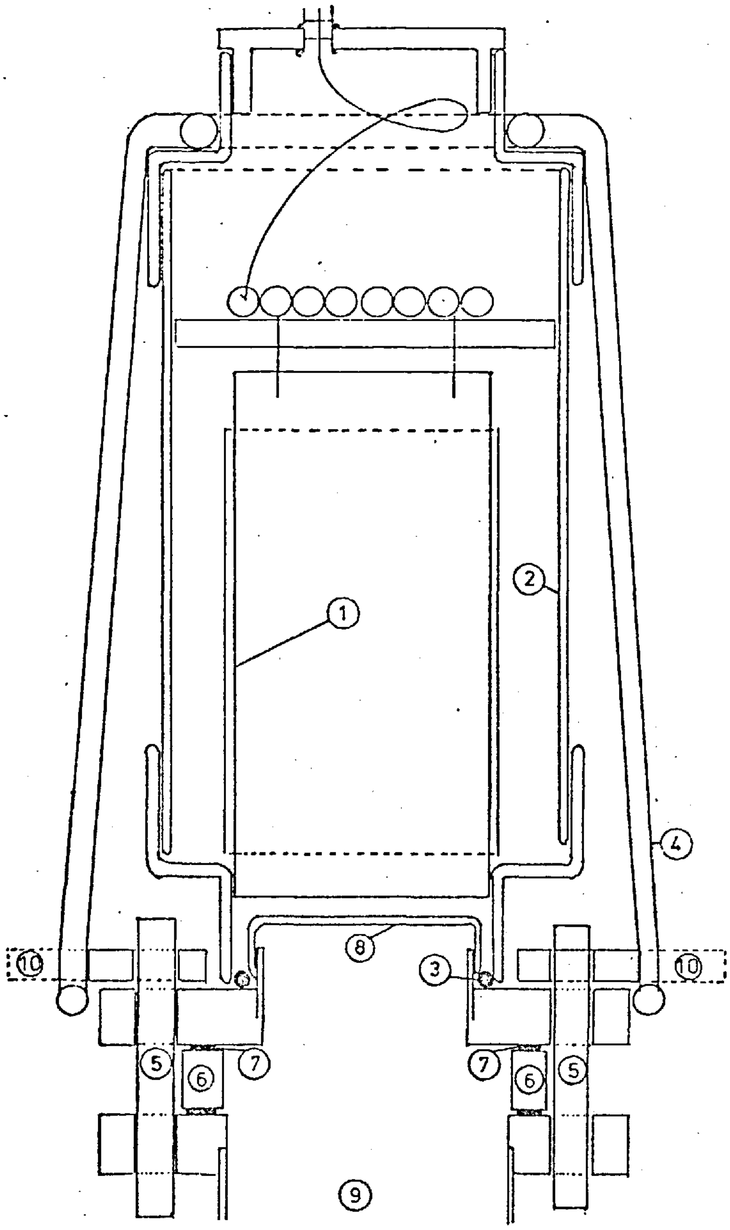

Fig.4.13 Photomultiplier housing.

1, Photomultiplier
2, Black plastic drain pipe.
3, Vacuum 'O' ring.
4, Elastic shock chord.
5, Teflon bolts.
6, Teflon insulating ring.
7, viton gasket.
8, window
9, Vacuum chamber
10, Lug for shock chord.

whole length of the tube. The tube was wired in the current mode, collection of the current being at earth potential. The wiring is shown in Fig. 4.14.

The photomultiplier housing was a close fit on the window of the analyser and a light tight seal was made using a vacuum 'O' ring. The photomultiplier was held in place by shock chord attached to lugs on the window flange. This provided a simple and quick means of removal of the tube, which was only left in place when the system was under vacuum.

The window and the screen could be floated to +10 kV relative to the main chamber when the teflon ring, shown in Fig. 4.13, was fitted. Two viton gaskets were used to provide the vacuum seal, which proved suitable to 6×10^{-6} Pa at room temperature. Specially made teflon bolts were used to bolt up this flange.

When the rear window was floated a phosphor was fitted as in Fig. 2.4.

4.10 The E.H.T. system

The basic EHT lay out (Fig. 2.6) was not altered from that of Dr. Dennis but it was almost entirely rebuilt and changed in detail by the author (Fig. 4.15).

The power to the filament was supplied from nine 1.2V 10 ampere hour batteries ('Saft' VR-10). These nickel cadmium cells were arranged in a battery pack providing 3.6V with a capacity of 30 Ah. This pack gave up to 10 hours running time and was charged every night. Current control for the filament was provided by a 0-4 Ω variable resistor.

The grid of the electron gun was biased by two B101 batteries in series controlled by a 2M Ω potential divider. An autobias system of the type used by Dolby and Swift (1960) was tried, but it was found that it was necessary to alter the beam current without affecting the focus condition of the electron optical system, and as this was not possible with the auto bias system the simpler method was adopted.

Typical Voltage-Divider Arrangement for Fast Pulse Response and High Peak Current Systems. Anode Return at Ground Potential.

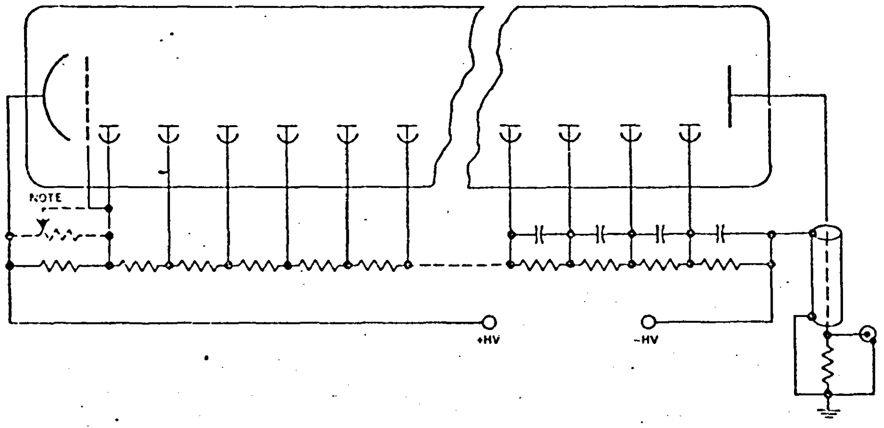

Fig.4.14 Photomultiplier circuit.

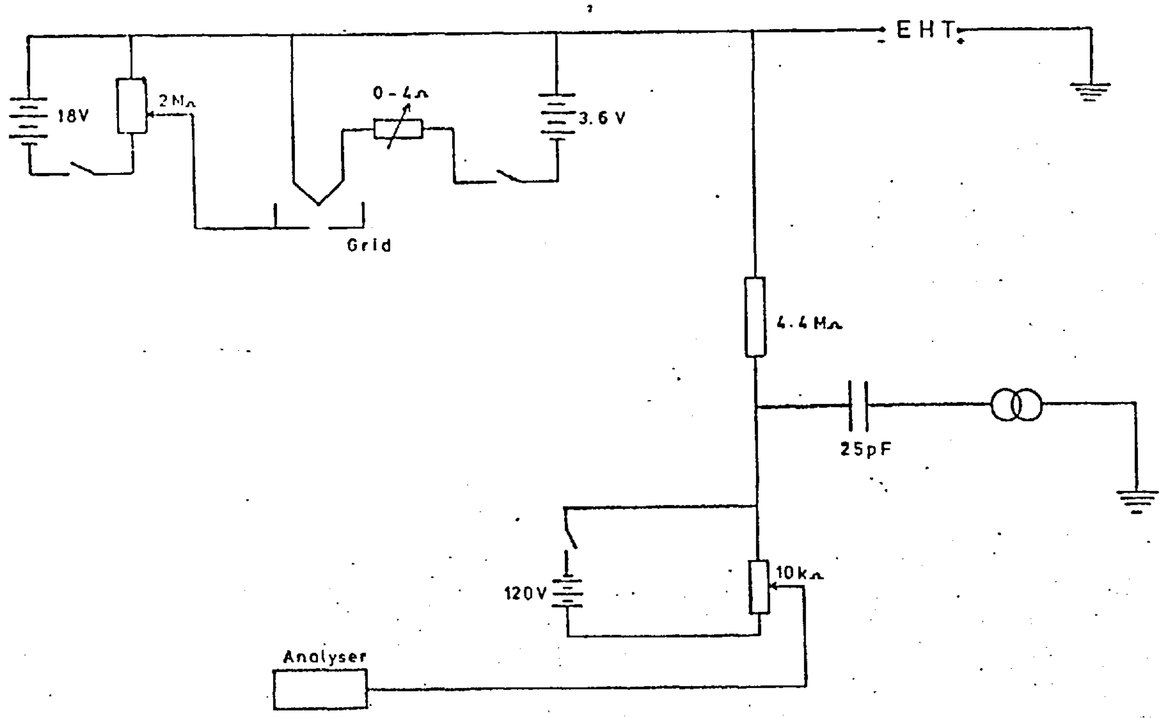

Fig. 4.15 High voltage supply.

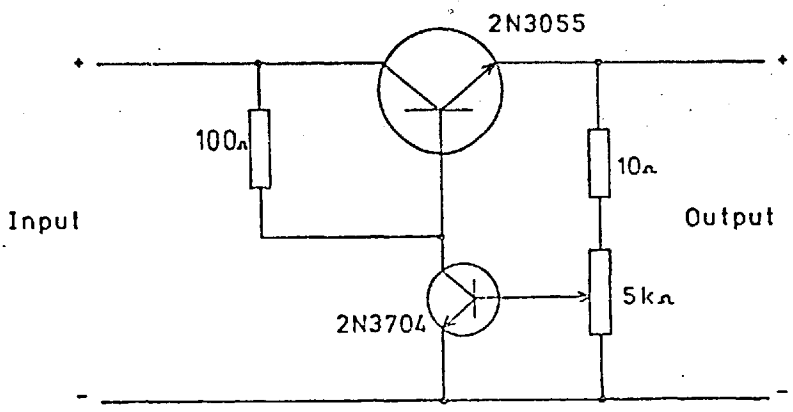

Fig. 4.16 Deflection coil voltage regulator

The bias was usually set to a value below the optimum in such a way that minor fluctuations in the bias voltage had no effect on the beam current. This did mean that more current was drawn from the filament than was necessary, but the local heating of the anode that this caused was minimal.

The gun was linked directly to the negative H.T. as shown. H.T. to the filter was supplied via the 4.4 M Ω resistor shown. This resistor was used to prevent the modulating voltage applied to the filter for electrical differentiation being applied to the gun. It was effective because of the relatively low impedance of the H.T. supply. The advantage of the resistor over the tuned L.C. filters used by several authors was that it was effective over a wide range of modulating frequencies, whereas the filter is specific. In practice, frequencies between 15 Hz and 500 Hz were used, and, at worst, 1% modulation of the gun voltage, as compared with that of the filter, was observed.

The main drawback in using a resistive filter is that if direct current is drawn from the filter electrode or any part of the circuit after the resistive filter, the voltage at the filter electrode decreases because of the voltage drop at the resistor. It is doubtful if such a drop occurred in practice, as no instability was noticed in the filter voltage. This would have been expected had any large current (~ 10 μA) been drawn by field emission or corona discharge.

Positive bias relative to the H.T. supply was applied to the filter from a potential divider, as shown. The divider was driven by one of two synchronous motors of 6 rpm or $\frac{1}{2}$ rpm via a 3 : 1 chain drive, giving scan rates of 24 V/min or 2 V/min. The linearity of the scan voltage against time was checked on several occasions and found to be accurate to within 1 volt of the expected value in a 100 volt scan.

A modulating voltage of between 100 mV and 10 V was supplied to the filter from an Advance J2 signal generator via a 25 pF, 50 kV capacitor.

The filter electrode could also be supplied independently by a separate HT unit (Brandenburg 807R) to give a complete scan of the filter voltage from 0 V to the beam accelerating potential. For this purpose the single turn control potentiometers on the 807R were replaced by ten turn versions driven via a 1 : 1 chain drive by a $\frac{1}{2}$ rpm motor. This gave scan rates of 1.5 kV/min or 150 V/min on the coarse and fine controls respectively.

4.11 Coil controls

The various deflection coils were originally supplied by Weir 413 or similar commercial low tension supplies. If, as often happened, the HT supply discharged to earth one or other of these supplies would be damaged. This caused so much waste of time that the units were replaced by 12V lead acid cells controlled by the simple current control shown (Fig. 4.16). This circuit has some degree of current stabilisation control, and it was found that it was sufficiently stable for the purpose. Whilst the circuit was not immune to HT damage, it was a simple matter to replace one or both transistors in the event of a breakdown.

4.12 Detection and recording

The layout of the various different recording systems is described below, the merits and demerits of each as regards scan time and signal to noise ratio are described in Chapter 5.

Fig. 4.17 shows the various detection systems. In all cases recording was done on an X-Y recorder, the X axis of which was driven by a simple time base (Fig. 4.18) with the potential divider driven by a $\frac{1}{2}$ rpm motor. The advantage of this over an electrical time base was that by switching the various motors together the relationship between the X axis of the recorder and the voltage on the retarding electrode was maintained. Fig. 4.20 shows a direct plot of electrode potential against assumed potential derived from the time base over a range of 100 V. It can

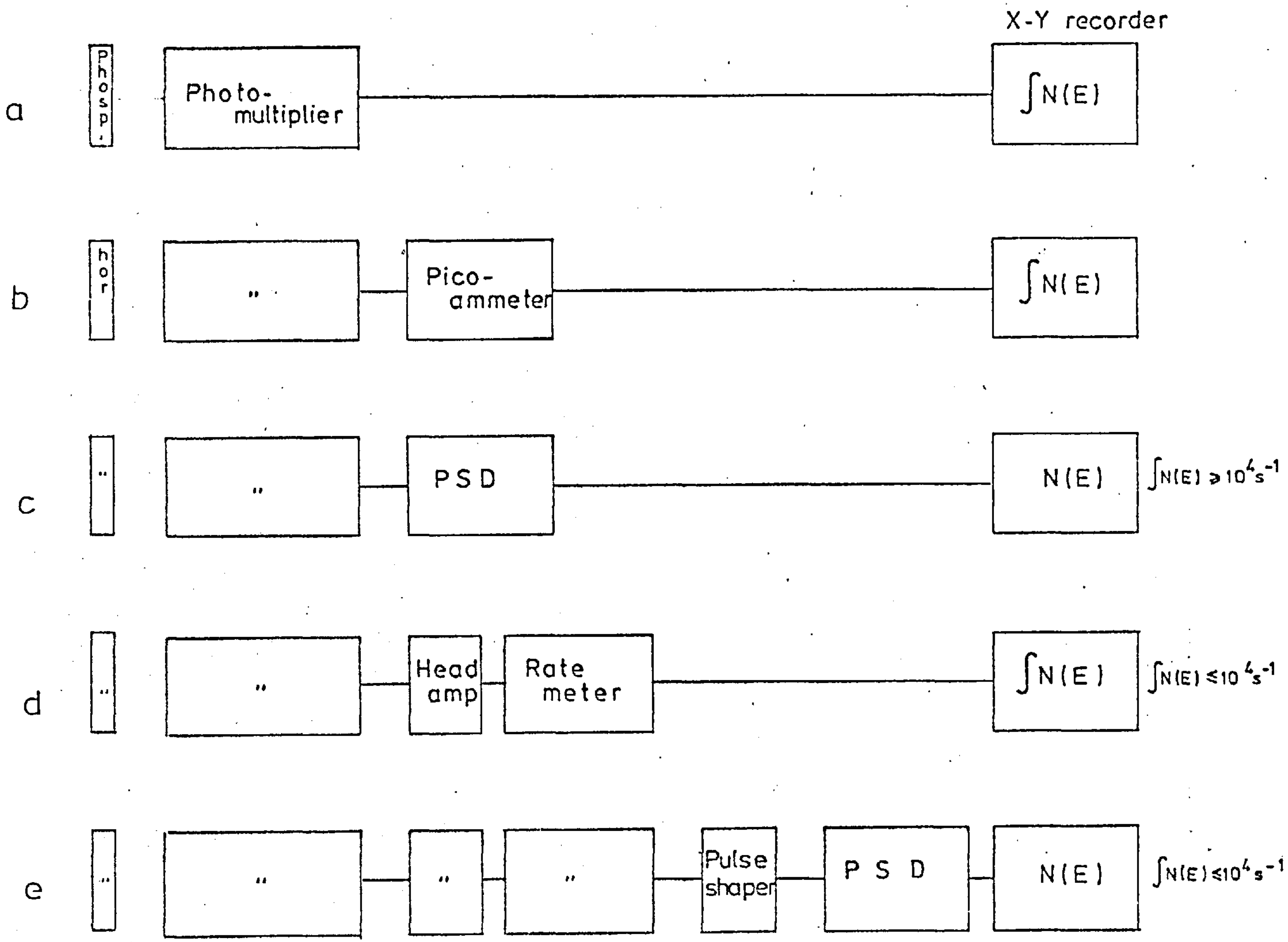

Fig.4.17 Possible recording modes.

seen that the maximum error resulting from this is 2V and that this would be less for smaller scans.

The recording systems divide into two distinct types, those recording $\int_{E_o}^{\infty} N(E)$ (Fig. 4.17a, b, d) and those recording N(E) (Fig. 4.17c, e) by the use of phase sensitive detection. Good accounts of this method are given by Leder and Simpson (1958), Denbigh and Grigson (1965) and Curtis and Ferrier (1970), and it is further discussed in Chapter 5.

The first three detection systems need little explanation. 4.17b is an extension of 4.17a, adding the luxury of half decade range changing and easy current monitoring. 4.17c is the simple differentiating system described in the above references.

The two systems, 4.17d and 4.17e, were used where the count rate fell in total below 10 kHz. In this case the photomultiplier tube was used in the pulse counting mode by the addition of a 0 - 1 MΩ variable resistor across its output. The output was then fed into a ratemeter (J & P Engineering MS301) via a head amplifier. In Fig. 4.17d the rate was directly recorded on the XY recorder, whereas in Fig. 4.17e the ratemeter was used as a discriminator to sort the signal from the photomultiplier noise. The train of pulses representing the signal were then shaped by the 'discriminator' (Fig. 4.19) in order to lengthen them and electrically differentiated using the phase sensitive detector.

The 'discriminator' (Fig. 4.19) was initially built as such for use in conjunction with the head amplifier built by the author (Fig. 4.21). This system, eliminating the need for the commercial ratemeter, was used with a frequency meter to simulate 4.17d and was used as a direct replacement for the ratemeter in 4.17e. It was less reliable and offered less discrimination between signal and noise than the commercial ratemeter system that was available and so was not pursued. However, it is felt that it would be possible to improve on the performance of this simple system if it is necessary to save

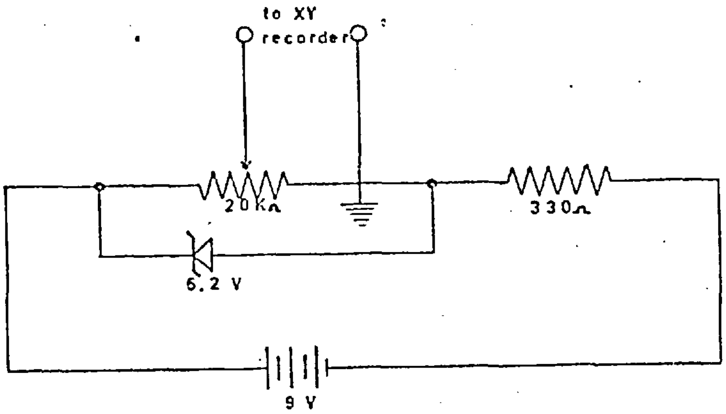

Fig.4.18 Mechanical voltage ramp for X-Y recorder.

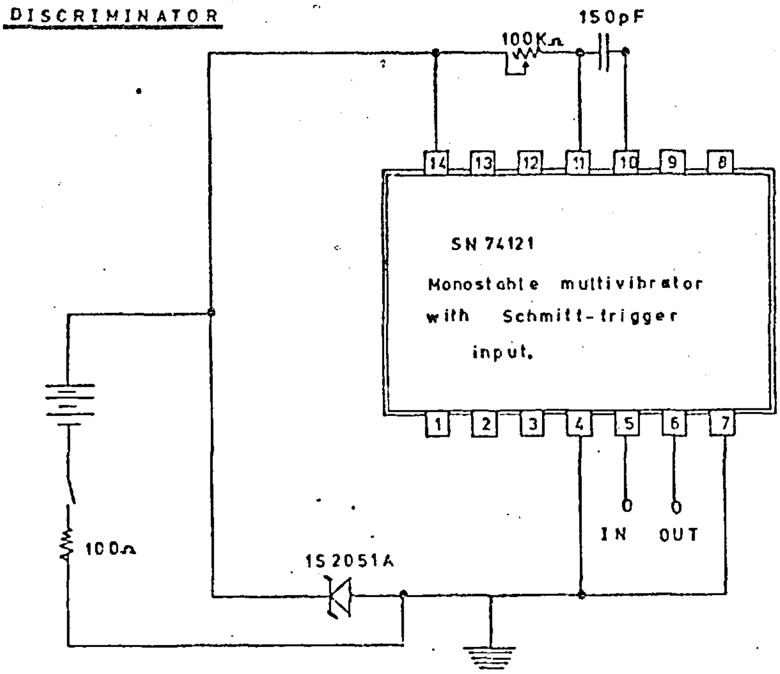

Fig.4.19 Pulse height analyser.

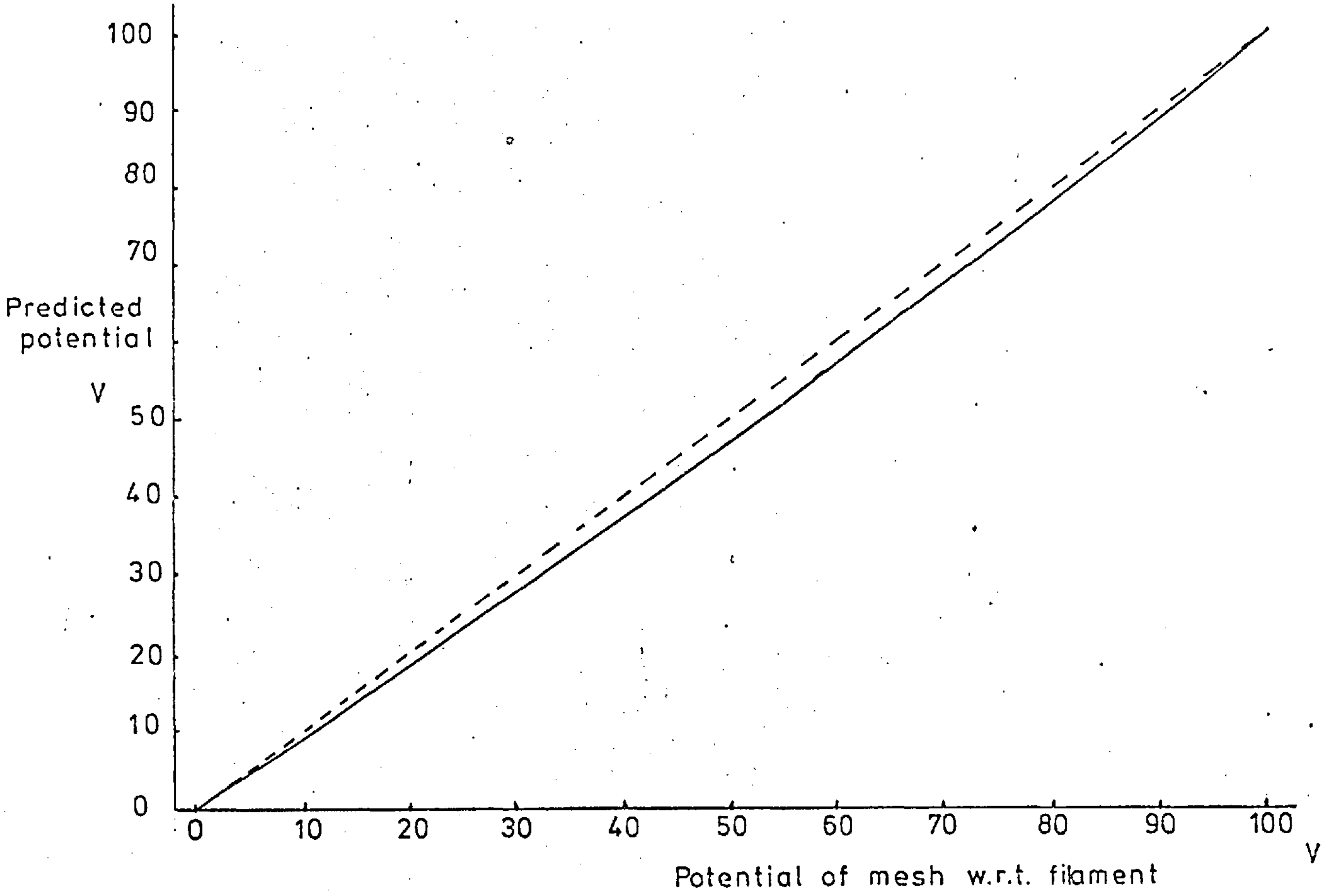

Fig.4.20 Calibration curve for X-Y recorder. The mesh potential with respect to the filament is plotted against the potential predicted by use of the voltage ramp, solid line. The assumed linear relationship is shown, dotted line.

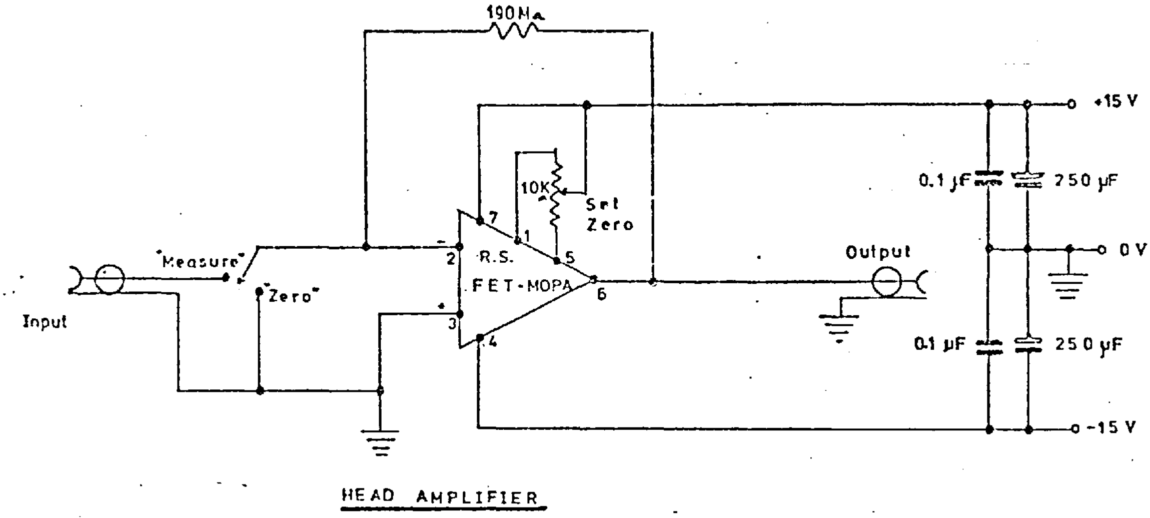

Fig.4.21 Head amplifier

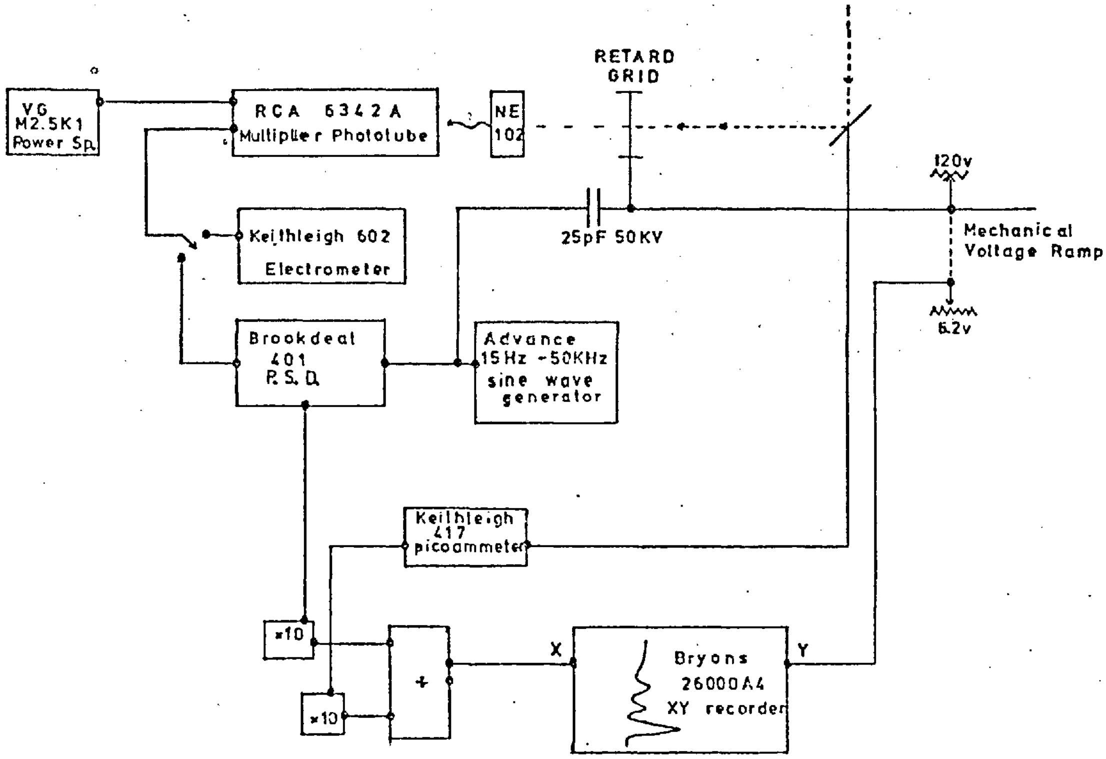

Fig.4.22 Recording using artificial beam stabilization

considerable capital cost.

4.13 Artificial stabilization of the beam

During the development of the electron gun described above, beam fluctuations were at times as high as 10% in 5 minutes. A means of effectively reducing this by monitoring the beam current and ratioing it with the signal to give an output independent of the initial beam current was devised by the author and is shown in the schematic diagram (Fig. 4.22). A reference was obtained from the specimen which was directly proportional to the beam current. (Bishop, 1965, shows implicitly that the backscattering coefficient, η , does not vary with incident beam current for conducting specimens). This current, $I_o (1 - \eta)$ where η is adjusted for the angle of incidence of the beam at the specimen, was fed via a picoammeter to the denominator input (Vx) of the divide circuit (Fig. 4.24). Similarly the numerator of the divide circuit (V_Z) was supplied from the normal signal output, either the other picoammeter or the phase sensitive detector, depending whether 4.17b or 4.17c was in use. The output ($V_o = 10 V_Z / V_X$) was displayed on the XY recorder in the normal manner.

The input voltage for both the numerator and denominator were expected to lie in the range 0 to 1 volt. This was insufficient to operate the divider and hence each input was amplified by a factor of 10, using the non-inverting amplifiers (Fig. 4.23).

The system greatly improved the stability of the system. In the situation where the beam was only stable to 5% the divide circuit would give 0.4%, as indicated in Fig 4.25a.

The circuit was, however, of little use when the beam stability approached 0.5% as it could not improve on this and itself introduced constraints in the operation of the system.

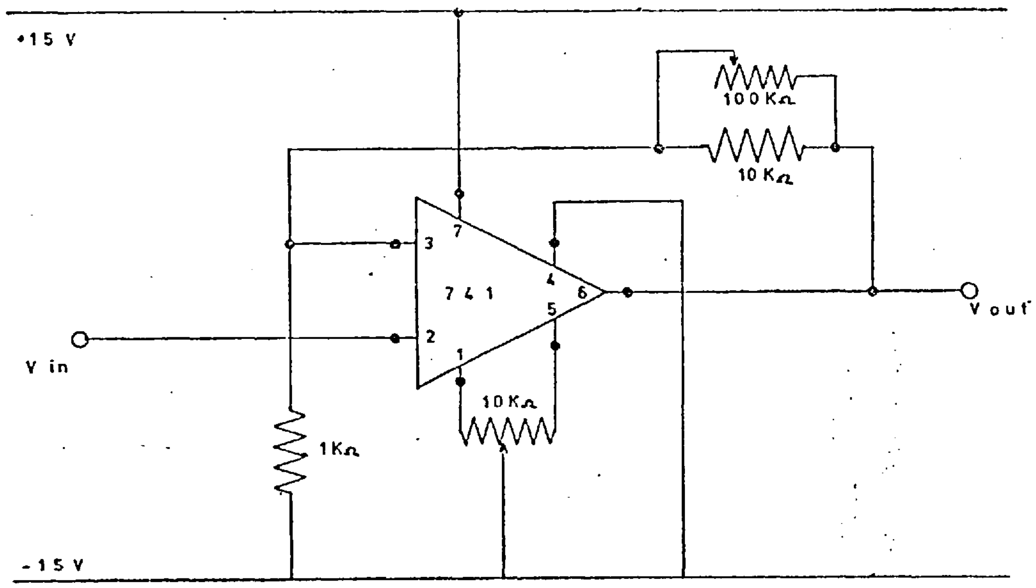

Fig.4.23 x10 Non inverting amplifier.

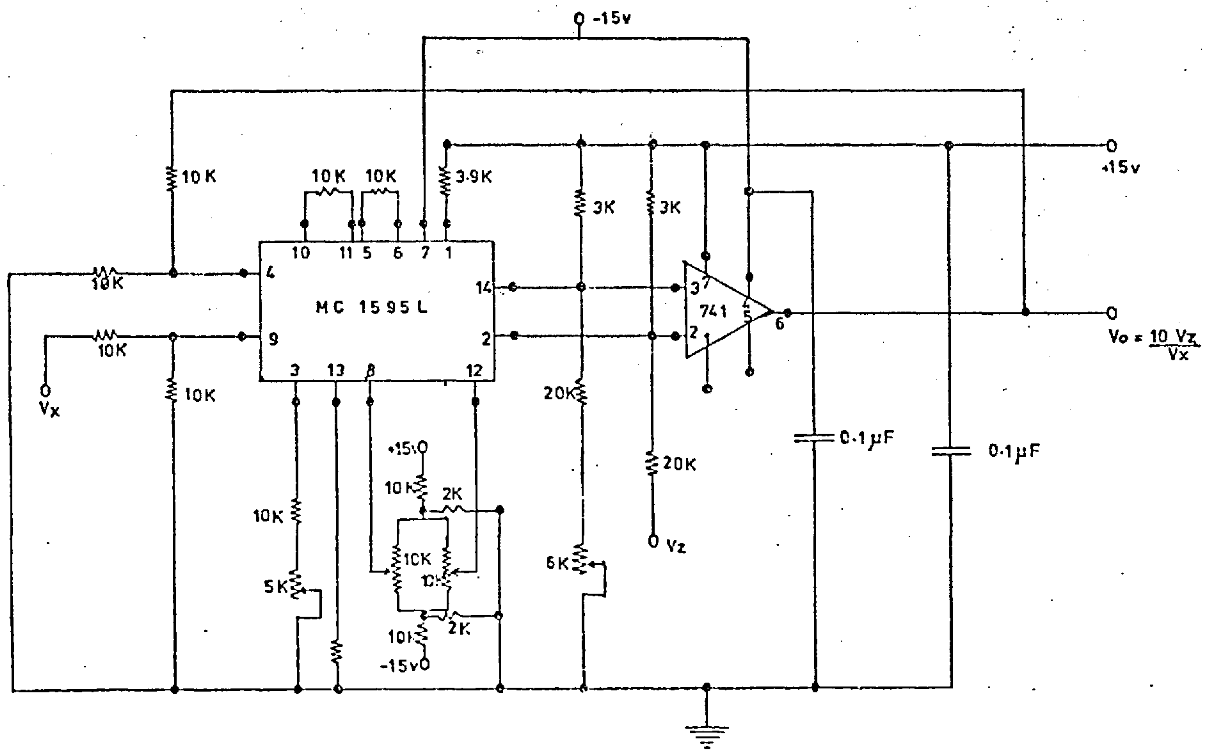

Fig.4.24 Divide circuit $V_o = 10V_z / V_x$

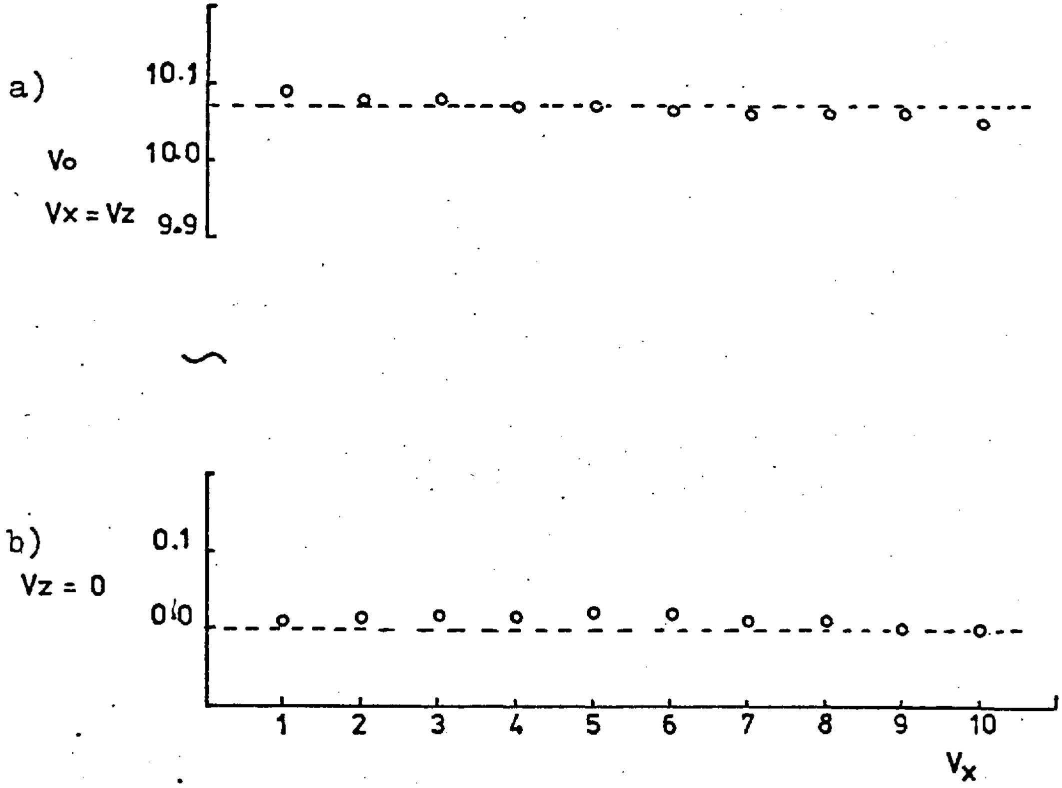

<u>Fig.4.25</u> Calibration of divide circuit

a) V_o vs V_x , $V_x = V_z$

b) V_o vs V_x , $V_x = V_z$

For optimum performance the system had to be operated with the time constants of the two input voltages the same.

The other restrictions on the system are :-

1) The signal to noise ratio drops if the beam current is allowed to fall.

2) Vz must always be less than Vx.

3) Vx must lie between 1 and 10 volts.

4) In the mode of operation described, care must be taken to make sure that the specimen current is in the same direction. If η becomes greater than 1, as can happen at glancing angle, the polarity of the picoammeter measuring the reference current must be reversed.

4.14 Conclusion

In this chapter, the main elements of the modified apparatus have been described, and the reasons for adopting them discussed. The performance of the system, and particularly of the analyser, is discussed in Chapter 5.

CHAPTER 5

THE ANALYSER PERFORMANCE

The ideal retarding field energy analyser should have an energy transfer function, which records all electrons with energy greater than a particular value eV, where V is the potential of the analyser electrode. All electrons with energy less than eV would be rejected. This transfer function is of the form $\int_{eV}^{\infty} a\,\delta(E)\,dE$ (Fig. 5.2a). Similarly, an ideal differential filter should have a transfer function $a\,\delta(E)$ (Fig. 5.1a). In each case, a is a constant and $\delta(E)$ the Dirac delta function.

If these ideals were met, the convolution of an electron energy distribution g(E) with the differential transfer function would return the function ag (E) as the analyser output and the convolution of the function g(E), with the retarding field or integral transfer function, would produce a function $a \cdot \int_{eV}^{\infty} g(E)\,dE$. In practice these ideals are not met with. In this chapter, an attempt is made to identify criteria that can be used to assess the analyser used and to see how closely it approaches the ideal performance.

5.1 Resolution

Several authors have discussed the transfer function of a simple planar mesh when used as an electron energy filter (Denbigh, 1965; Sheppard, 1973; Ward, 1976). The two separate features coming out of such discussions are the width and shape of the functions. Generally the width (full width at half height, fig. 5.1b) has been regarded as of prime importance as most authors have regarded this as defining the energy resolution of the filter. It is generally assumed that the shape of the transfer function will be Gaussian when the analyser is "correctly" aligned, i.e. when the mesh plane is normal to the electron beam.

In practice, the transfer functions of most simple analysers are very similar to

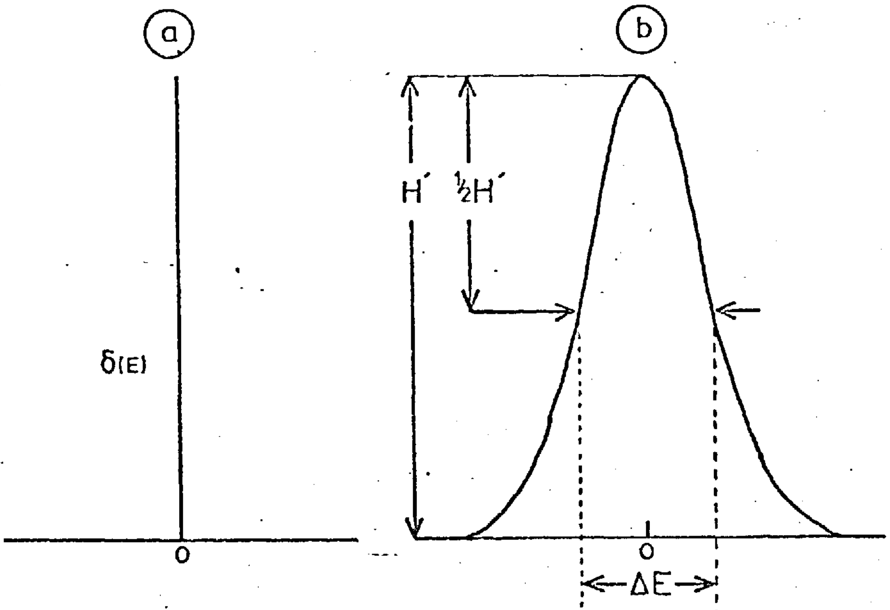

Fig.5.1

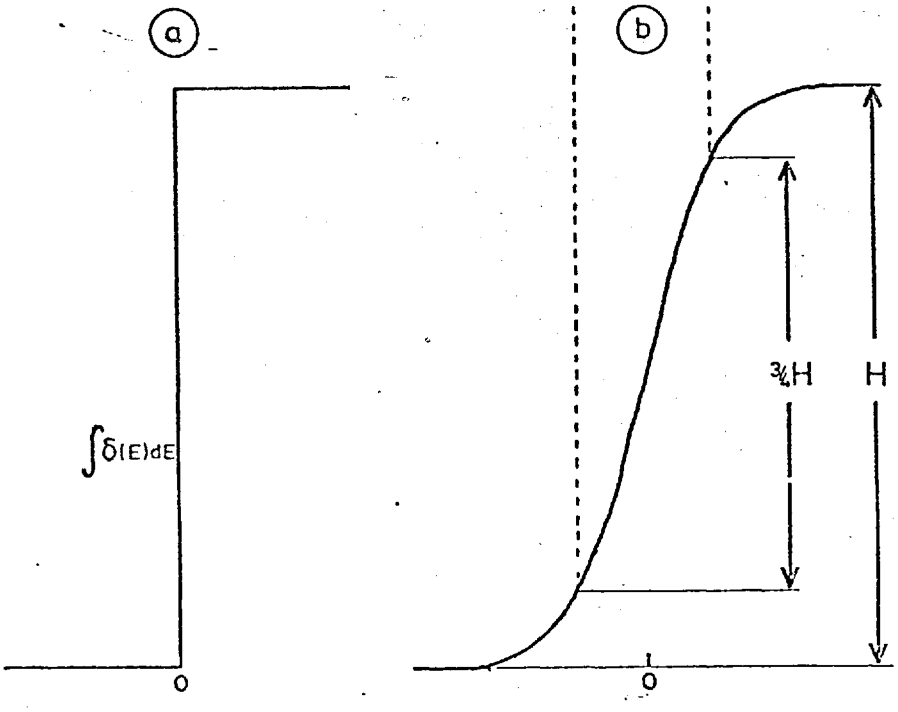

Fig.5.2

Fig.5.1 Transfer function of differential analyser,
a) ideal , b) practical.

Fig.5.2 Transfer function of integral analyser
a) ideal , b) practical

those shown in fig. 5.1b for the differential analyser and fig. 5.2b for the integral analyser. The resolution is defined as $V/\Delta V$, where V is the potential at which the analyser is set and $e\,\Delta V$ is the energy width at half height of the differential transfer function. $e\,\Delta V$ is also the energy gap between 1/8 and 7/8 of the total rise of the integral transfer function (Fig. 5.2b). $V/\Delta V$ is a more suitable criterion for the judgement of resolution than ΔV because most of the fields around the analyser are dependent on the potential of the retarding element and thus on V.

5.2 Beam divergence

The first of the factors affecting resolution is the divergence of the beam entering the analyser. The analyser simply measures the normal component of momentum towards it and thus if the beam has a spread of $\pm\,\alpha$ about the normal, the normal velocity v will be measured as ranging from $v\cos\alpha$ to v. This means that the energy spread will be from $e\,V\cos^2\alpha$ to eV, a spread of $e\,V\sin^2\alpha$ ($eV = \frac{1}{2}\,m\,v^2$).

The angular divergence of the beam in the present work was 1/200 rad, thus the energy spread ΔE produced would be $\Delta E = E/40000$ equivalent to a resolution of 40000. This spread was in fact only a minor part of the resolution.

5.3 Effect of entrance aperture

The electrons entering the analyser must enter via an aperture, of diameter a, which itself causes the field to be non uniform. This non uniformity produces a diverging lens of focal length

$$f = \frac{4\,V}{E_2 - E_1} \tag{5.1}$$

where E_1 is the field in the region in front of the aperture, E_2 field in the analyser and the electron energy is eV. This formula, due to Davison and Calbick (1931) is quoted in Klemperer and Barnett (1971, p.78) and most other texts on electron optics.

In the present work the effective aperture r is 1 mm.

$E_1 = 0$ $\quad$ $E_2 = V/p$ $\quad$ where V = mesh potential

p = distance between mesh and entrance aperture (Fig. 5.3)

Thus from 5.1 the angular spread in the beam is

$$\alpha' = \alpha + r/4p \qquad (5.2)$$

$$\alpha = 1/200 \text{ rad} \qquad p = 37{\cdot}5 \text{ mm}$$

$$\therefore \alpha' = 1/86 \text{ rad}$$

This divergence would result in a resolution of 7350.

5.4 Effect of other non uniform fields

It is clear from Fig. 5.3 that the field gradient is non uniform in places other than the entrance aperture. It is therefore to be expected that further focusing effects and loss of resolution will occur.

In the region between the entrance aperture A and the analyser grid B, the presence of the external vacuum walls, D and E will cause a curvature of the equipotential lines (Fig. 5.3), resulting in increased divergence of the beam in this region. However, the mesh mounting ring will cause a curvature of the equipotentials near to the mesh in the opposite direction, and hence will result in a focusing of the beam as it nears the mesh. These effects are small, opposite and nearly equal in magnitude, though it is probable that the latter effect is larger.

The observed resolution of 5800 including all other effects, particularly the mesh shape, indicates that the beam divergence was in fact less than predicted by these arguments.

It is probable that this was due to suitable, accidental, choice of the correct depth for the mesh holder, which to some extent cancelled out the diverging effect of

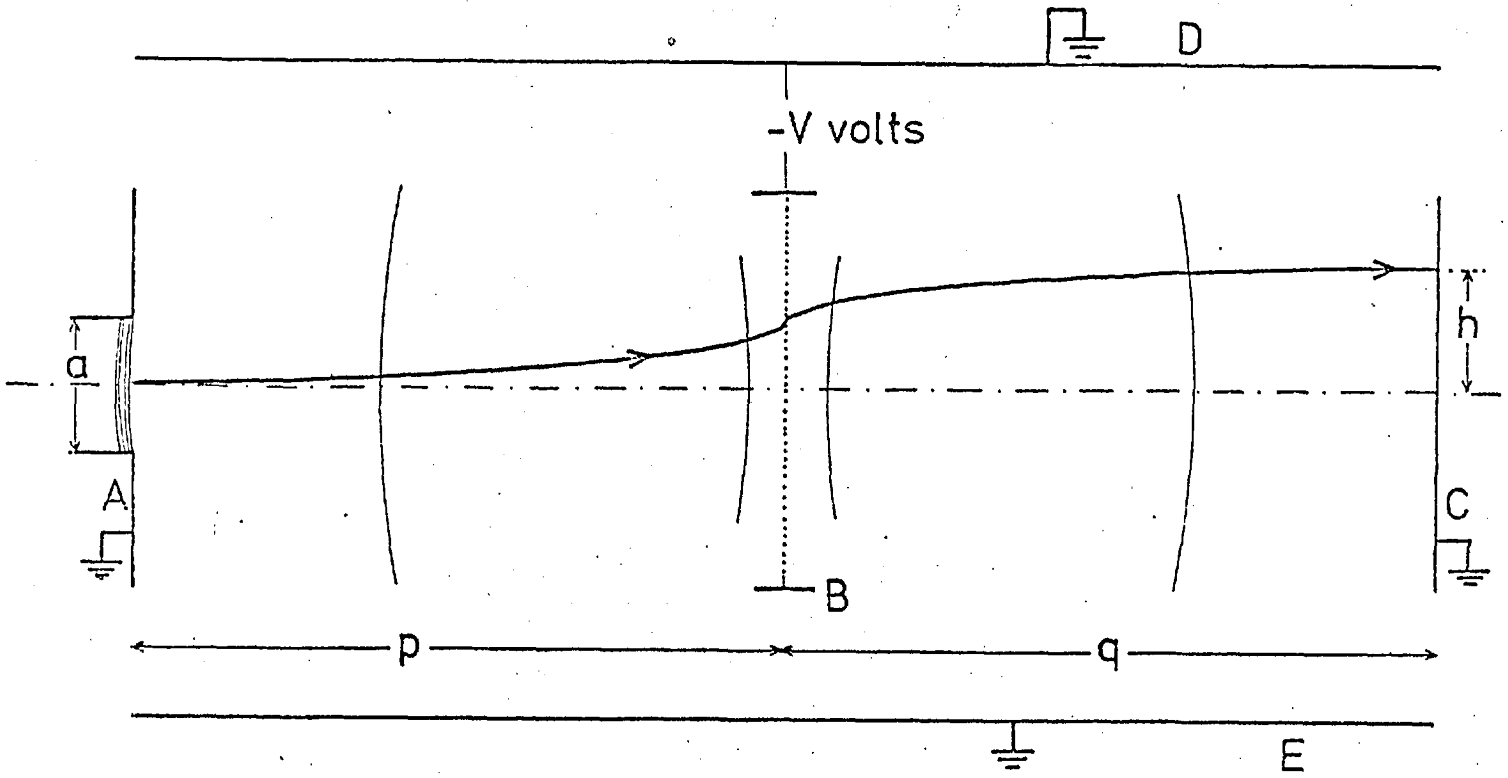

Fig. 5.3 Typical electron trajectory within the analyser.
Some equipotentials are shown to indicate the nature of the focusing produced.

A Entrance aperture.
C Phosphor
B Mesh
D&E Earthed walls.

the entrance aperture and the region between the aperture and the mesh.

5.5 Mesh cell size

The mesh has in the preceding sections been considered to be a plane. In practice, the finite structure needs to be considered.

The effect of mesh cell size has usually been considered in terms of the potential drop between the mesh bar and the centre of the mesh hole. The effect of this difference has been to produce a range of values of the mesh potential V' which will just prevent electrons of energy eV passing through the mesh, depending on which point the electrons meet the holes. An electron of energy eV passing near to a mesh bar will be rejected if the potential of the bar is V; however, it will easily pass through the centre of the hole.

However, if electrons are not to pass through the centre of the mesh, its potential must be raised by an amount $\Delta V'$ in order that the potential at its centre is V . The resolution of the mesh is then taken as $\Delta V'/V$.

Several analytic expressions have been derived for $\Delta V'/V$ from the work of Verster (1963). Two are regularly quoted. Denbigh (1964) derived

$$\frac{\Delta V'}{V} = \frac{D}{\pi p} \ln \frac{D}{\pi r} \qquad (5.3)$$

while Sheppard (1973) gives the expression

$$\frac{\Delta V'}{V} = \frac{D}{2\pi p} \ln 2\left[1 - \cos \frac{2\pi r}{D}\right]^{-1} \qquad (5.4)$$

In each case D is the mesh spacing, $2r$ the diameter of each wire, and p the distance of the mesh from the entrance aperture. Each author has assumed that p = q (Fig. 5.3).

These expressions are far from suitable for any accuracy of field plotting around the very small meshes used in these analysers. This is fully discussed in Appendix 1.

The other expression used by Ward to derive $\Delta V'/V$ is that due to El Kareh and El Kareh ((1970, p.186) for the saddle potential at the centre of an einzel lens.

$$\frac{\Delta V'}{V} = \left(\frac{D}{\pi p}\right)\left(1 - \left(\frac{2d}{D}\right)\left(\frac{\pi}{2} - \arctan\frac{2d}{D}\right)\right) \qquad (5.5)$$

Here D is taken as 1.2 x (side of mesh bar). 2d is the plate thickness, and p the distance to the outer, grounded elements.

The expression of El Kareh and El Kareh predicts a resolution of 8500 for the present system. This is on the high side because the average potential of the centre plate of an einzel lens is V, whereas of a mesh plane it is $V - \frac{\Delta V'}{2}$ where both the plate and the mesh are at a potential V. The field around the mesh is thus on average higher and greater penetration occurs than with the einzel lens.

5.6 The analyser in practice

The basic effects of analyser position relative to the beam have been examined and a resolution of about 7000 might be expected with the system in use on this basis.

In practice, the analyser performed well both with the plastic scintillator and the phosphor within the limitations discussed in Appendix 3. The scintillator was used in the spectrometer at high currents. The integral and differential output in this mode is shown in Figs. 5.4 and 5.5 for a 20 keV beam with the analyser set for optimum resolution. Fig. 5.6 shows the output produced by a very low current beam, 10^{-17}A, at 20 kV.

The latter represents a stringent test as the scan is made over a range from 0 keV to 22 keV. The features on the low energy side of the curve are entirely noise, and several scans showed no consistent placing of any of them. They represent the instability of the gun used at this very low current.

These curves show a practical resolution of 5800 at 20 keV and above, which was found to reduce to 1500 at 2 keV. This includes the effect of the finite energy width of the beam (Appendix 2). If this width is assumed to be 1 eV and both functions are near Gaussian, the actual resolution achieved by the analyser is 6500

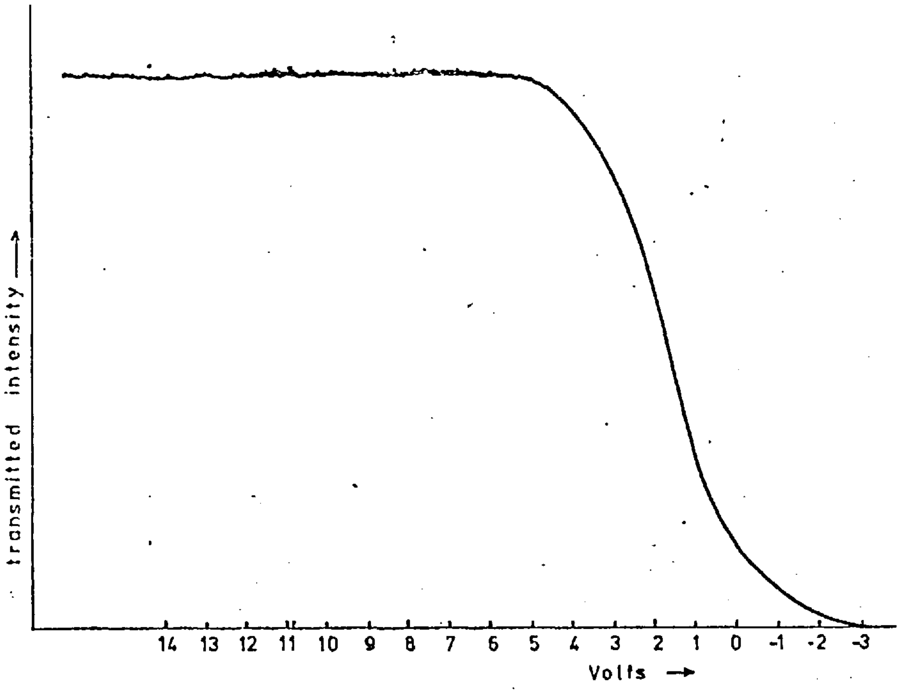

Fig.5.4 Measured, high resolution, integral transfer function for analyser. Energy spread of beam 1eV

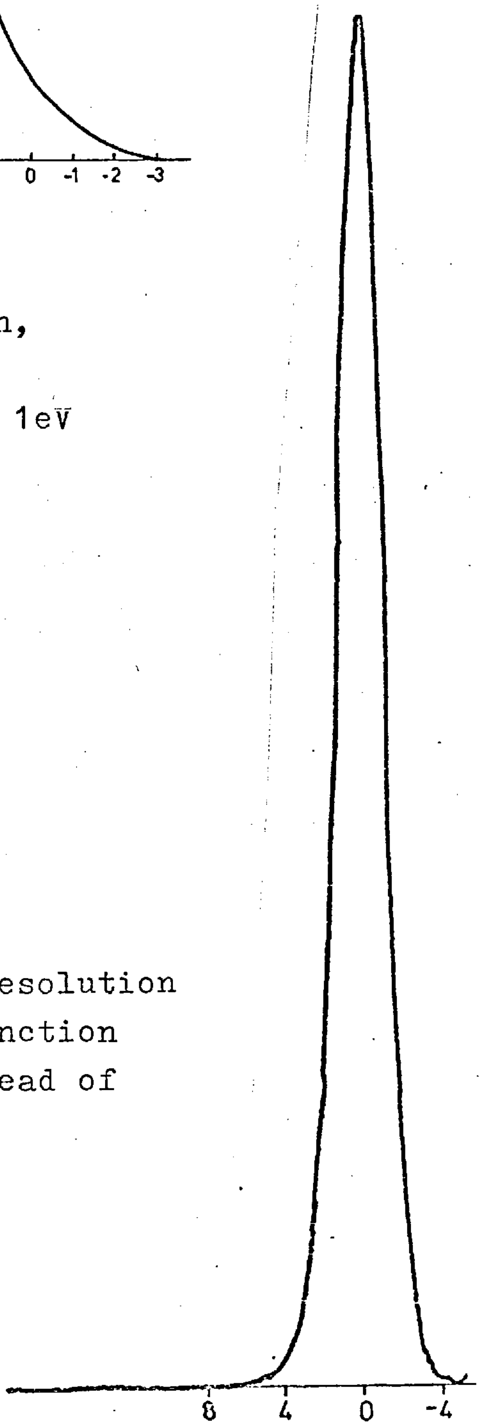

Fig.5.5 Measured, high resolution differential transfer function for analyser. Energy spread of beam ~1eV.

at 20 keV, falling to 2000 at 2 keV.

5.7 Correct alignment

Several experiments were carried out to find the position in which the analyser gave the best resolution. It was assumed initially that this would be when the beam was normal to the mesh. In this position the applied potential would be a maximum to cut off the beam, thus the mesh was set at a potential at which about half the beam was cut off, then its position and angle relative to the beam were altered to increase the measured signal. The potential was raised until the beam was partly cut off, and the process repeated until no movement in either position or angle would increase the signal. In this setting the position could be altered by 2 - 3 mm without altering the cut off, but a change in angle of 0.005 rad would completely cut off the beam.

Contrary to expectation the resulting differential spectrum was not Gaussian and had overshot the N(E) = 0 axis when the analyser potential was reduced a few volts below the beam accelerating potential (Fig. 5.7(1)). This indicates that the transmission of the filter falls as the potential of the filter is lowered. The maximum transmission occurs when the analyser potential is a few volts below complete cut off. (cf. Fig. 5.12)

The analyser was known to function well with a near Gaussian transfer function and with no overshooting of N(E) = 0 axis in the differential spectrum, when set up nearly correctly, i.e. with a cut off a few volts below the beam accelerating potential. An investigation was carried out to determine the reason for this fall off in resolution in what should be the best possible position of the mesh relative to the beam. The following discussion refers to an electron accelerating potential of 20 kV.

5.8 Effect of angle of the mesh on analyser resolution

The transfer function of the analyser was determined for several different mesh angles. A set of these is shown in Fig. 5.8. From these the peak width at half height

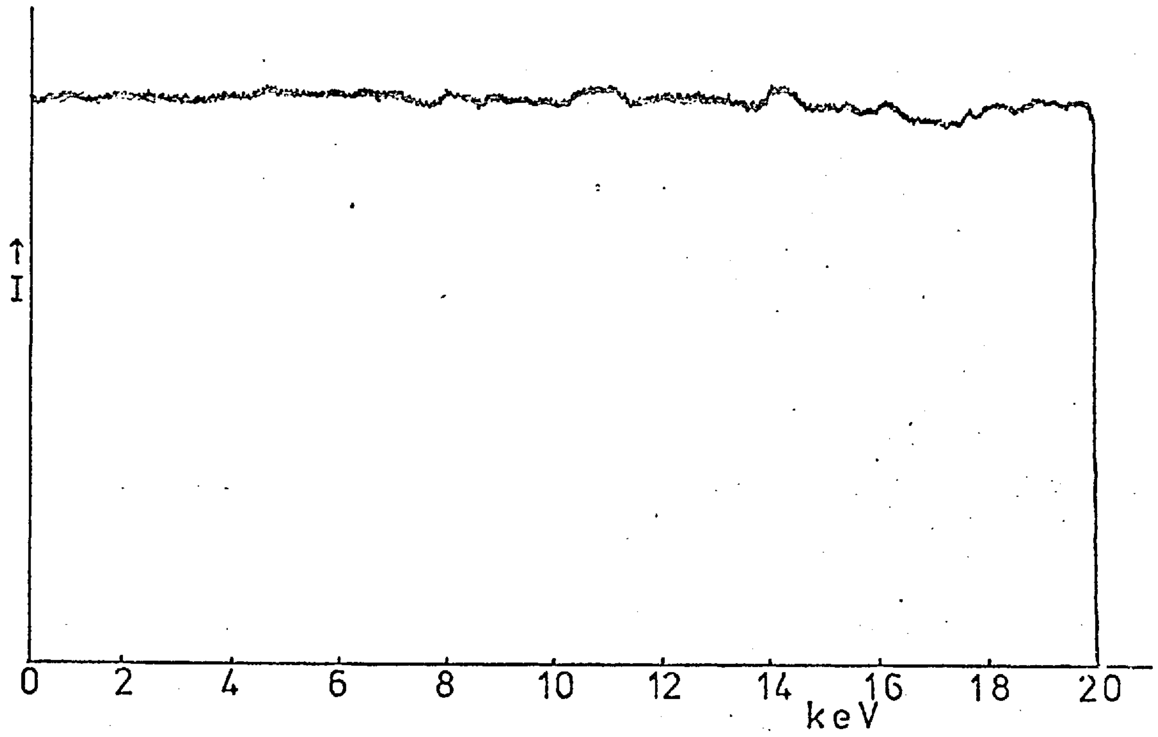

Fig.5.6 Measured, low resolution, transfer function for analyser. The noise in the region 7-18keV was not reproducable and was not a function of the analyser. It was produced by instabilities in the electron gun when operated at 10^{-15}A.

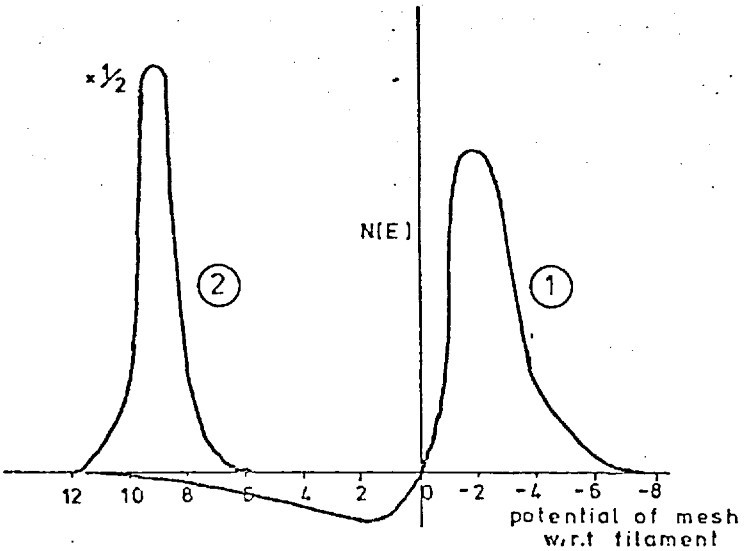

Fig.5.7 Variation of peak width with mesh angle.

1) Analyser set so that peak is moved to highest energy. Note physically meaningless region N(E) $<$ 0

2) Analyser set at an angle to the beam such that N(E) is always greater than zero.

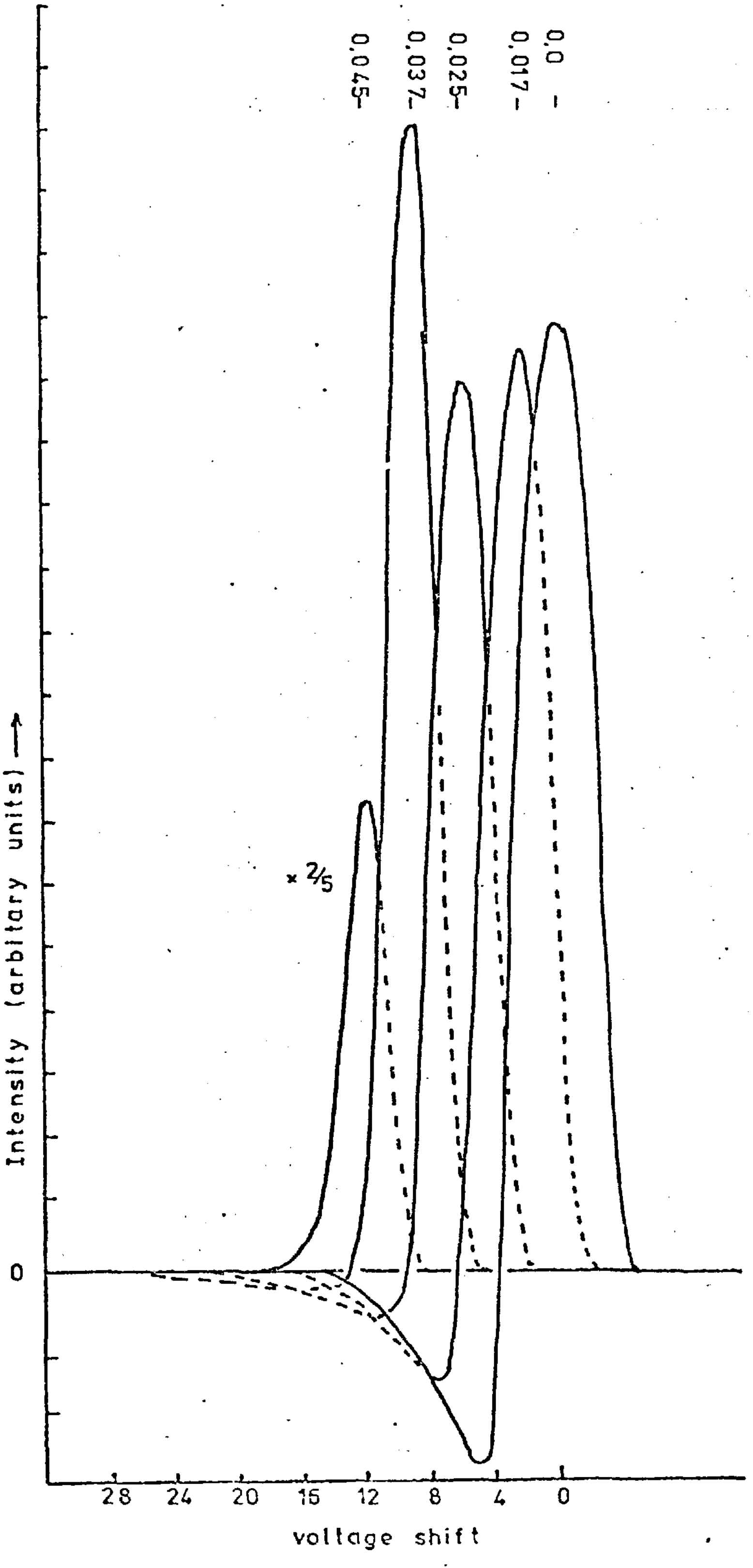

Fig.5.8 Variation of differential transfer function with angle between the normal to the mesh and the beam in the range 0.0 - 0.045 rad.

above N(E) and the maximum overshoot were measured. These are shown in Figs. 5.9 5.10. It can be seen from these that at a mesh tilt of 0.05 radians the resolution has become constant with angle and the overshoot is minimal.

The effect of the tilt on the point at which the maximum of the differential curve occurs is shown in Fig. 5.11 (3). The maximum of the curve at normal incidence is taken as zero.

The relation between the voltage shift and angle often quoted (e.g. Ward, 1976) is

$$\Delta V' = V \sin^2 \vartheta \qquad (5.6)$$

where V = voltage shift

V = accelerating potential of the electrons

ϑ = angle between normal to mesh and the beam

This is shown in Fig. 5.11 (1). It is clear that this does not reflect the actual value of the observed shift. Equation 5.6 represents the expected shift when all equipotentials are turned through the same angle (Fig. 5.12a). The situation in practice is that the mesh is turned relative to the entrance aperture and thus the equipotentials are uniformly spread in angle, forming the wedge shape shown in Fig. 5.12b. A simple, though lengthy, calculation on a pocket calculator, Appendix 6, predicts the shifts to be as shown in Fig. 5.11 (2). This is calculated by using Snell's law (Appendix 5) on successive equipotentials, adding the difference between successive equipotentials to the angle the beam makes with the mesh normal, until this angle is greater than $\pi/2$. For small mesh angles ϑ the shift is approximately given by

$$\Delta V' = \frac{V \sin^2 \vartheta}{2\cdot 5} \qquad (5.7)$$

This function corresponds quite well with the observed shift. In practice, the mesh may not be perpendicular to the side walls of the analyser chamber, and this will

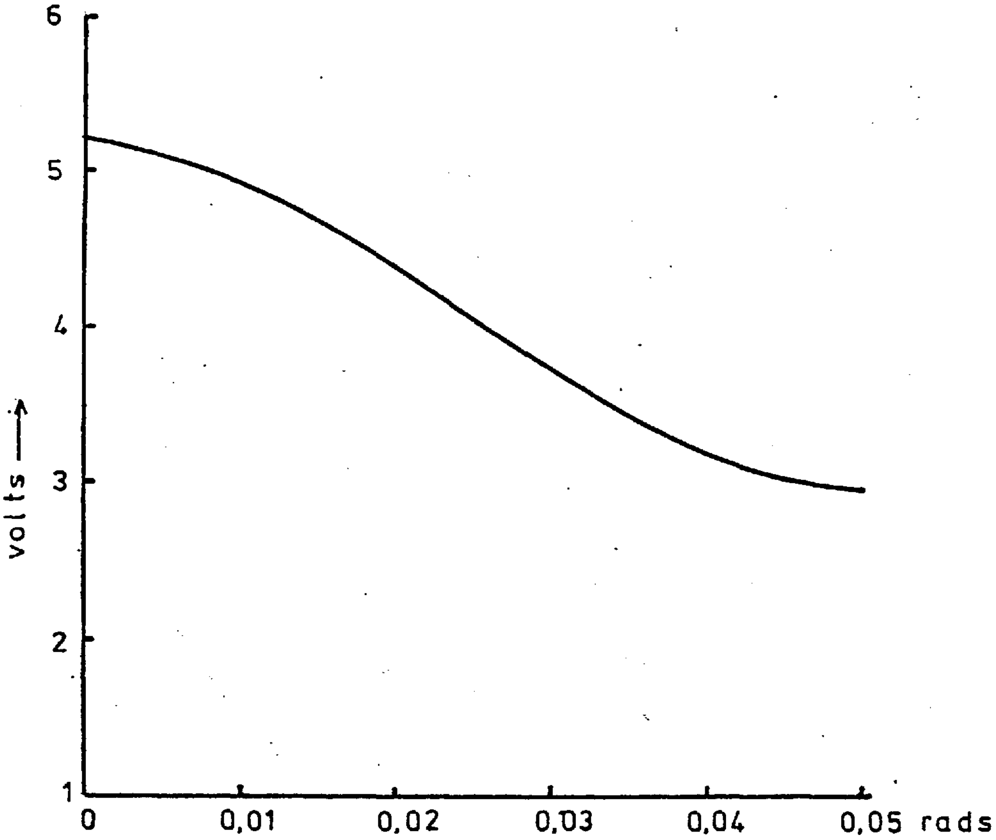

Fig.5.9 Variation of transfer function width at half height, measured above the axis, with the angle between the normal to the mesh and the beam.

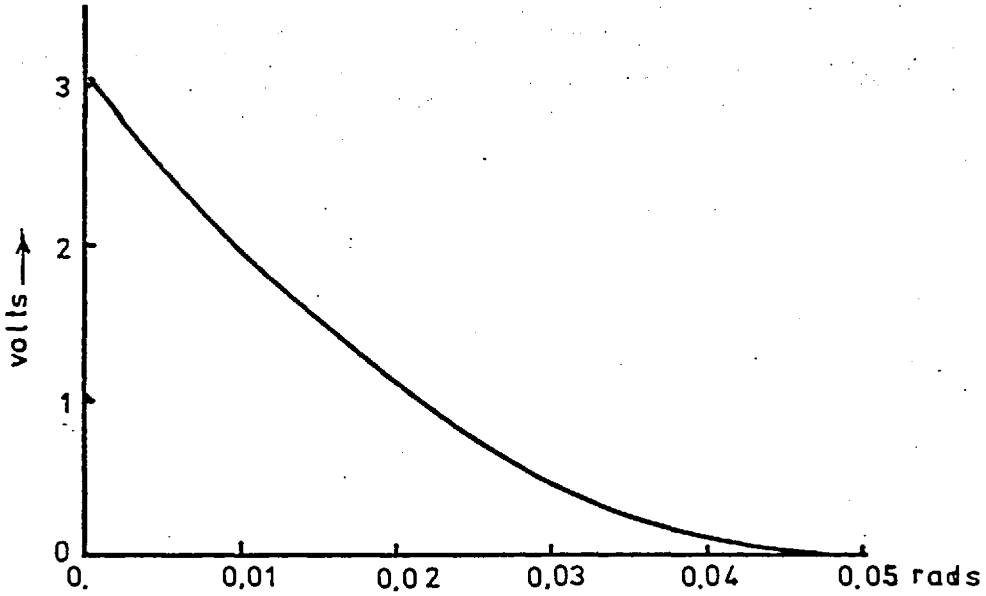

Fig.5.10 Variation of 'below axis dip' of the transfer function with the angle between the normal to the mesh and the beam.

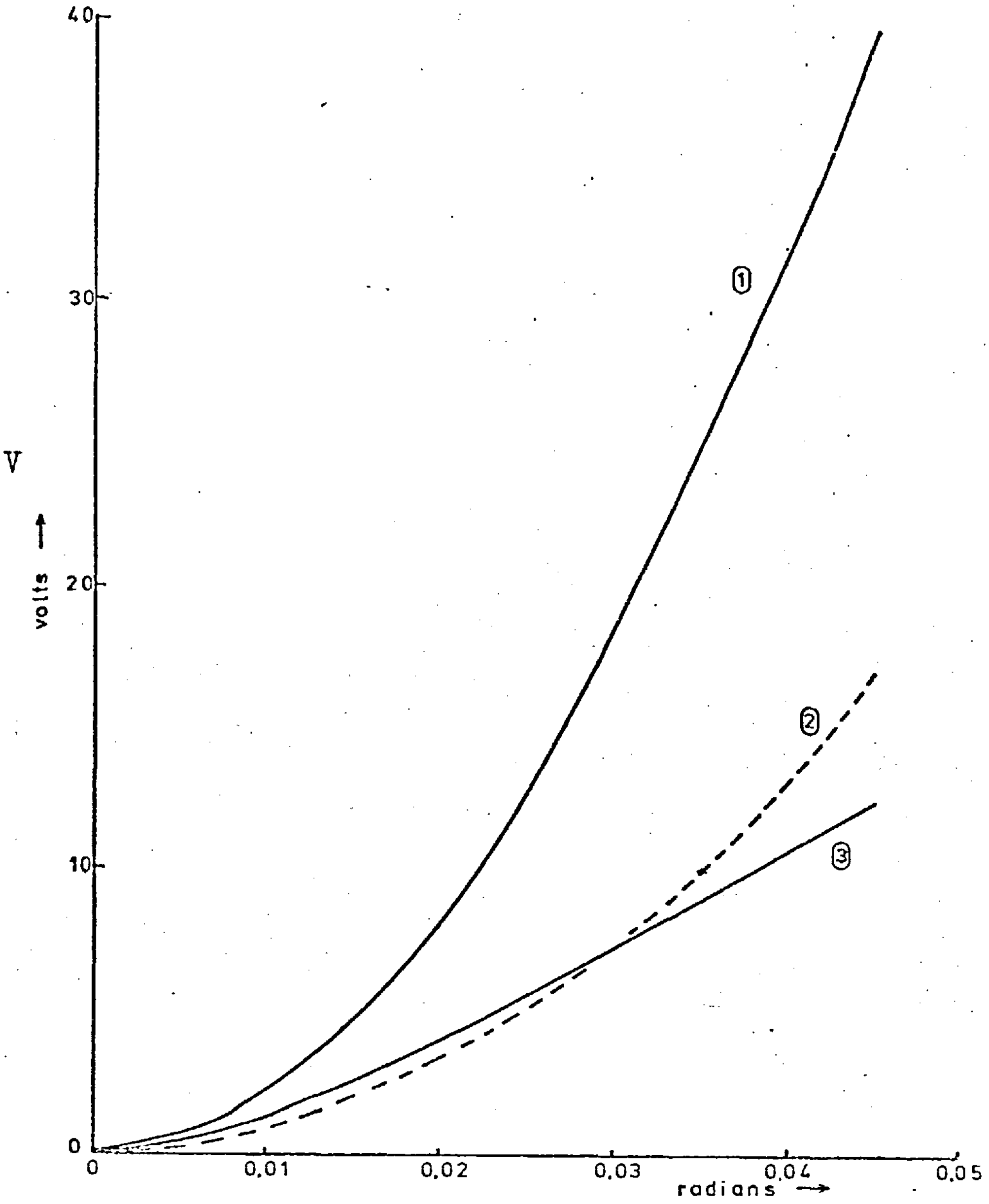

Fig.5.11 Variation of cut off potential, V, with angle between the mesh normal and the beam. V is measured below beam accelerating potential for a beam energy of 20keV.

1) Mesh parallel to entrance aperture, Fig.4.12a, calc.
2) Mesh at an angle to the beam, entrance aperture perpendicular to beam. Fig.4.12b, calculated.
3) As 2) , measured.

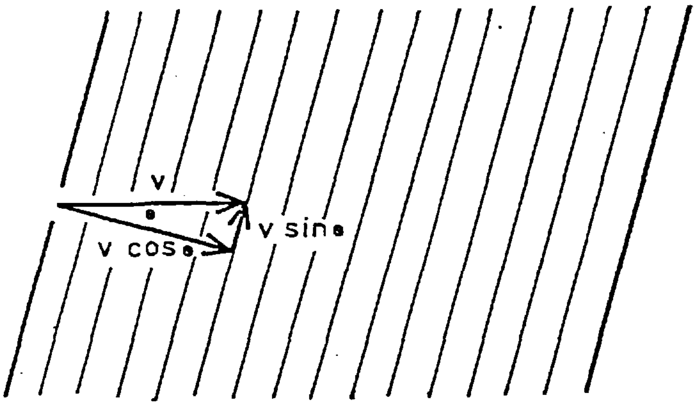

Fig.5.12a Potentials between entrance aperture and mesh, both set at the same angle to the beam.

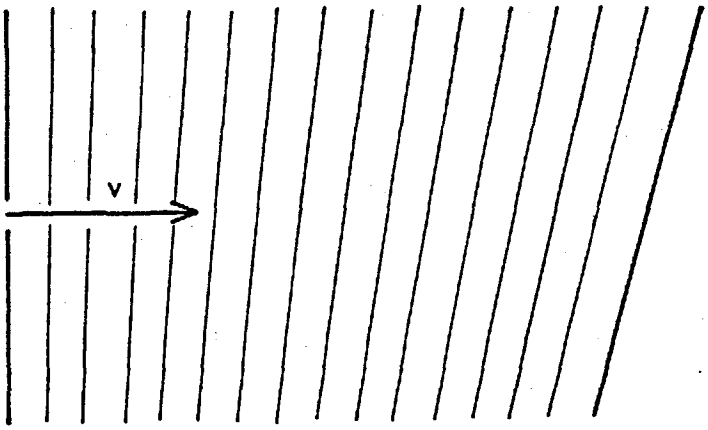

Fig.5.12b Potentials between entrance aperture and mesh, mesh set at an angle to the beam.

result in a further shift in the peak position.

In practice this shift has probably occurred on several occasions. Most analysers have a retarding element bolted into the chamber. These can usually be fitted only to an accuracy of 0.02 rad, hence a wedge shaped equipotential system will be formed. It will not, in general, be noticed as this will only produce a shift of 2-3 eV.

5.9 Theoretical resolution

The trajectories of electrons passing through the mesh were calculated for different angles of the mesh relative to the beam (Appendix 5). From this calculation the effective aperture of the mesh for electrons, as the mesh potential is varied, was found. The larger the effective aperture, the greater is the transmission of the mesh and hence the larger the number of electrons which reach the scintillator. The measured signal current is thus increased.

The results of these calculations are shown in Figs. 5.13 and 5.14. Figure 5.13 shows the transmission of the mesh as a function of mesh potential for electrons incident normally on the mesh. Figure 5.14 shows the transmission when the cut off predicted by Eqn. 5.7 would be 17 Volts. These results correspond well with the experimentally observed effects. Although the calculations explain the reasons for the enhanced transmission, they cannot be relied on in detail, because they are based on a two dimensional, rather than three dimensional, field plot. The trajectories are also plotted by hand, and rely to some extent on experience for accuracy. Nevertheless this treatment is adequate to show the principles involved.

5.10 Effects of electron velocity near the mesh

The electron velocity, as it is about to pass through the mesh, is the governing factor in determining whether or not the effective aperture is the same as the geometric aperture. Electrons with relatively high energy at the mesh will see an effective aperture exactly the same as the geometric aperture because they will not be deflected

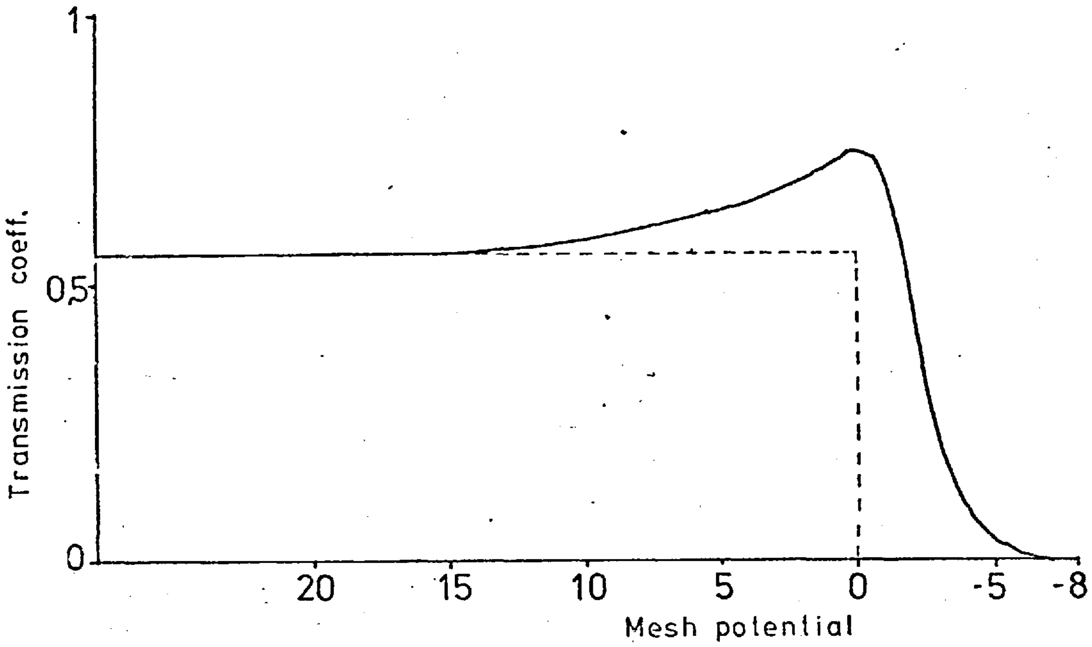

Fig.5.13 Theoretical transfer function, mesh normal to the beam.

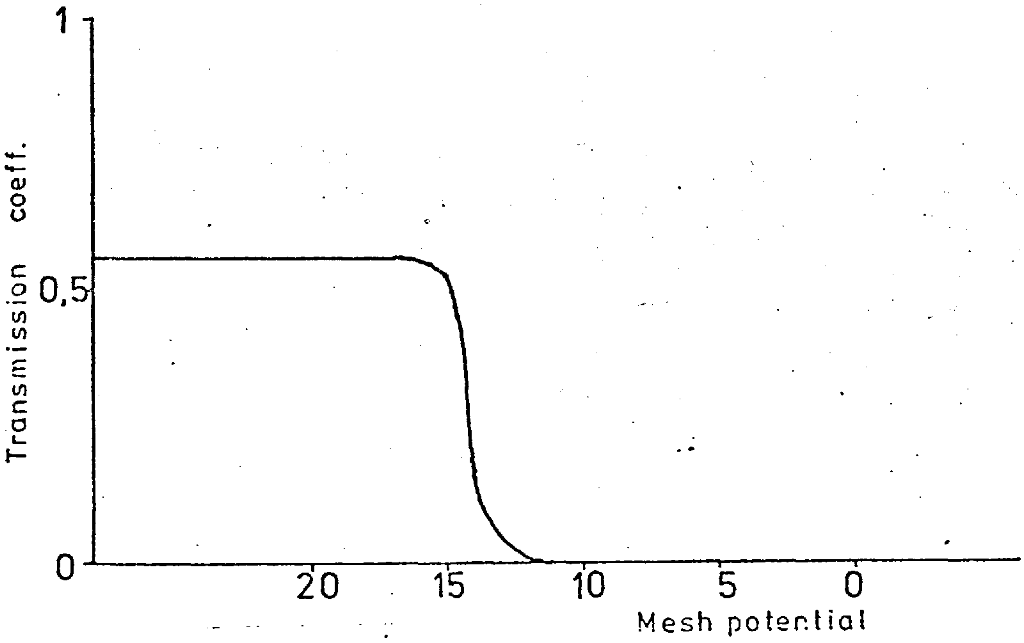

Fig.5.14 Theoretical transfer function, mesh inclined at 0.045 rad to the beam

strongly by the potential. Similarly, if an electron has a relatively low energy near the mesh, it will be strongly deflected by the potentials around the mesh. Consider an electron that is incident normal to the mesh with such an energy that it can just pass through the mesh (Fig. 5.15a). Even if its initial path is such that it would strike the mesh, the electron may be deflected through the mesh if its path takes it near to the edge of a mesh bar and its energy is low enough. The result of this is that an enhanced transmission will be observed. As the potential of the mesh is lowered the electron will be deflected less and will strike the bar. Therefore as the potential is lowered the transmission coefficient will tend to the geometric value obtained by direct linear measurement (Fig. 5.15b).

Electrons that are incident at an angle to the mesh have a large velocity component tangential to the mesh, even if they only just pass through. They are thus relatively unaffected by the local fields around the mesh and are only subject to the average potential of the mesh plane. Therefore the effective aperture for such trajectories is the same as the geometric aperture at all values of the mesh potential and no enhanced transmission results.

The effect of enhanced transmission has been noted by several workers : particularly in LEED/AUGER hemispherical analysers, e.g Huchital and Rigden (1972) The effect of tilt has, however, not been investigated as the LEED screen should everywhere be normal to the incoming beam. Ward (1976) and Sheppard (1973) noted similar effects, but as they were only interested in filtering the beam in a scanning high energy electron diffraction system it did not concern them and they were apparently content when they found an analyser position that gave a good cut off.

5.11 Noise and breakdown

The main source of noise in the signal was caused by the field emission from the retarding electrode. This has been the major weakness of many retarding analyser

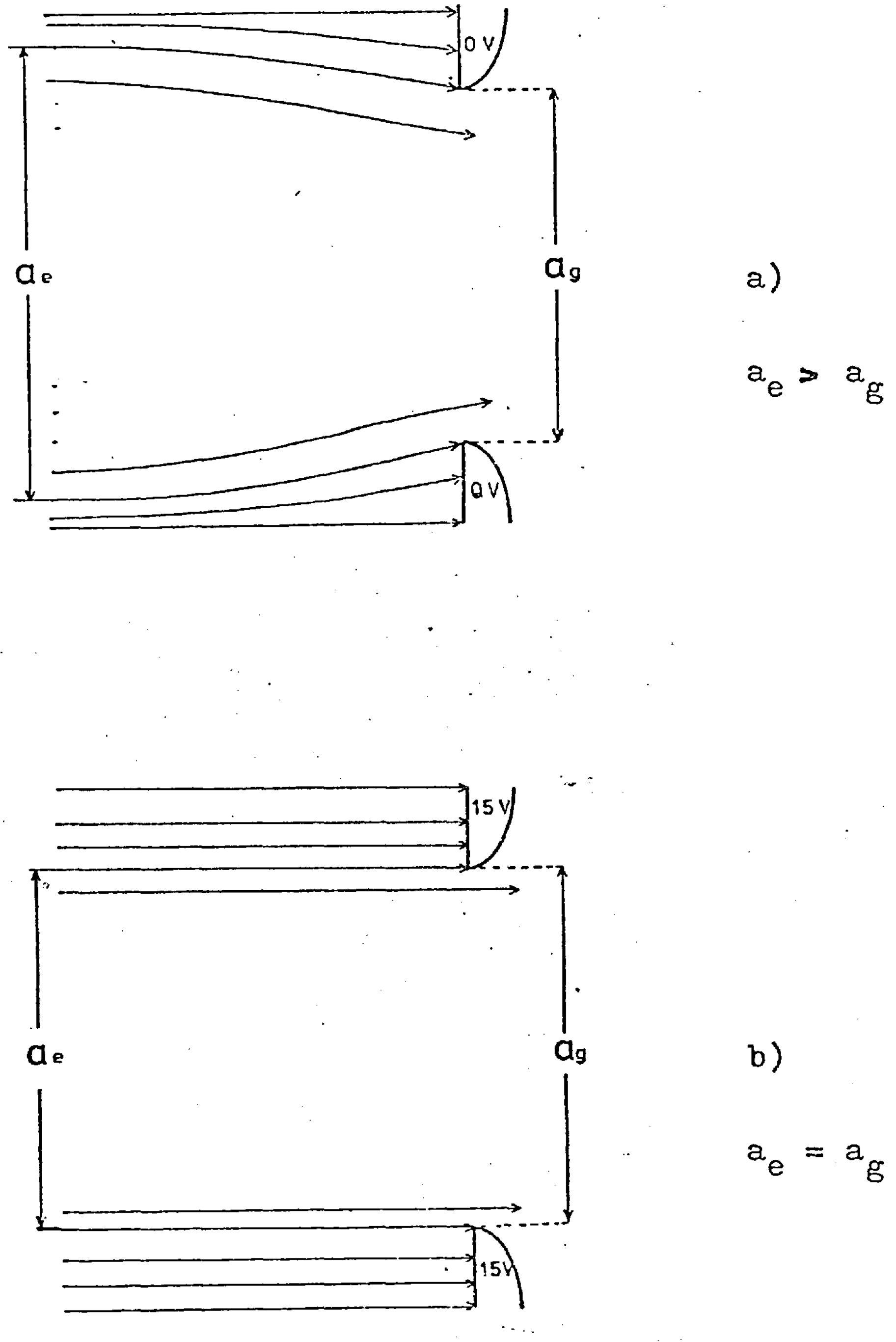

Fig.5.15 Electron trajectories near the mesh.

a) Mesh potential equal to the beam accelerating potential. Beam energy 20keV.

b) Mesh potential 15V below the beam accelerating potential. Beam energy 20keV.

a_e = effective aperture

a_g = geometric aperture

systems. Ward was limited to 20 kV, and Tompsett (1966) to 17 kV by breakdown in the analyser. Denbigh comments that conventional insulating lengths are inadequate, but in common with the other authors he does not state why.

All analysers of the type used have been of similar size with typical field strengths of 10^5 V m^{-1} in the chamber. Field emission would normally be expected to set in when the macroscopic field strength is 10^7 V m^{-1} (Bolin et al, 1970) and thus a safe margin would appear to have been left. Under these conditions, safe operation up to at least 40 kV might be expected.

In practice, the field at the mesh is much stronger than predicted from the equation

$$E = V/d$$

where V = electrode potential

d = minimum distance between electrode and wall

The mesh itself increases the field by a factor of between 4 and 6 because of its curvature. The macroscopic field is thus $\sim 5 \times 10^5$ V m^{-1}.

Microscopic examination of the mesh surface showed it to be rough on a sufficient scale to lead to a further increase of the field by a factor of 2 - 3. The minimum field expected in the region of the mesh, without considering submicroscopic asperities, is 10^6 V m^{-1} The nature of the etched copper is such that it may be expected to have a rough surface with a loose oxide coat, thus field emission can be expected. In the present system, using an untreated mesh, field emission occurred at a mesh potential of 16 kV, leading to a continuous breakdown at 24 kV. The current recorded at the scintillator as a function of mesh potential is shown in Fig. 5.16.1.

Removal of the mesh from its mount almost completely eliminated the field emission (Fig. 5.16.2).

The mesh was treated to reduce field emission by coating it with molybdenum.

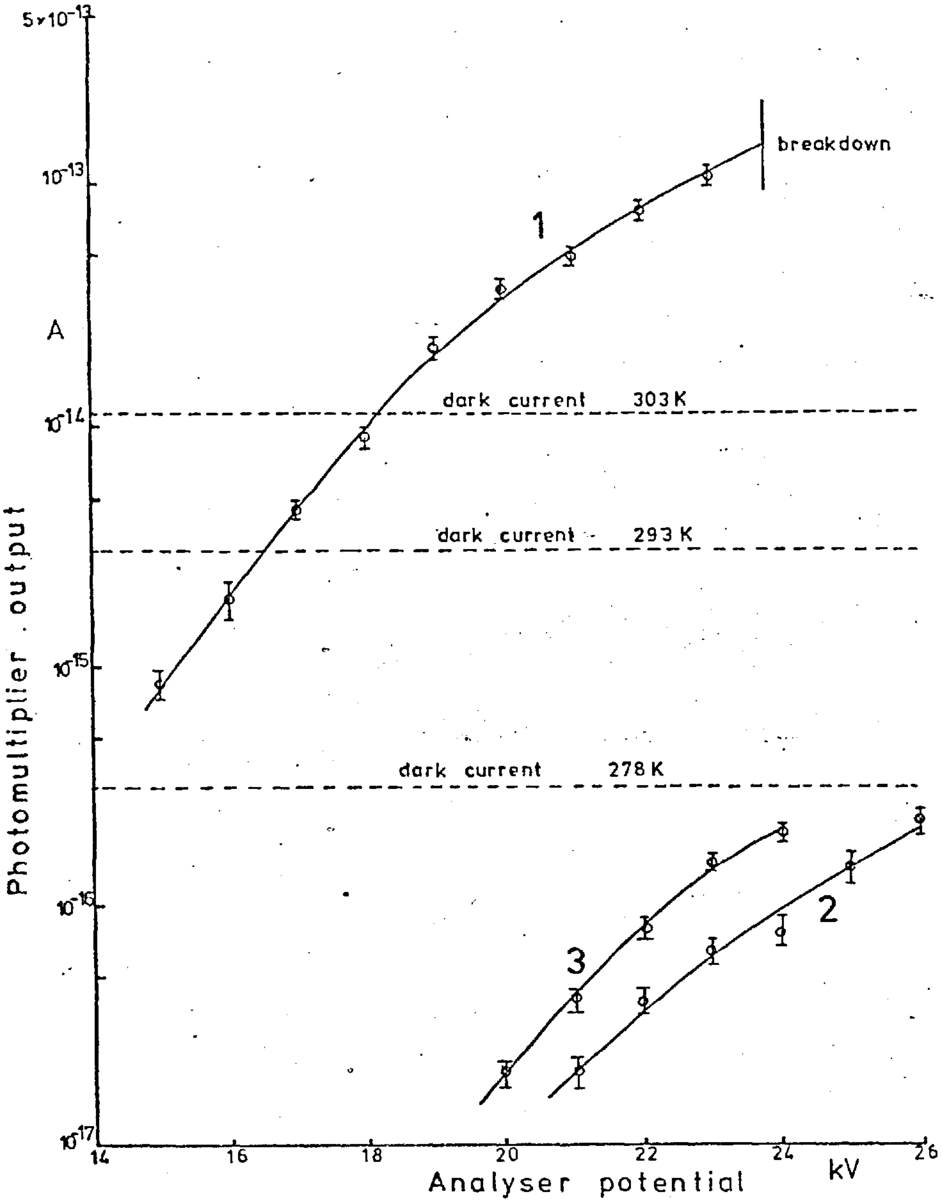

Fig.5.16 Noise current within the analyser as a function of the mesh potential above ground.

1) Untreated copper mesh.
2) No mesh in mounting ring.
3) Coated mesh, see text.

This has a marginally higher work function than copper oxide and also forms a more stable layer that can stand higher field stresses.

The method adopted for coating the mesh was vacuum deposition. A 0.5mm diameter molybdenum wire was wound closely on 1 mm diameter tungsten rod and the ends of both the wire and rod clamped to the evaporator terminals. When current was applied, both the molybdenum and tungsten were electrically heated to sufficient temperature to melt the molybdenum which then wetted the tungsten and continued to evaporate. When molybdenum was wound on tungsten in the normal manner for vacuum deposition it did not reach a sufficient temperature to evaporate. The tungsten and molybdenum were outgassed for 1 - 2 hours at about 1500 K before deposition with a screen between the mesh and the filament. There was still a tendency for the tungsten to spit when heated above 2000 K so the mesh was mounted 10 cm above the filament. The mesh was coated on both sides in two separate depositions, about 50 nm of molybdenum being deposited on each side. During deposition the mesh was heated to dull red, and it is probable that some annealing of the mesh also took place. Annealing of an uncoated mesh was not, however, sufficient to prevent field emission.

The mesh was replaced in the analyser and it was found that the field emission had been reduced by a factor of 2000 (Fig. 5.16.3). The recorded emission was now 2×10^{-17}A at 20 kV; this was later confirmed when the phosphor and rate meter were used when background count rates at 20 kV were rarely above 50 cps (the response of the phosphor was 42% at 20 kV).

Other factors affecting emission were the condition of the phosphor and the length of time the system had been in use. A new phosphor placed in the system always resulted in increased field emission, probably because local outgassing caused movement of any loose powder which would be attracted to the mesh. A well used phosphor was always preferable, though the last one used in the system broke up, the backing having been loosened by repeated vacuum cycling. The field emission could be reduced by cycling at high voltage, and this was always done after the system had been re-evacuated from atmospheric pressure. On one occasion it was tried rather too early, and the resulting glow discharge melted the mesh, although the phosphor was apparently unaffected.

5.12 Spurious signal due to secondary electron production

One objection raised to retarding mesh filters (Bunting, 1971a) is that secondary electrons produced by collision of electrons with the mesh would add to the signal recorded at the phosphor.

Secondary electrons are produced when a high energy electron strikes a material surface. The average number of secondary electrons produced by a single incident electron varies typically between 0 and 5, though can be as high as 25. This coefficient depends on the material and on the angle of incidence and energy of the primary electron. The energy of the primary beam must be at least a few tens of eV, and the maximum probability occurs with an incident energy of between 100 eV and 1000 eV, depending on the material (Wells et al, 1974).

As the analyser potential is lowered a signal would be expected to appear 100 - 1000 eV below any strong feature in the spectrum. In practice, no such signal was found. The reason for this is that the faces of the mesh are almost flat (Fig. 5.17). The electrons will generally strike the mesh normally and the secondary electrons will be produced with an energy of between 5 - 50 eV. Their velocity will be directed away from the mesh, and thus most of the electrons will be accelerated back towards the entrance aperture. Only the electrons which strike the mesh very near a hole would be expected to produce secondaries with a component velocity through the mesh. The probability of secondary electron production is believed to be greatest in the specularly reflected direction, thus secondary electrons would be expected to pass

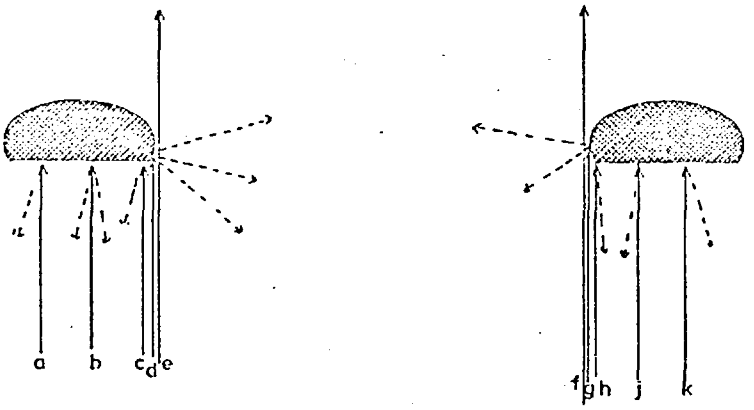

Fig.5.17 Secondary electron production around a D shaped mesh.

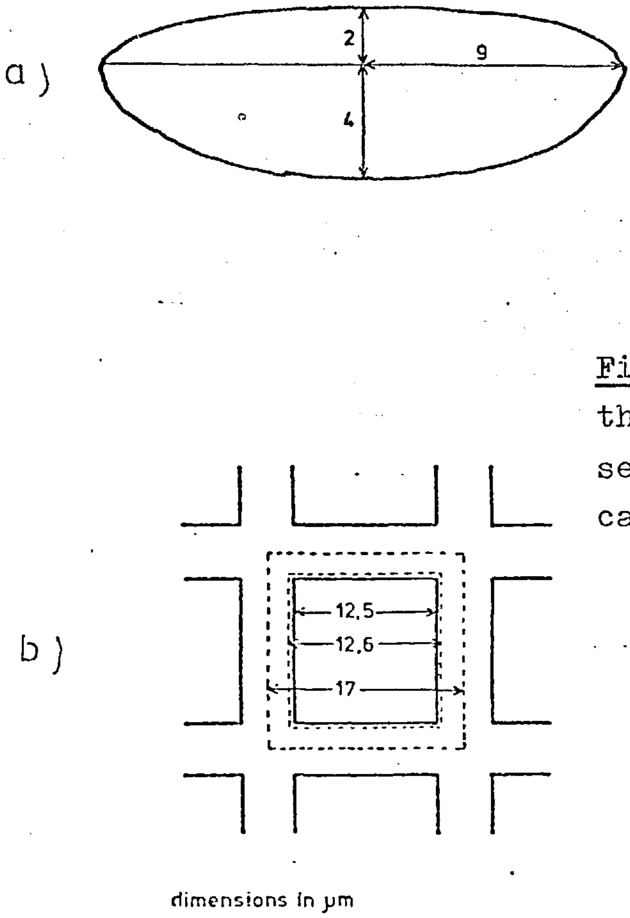

Fig.5.18 Mesh bar shape showing the limited region in which secondaries affecting the signal can be produced.

through the mesh if they are produced at a surface which makes an angle of greater than 45° to the mesh plane. The mesh section varies from the D section already discussed to the shape shown in Fig. 5.18, which has two elliptical faces, one with ratio of semi axes 2 : 9, the other 4 : 9. The electrons strike the mesh on its flatter side. The region of the mesh bar which makes an angle of greater than 45° with the mesh bar is shown. This is the region of the mesh from which forward scattered secondary electrons will be emitted and assumes that the bars have an elliptical section with semi-axes in the ratio of 2 : 9. The area from which secondaries are emitted is 2% of the area of the mesh hole, thus assuming a secondary production coefficient of 2 (Wells et al, 1974) secondaries might be expected to produce a signal of 4% of the current transmitted through the mesh. If this current is produced, It would appear when the mesh potential is between 100 and 600 eV below the point where the main signal is recorded. This energy difference means that when the analyser is used over a narrow range (e.g. 0 - 70 eV below main beam potential) there will be very few secondaries present. When the analyser is used over a wide range there will be an almost uniform background produced by the secondaries, but in the case of the present analyser the occurrence of absence of such a background could not be detected as its level fell below the operating stability of the gun/analyser combination.

5.13 Resolution tests

The resolution of the analyser was tested by transmission of the electron beam through a 100Å aluminium film. The film was prepared in the usual manner by vacuum deposition onto glass, floating off and retrieval on microscope grids. A grid with a single hole aperture was used. The very thin films were found to break up when picked up on the grid from pure water, because of the action of the surface tension, but could easily be picked up if the water was diluted with alcohol to reduce the surface tension. This technique also allowed the grids to be almost completely dried with blotting paper and resulted in cleaner specimens.

The grids were mounted in a clamp normal to the beam, and the central spot of the resulting diffraction pattern was analysed. The results, at differing beam energies, are shown in Figs. 5.19 to 5.22.

In all cases the main features produced by multiple bulk and single surface plasmons were resolved. This was to be expected from the measured resolution. The relative areas of these bulk plasmon peaks is governed by the mean free path, by the angle of acceptance of the collector and the divergence of the beam.

The relative areas of the peaks are given in Table 5.1. The mean free path, λ, is derived from the ratio of these areas, as discussed by Marton et al (1962) and Klemperer and Shepherd (1963). The angular divergence of the incident beam was similar to the acceptance of the analyser collector and to the divergence in the beam produced by a single plasmon scattering event. Because of this the mean free paths obtained from the ratio of the elastic peak area to that of the first plasmon peak is artificially large. The ratio of the first and second plasmon loss, however, should give a value of the mean free path, which is more reasonable. This is because the angular spread of the beam having undergone one plasmon loss, is not greatly different from the spread of the beam that has suffered two losses. A sample taken near the centre of the beam, as it will be, will receive a correct weighting between the first and second plasmons.

The results for aluminium were compared with the simple theory due to Quinn (1962) and with recent experimental work due to Ishigure et al (1978). It can be seen (Figs. 5.23 and 5.24) that the mean free path derived from the ratio of first to second plasmon peak heights compares well with previous values. The spectrometer did not, therefore, introduce any gross errors in the analysis, although it was not designed for detailed paraxial work of this type.

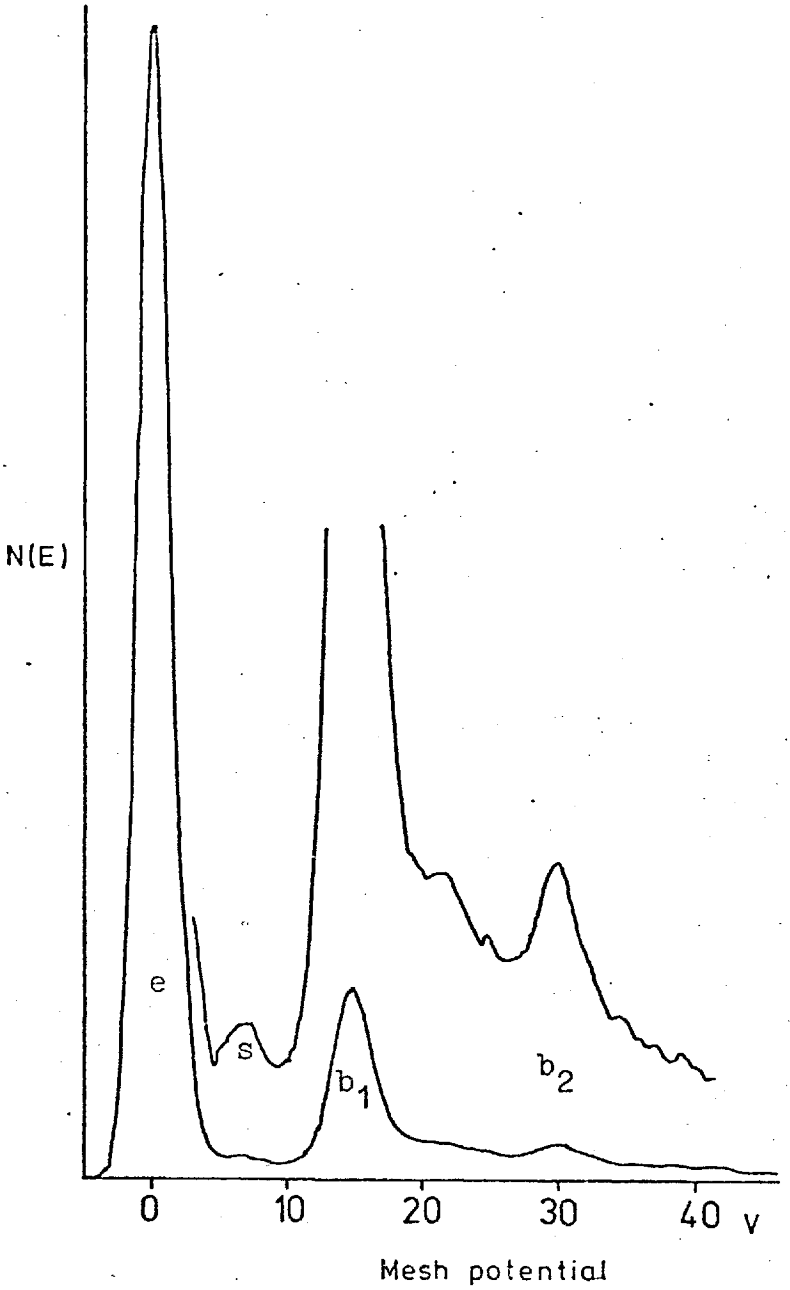

Fig.5.19 Energy spectrum of electrons transmitted through a 10nm thick Aluminium film. Beam energy 20keV.

e) Elastic, no energy loss, peak.

s) Surface plasmon loss peak.

b_1, b_2) Bulk plasmon loss peaks.

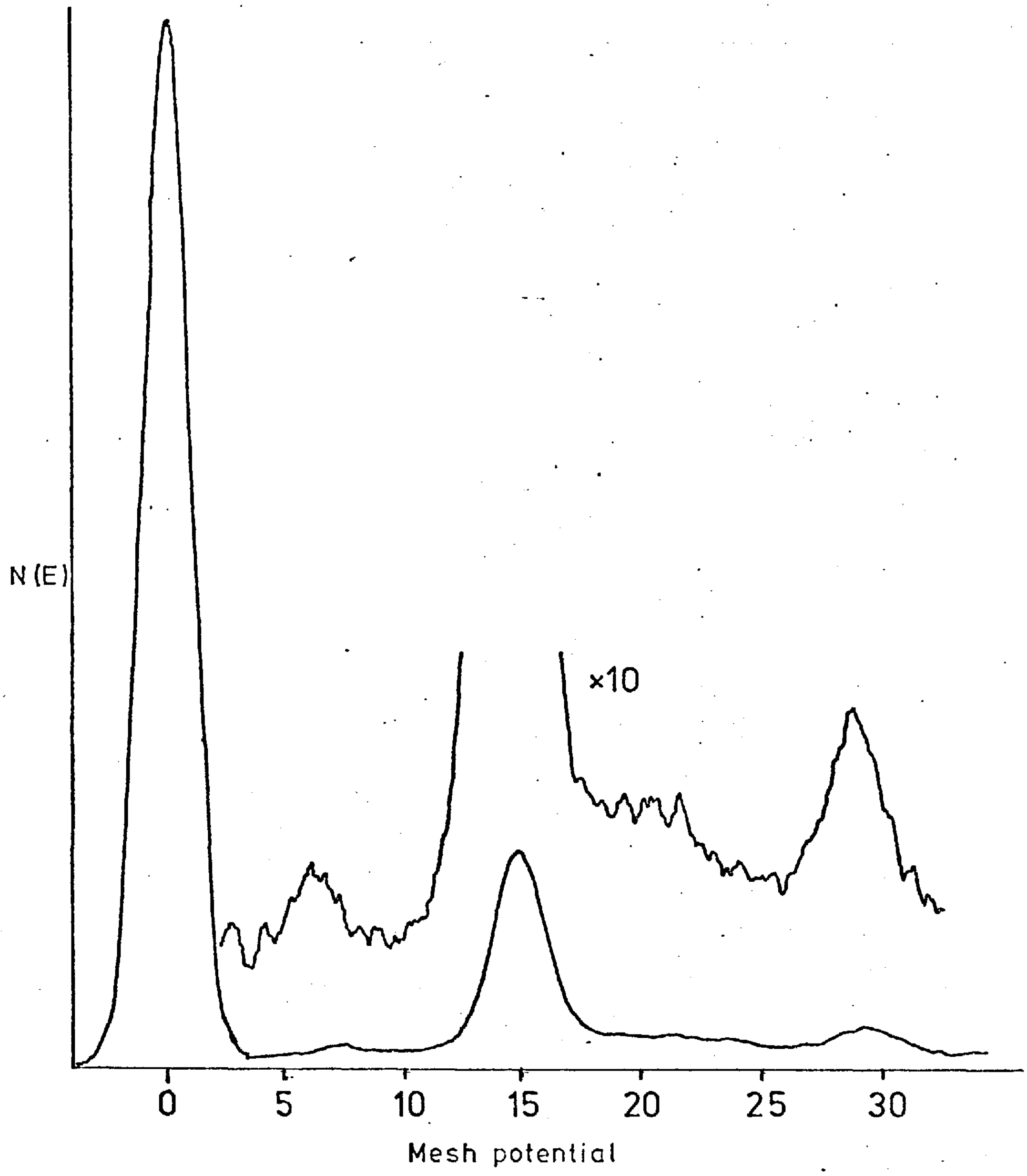

Fig.5.20 As Fig.5.19 , incident beam energy 16keV

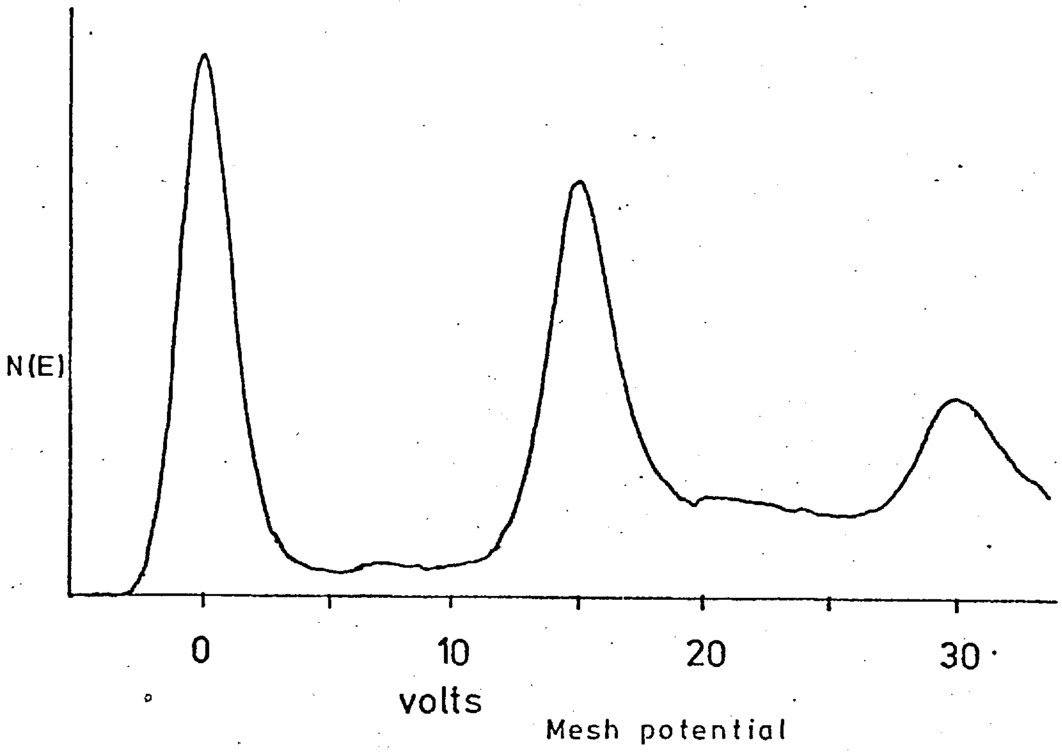

Fig.5.21 As Fig.5.19, incident beam energy 10keV.

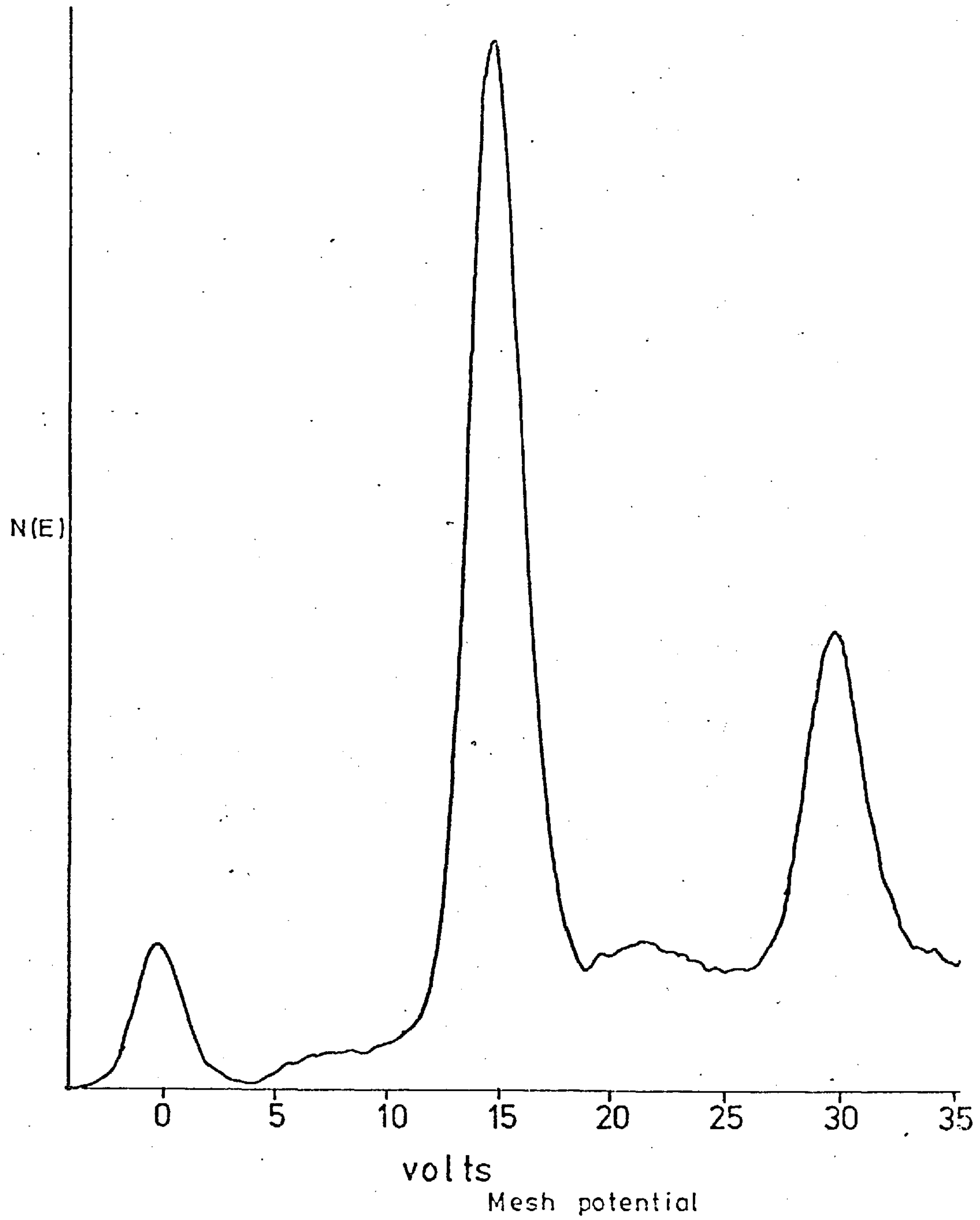

Fig.5.22 As Fig.5.19, incident beam energy 7keV.

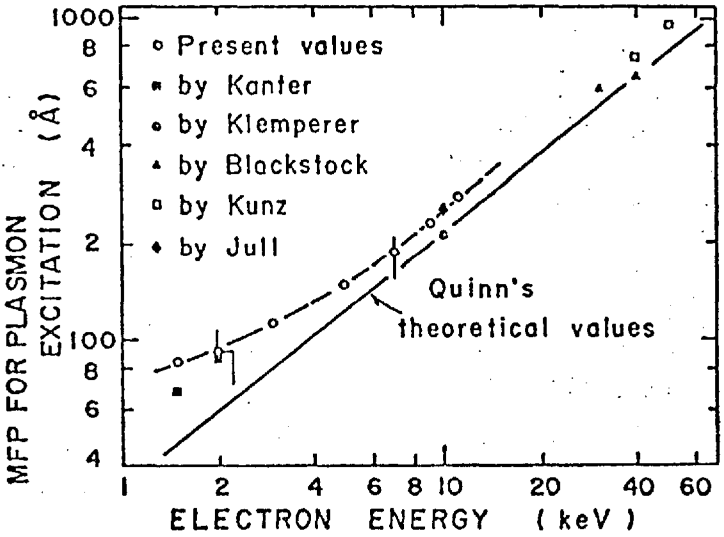

Fig. 8. The mfp for plasmon excitation obtained in this experiment.

Fig.5.23 Electron mean free path for plasmon excitation from Ishigure et al (1978).

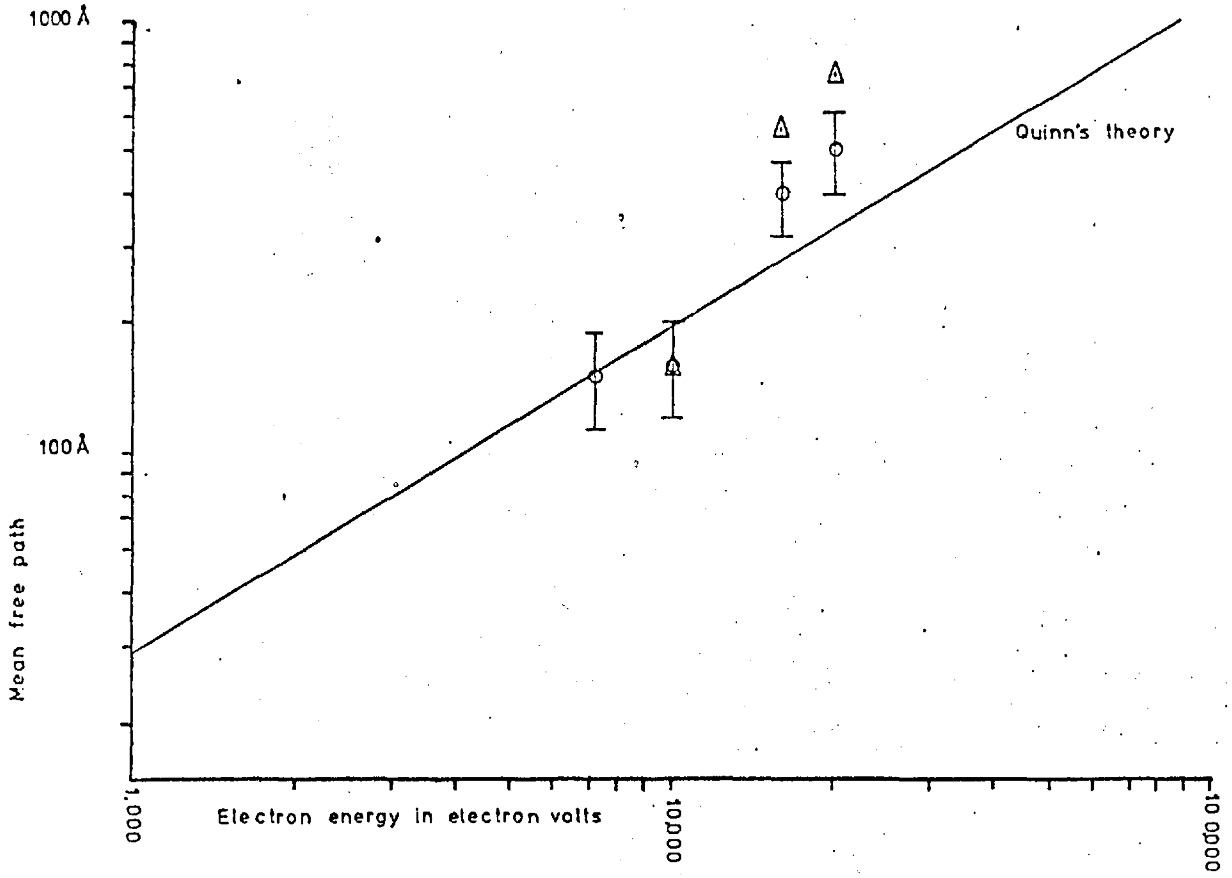

Fig. 5.24 Mean free path for bulk plasmons calculated from these experiments.
△ No loss and one loss, o One loss and two losses.

These values correspond well to previous experiment, Fig.5.23, and to Quinn's theory.

Table 5.1

Beam energy keV	Peak heights (relative)		
	No loss	One plasmon	Two plasmons
20	7,5	1,0	0,10
16	5,7	1,0	0,12
10	1,58	1,0	0,33
7	0,16	1,0	0,34

Table 5.2

Beam energy keV	Mean free path	
	Derived from no loss and one plasmon	Derived from one and two plasmons
20	75,0nm	50,0nm
16	57,0nm	42,0nm
10	15,8nm	15,0nm
7	1,6nm	14,7nm

It has been pointed out that the thickness of the specimens used might not have been sufficiently great, in that some of the electrons that traversed the films might have been scattered out had the films been thicker. Whilst there is no doubt that the thickness of all the films used would allow some electrons to pass through, this does mean that any of those electrons would have a finite probability of returning through the film.

Bishop (1965) shows that the backscattered fraction of the electron beam becomes independent of the film thickness before complete penetration of the film is prevented. For the materials that he tested (Cu, Ag, Au) he found that the mass thickness required was 120 μgm cm^{-2} at an incident energy of 10 keV. Extrapolating from these results a mass thickness of about 360 μgm cm^{-2} would be required at 20 keV. This corresponds to a thickness of 400 nm in Cu and 1.3 μm in Al.

There is, thus, no doubt that the specimens of C, Cu, Ag, Au and Pb were of sufficient thickness. The specimen of Al was only 1.2 um thick and so some doubt must be expressed about this sample. It should, however, be noted that the mounting stub was also made of Al and thus no great error should be introduced in assuming the specimen to be pure.

CHAPTER 6

ELECTRON BACKSCATTERING SPECTRA

6.1 Scattering through 150°

This chapter shows the energy spectra, both at low and high resolution, obtained when 20 keV electrons were scattered through 150° by metal specimens placed normal to the incident beam.

6.2 Mounting and preparation of specimens

The specimens were mounted on a small turntable on the manipulator (Fig. 6.1). The specimens were aluminium scanning microscope stubs with the top face polished to optical smoothness on a lapping wheel and coated by vacuum deposition with specimen material. The metals used were :-

Aluminium

Copper

Silver

Gold

Lead

The film thickness was measured by placing a second, partly masked stub next to the specimen stub in the evaporator. The masking produced a step on the second stub between its surface and the evaporated layer, which was examined using a Twymann-Green interferometer to find its thickness. All specimens were found to be between 500 nm and 1 μm thick. This is a sufficient thickness to ensure that no electrons traverse the sample and are reflected from the stub.

A carbon specimen could not be prepared in this way, so a vitreous carbon crucible was mounted at the centre of the turntable to provide the carbon sample.

The specimens were replaced after 2-3 hours use though, with the exception

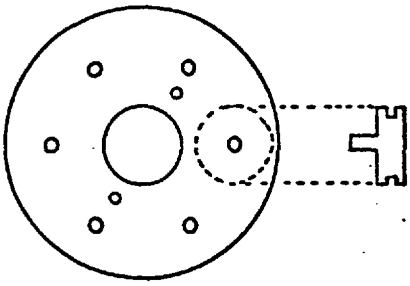

Fig.6.1 Specimen turntable and one of six specimen stubs.

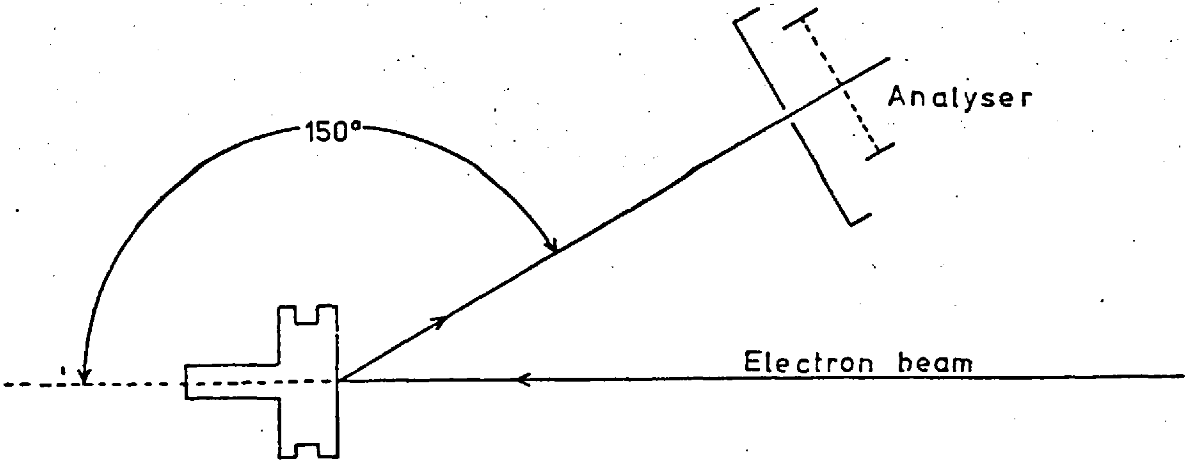

Fig.6.2 Geometry of high angle scattering.

of the high resolution spectra, no difference was found between the spectra or backscattering coefficient obtained from old and new specimens.

6.3 Backscattering

The analyser was transferred to the port closest to the gun, which meant that electrons entering the analyser had been scattered through 150° (Fig. 6.2). The specimens were mounted normal to the beam and moved back and forth to obtain the strongest signal at the analyser with the analyser mesh set at anode potential. The analyser output was recorded as an integral spectrum at low resolution and as a differential spectrum at high resolution.

The total current collected was found to be about one third of the predicted value (Appendix 7). This meant either that all the electrons expected to reach the mesh were not doing so, or that only about one third were producing scintillations of sufficient strength to be recorded. This latter proved to be the case, and meant that the phosphors had to be calibrated (Appendix 3). When the response of the phosphors was taken into account the collected current was found to agree well with that predicted.

The collection efficiency did not vary with atomic weight of the material once the phosphor response was taken into account (Fig. 6.3). This indicates that there was little or no cut off of the low energy electrons in the scattered beam within the analyser. Such cut off could have been produced if stray magnetic fields and local charging had occurred within the analyser.

6.4 Low resolution spectra

Low resolution energy spectra were obtained in integral form by direct plotting from the rate meter. These spectra were then differentiated by hand and corrected for the energy response of the phosphor. As a check on the process, it was repeated

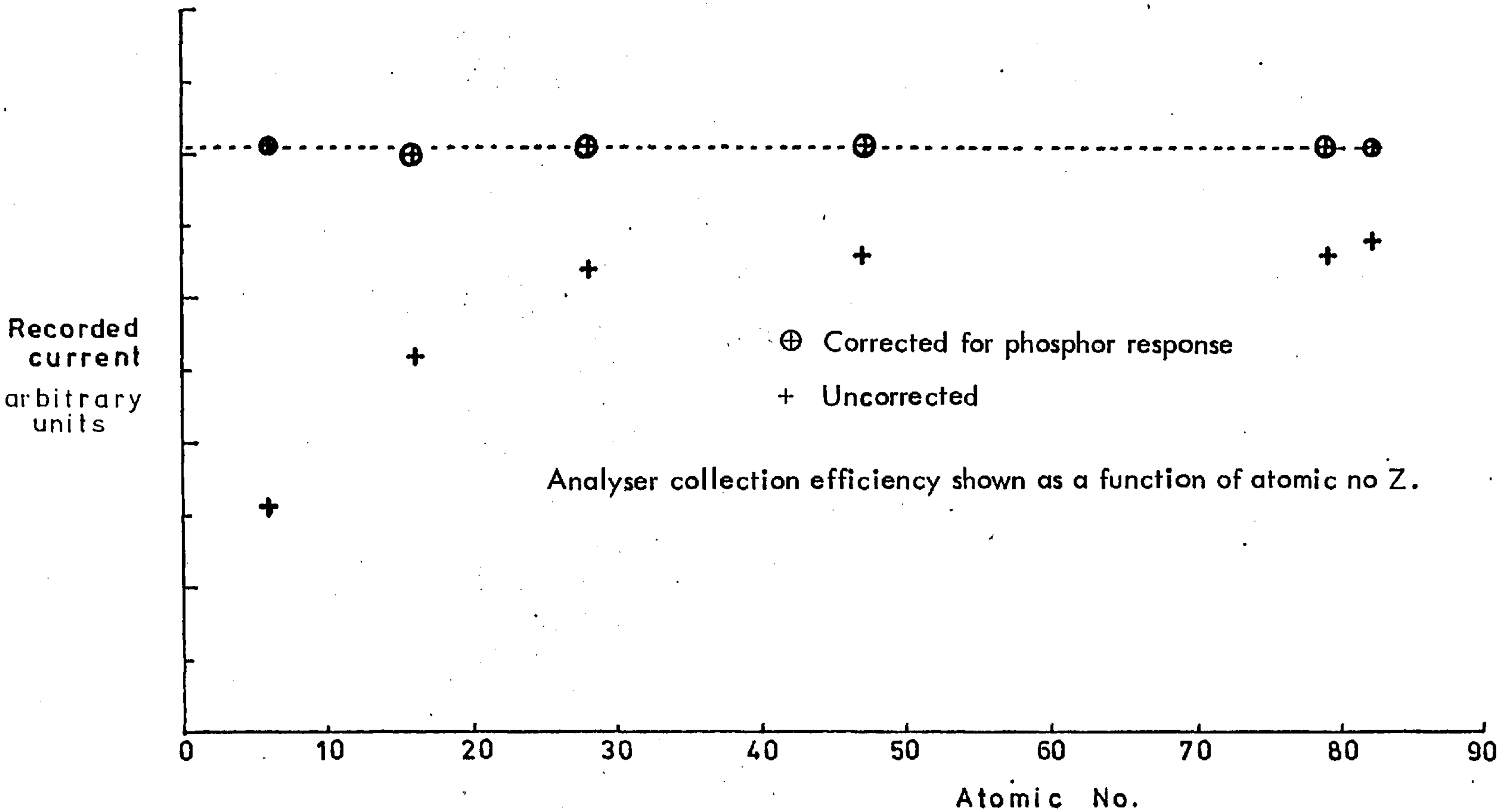

Analyser collection efficiency shown as a function of atomic no Z.

Fig. 6.3

several times on each of two different sets of data and was found to produce very similar differential curves. The integral area under these differential curves differed by at most 5% from the maximum value of the original integral curve.

The three stages are shown in Fig. 6.4 for a spectrum of silver.

The low resolution energy spectra obtained at 20 keV for all the materials under investigation are shown in Fig. 6.5.

6.5 Comparison with previous work

Much work has been done on low resolution backscattering, notably Kanter (1957), Kulenkampff and Spyra (1954), Matsukawa et al (1974), Darlington (1971, 1972, 1975). Of this work, Darlington (1974) seems to provide a good summary, though all the spectra shown are his own.

Comparison between the spectra reported by Darlington (1971) and the present work (Figs. 6.6 and 6.7) show that the spectra obtained in this work have a larger component near to the incident beam energy than do his, although any exact comparison is difficult because of the different experimental conditions.

Darlington's spectra were produced on using a sector analyser (Darlington, 1971). The output of the analyser was dependent on the energy at which it operated making noise a great problem at low energies. This was accentuated by the use of a Faraday cup to collect the electrons. As with the present results, Darlington had to redraw corrected curves from his data. He also had to extrapolate his curves to zero at zero energy as below $E/E_o = 0.4$ noise made his data unusable. This polynomial fit was subject to some error as he shows in Darlington (1971, diagram facing page 44). The range of this doubt covers to some considerable extent the data reported here and had he chosen the opposite extreme in his curve fitting they would have been in quite close agreement.

It is difficult to ascribe more accuracy to one set of data than the other, particularly as Darlington does not show any resolution tests for his analyser. Whilst

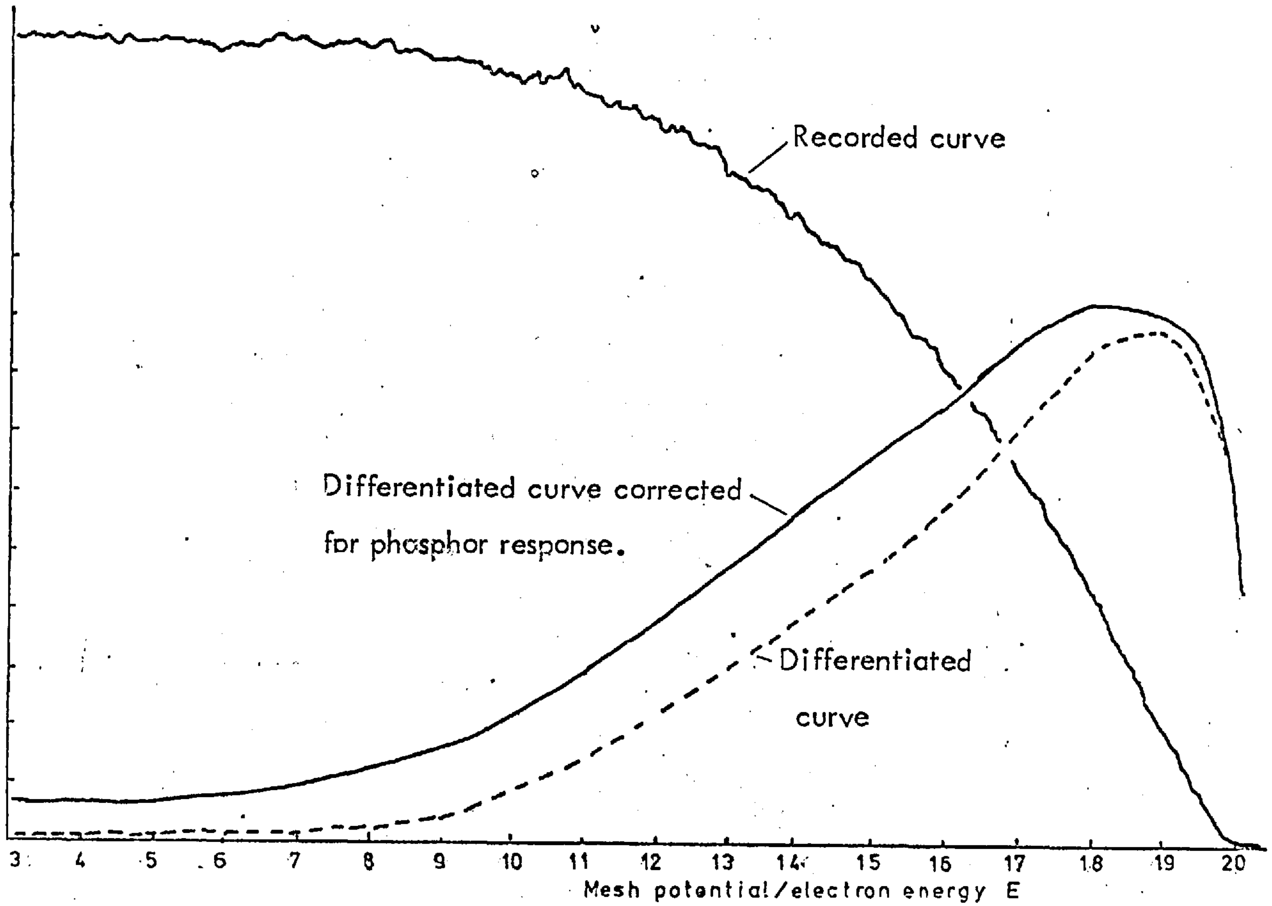
Recorded curve
Differentiated curve corrected for phosphor response.
Differentiated curve
3
4
5
6
7
8
9
10
11
12
13
14
15
16
17
18
19
20
Mesh potential/electron energy E

Fig. 6.4

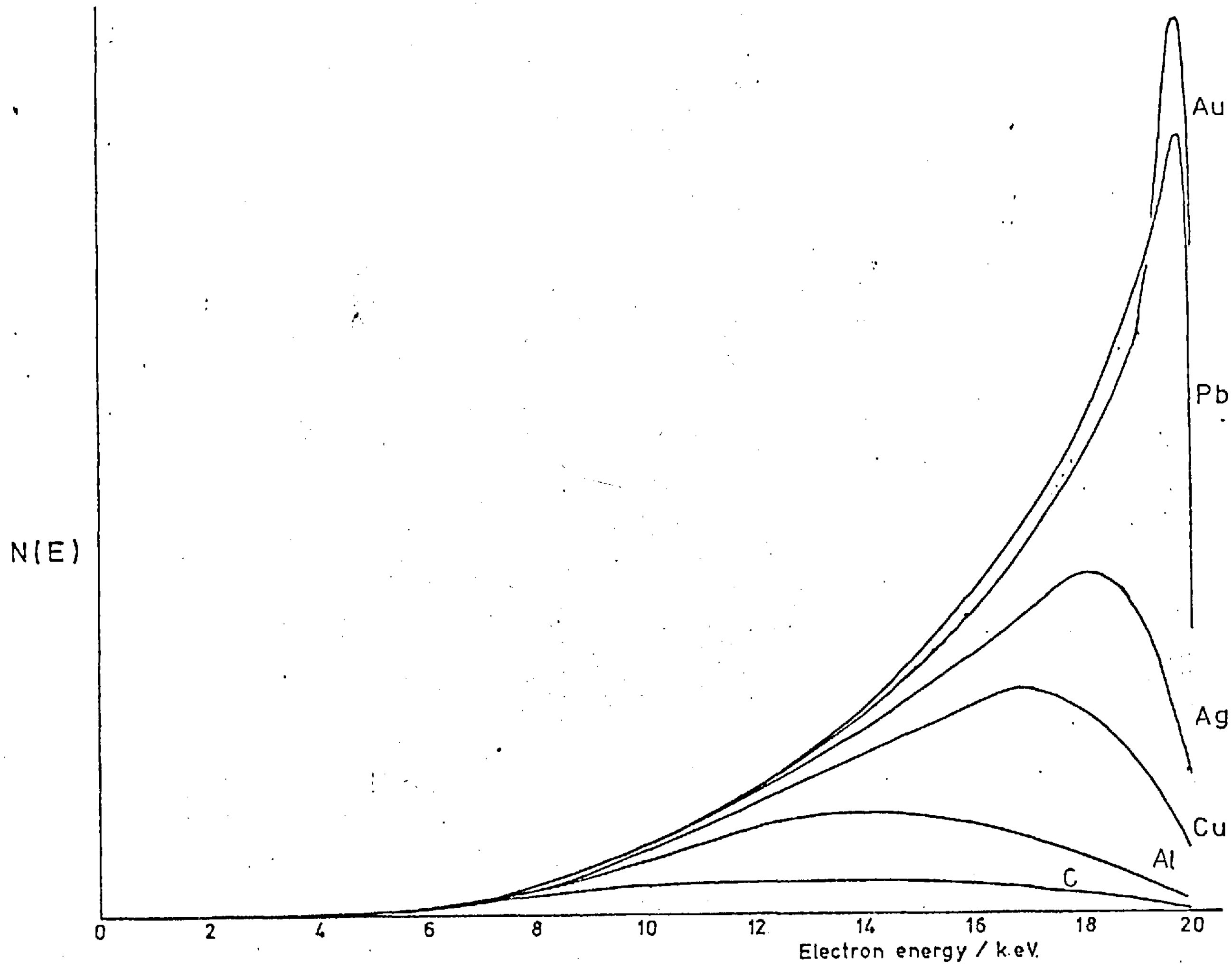

Fig. 6.5 Backscattered spectra for Pb, Au, Ag, Cu, Al and C.
Primary energy 20keV, angle of scatter 150°

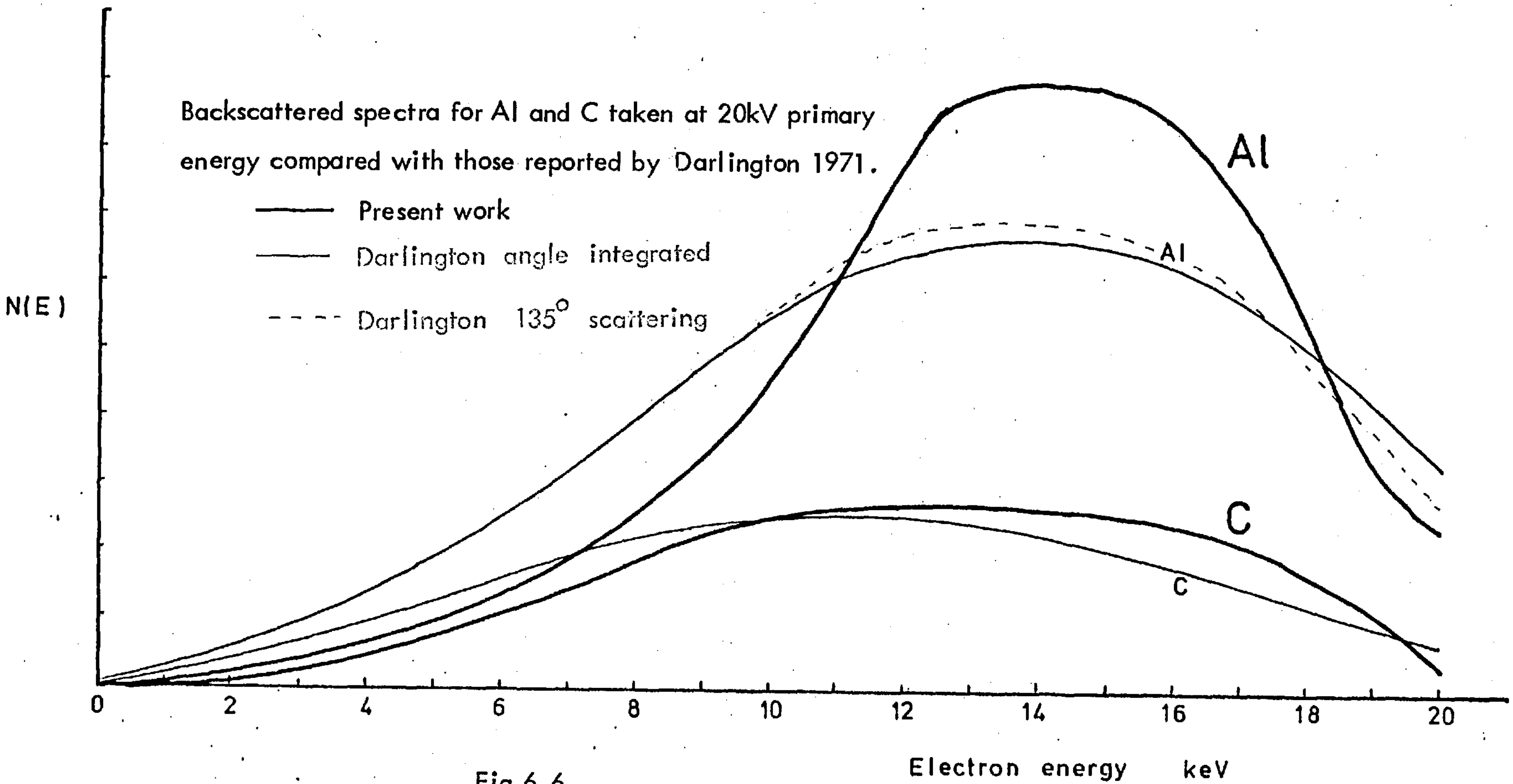

Backscattered spectra for Al and C taken at 20kV primary energy compared with those reported by Darlington 1971.

Fig 6.6

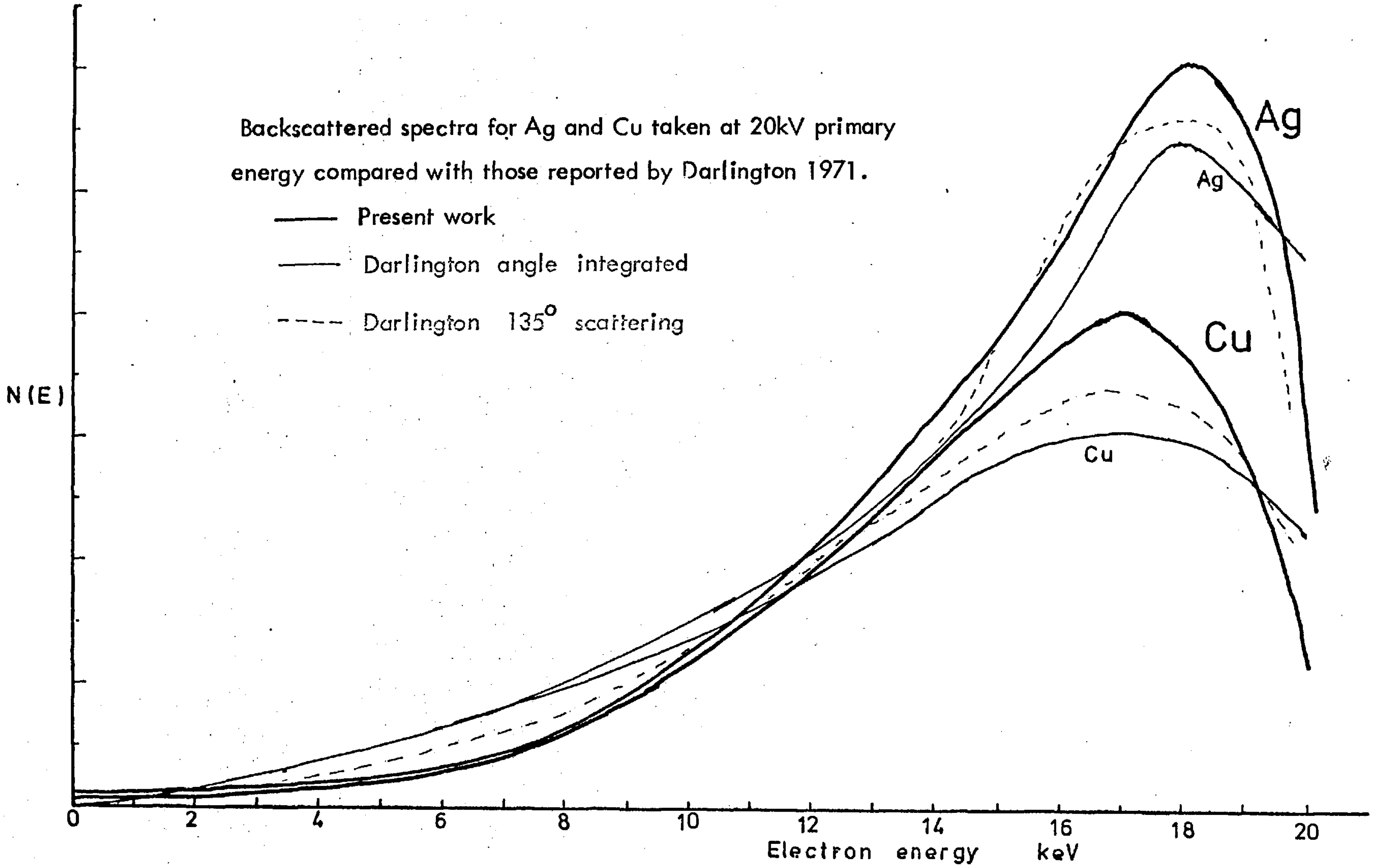
Backscattered spectra for Ag and Cu taken at 20kV primary energy compared with those reported by Darlington 1971.
Present work
Darlington angle integrated
Darlington 135° scattering
Ag
Ag
Cu
Cu
N(E)
0
2
4
6
8
10
12
14
16
18
20
Electron energy keV

Fig. 6.7

from a noise point of view a differential analyser should be better than an integral one, sector analysers can produce spurious signals at low energy when a high energy beam enters them (Roy et al, 1975), particularly when no precautions appear to have been taken to prevent this (Chapter 3). Such a signal would shift the peak of the energy curve to lower energies.

It is interesting to note that all the above references use relatively crude analysers and none give stringent tests of them. A shift in energy, if it is to occur, will be towards the lower energies, and it is probable that this occurs to a greater or lesser extent in all these analysers. Darlington (1971) reports a range of values for the peak position. This work is at the upper end of the range, and his own at the lower end.

It must be pointed out that all reported spectra are similar in general form but different in detail. Theory cannot be evoked to support any one experiment, as there is no sufficiently accurate model available to simulate the scattering process through such large angles.

6.6 High resolution spectra

The apparatus was used to show the presence of quasi-elastically scattered electrons in the spectrum of gold, silver and lead obtained at 150° from the main beam direction. The primary beam energy was 20 keV.

The analyser was used in the differential mode, using a modulating voltage sufficient to give a resolution of ~ 5 eV (Appendix 4). The area under the elastic peak was found by recording the difference between the ratemeter readings with the analyser set at each end of the peak. The differential spectrum was thus used to give the peak shape and position, whereas the integral output, which was subject to much less noise, provided the peak area.

In each case the total current scattered into the analyser when the mesh was at anode potential was also recorded.

6.7 Elastic peaks

Resolvable elastic peaks were found in the spectra of silver, gold and lead. Copper, the next lowerst atomic number available, did not produce a resolvable peak, which was not unexpected as the silver elastic peak to background noise ratio was only about 4 : 1. The spectra are shown in Figs. 6.8, 6.9 and 6.10. In each case the width of the peaks is about 7 eV. This indicates that no characteristic energy losses were present.

The relative size of the elastic peaks is shown in the table, Fig. 6.11. The results have been corrected for the energy response of the phosphor and the screening effect of the analyser mesh. In each case they are produced by a beam of 8×10^{-8}A.

These results proved to be reproducible from day to day, showing that they were not artifacts of local charging of the specimen.

With clean surfaces the peak width was constant, but if several runs were done on the same spot the contamination produced by cracked pump fluid vapour caused the width to increase markedly.

Each run took between 15 and 20 minutes in order to allow the phase sensitive detector a sufficiently long time constant for good resolution. The broadening produced in the elastic peak during the recording of three successive spectra from the same point in a gold sample is shown in Fig. 6.12.

This investigation was severely limited by time and by the detachment of the very sensitive and stable phosphor used from its mounting glass. It was not possible in the time available to condition and calibrate a new phosphor, also none could be found with high enough sensitivity. Thus experiments were abandoned at this point.

6.8 Discussion of high resolution spectra obtained

The occurrence of a 2% elastic component in the backscattered spectrum is

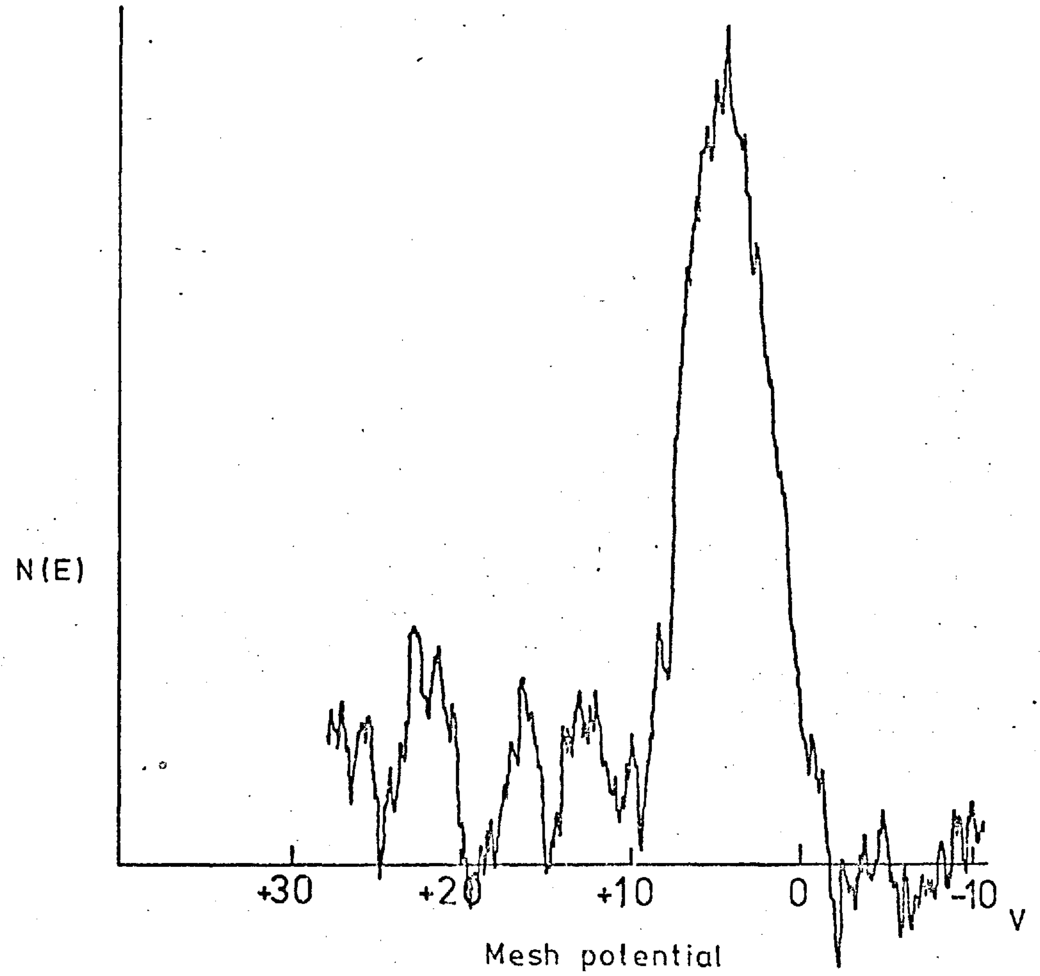

Fig.6.8 High resolution backscattered electron spectrum for Pb. Mesh potential measured w.r.t beam accelerating potential. Beam energy 20 keV.

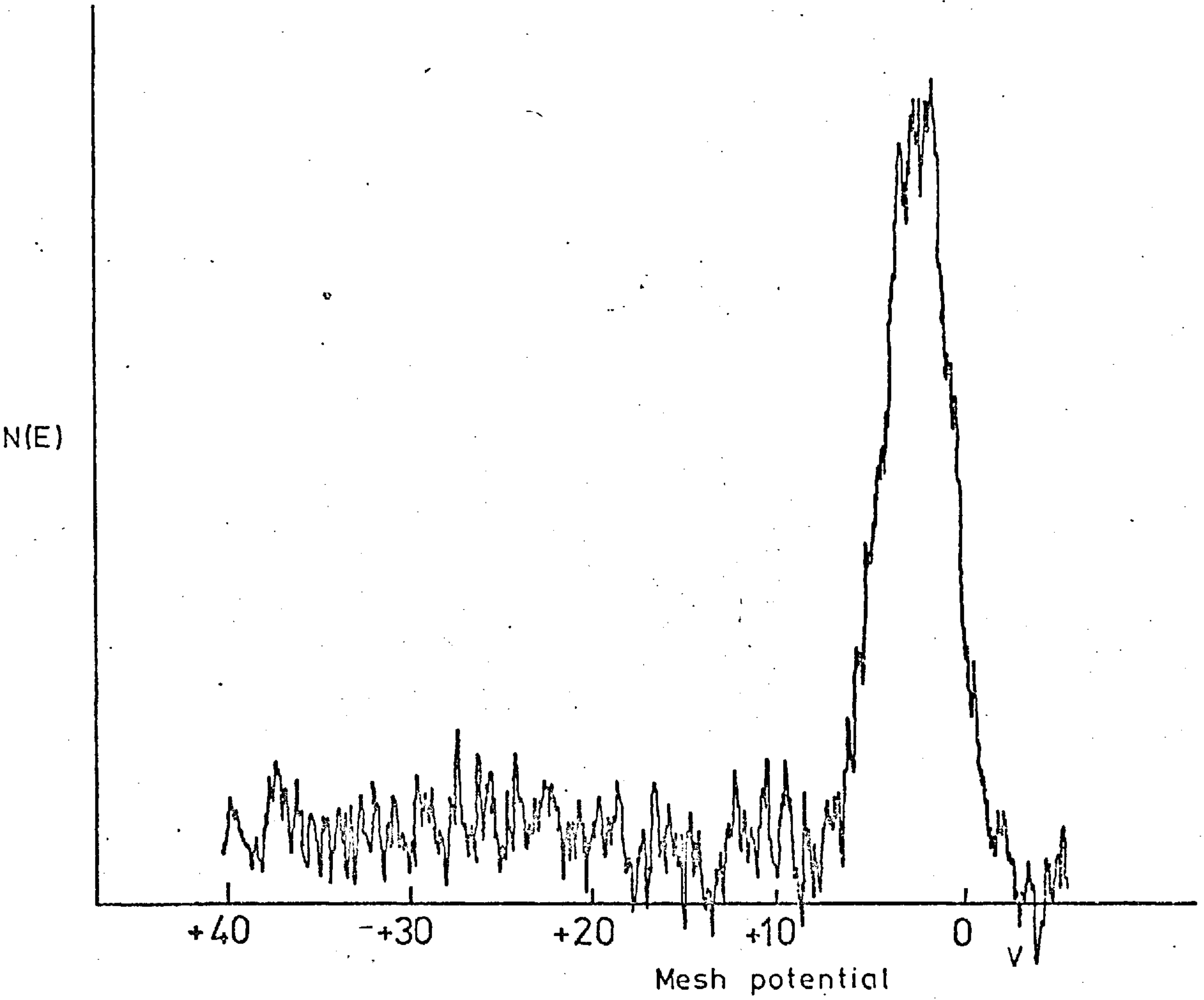

Fig.6.9 High resolution backscattered electron spectrum for Au.
Beam energy 20 keV.

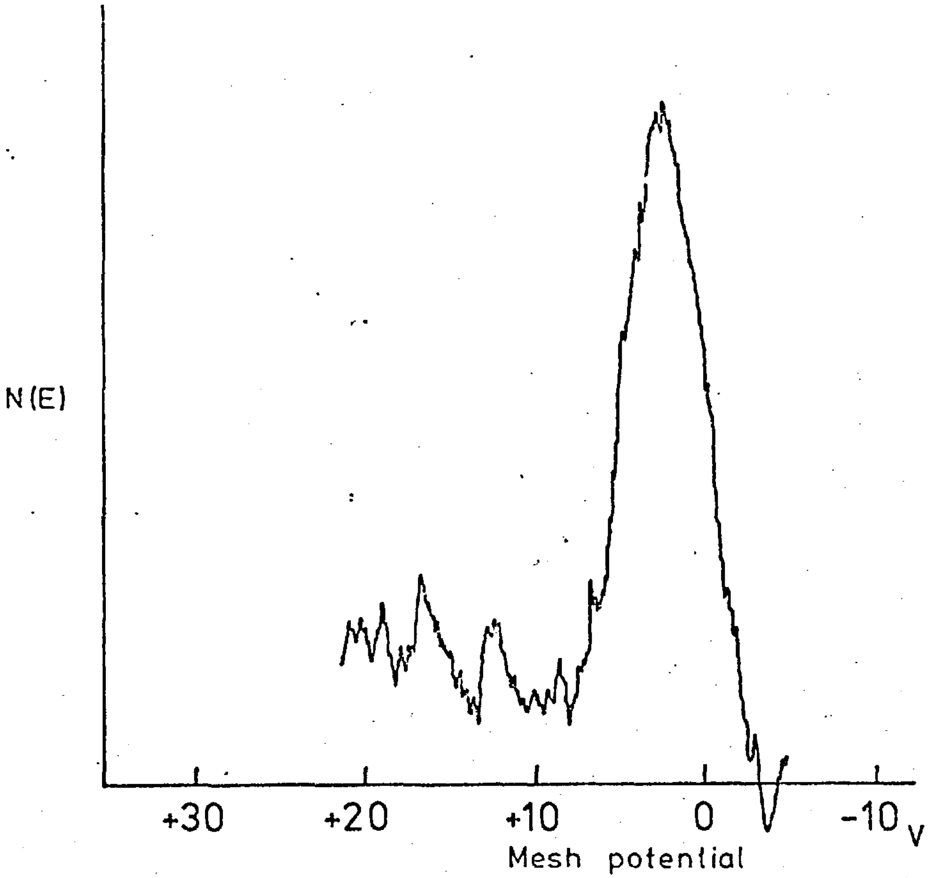

Fig.6.10 High resolution backscattered electron spectrum for Ag.
Beam energy 20 keV.

	Total scattered current 10^4 electrons/second	Elastic current 10^3 electrons/second	Ratio %
Au			
1	6·9	1·7	2·5
2	6·3	1·6	2·5
3	6·6	1·5	2·3
4	7·3	1·8	2·5
Pb			
1	6·3	0·74	1·2
Ag			
1	5·0	0·37	0·74
2	5·6	0·35	0·63
3	5·4	0·36	0·67

Fig.6.11 Ratio of elastic to total scattering at 150 for Pb, Au and Ag.

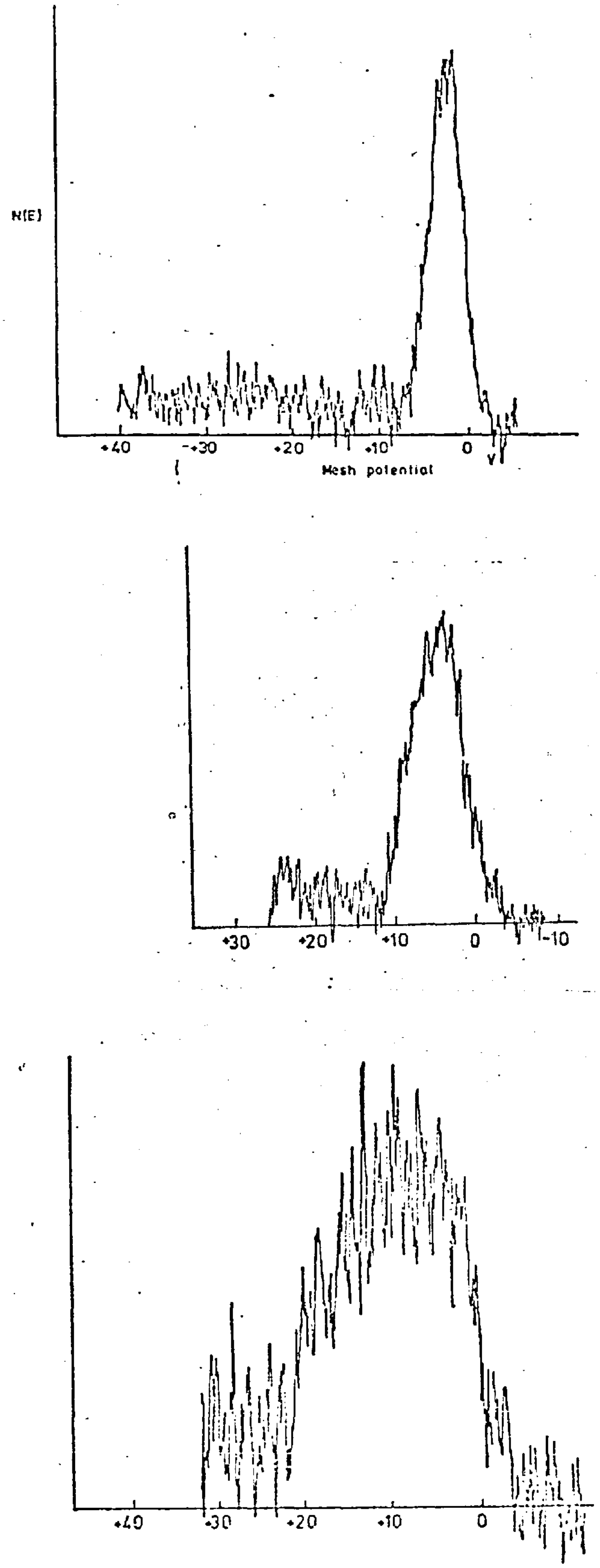

Fig.6.12 The effect of contamination on the backscattered spectrum from Au at 150 . The three spectra were recorded from the same spot in a period of 1hr.

initially surprising and has not previously been recorded at such high angles. Such an addition alters the spectra of Ag, Au and Pb as shown in Figs. 6.13, 6.14 and 6.15. These alterations are in fact more reasonable when the energy spectra in the range 0 - 10 keV are examined (Darlington and Cosslett, 1972) (Fig. 6.16). Here an elastic peak becomes clear as the resolution of the instrument improves. This effect has been reported by Cosslett and Thomas (1964) and by Darlington (1971)

6.9 Calculation of scattering from a thin gold slab

Rutherford scattering

The most probable interaction producing high angle scattering is that between the incident electron and the atomic nucleus. This has been discussed by Cosslett and Thomas (1964b) and by McDonald et al (1971). The differential cross-sections for Rutherford scattering, including the effects of screening and electron exchange, are given in Fig. 6.17 (Wells et al, 1974).

The probability P (φ , $\delta\Omega$) of the deflection of an electron through an angle, φ, into an element of solid angle $\delta\Omega$, while the electron travels a distance δs is

$$P(\varphi, \delta\Omega) = n \cdot \frac{d\sigma}{d\Omega} \cdot \delta s \cdot \delta\Omega \qquad (6.1)$$

where n is the number of electrons per unit volume in the material.

For Au,

$$n = 5.9 \times 10^{28}\ m^{-3}$$

$$\frac{d\sigma}{d\Omega} = 2.3 \times 10^{-24}\ m^2/(\text{atom})\ (\text{sterad}) \qquad 150^\circ \text{ scatter @ } 20\text{ keV}$$

Thus, in a slab of thickness 10^{-9}m the proportion of the beam scattered into unit solid angle at 150° will be

$$P(\varphi) = 5.9 \times 10^{28} \times 2.3 \times 10^{-24} \times 10^{-9}$$

$$= 1.3 \times 10^{-4}\ \text{sterad}^{-1}$$

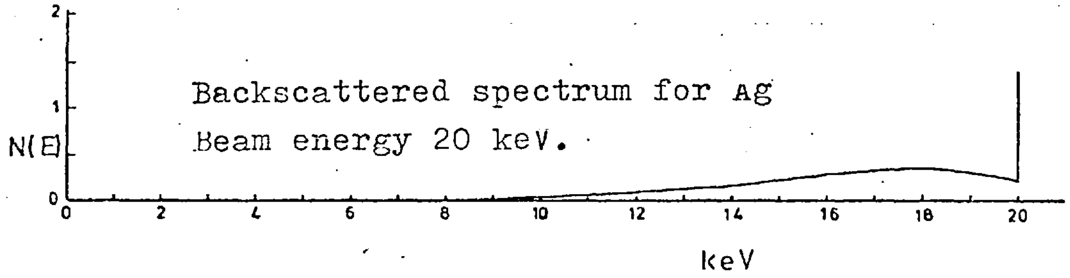

Fig.6.13

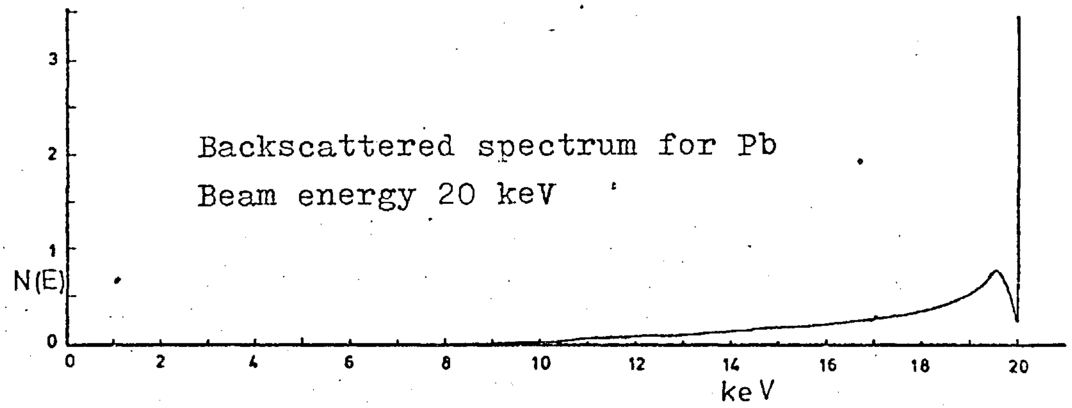

Fig.6.14

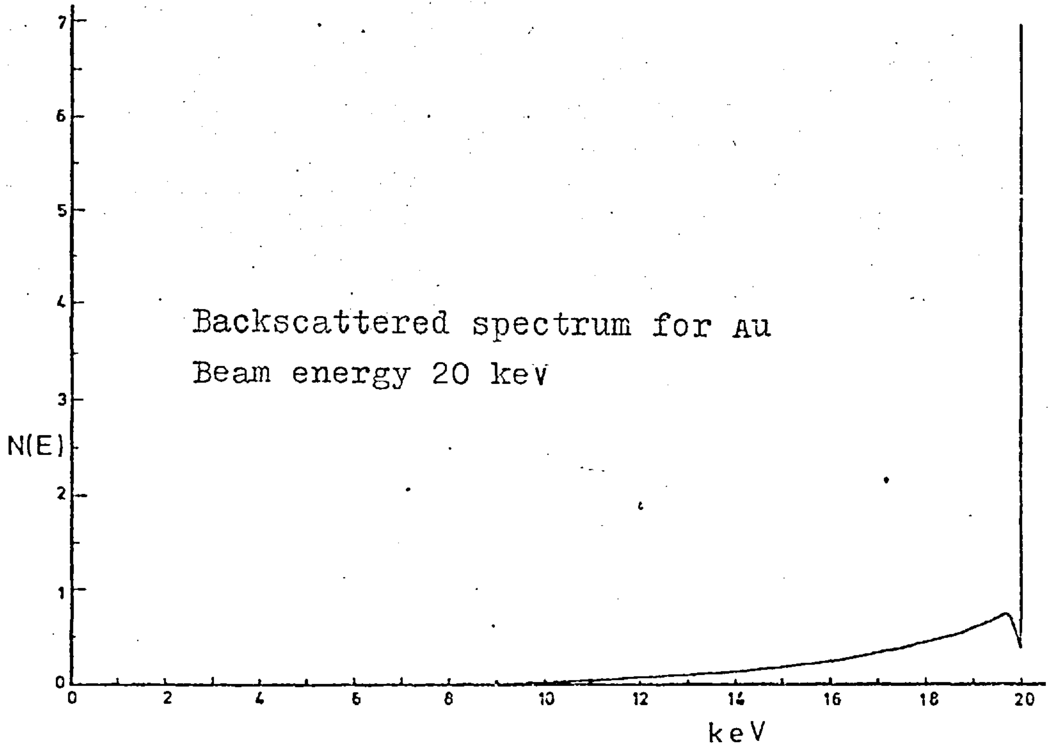

Fig.6.15

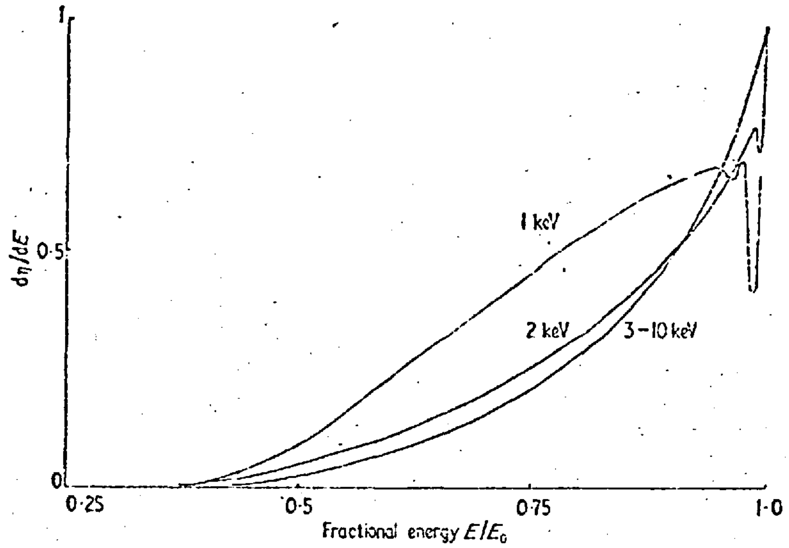

Figure 10. Energy spectra $d\eta/dE$ for silver at several beam energies.

Fig.6.16 Backscattering spectra at low energy from Darlington (1971)

The collector aperture of the analyser was of area $6.2 \times 10^{-8} m^2$ at a distance of 0.15 m from the specimen. Thus the proportion of the incident beam elastically single scattered into the aperture would be :

$$P(\varphi, \delta\Omega) = 1.3 \times 10^{-4} \cdot \frac{6.2 \times 10^{-8}}{0.15^2}$$

$$= 3.7 \times 10^{-10}$$

The incident current used was 3×10^{-8}A, thus a count rate of 70 electrons/second would be expected to be produced by a slab 1 nm thick.

The thickness of Au required to produce the observed elastic scattering would be 25 nm, assuming that the cross section for inelastic scattering is low.

Wells et al (1974), Fig. 6.18, give the mean free path for inelastic scattering as 18.2 nm. Using this figure, the maximum elastic backscattered current that could be obtained would be 1.3×10^3 electrons/second. This is considerably below the observed value; however, it totally ignores the effect of multiple scattering. This is a small but noticeable effect which may well account for the difference.

The value of mean free path of 1.82×10^{-8}m does include inelastic processes which may not be resolved in these experiments. It is probable that the effective mean free path for inelastic processes in which more than 8 eV is lost is rather larger than this. The value required to explain the observations is a minimum of 2.4×10^{-8}m, which is within the range of quoted values (Fig. 6.18).

The explanation given above is obviously a gross oversimplification. It leads to an electron distribution which depends on the scattering cross-section, whereas in practice the distribution with angle depends on cos φ (Kanter, 1957).

There has been no rigorous calculation of the elastic component in a backscattered distribution with which to compare these experimental results, though the calculation above tends to support them.

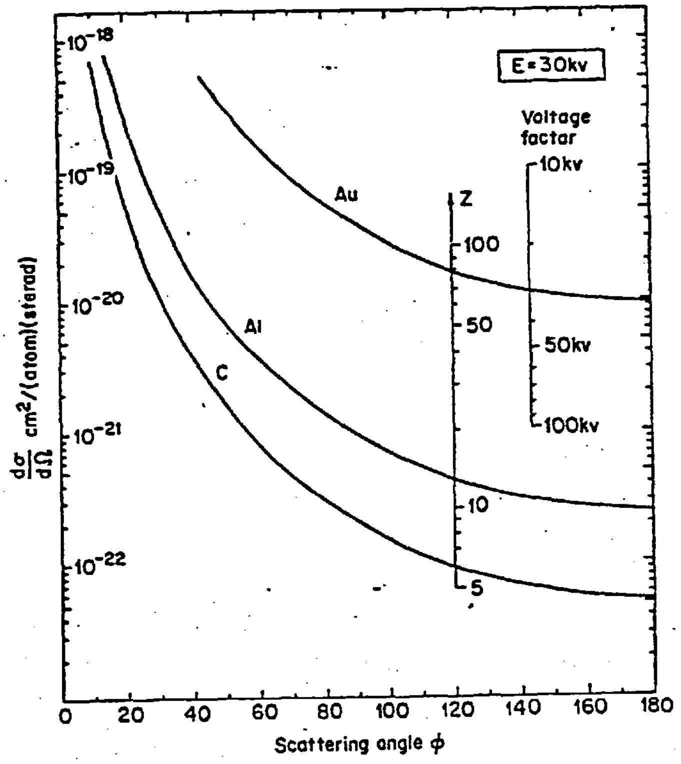

(a)

(*a*) Differential Rutherford scattering cross section for C, Al, and Au

Fig.6.17 from Wells et al (1974)

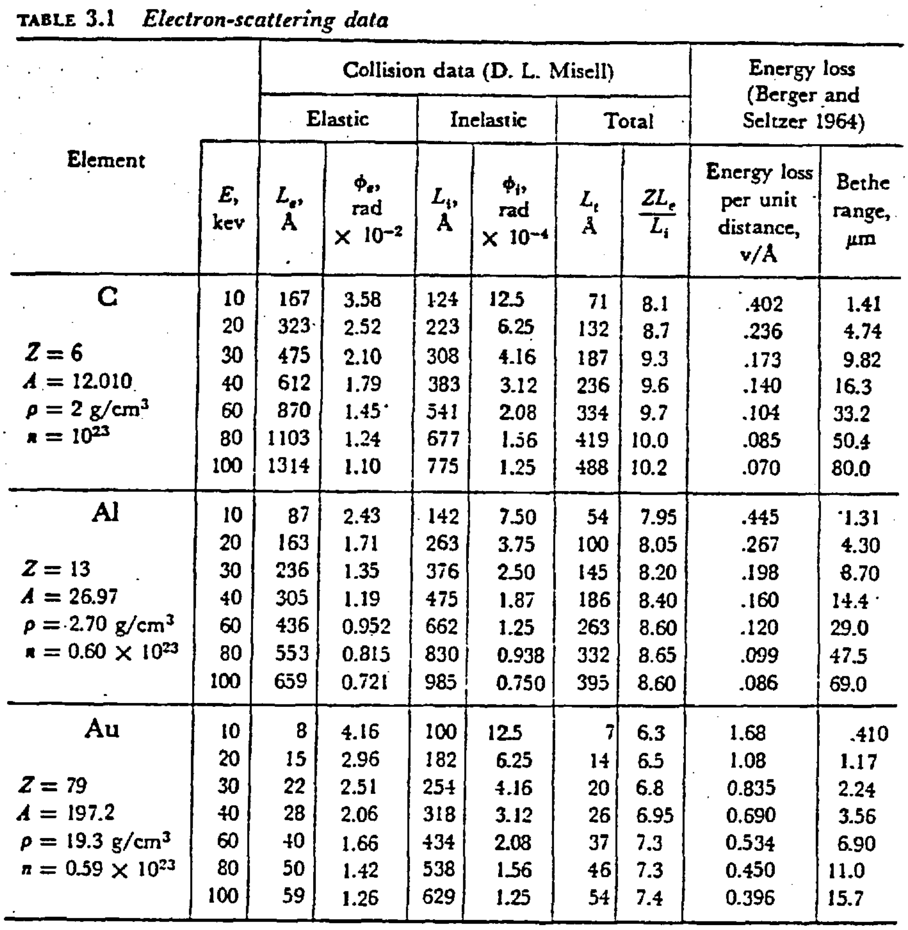

TABLE 3.1 *Electron-scattering data*

Element		Collision data (D. L. Misell)						Energy loss (Berger and Seltzer 1964)	
		Elastic		Inelastic		Total			
	E, kev	L_e, Å	ϕ_e, rad $\times 10^{-2}$	L_i, Å	ϕ_i, rad $\times 10^{-4}$	L_t Å	$\frac{ZL_e}{L_i}$	Energy loss per unit distance, v/Å	Bethe range, μm
C	10	167	3.58	124	12.5	71	8.1	.402	1.41
	20	323	2.52	223	6.25	132	8.7	.236	4.74
$Z = 6$	30	475	2.10	308	4.16	187	9.3	.173	9.82
$A = 12.010$	40	612	1.79	383	3.12	236	9.6	.140	16.3
$\rho = 2$ g/cm³	60	870	1.45	541	2.08	334	9.7	.104	33.2
$n = 10^{23}$	80	1103	1.24	677	1.56	419	10.0	.085	50.4
	100	1314	1.10	775	1.25	488	10.2	.070	80.0
Al	10	87	2.43	142	7.50	54	7.95	.445	1.31
	20	163	1.71	263	3.75	100	8.05	.267	4.30
$Z = 13$	30	236	1.35	376	2.50	145	8.20	.198	8.70
$A = 26.97$	40	305	1.19	475	1.87	186	8.40	.160	14.4
$\rho = 2.70$ g/cm³	60	436	0.952	662	1.25	263	8.60	.120	29.0
$n = 0.60 \times 10^{23}$	80	553	0.815	830	0.938	332	8.65	.099	47.5
	100	659	0.721	985	0.750	395	8.60	.086	69.0
Au	10	8	4.16	100	12.5	7	6.3	1.68	.410
	20	15	2.96	182	6.25	14	6.5	1.08	1.17
$Z = 79$	30	22	2.51	254	4.16	20	6.8	0.835	2.24
$A = 197.2$	40	28	2.06	318	3.12	26	6.95	0.690	3.56
$\rho = 19.3$ g/cm³	60	40	1.66	434	2.08	37	7.3	0.534	6.90
$n = 0.59 \times 10^{23}$	80	50	1.42	538	1.56	46	7.3	0.450	11.0
	100	59	1.26	629	1.25	54	7.4	0.396	15.7

Fig.6.18 from Wells et al (1974)

6.10 Comparison between the elastic peak heights

Fig. 6.19 shows the proportion of elastic electrons in the spectra of Au, Ag and Pb plotted against the square of their atomic number, Z . For Au and Ag the proportion is approximately dependent on Z^2. Pb, however, does not fit. It should be similar to Au, but is not, probably because of a surface oxide layer which would reduce the effective atomic weight near the surface.

The observed elastic peak area for Pb is consistent with the values for Au and Ag if it is assumed to be PbO and a mean value of Z^2 for Pb and O is used (Fig. 6.19).

A dependence on Z^2 is not very surprising as the inelastic mean free path is similar for most materials but the elastic cross-section is dependent on Z^2 (Chapter 1).

There is evidently considerable scope for checking this relationship and extending both to lower Z and different angles of incidence. Such an investigation would be of interest as it would provide an easily confirmed check on any detailed scattering theory.

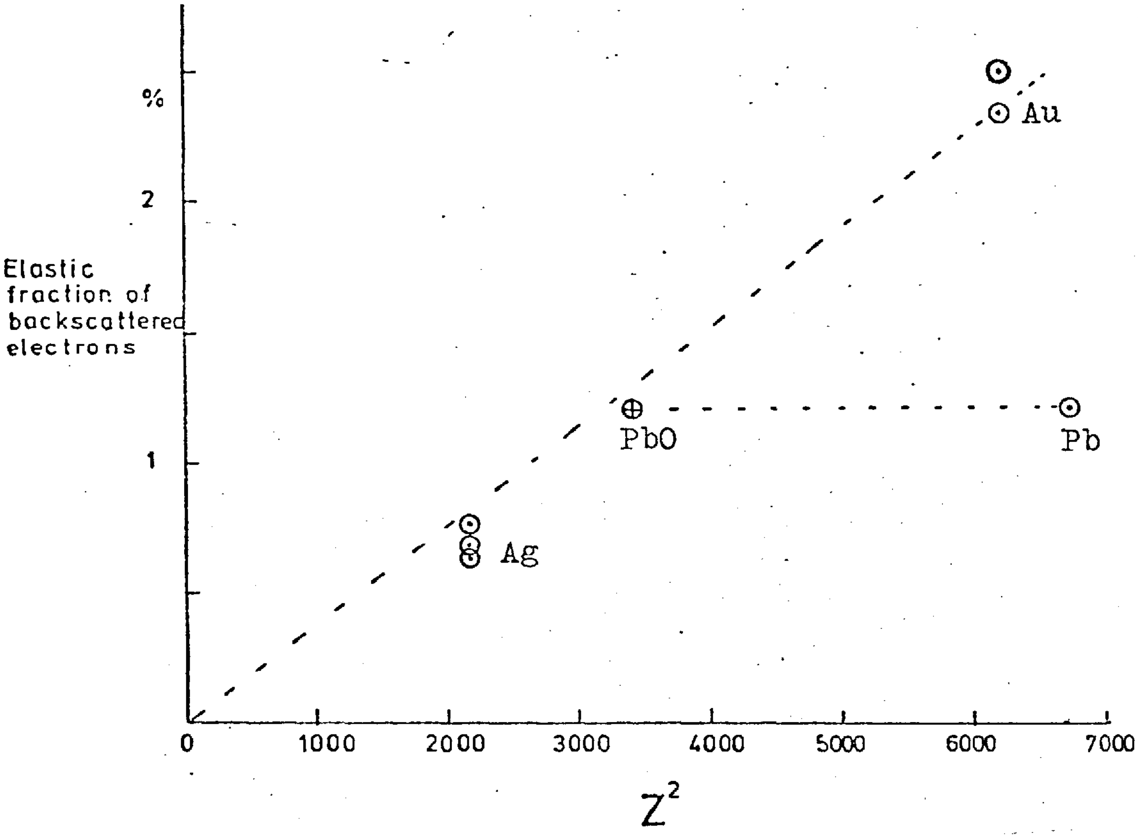

Fig.6.19 Dependence of the elastic fraction of the total backscattered current on the atomic number Z.

CHAPTER 7

KIKUCHI BAND FORMATION

7.1

Kikuchi patterns were first observed by Kikuchi (1928). He observed that when electrons with an energy of 60 keV passed through a 0.3 um thick flake of mica (cf. Fig. 7.2) a set of lines and bands appeared, as well as the usual Bragg diffraction spots. He also noted that this pattern was related in geometry to the crystal position alone, rather than to the relative position of the incident beam and crystal as with Bragg spots. The pattern was found to rotate with the crystal as though rigidly fixed to it.

Nishikawa and Kikuchi (1928) and Thomson (1931) observed similar patterns produced by electrons scattered from the surfaces of cleaved or polished single crystals (Fig. 7.1).

Since then, most workers using electron diffraction cameras or electron microscopes have observed Kikuchi bands and many theoretical and experimental studies of them have been made. Reviews of the theory have been made by Hall (1970), Uyeda (1974) and Rez et al (1977), and of experiment by Alam (1952) and Uyeda (1974) at high energy and Mosser et al (1976) and Murukami et al (1978) at low energy.

7.2 Geometry of Kikuchi patterns

The main feature of the geometry of Kikuchi patterns is that the median lines of bands or complementary pairs of Kikuchi lines represent the intersection of crystal net planes with the recording plate or film. The result of such intersections is a set of hyperbolae, or straight lines.

Fig. 7.3 shows the three principal axes and planes of a cubic crystal, from which it can be seen that the Kikuchi pattern has a very high symmetry and can be

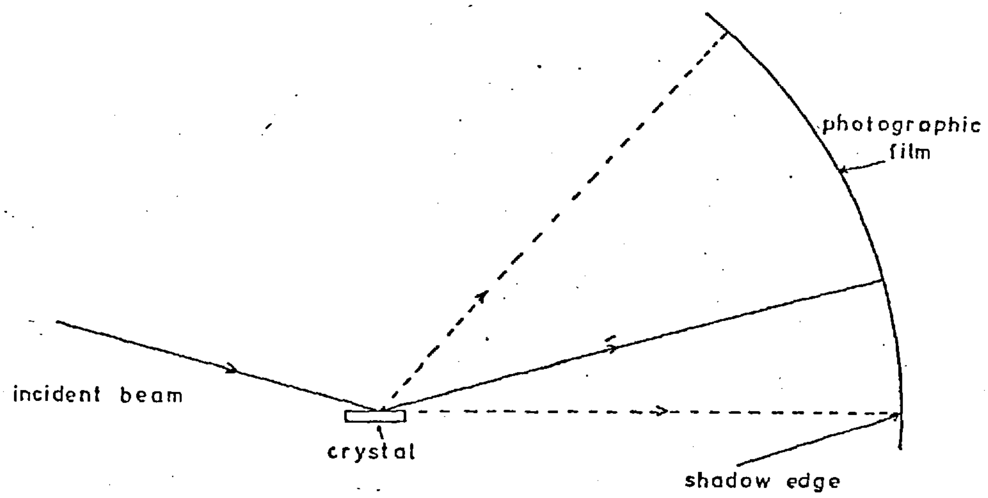

BRAGG CASE

Fig.7.1

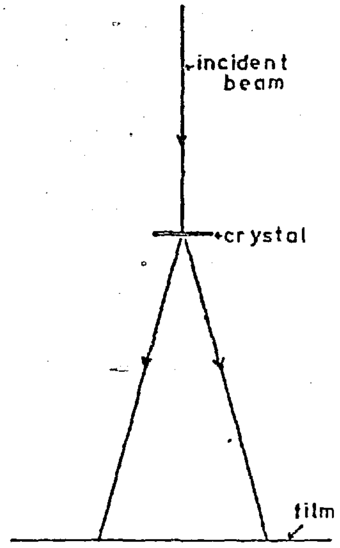

LAUE CASE

Fig.7.2

completely represented by only a small section of the total pattern. For a cubic crystal the surface bounded by the three octants between the [001] , [011] and [111] axes shows all the features of the pattern geometry (Fig. 7.4).

The intersection of a crystal axis with the film is shown by the crossing of two or more planes and are the "poles" of the patterns. The detail of the indexing of the Kikuchi patterns, originally done by Wilman (1948), is reviewed in Hirsch et al (1965) and Coates (1969). The latter paper reviews the geometry in the context of electron channelling, but the results are the same for both Kikuchi and channelling patterns.

7.3 Band width and line separation

In the region where lines can be seen they occur in complementary pairs. One line is of excess type, having a higher electron density than the immediate background, the other of defect type, showing lower electron density than the background. The lines are parallel or share the same focus and have an angular separation ϑ_B from their median line where ϑ_B is the Bragg angle for the reflection at the plane defined by the median line.

$$\sin \vartheta_B = \frac{n\lambda}{d} \qquad (7.1)$$

n = order number

λ = wavelength of electrons

d = plane spacing

In the same way the angular width of the Kikuchi bands is approximately $2\vartheta_B$ (Chapter 8).

Formation of Kikuchi features

a) Lines

Kikuchi (1928) suggested that the lines were formed by Bragg diffraction of those electrons already scattered through small angles out of the main beam. The locus of all points in reciprocal space which will give rise to Bragg diffraction for a

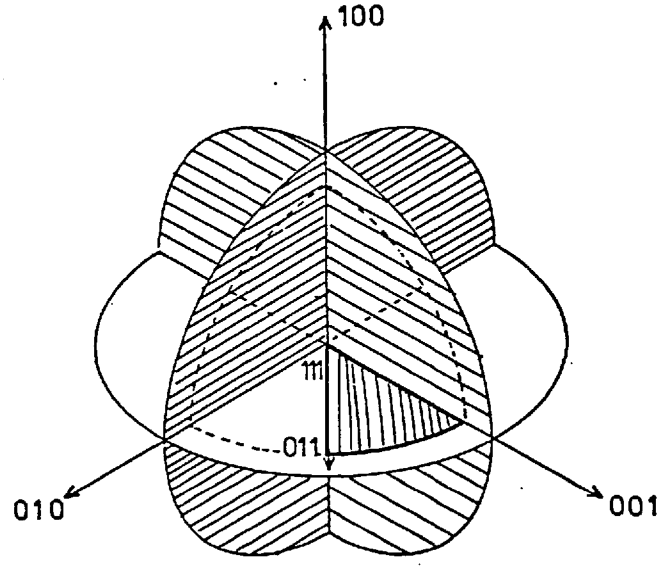

Fig.7.3 Symmetry of reciprocal space for cubic real space lattice.

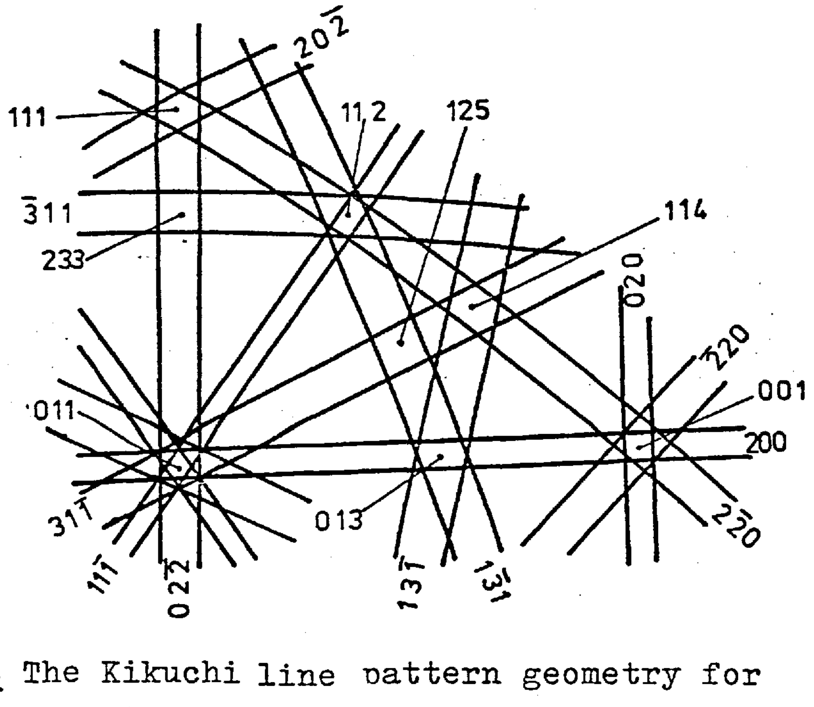

Fig.7.4 The Kikuchi line pattern geometry for a face-centered cubic crystal. The pattern has mirror symmetry about the medians of the (200), (2$\bar{2}$0) and (02$\bar{2}$) line pairs.

particular wave vector through a reciprocal lattice vector $\underline{g}$ is a circle. If the ends of any wave vectors, $\underline{k}$, lie on this circle the wave will be strongly diffracted (Fig. 7.5).

Kikuchi argued that the electrons entering a crystal would be spread out in angle by diffuse scattering into a cone of increasing angle. If this cone overlapped the circle (Fig. 7.6) those electrons with wave vectors on the circle would be strongly diffracted and thus removed from the cone. The result of this is to produce a defect line near to the main beam and an excess line separated from it by an angle $2\vartheta_B$, in accordance with observation.

In Fig. 7.6 the main beam lies on the diffracting circle, and thus there will be a strongly diffracted Bragg spot resulting in the pattern shown in Fig. 7.7.

This explanation, though simple, predicts accurately both the position and type of the lines produced when a beam is incident asymmetrically on a set of Bragg planes. Much work has been carried out on the detail of the line intersections with Bragg spots and with other lines (Takagi, 1958; Miyake et al, 1975); however, the basic principle of incoherent scattering followed by Bragg diffraction remains.

In general, the electrons forming Kikuchi lines are not phase linked to the main beam and thus not to each other.

b) Bands

The simple explanation of line formation cannot be extended to the production of bands, in fact it predicts that bands should not appear.

Consider an electron beam incident parallel to a set of crystal planes of spacing 1/g (Fig. 7.8). The electrons will be scattered into a cone (dotted) and some will meet the planes at the Bragg angle. If the scattering is symmetric, the number of electrons meeting the planes along (A, 0) will equal the number meeting them along (A', 0). Of the electrons moving in the direction (A, 0) a proportion

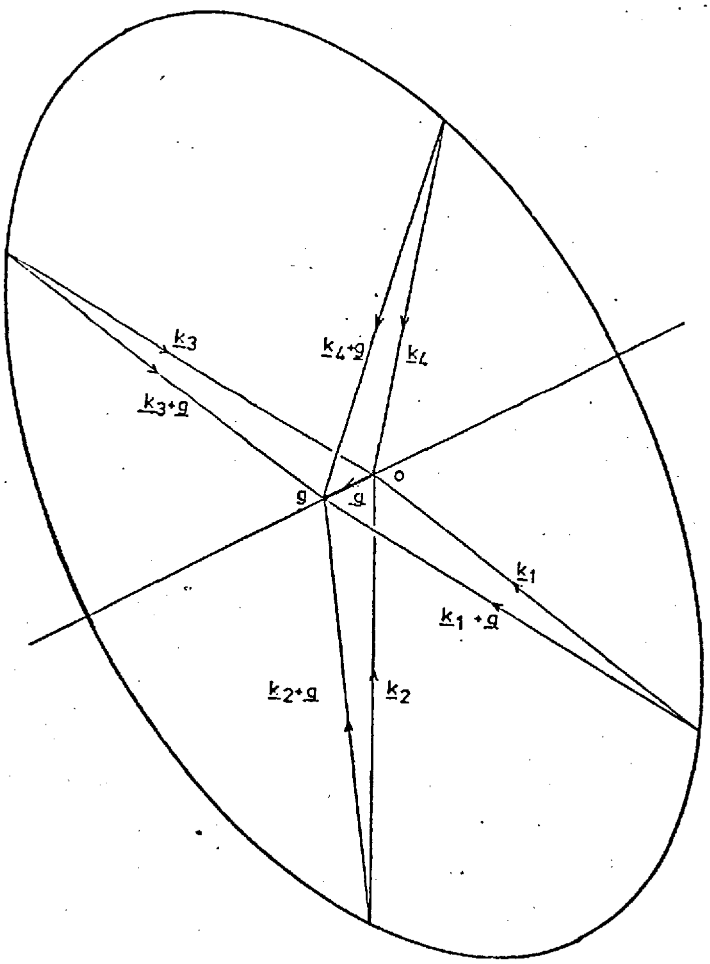

Fig.7.5 Locus of Ewald sphere centres of all beams $\underline{k}_n$ that are diffracted through a reciprocal lattice vector, $\underline{g}$, to give a strong beam $\underline{k}_n+\underline{g}$.

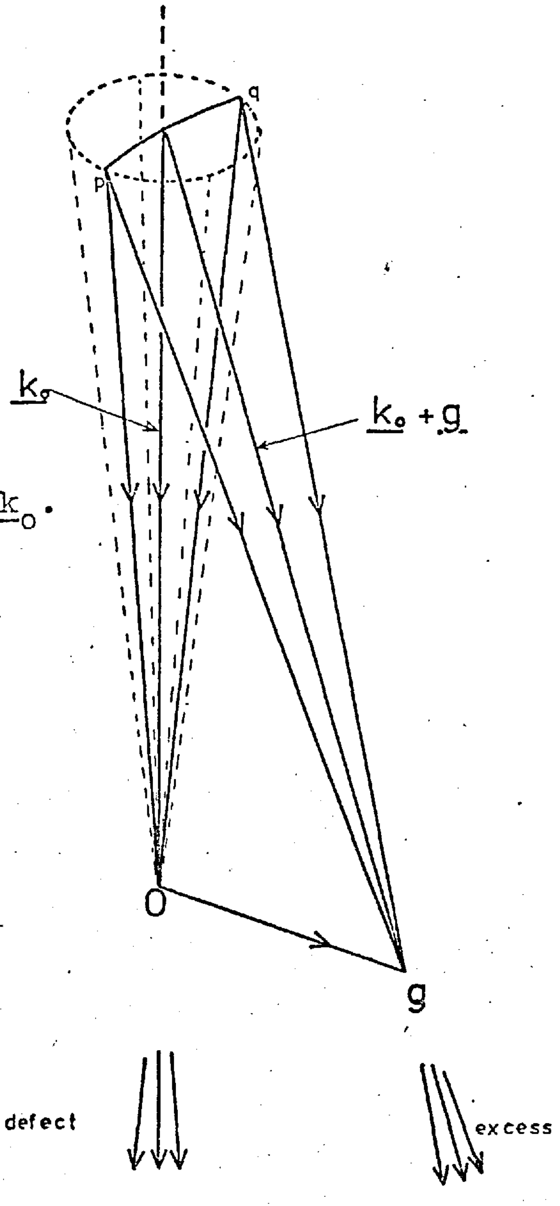

Fig.7.6 Reciprocal lattice geometry for the formation of excess and defect lines near to the incident beam $\underline{k}_o$.

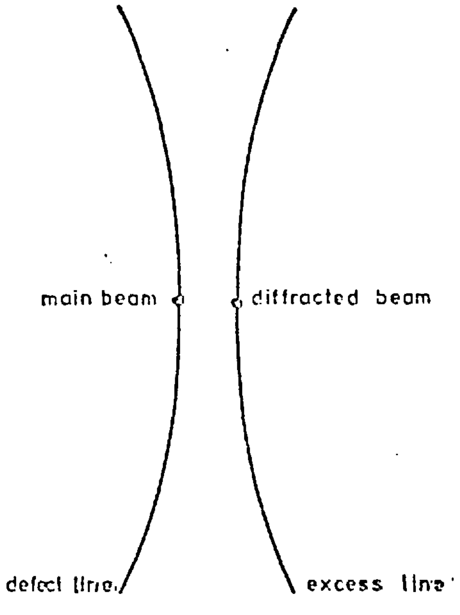

Fig.7.7 Excess and defect lines formed by the scattering geometry of Fig.7.6. The pattern is recorded on a plane surface producing hyperbolic lines.

will be scattered along (A, - g), similarly a proportion of those moving in the direction (A', 0) will be scattered along (A', g). As the scattering is symmetric the number of electrons scattered from the (A, 0) beam will equal the number scattered from the (A', 0) beam. (A, 0) and (A', g) are in the same direction, thus the net scattering out of (A, 0) is zero, as is the net scattering out of the (A' 0) beam. In fact, a band edge can always be seen.

In order to produce any adequate description of Kikuchi bands, a dynamical wave theory must be used. The theory needs some considerable explanation before the consequences of its use become clear. The theory is considered in the next section.

The main features that need to be explained by any theory are the formation of the band and its intensity relative to the diffuse electron background. The band contrast produced by transmission of high energy electrons through thin crystals is of excess type, while thick crystals or low energy electrons produce defect bands. If the ratio of electron energy to crystal thickness is chosen correctly, both the excess and defect bands can be seen in the same pattern. Shinohara and Matsukawa (1933) demonstrated the change in band type excess to defect with increasing electron energy by obtaining diffraction patterns from the same mica sheet at 27 keV, 45 keV and 57 keV. The photographs produced with 57 keV electrons showed excess bands, with 45 keV electrons both excess and defect bands, and with 27 keV electrons only defect bands. The bands of excess type are often referred to as "anomalous" and those of defect type "normal" by microscopists. However, both occur in most diffraction patterns if enough of the pattern is recorded.

7.4 The dynamical theory of electron diffraction

The dynamical theory of electron diffraction is an attempt to describe an electron wave function, $\psi(\underline{r})$ in a crystal potential $V(\underline{r})$. The complete solution must be consistent both with the Schrödinger equation,

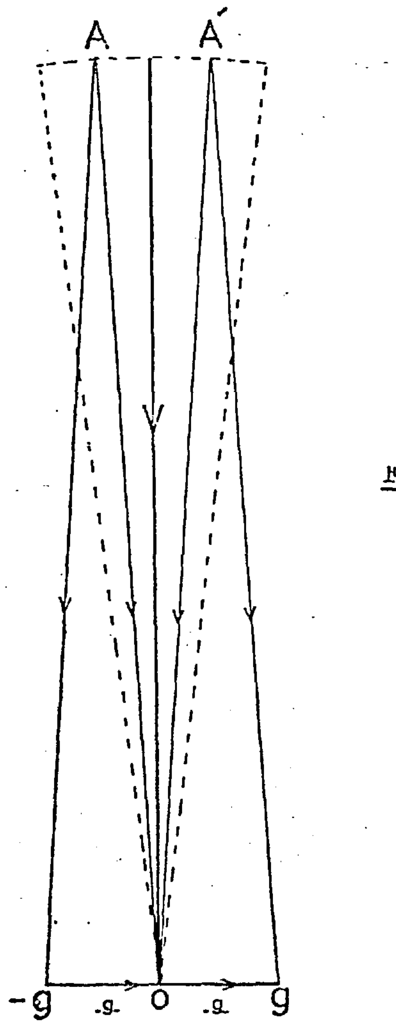

Fig.7.8 Symmetrical line formation.

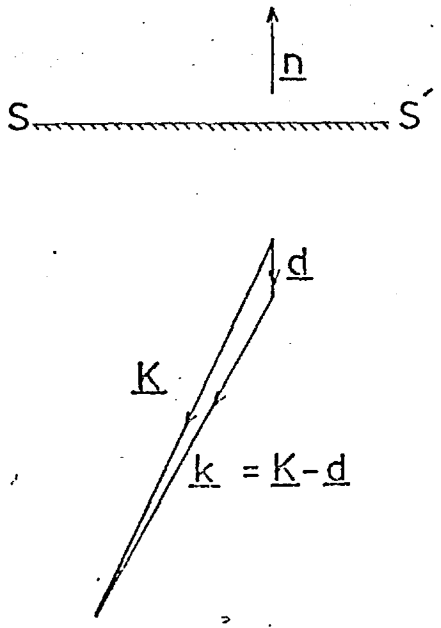

Fig.7.9 Relation between the main scattering wave vectors.

$$\nabla^2\psi(\underline{r}) + (8\pi^2 me/h^2)(E + V(\underline{r}))\ \psi(\underline{r}) = 0 \qquad (7.4.1)$$

and with the external boundary conditions imposed by the electrons' entry into or exit from the crystal.

A solution that can be shown to be consistent with (7.4.1) is a general Bloch wave, (Bloch, 1928)

$$\psi = \int_{h=-\infty}^{\infty} \psi_h (\exp 2\pi i((\underline{k}_o + \underline{h}).\ \underline{r})) \qquad (7.4.2)$$

where $\underline{h}$ ranges over all reciprocal lattice vectors. $\underline{k}_o$ is a wave vector defined by the boundary conditions.

Note that in (7.4.2) the crystal potential is assumed to be continuous. If, as is usually the case, the crystal potential is periodic of the form

$$V(\underline{r}) = \sum_g V_g \exp(2\pi i\, \underline{g}.\underline{r}) \qquad (7.4.3)$$

the Bloch wave can be simply written as :

$$\psi = \sum_h \psi_h \exp 2\pi i((\underline{k}_o + \underline{h}).\ \underline{r}) \qquad (7.4.4)$$

where $\underline{h}$ is restricted to integer multiples of the reciprocal lattice vector $\underline{g}$ (Brillouin, 1946).

The equation (7.4.2) does not allow arbitrary external boundary conditions to be imposed. The only way a flexible solution, which can accommodate boundary conditions, can be constructed is to sum a set of Bloch waves (7.4.4)

$$\Psi = \sum_j \psi_j \qquad (7.4.5)$$

$$\psi_j = \sum_h \psi_{hj} \exp\ 2\pi i((\underline{k}_{oj}\ \underline{h}).\underline{r}) \qquad (7.4.6)$$

This set should range for completeness over all h and all j.

In practice, this solution is too unwieldy and has to be simplified by restricting j and h to a few terms (usually the same number). The production of a solution that is analytically manageable and yet accurate is one of the main problems of Solid State physics.

One beam solution

Often a crystal can be placed in such a position that only a few electron beams are weakly excited within it. The incident angle can be set well away from one of the Bragg angles and so most of the intensity remains in the main beam.

In this situation the wave in the crystal may simply be represented by a plane wave,

$$\psi_0 \exp (2 \pi i \, \underline{K} . \underline{r}) \qquad (7.4.7)$$

The vector $\underline{K}$ is the wave vector in the crystal. Its magnitude is given by :-

$$| \underline{K}^2 | = \frac{2 m e}{h^2} (E + V_0) \qquad (7.4.8)$$

where E is the electron energy in vacuuo and V_o is the mean, non periodic crystal potential. (The magnitude of wave vector in vacuuo $\underline{K}_v$ is given by

$$| \underline{K}_v^2 | = \frac{2 m e}{h^2} E$$

$\underline{K}_v$ and $\underline{K}$ are linked by the conservation of their tangential components across the crystal/vacuum interface.)

The scattering is assumed to be small so the coefficients V_g are small and (7.4.1) is approximately obeyed. This plane wave solution is of little use in the case where one or more diffracted waves are strongly excited as it represents only the refracted beam. The solution must therefore be extended.

Two beam theory

The next stage of complexity is that of two strong beams, the incident beam and one diffracted at, or very near to, the Bragg condition by a small reciprocal lattice vector $\underline{g}$.

If it is assumed that $V_o \sim V_g$ and that $V_g >> V_n$ where $n \neq g, 0$, then the Schrodinger equation gives a set of equations

$$(\underline{K}^2 - (\underline{k}_{oj} + \underline{h})^2)\, \psi_{hj} + \sum_g{}' U_g \psi_{h-g} = 0 \qquad (7.4.9)$$

where $$U_g = \frac{2me}{h^2} V_g$$

$\underline{k}_{oj}$ is the wave vector of the j^{th} Bloch wave within the crystal in a direction near to $\underline{K}$ related by a vector $\underline{d}_j$ which is normal to the crystal surface. $\underline{k}_{oj} = \underline{K} - \underline{d}_j$ (Fig. 7.9). The prime on the summation indicates that $g \neq 0$.

The equations (7.4.9) are

$$[\underline{K}^2 - (\underline{k}_{oj})^2]\, \psi_{oj} + U_g \psi_{+gj} = 0 \qquad (7.4.91)$$

$$[\underline{K}^2 - (\underline{k}_{oj} + \underline{g})^2]\, \psi_{gj} + U_o \psi_{gj} = 0 \qquad (7.4.92)$$

$$[\underline{K}^2 - (\underline{k}_{oj} - \underline{g})^2]\, \psi_{-gj} + U_g \psi_{oj} = 0 \qquad (7.4.93)$$

The terms with $h \neq 0$, g, $-g$ have been ignored as it has been assumed that only ψ_{gj} and ψ_{oj} are strong, and that $U_g = U_{-g}$ and is large compared to $h \neq g$. However, this leads to trouble.

From (7.4.93)

$$U_g\, \psi_{oj} = 0 \qquad (\psi_{-gj} = 0) \qquad (7.4.10)$$

but U_g is finite and ψ_{oj} is assumed strong. Here is the weakness in truncating the Bloch wave sets from an infinite number of terms to, in this case, two. ψ_o and ψ_{+g} are both much stronger than ψ_n $n \neq 0$, g but for a consistent set of equations (7.4.9) all ψ_n must be included. Physically, this means that even when a crystal is set at a Bragg angle many more than one diffracted beam will be excited.

These inconsistencies show the limitations of the two beam solution, which does, however, offer an insight into the main properties of a dynamical solution in a surprising number of situations.

Limitation on j

The number, j, of Bloch wave sets used is usually dictated by the boundary conditions. Two strong crystal rays require two Bloch waves if they are to be linked to a single incoming plane wave.

Limits on U_n

U_n is the fourier coefficient of the lattice at the reciprocal lattice vector $\underline{h}$. There is no restriction on U_n except that the more values $\underline{h}$ is allowed to have where U_n is large, the larger the number of Bloch waves needed to describe the resulting diffraction.

In general the solution of an n beam diffraction problem requires the manipulation of an n x n matrix (Hirsch et al, 1965). Often a six or seven beam calculation is regarded as sufficiently accurate for close comparisons with experiment (cf. Sandstrom and Humphries).

Two beam dynamical diffraction

Dispersion conditions

In equation (7.4.9), the relationship $\underline{k}_{oj} = \underline{K} + \underline{d}_j$ was quoted. $\underline{d}_j$ is a vector normal to the crystal surface linking $\underline{K}$ (the refracted beam) with $\underline{k}_{oj}$ (the diffracted beam in the j^{th} Bloch wave). $\underline{d}_j$ can be found analytically in the two beam case from (7.4.91) and (7.4.92).

These equations are consistent only if

$$\begin{vmatrix} \underline{K}^2 - \underline{k}_{oj}^2 & U_{-g} \\ U_g & \underline{K}^2 - (\underline{k}_{oj} + g)^2 \end{vmatrix} = 0 \qquad (7.4.10)$$

From Fig. 7.9 it can be seen that

$$|\underline{K}| = |\underline{k}| + |\underline{d}| \cos\vartheta \qquad (7.4.11)$$

$$|\underline{k} + \underline{g}| = [(|\underline{g}| - |\underline{K}| \sin\vartheta)^2 + (|\underline{K}| \cos\vartheta - |\underline{d}|)^2]^{1/2} \qquad (7.4.12)$$

Thus, from (7.4.11)

$$\underline{K}^2 - \underline{k}_{oj}^2 = 2|\underline{K}||\underline{d}_j| \cos\vartheta \quad (-\underline{d}_j^2 \cos\vartheta) \qquad (7.4.13)$$

from (7.4.12)

$$\underline{K}^2 - (\underline{k}_{oj} + \underline{g})^2 = 2Kd\cos\vartheta + 2Kg\sin\vartheta - g^2 (-d^2) \qquad (7.4.14)$$

In the following the terms in parentheses in (7.4.13) and (7.4.14) are ignored as being too small.

Thus from (7.4.10), substituting (7.4.13) and (7.4.14)

$$2Kd_j\cos\vartheta\,(2Kd_j\cos\vartheta + (2Kg\sin\vartheta - g^2)) - U_g^2 = 0 \qquad (7.4.15)$$

$$\therefore\ d_j^2 + d_j\left(\frac{2Kg\sin\vartheta - g^2}{2K\cos\vartheta}\right) - \left(\frac{U_g^2}{4K^2\cos^2\vartheta}\right) = 0 \qquad (7.4.16)$$

$$\therefore\ d_j = \frac{1}{2}\left(\frac{g^2 - 2Kg\sin\vartheta}{2K\cos\vartheta}\right) - (-1)^j\sqrt{\left(\frac{2Kg\sin\vartheta - g^2}{4K\cos\vartheta}\right)^2 + \left(\frac{U^2}{4K^2\cos^2\vartheta}\right)} \qquad (7.4.17)$$

where $j = 1$ or 2.

The variation of d with ϑ is shown in Fig. (7.10).

Note i) $d_1 \times d_2 = -\dfrac{U_g^2}{4K^2\cos^2\vartheta} = -\dfrac{1}{\alpha^2}$ where $\alpha = \dfrac{2K\cos\vartheta}{U_g}$

ii) when $\sin\vartheta = \dfrac{g}{2K}$ $\quad d_1 = -d_2 = \dfrac{1}{|\alpha|}$

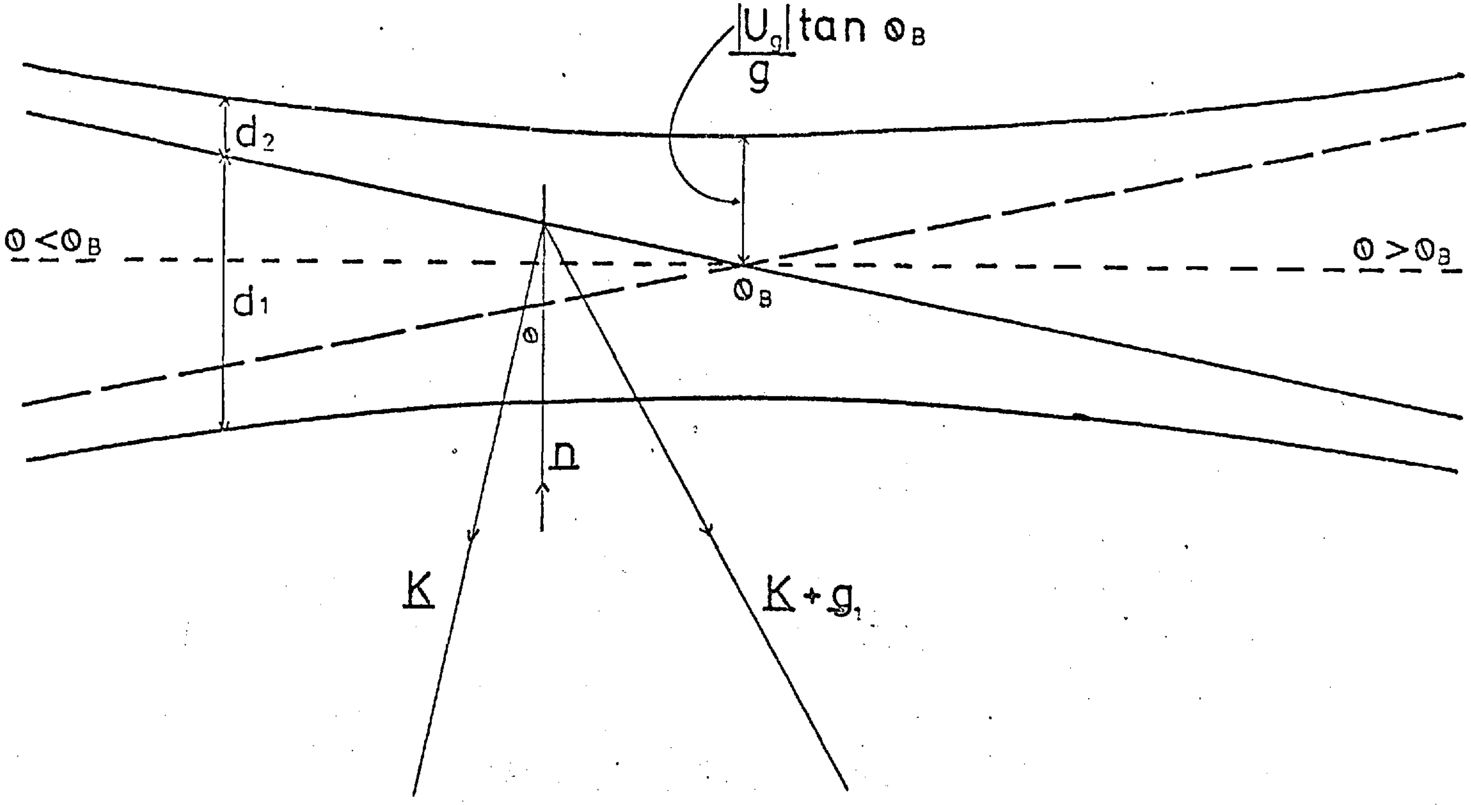

Fig. 7.10 Dispersion surfaces for d_I and d_2 showing the variation over a small range of θ. n is the surface normal and the crystal is assumed to be in the Laue orientation.

The equation (7.4.17) shows the relationship of d_j to the angle of incidence of the beam with the normal to the surface of the crystal, and assumes that $\underline{g}$ is parallel to the surface (the Laue condition). For the more general case, where the crystal planes are at an angle α to the surface normal $\underline{n}$ this equation becomes

$$d_j = \frac{1}{2} \cdot \frac{g^2 - 2Kg \sin(\vartheta - \alpha)}{2K\cos\vartheta} - (-1)\sqrt{\left(\frac{2Kg\sin(\vartheta\ \alpha) - g^2}{4K\cos\vartheta}\right)^2 + \frac{U_g^2}{4K^2\cos^2\vartheta}} \quad (7.4.18)$$

Figure (7.11) shows the relationships between $\underline{K}$, $\underline{d}$, $\underline{g}$, etc. in this case. Only one value of $\underline{d}$ has been shown for clarity.

Boundary conditions

The simplest approximation to a solution of the Schrödinger equation for an electron beam entering a crystal with its principal diffracting planes parallel to the surface normal is given by two truncated Bloch waves.

The total wave function is $\psi = \psi_1 + \psi_2$ where

$$\psi_1 = \psi_{o1} \exp(2\pi i(\underline{k}\ .\underline{r})) + \psi_{g1} \exp(2\pi i(\underline{k}_{01} + \underline{g}).\underline{r}) \quad (7.4.19)$$

and

$$\psi_2 = \psi_{o2} \exp(2\pi i(\underline{k}\ .\underline{r})) + \psi_{g2} \exp(2\pi i(\underline{k}_{o2} + \underline{g})\ \underline{r}) \quad (7.4.20)$$

These solutions must fit the boundary conditions of a plane wave $\psi_v = \exp(2\pi i \underline{K}_v.\underline{r})$ entering the crystal

$\psi_{01} + \psi_{02} = 1$ (7.4.21)

$\psi_{g1} + \psi_{g2} = 0$ (7.4.22)

[The total wave amplitude is constant]

$\underline{\Gamma}_0 = (\underline{\Gamma}_0 + \underline{d}_1)\psi_{01} + (\underline{\Gamma}_0 + \underline{d}_2)\psi_{02}$ (7.4.23) [continuity of the first derivative of the wave-function across the surface where Γ_0 is the normal component of $\underline{K}_v$ (this ignores the reflected wave that should exist)].

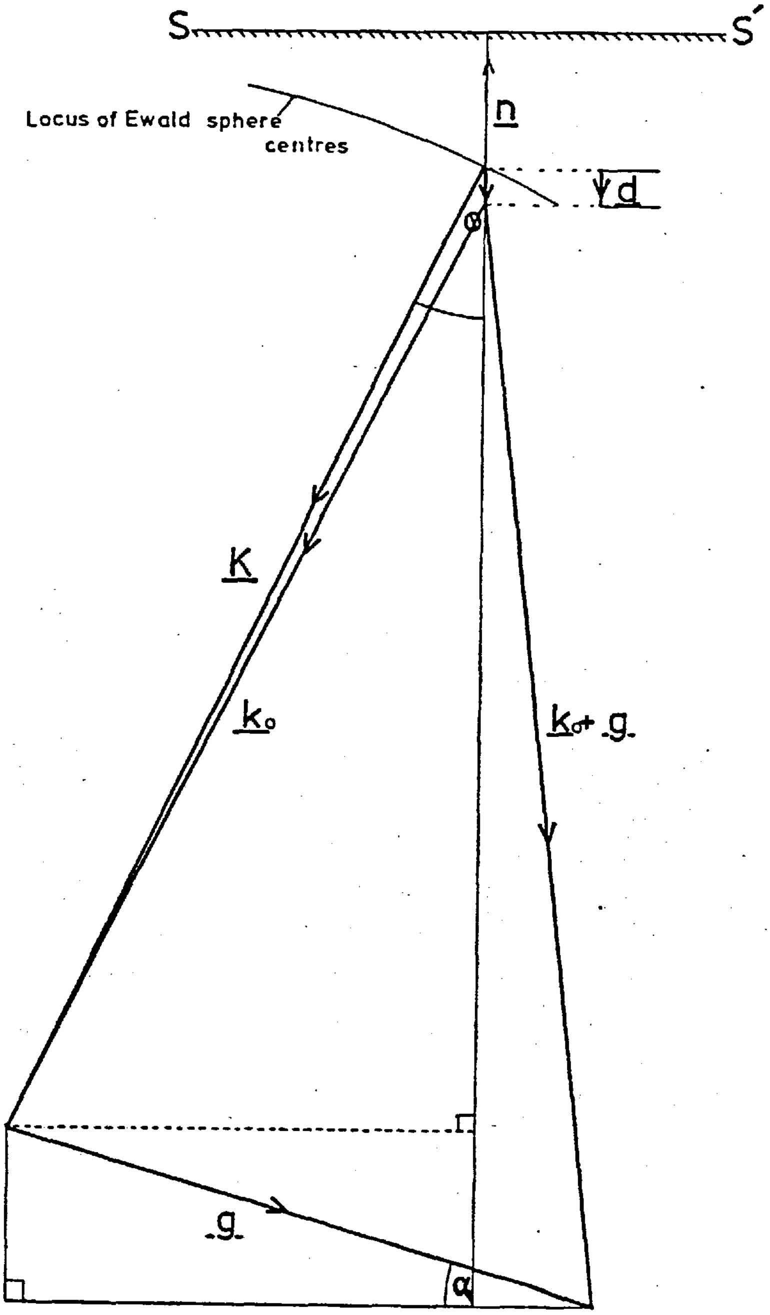

Fig.7.11 Scattering vectors for non-symmetric scattering, crystal planes not parallel with the entry or exit surfaces.

From (7.4.21) and (7.4.23)

$$\psi_{01} = \frac{-d_2}{d_1-d_2} \qquad (7.4.24)$$

also

$$\psi_{02} = \frac{d_1}{d_1-d_2} \qquad (7.4.25)$$

Substituting in (7.4.9)

$$\psi_{g1} = \frac{d_1 . d_2}{d_1 - d_2} . \alpha \qquad \text{where } \alpha = \frac{2K\cos\vartheta}{U_g}$$

$$\psi_{g2} = \frac{-d_1 . d_2}{d_1 - d_2} \cdot \alpha$$

The Bloch waves are thus

$$\psi_1 = \frac{-d_2}{d_1-d_2} . [\exp 2\pi i(\underline{k}_{01} \underline{r})].(1 - d_1\alpha \exp 2\pi i(\underline{g} . \underline{r})] \qquad (7.4.26)$$

$$\psi_2 = \frac{d_1}{d_1-d_2} \cdot [\exp 2\pi i(\underline{k}_{02} . \underline{r})].(1 - d_2\alpha \exp 2\pi i(\underline{g} . \underline{r})] \qquad (7.4.27)$$

There are several points that should be brought out about these equations :

1) These solutions are independent and can therefore exist separately within the crystal. They are phase linked only at the boundary, by the requirement that they are formed by a single plane wave.

2) They obey the reciprocity law.

3) They have different probability distribution within the crystal.

This last point gives rise to Kikuchi bands.

Asymmetry of electron distribution between different Bloch waves

The probability of an electron being at any point is given by the square of the wave function. Thus, for the j = 1 wave,

$$\psi_1\psi_1^* = \left[\frac{d_2}{d_1-d_2}\right]^2 \cdot (1 + \alpha^2 d_1^2 - 2\alpha d_1 \cos 2\pi \underline{g}.\underline{r}) \qquad (7.4.28)$$

$$\psi_1\psi_1^* = \frac{1}{(d_1-d_2)^2}\left(d_2^2 + \frac{1}{\alpha^2} + \frac{2d_2}{\alpha}\cos 2\pi \underline{g}.\underline{r}\right) \qquad (7.4.29)$$

Similarly for the j = 2 wave,

$$\psi_2\psi_2^* = \frac{1}{(d_1-d_2)^2}\left(d^2 + \frac{1}{\alpha^2} + \frac{2d_1}{\alpha}\cos 2\pi \underline{g}.\underline{r}\right) \qquad (7.4.30)$$

From (7.4.17) it can be seen that $\underline{d}_1$ must always be + ve and $\underline{d}_2$ always be - ve in the region around $\vartheta = \vartheta_B$ (ϑ_B = Bragg angle = $\sin^{-1} g/2K$). Thus, from (7.4.29)

$$\psi_1\psi_1^* = \frac{1}{(d_1-d_2)^2}\left(\left(d_2^2 + \frac{1}{\alpha^2}\right) - \left(\frac{2|d_2|}{\alpha}\cos 2\pi \underline{g}.\underline{r}\right)\right) \qquad (7.4.31)$$

$$\psi_2\psi_2^* = \frac{1}{(d_1-d_2)^2}\left(\left(d^2 + \frac{1}{\alpha^2}\right) + \left(\frac{2|d_1|}{\alpha}\cos 2\pi \underline{g}.\underline{r}\right)\right) \qquad (7.4.32)$$

The probability $\psi_1\psi_1^*$ has a constant term $(d_2^2 + 1/\alpha^2)$ and a periodic term $\frac{-2|d_2|}{\alpha}\cos 2\pi \underline{g}.\underline{r}$. The period of the oscillating term is 1/g and it has maxima in the interstitial region between atom planes. $\psi_2\psi_2^*$ has a similar uniform term $(d_1^2 + 1/\alpha^2)$ and a periodic term $\frac{2|d_1|}{\alpha}\cos 2\pi \underline{g}.\underline{r}$. The latter term has a period 1/g and is peaked on the atom planes. (Fig. 7.12). In the following discussion this wave (j = 2) will be referred to as type 2 and the wave with maximum probability in the interstitial regions (j = 1) as type 1.

The change of distribution with angle

The distribution of electrons within the crystal depends not only on the wave

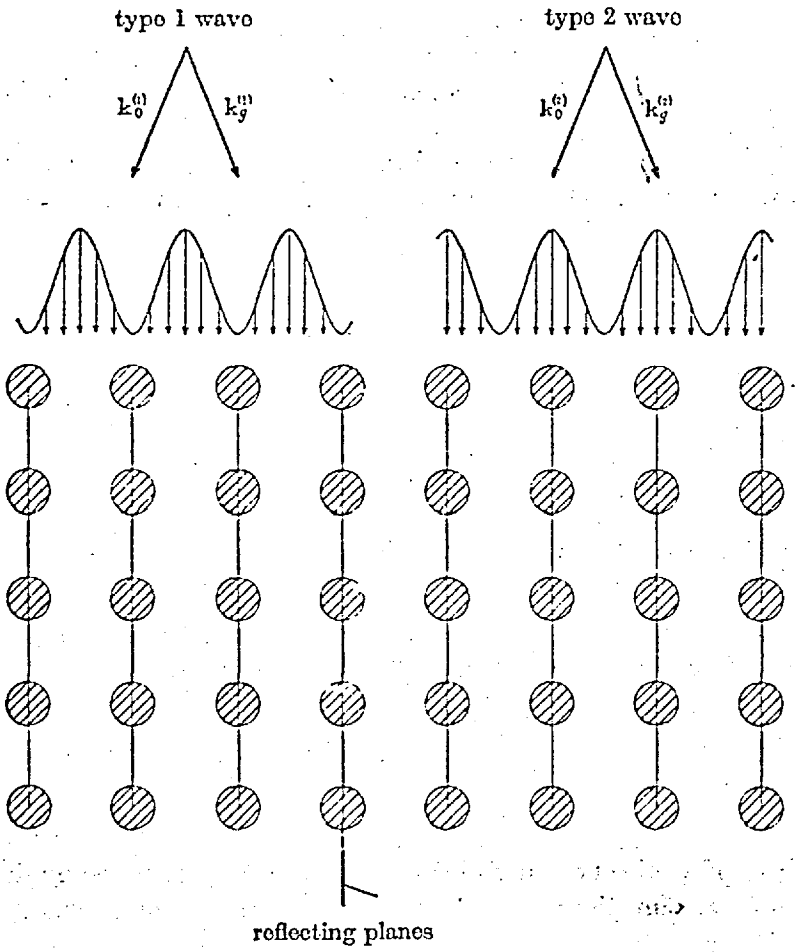

FIGURE 2. Schematic diagram of the two types of crystal wave field at the reflecting position in a simple cubic lattice. The current flow vector is parallel to the reflecting planes. Absorbing regions at atoms are shaded. The type 2 wave is absorbed more than the type 1 wave.

Fig.7.12 Relative positions of type 1 and type 2 waves within the crystal, from Hashimoto et al (1962).

The initial electron beam outside the crystal

On entering the crystal at least two sets of beams are formed.

The beams are scattered, type 2 more strongly than type I.

With increasing depth type I intensity becomes equal to type 2. Type 2 begin to be further scattered.

The type 2 wave is eventually removed by further scattering, leaving only the type I beam.

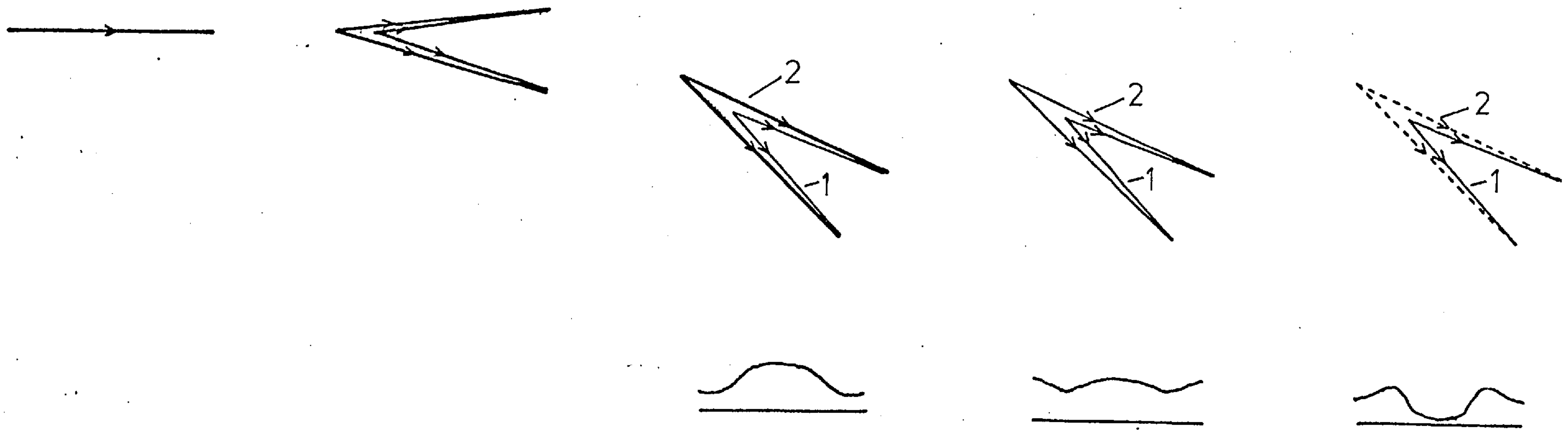

The band formed is 'anomalous'.

The band is reduced in contrast.

The band assumes the 'normal' form.

Fig. 7.13 Stages in the formation of Kikuchi bands.

type (j = 1 or j = 2) but on the angle of incidence, ϑ , of the beam relative to the surface normal of the crystal.

The total average intensity of the electrons at $\underline{r} = 0$ is given by

$$(\psi_1\psi_1^* + \psi_2\psi_2^*)_{\underline{r}=0} = \frac{1}{d_1-d_2}\left((d_1^2 + d_2^2) + \frac{2(d_1+d_2)}{\alpha} + \frac{2}{\alpha^2}\right) \qquad (7.4.33)$$

Kikuchi bands

The difference of the electron distribution between the two Bloch waves, ψ_1 and ψ_2 has been used by Hirsch et al (1965) to explain the occurrence of "normal" Kikuchi bands. (This band has more electrons on the edges than at the centre (Fig. 7.13d)).

Hirsch et al argue that the main agency for high angle scattering of electrons of energy > 1 keV is Rutherford scattering. (Simple Coulombic scattering described in Chapter 6). The cross section for this scattering is highly localized around the nuclear sites. Thus the Bloch wave with a high probability distribution around the nucleus will be preferentially scattered out of the original Bloch wave system. This results in the eventual complete loss of one Bloch wave, leaving the other relatively strong. One immediate consequence of this is the fading out of thickness fringes produced by the "pendulum" (pendellosung) effect of the interference of the two original, phase linked, Bloch waves (Hirsch et al, 1965). A similar effect has been observed by Borrmann (1941, 1950, 1955a and b) for x rays, and by Duncumb (1962) for the production of X-rays by electrons in a single crystal.

Hirsch et al show that if a Bloch wave is incident on a crystal slab it will be more likely to be heavily scattered if its principal wave vector $\underline{k}_{oj}$ makes an angle less than ϑ_B with diffracting planes than if this angle is greater than ϑ_B .

The wave transmitted through the slab is thus more attenuated if it lies between the two Bragg angles and the normal form of the Kikuchi band results (Fig. 7.13d).

Anomalous Kikuchi bands

The normal form of the Kikuchi band is found for electrons passing through thick (greater than two electron mean free paths) crystals. The anomalaus form of the Kikuchi band is found when thinner crystals are used (Fig. 7.13a).

The anomalous band has a greater number of electrons at its centre than at the edge of the band (Fig. 7.13a) and cannot be explained by the simple argument of Hirsch et al.

Hall (1970) uses thermal scattering and core electron scattering to trace the progress of electrons through successive crystal slabs. He was able to predict the formation of the anomalous bands from this when a thin crystal was used, progressing to the normal form as the thickness was increased (Fig. 7.13a - d).

In his work Hall used the assumption, first made by Hashimoto, Howie and Whelan (1962) that the symmetry of a (type 2) wave will be preserved (i.e. it will remain as a type 2 wave) when it is strongly scattered by thermal (Rutherford) scattering. This is a reasonable assumption based on the premise that the laws of reciprocity apply to these forms of scattering. If this is true, the scattered wave must exist at the point at which the incident wave is scattered. This happens near the core (either for core or thermal scattering) and it is considerably more probable that an electron existing near the core is of type 2 rather than type 1. Thus, the wave scattered from a type 2 wave is very likely to be of type 2.

This argument predicts that at small angles of scatter, whether due to plasmon or thermal means, the wave symmetry will not be preserved because the cross sections for both these small angle processes encompass a large proportion of the interstitial region. In this region the existence of a type 1 wave is slightly more probable, but as the cross sections extend considerably on either side of the centre of the region the scattering of a type 1 wave is almost as likely to produce a type 2 wave as a type 1. This argument applies equally to the scattering of type 2 waves through small angles.

The production of an anomalous band can thus be predicted without further calculation.

Qualitative prediction of anomalous bands

If a crystal direction is considered which is near the Bragg angle for a particular set of planes, but widely separated from the initial beam direction (Fig. 7.14).

The initial beam sets up a pair of Bloch waves $\psi = \psi_1 + \psi_2$

$$\psi = \sum_{j=1,2} \sum_{g} \psi_{jg} \exp 2\pi i ((\underline{k}_0 + \underline{g}) \cdot \underline{r}) \tag{7.4.34}$$

and is scattered into a second pair of Bloch waves $\Phi = \Phi_1 + \Phi_2$

$$\Phi = \sum_{j=1,2} \sum_{g} \Phi_{jg} \exp 2\pi i ((\underline{k}_0 + \underline{g}) \cdot \underline{r}) \tag{7.4.35}$$

(Fig. 7.14)

Initially the scattered wave will be produced by electrons which have been scattered once through a high angle. These waves will be of type 2 and will result from a type 2 wave.

The type 2 scattered wave will most probably lie in the region $\vartheta \leqslant \vartheta_B$ where $\vartheta_B = \sin^{-1} h/2K$ (Fig. 7.14) as this is the region where type 2 waves exist strongly. This means that, as long as the crystal remains thin, the scattered waves will lie in the region between the two Bragg positions and an anomalous

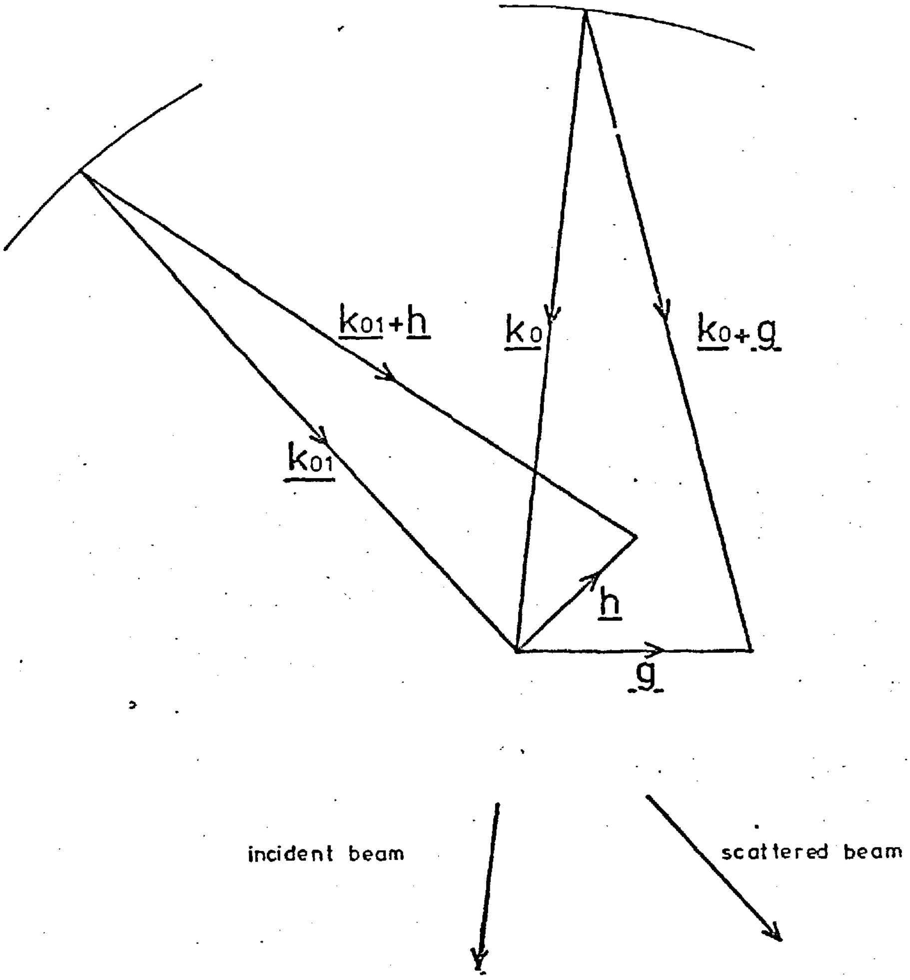

Fig.7.14 Independence of incident and Rutherford scattered beams.

band will result.

If the crystal is thickened, multiple scattering and a drop in the intensity of the incident beam with thickness will result in almost equal intensities of type 1 and type 2 waves at some thickness. After this the arguments of Hirsch et al apply and a normal Kikuchi pattern results (Fig. 7.13.d).

Kainuma (1953) was the first to complete a quantum mechanical treatment of the scattering of an electron wave into a Bloch wave. His work, based on core electron scattering of a plane electron wave into a two beam Bloch wave, predicted the type of effect described above. This detailed treatment was the first to predict Kikuchi bands with the correct contrast, but, because it did not go on to further scatter the resulting Bloch wave, only predicted the formation of the anomalous form of the Kikuchi band. Kainuma (1955) pointed out the effect of anomalous absorption of one of the waves in the production of normal (defect) bands, but no systematic link between his two ideas was made until Hall's (1970) treatment of it.

Hall (1970) could not treat the successive scattering of each Bloch wave rigorously. To predict the formation of a normal Kikuchi band would require the following stages :-

1) Scatter of incoming beam into all angles of interest.
2) Further scatter of each scattered beam out of the angles of interest.
3) Energy loss at each stage
4) Rescattering back into the beam of interest of electrons from other parts of the pattern.

In fact, Hall assumed that the incident beam was a two component Bloch wave set at the Bragg angle and then used the methods of Whelan (1965a) and Hall (1966) to describe the thermal scattering of one Bloch wave into another. He describes the decay of the scattered Bloch wave by use of the crystal absorption coefficients given by (e.g. Hashimoto et al, 1962)

$$\mu_g^i = \pi \left(\frac{1}{\varepsilon_0'} + \frac{(-1)^i}{\varepsilon_g' (1 + x^2)^{1/2}} \right)$$

where x is a parameter which describes the deviation from the Bragg position, ε_0' is the absorption distance for the averaged scattering potential and ε_g' is the absorption distance for the anomalous scattering potential. The values ε_0' and ε_g' are found experimentally (Hirsch et al, 1965) by reference to the intensities of thickness fringes of wedge shaped crystals.

In his method Hall ignores both the energy loss of the electrons and the rescattering of electrons into the Kikuchi band from directions other than the main beam. Hall's results predict both excess bands from thin crystals and defect bands from thick crystals, but the changeover from one to the other is found to happen more slowly with increasing thickness (Uyeda and Nonoyama, 1968) than is predicted by Hall's calculation. This is due to the non-inclusion of rescattering. If this were to be included, the excess band would be preserved at a greater crystal thickness (or scattering angle) because of the steady transfer of intensity into the type 2 wave from other crystal directions. Similarly, electrons from the band must go into other bands and will continue to preserve the anomalous form.

Hall's lack of consideration of energy changes is quite justified in the light of his use of a two beam model. The band shape he predicts certainly does not represent a true description of the band shape and thus the addition of a complex calculation in order to modify the shape only slightly is not justified (cf. Chapter 8).

Summary

The arguments used in this chapter have been far from rigorous, but serve to point the main lines of Kikuchi band formation.

Fig. 7.13 serves to summarise the main stages in band formation. The changes may be made to occur in three ways :

1) Increased crystal thickness
2) Increased angle of scatter considered
3) Reducing the beam energy

The main point of the dynamical theory is that there is a difference between the probability distribution of the electrons in different Bloch waves, and hence in the interactions of these waves with the crystal. The Bloch waves are independent solutions of the Schrodinger equation and thus, apart from the phase linkage at the boundary or at a scattering site, they are unrelated to each other.

No adequate treatment of the changeover between excess and defect bands has been made. This could not be done accurately as it would involve modelling of the whole crystal. The simplest way to overcome this would be to modify the crystal scattering potential U_g to include an imaginary part (cf. Hirsch et al, 1965), as this would represent a net reduction in the scattering, consistent with experimental observations. Short of making this a "fudge" factor, however, there seems no way of making a suitable estimate of the value that should be used.

There has been no theoretical consideration of the effect on band width of the change in energy of the electrons, although Alam (1952) observed that, despite a large change in energy, 50% reduction for light materials, no great change in the band width of the principal bands could be observed. This is considered in Chapter 8.

CHAPTER 8

KIKUCHI BAND WIDTH

In Chapter 7 the mechanism for the production of Kikuchi bands and lines from monochromatic electrons was described. This type of pattern might be expected in RHEED patterns from single crystals at low angles of scatter, from LEED patterns at all angles of scatter and in transmission experiments. In each case the proportion of electrons which have lost a small amount of energy is large compared to the background and any diffraction of these electrons results in a pattern strong compared to the background.

Alam (1952) and later Venables et al (1973) found that Kikuchi patterns were also visible at high angles of scatter in RHEED for almost all materials investigated, including those of low atomic weight. Alam found that the light materials, e.g. LiF (Fig. 8.1 a) only showed bands corresponding to the principal crystal axes, whereas a heavy material such as PbO (Fig. 8.1 b) produced spectacular and much more detailed band patterns similar to the channelling patterns later observed by Coates (1967).

The fact that a pattern was visible even for heavier materials was a surprise to Alam et al (1954) as they had assumed the diffraction patterns to be produced by electrons that had lost little or no energy in transit through the crystal. Such electrons form only a small part of those backscattered from heavy materials and are almost undetectable in the spectrum from light materials.

The assumption that elastic or low loss electrons produced the Kikuchi patterns was borne out by Alam's measurement of the width of the bands at various angles of scatter. Within experimental error he could detect no broadening of the band with angle, the width at all angles corresponding to that predicted for elastically scattered

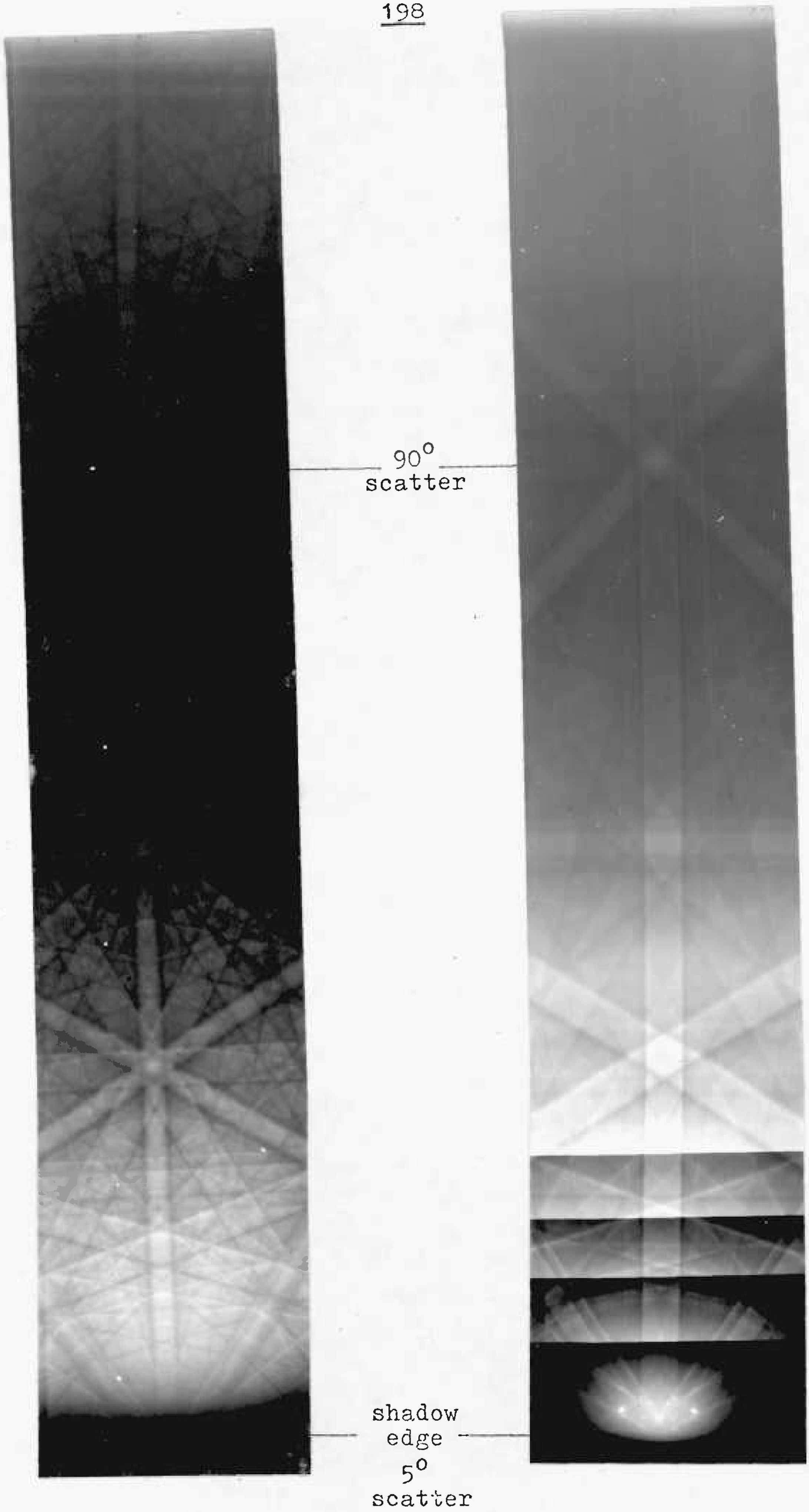

PbS LiF

Fig.8.1 High angle Kikuchi patterns taken at 30keV from the negatives recorded by Alam, 1952.

electrons.

The main points needing explanation were thus the formation of bands at high angle of scatter and their constant width, despite the strong dependence of the energy spectrum of the backscattered electrons with angle of Darlington (1971)

8.1 Kikuchi band production

In Chapter 7 the formation of a Kikuchi band was predicted on the basis of the two beam theory. This assumed an incident cone of monochromatic, though incoherent, electrons, was scattered by the crystal. The formation of this cone was not discussed except that it resulted from elastic scattering of the incident beam in a layer of material above the diffracting region (cf. Boersch, 1937). In practice, such scattering will produce a cone of electrons with a wide range of energies. However, because no phase linkage is required, this may be regarded as an infinite set of superimposed cones of monochromatic electrons. The observed diffraction pattern will be the sum of the intensities of the diffraction patterns produced by each cone separately.

The immediate reaction to this statement is that a pattern produced by a wide spectrum of electron energies will sum to an almost uniform level at all points. However, comparison with light optics shows that this need not be true if the diffraction conditions are suitably chosen.

In a Young's double slit experiment light from a narrow slit,S,is split by two slits A and B, and allowed to recombine on a screen to produce a diffraction pattern, Fig.8.2. The light passing through S may be monochromatic but need not be coherent, however an extensive diffraction pattern always results. The extent of the pattern can be reduced in two ways, either by increasing the size of the slit, S,or by using light with a range of frequencies. Fringes can still be observed using white light. The reason for this is clear when one considers the resulting diffraction patterns separately.

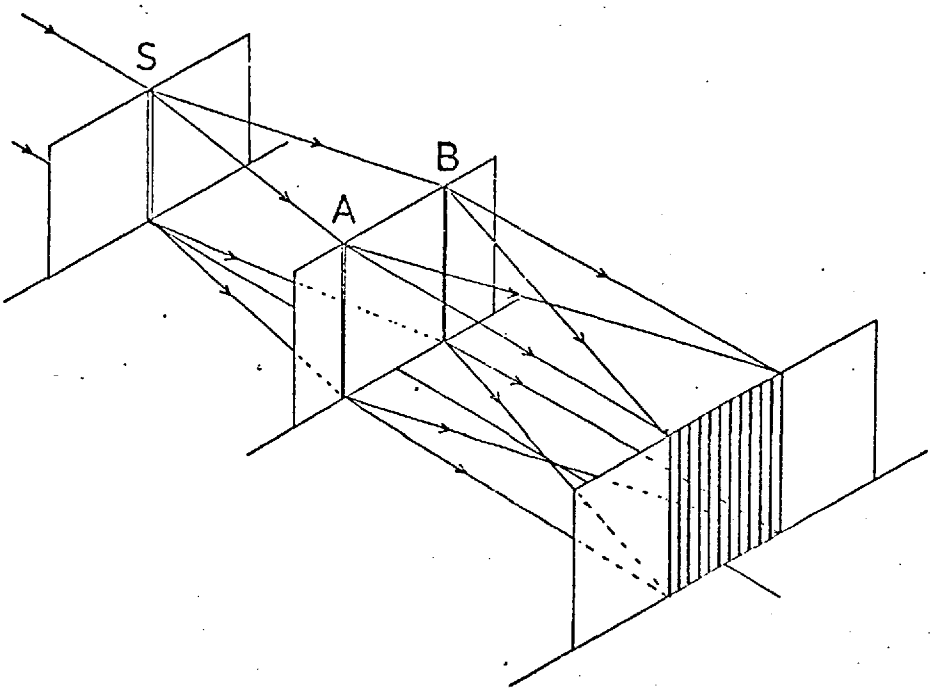

Fig.8.2 Youngs double slits

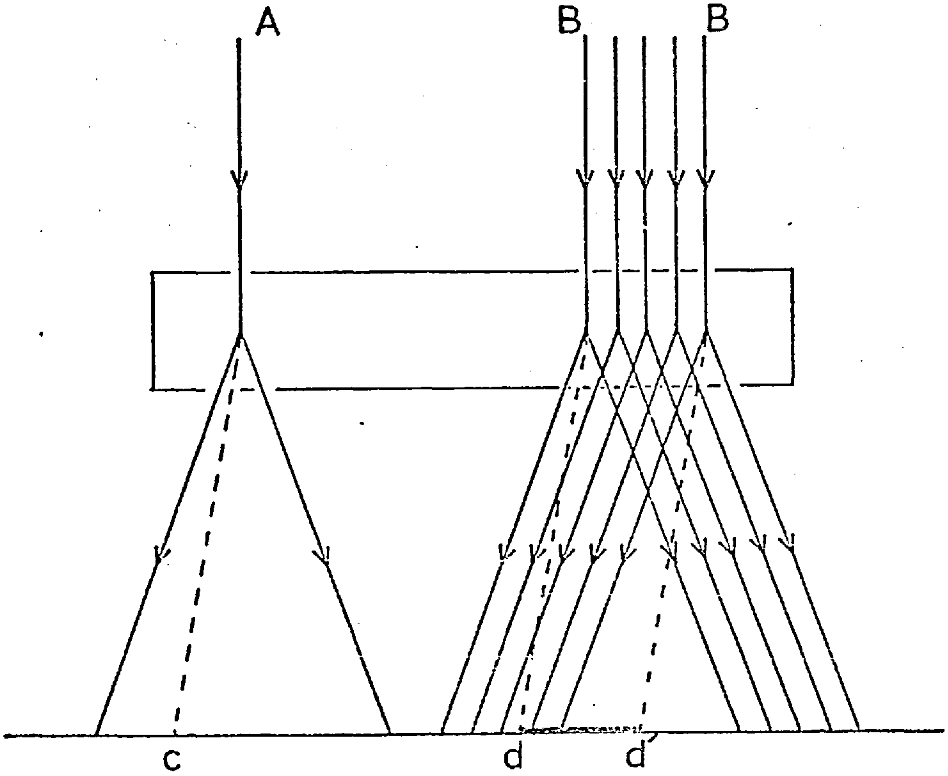

Fig.8.3 Spreading of Kikuchi band pattern because of finite beam size.

The patterns for all wavelengths have a maximum of intensity along the perpendicular bisector of AB (assuming AS = BS) but the distance of subsidiary maxima from this line depends on the frequency of the light. Thus the central maximum will always be visible, though the number of fringes on each side must depend on the frequency bandwidth of the light used. The pattern depends also on the slit width S, in that if the angle subtended by S at A (or B) is greater than the angle subtended at the central maximum, then the central maximum produced by light from one edge of the slit will overlap the first minimum produced by light from the other edge, and result in a reduction in the contrast of the pattern.

8.2 Comparison with Kikuchi band formation

The comparison of Kikuchi band formation with a white light Young's slit experiment yields two points of strong similarity. The first is that the position of the major feature of the diffraction pattern is independent of wavelength. In a Young's slit this is the maximum which lies along the perpendicular bisector of the slits; in Kikuchi bands it is the maximum or minimum of intensity lying between the two first Bragg angles for any given plane. The second feature is the size of the illuminating region. In the case of Young's slits this is the primary slit S and for Kikuchi bands it is the size of the region from which electrons effectively emerge, which depends on the beam width (Fig. 8.3).

It is obvious that in both cases the width of the central maximum (or minimum) depends on the wavelength or energy of the waves, thus the shape of the final pattern must depend on the exact energy spread. One other point that emerges from this comparison is that the extent and detail of the diffraction pattern in either case must again depend on the energy spread. In the Young's slit case the ideal pattern will be obtained using monochromatic light and will reduce to a few fringes as the band width of the light is increased. Similarly with Kikuchi bands, the diffraction pattern is sharpest and contains most detail when produced by nearly monochromatic electrons. As the energy spectrum is broadened, the detail in the pattern is reduced until only the bands associated with the principal crystal axes are visible. This explains the major difference between the high angle Kikuchi patterns produced by PbO and LiF (Fig. 8.1 a and b) as the PbO pattern is produced by much narrower energy bands than those which form the LiF Kikuchi patterns. This results from the strong dependence of the backscattered electron energy spectrum on atomic number (cf. Chapter 6).

8.3 Kikuchi band width

It is now left to consider why the width of the Kikuchi bands produced in the backscattered direction remains almost constant with angle, (Alam, 1952), despite the strong dependence of the spectrum on the scattering angle.

The method adopted was to sum the intensities of a series of Kikuchi patterns corresponding to different energies calculated on the basis of an elastic band shape and scaled to account for spectral intensity and energy of the electrons used. The basic analytic function was chosen to represent the band shape produced by monochromatic electrons. For each energy the width of the pattern was scaled to correspond to the width predicted by eqn. 7.1 , and in height to correspond with the known intensity at that angle. Lastly, the height was again scaled to take account of the non-linear energy response of the photographic film used by Alam to record his patterns.

8.4 The basic Kikuchi band shape

The analytic function used to model the band shape was based on the calculations of Sandstrom et al (1974). The justification for use of a channelling pattern calculation rather than a Kikuchi pattern is that simple Kikuchi calculations (Hall, 1970) do not predict the proportions of the pattern correctly, and more complex ones have recently been concerned more about excess/defect line contrast than band shape.

The main features of the function are the width of the central maximum and the position and relative intensity of the second order band. The region of interest was modelled by an empirical function, $F(x)$, where $x = 0$ corresponds to the centre of a band, and x represents the angle from the centre measured at right angles to the band (Fig. 8.4a).

The nearest fit of the function $F(x)$ to those calculated by Sandstrom et al was :

$$\begin{aligned} F(x) = \exp -0.645x^2 &+ 0.53 \exp - 2.8(x - 1.2)^2 \\ &+ 0.08 \exp - 0.32 (x - 0.65)^2 \\ &+ 0.69 \exp - 4.5 (x - 2.6)^2 \end{aligned} \tag{8.1}$$

This is a set of Gaussian curves filled to give a function with the same basic features as Sandstrom's spatial distribution. The two expressions are compared in Fig. 8.4.

8.5 Method of summation

The intensity at thirty points across the pattern was calculated for several equally spaced energies in the spectrum. The width of each pattern was governed by the value of the increments in x ($x = (n-1)y$) in equation 8.1. The maximum energy was always made to correspond to $y = 1$, and lower energy spectra were calculated by use of

$$y = \frac{E}{E_{max}}$$

where E = energy of the electrons
E_{max} = maximum energy of electrons considered

This was done because the pattern width depends on the electron wavelength which decreases inversely as the square root of energy. The width is thus expanded by making the intervals smaller between calculated points and then adding these to the

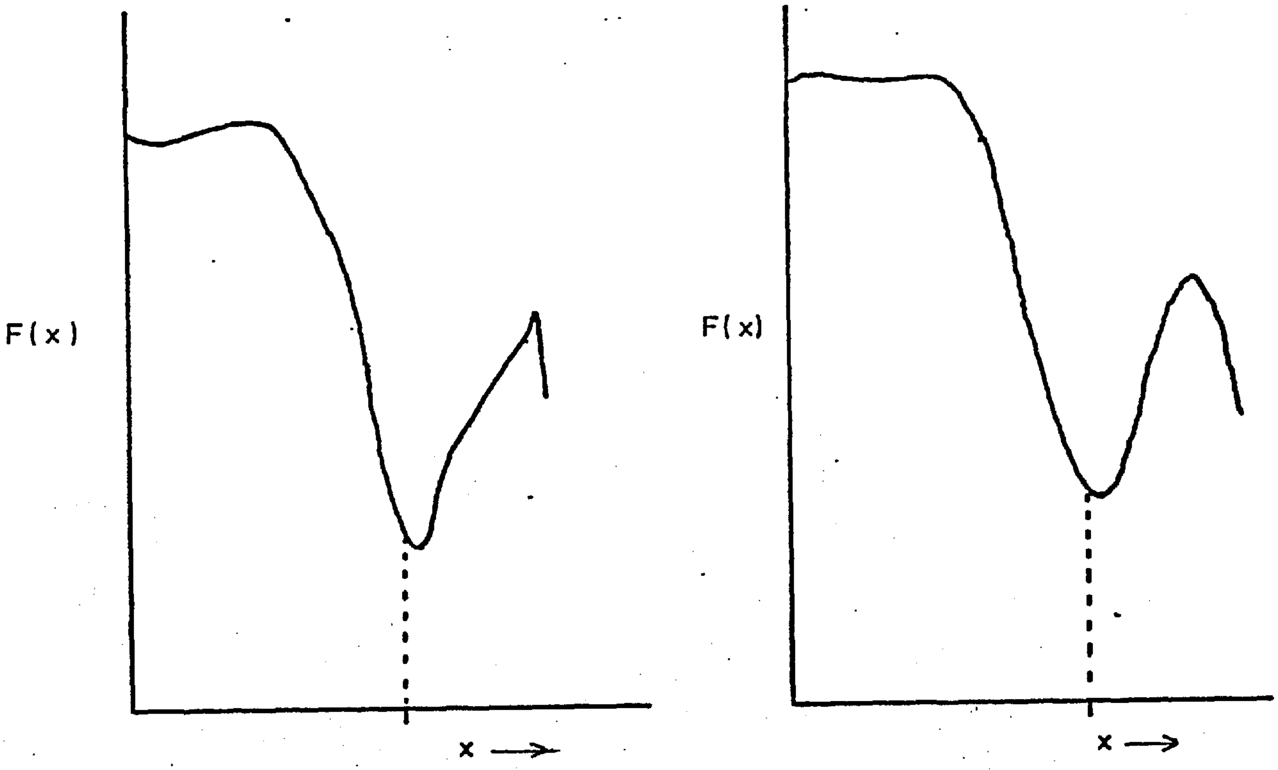

Fig.8.4

a

Band shape predicted by Sandstrom et al (1974)

b

Analytic expression, F(x), used in the calculation of Kikuchi band shape.

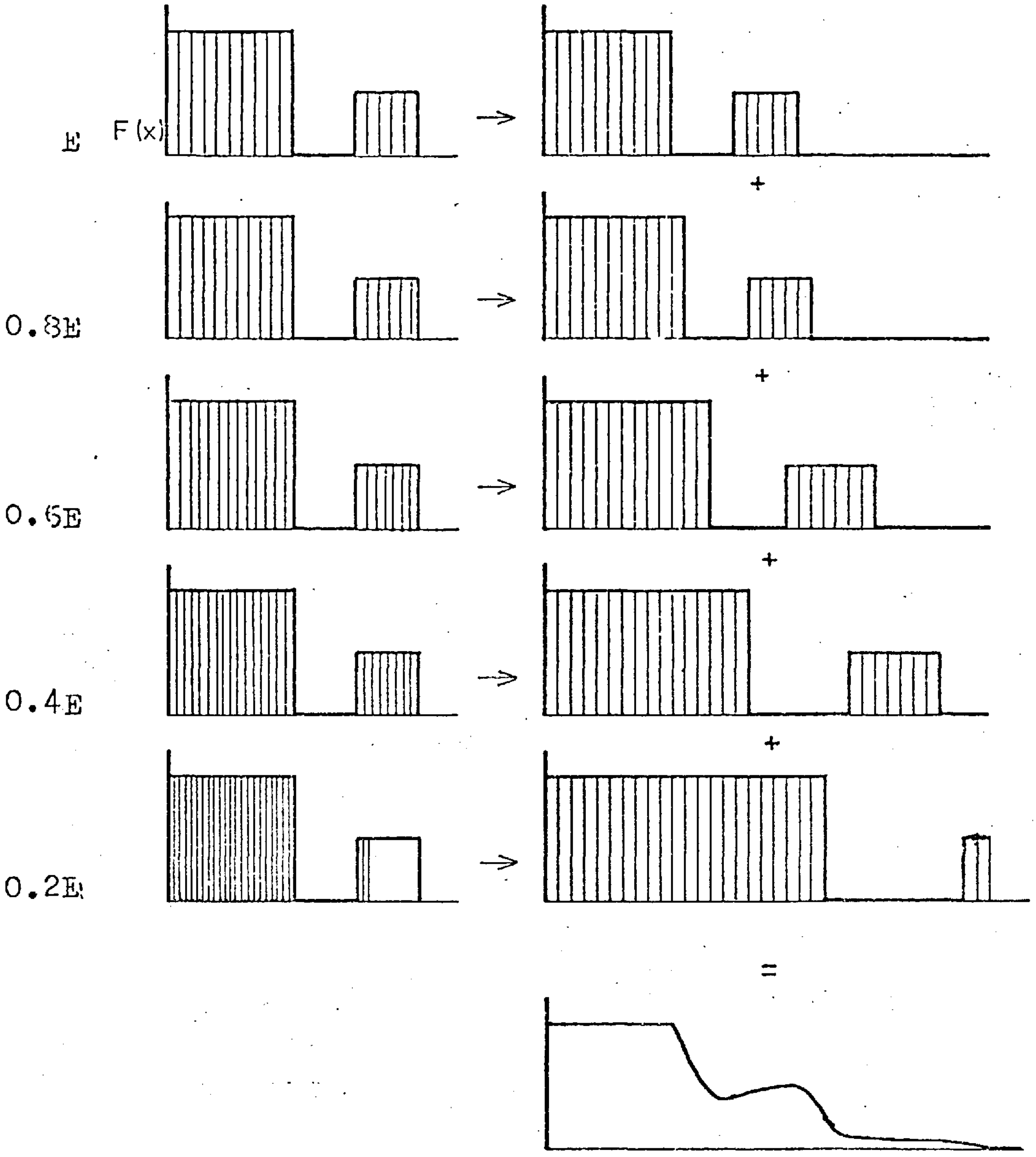

Fig.8.5 Method used to obtain the band shape produced by a wide range of energies. The width at each energy is calculated then summed and normalised to obtain the convolved band shape.

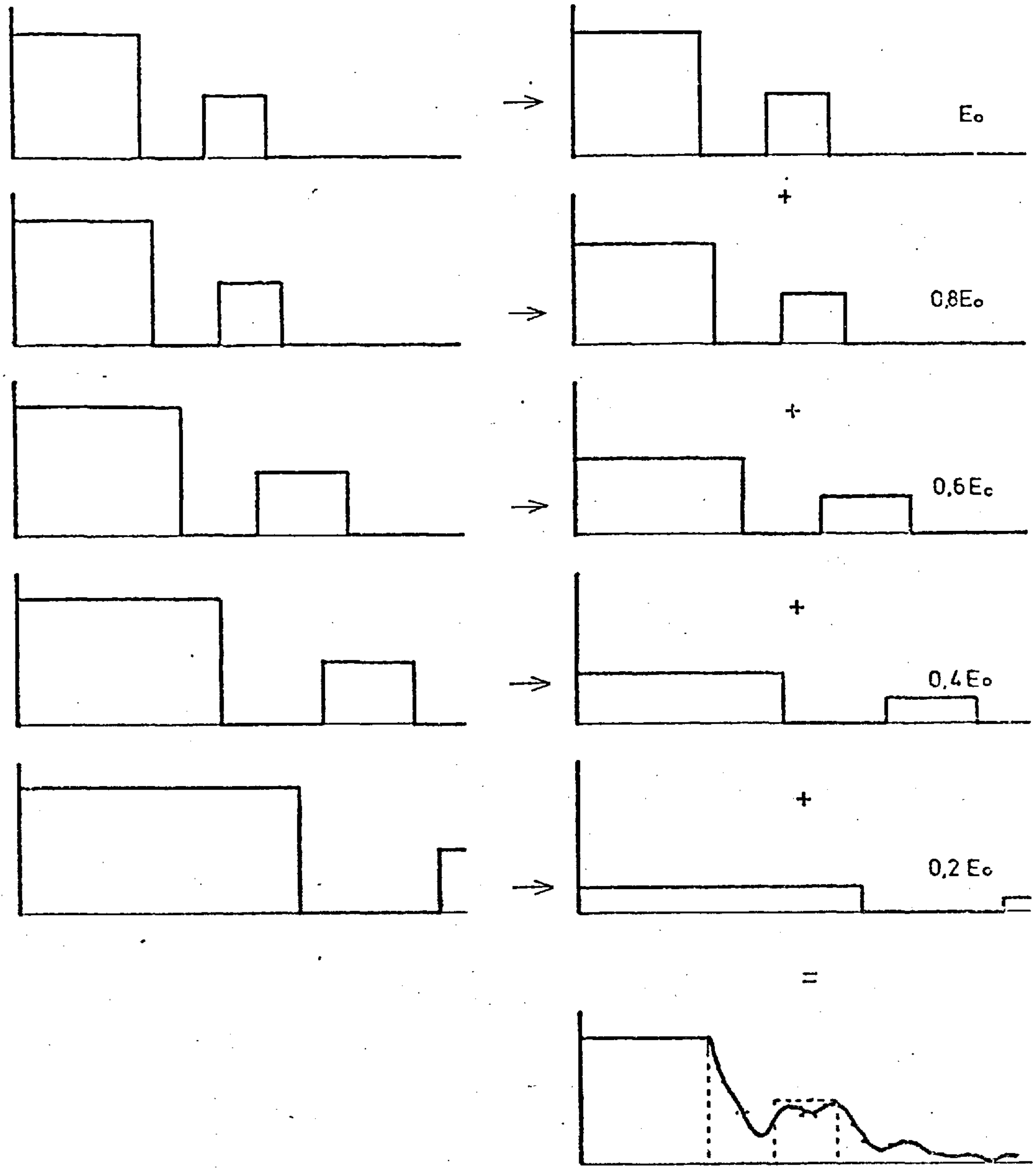

Fig.8.6 Effect of photographic response on the observed band width.

appropriate store (nos. n = 1 to n = 30). This process is shown in Fig. 8.5 for a simple rectangular function. It is interesting to note that even this crude function retains its basic shape when convolved with a uniform energy function.

8.6 Photographic response

The Kikuchi patterns observed by Alam were recorded on photographic film. It is therefore important to consider the effect on the pattern of the film's response to the electrons. Burge et al (1968) have shown that the response of a silver halide emulsion to electrons gives an intensity on the film that is proportional to the electron energy provided that the film is not saturated. In the particular case, inspection of the original negatives shows them to be, if anything, under exposed and thus it is a reasonable assumption that the response was linear with energy. The effect of this is analogous to observing white light fringes from a Young's double slit with orthochromatic film where, again, the long wavelength end of the spectrum is suppressed.

Using this assumption, the function 8.1 was adjusted by a factor E/E_{max} The effect of this can be seen by considering Fig. 8.6, in which the convolved function in Fig. 8.5 is adjusted for film response. From this it can be seen that a very detailed knowledge of the expected electron distribution is required before any information can be gained about the energy spectrum producing the final Kikuchi pattern.

8.7 Practical calculations

The flow chart for the calculations is shown in Fig. 8.7.

In order to explain Alam's observations, calculations were performed to predict the form of the Kikuchi bands for :

Carbon	at	20 keV incident beam energy
Carbon	at	30 keV incident beam energy
Aluminium	at	10 keV incident beam energy

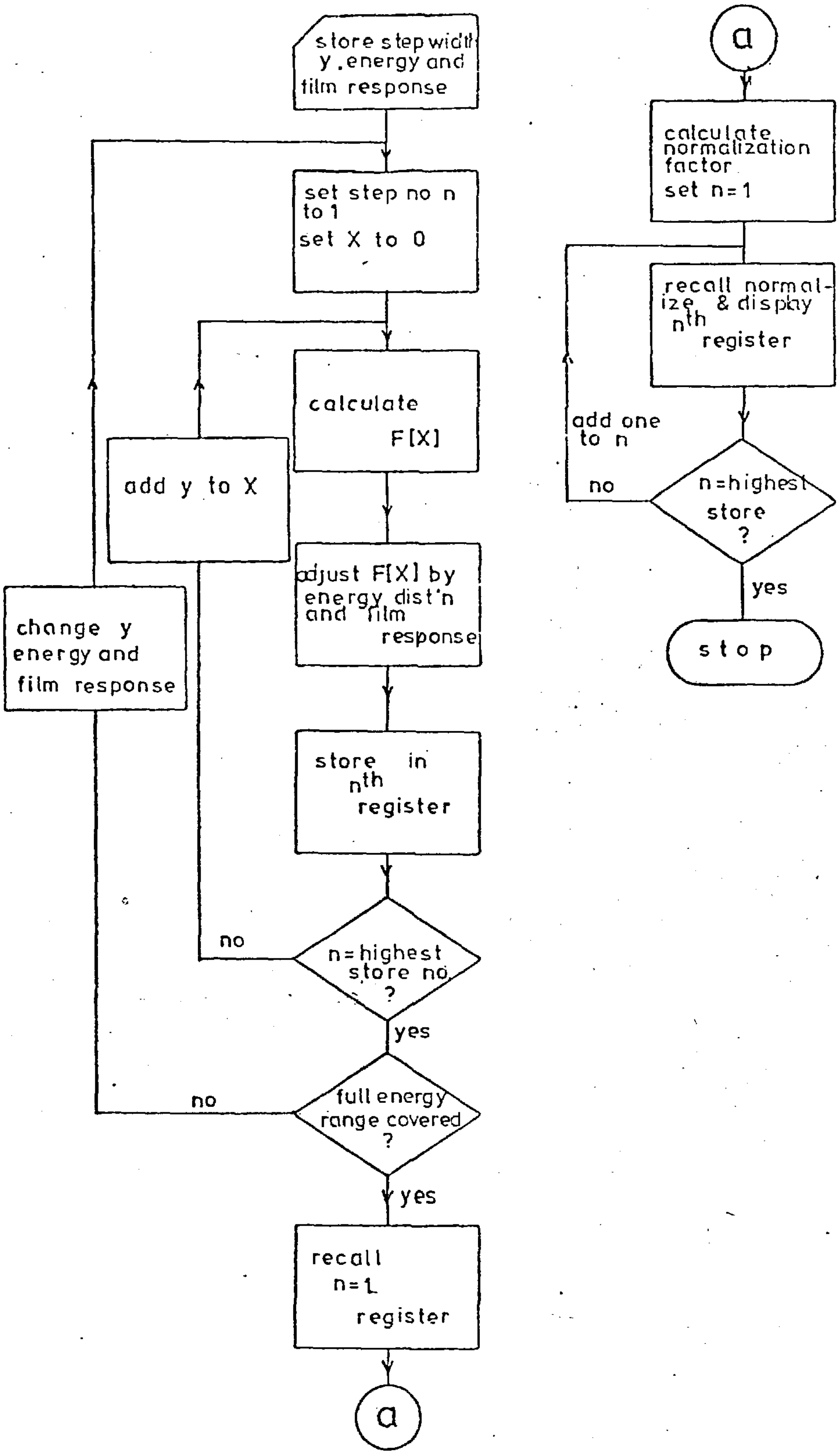

Fig.8.7 Flow chart of program to calculate Kikuchi band shapes.

Aluminium at 30 keV incident beam energy
Gold at 30 keV incident beam energy

These were calculated using the function F (x) adjusted for both backscattered probability and film response as already described. The backscattered energy distributions were [illegible] due to Darlington (1971). (These calculations were completed before the results reported in Chapter 6 were obtained. Substitution of these spectra for Darlington's in the most sensitive case, Carbon at 20 keV, made no difference to the resulting Kikuchi band shape, thus it was not felt worthwhile to recalculate the other bands).

The results of these calculations are shown in Figs. 8.8 to 8.12. For comparison the figures each show the function F (x) (pecked curve) for the primary energy normalised to the same intensity at x = 0 as the predicted photographic intensity distribution (lower solid curve). Each diagram also shows the Bragg position (solid vertical line) and the steepest point on the calculated photographic intensity distribution (pecked vertical line). The upper solid curve shows the distribution without correction for film response.

8.8 Bragg position

The exact Bragg position occurs not, as Alam assumed, at the steepest point on the Kikuchi band edge, but at a point near to the extreme edge of the band. This means that Alam measured an artificially narrow band width and Bragg separation. This error encouraged his conclusion that the Kikuchi band width corresponds to that produced by elastic electrons. It can be seen (Fig. 8.8) that the width he measured corresponded almost exactly to the Bragg width, though not to the width he would have measured had the pattern been produced entirely by elastic electrons.

Alam measured the width of bands over a range of scattering angles from 10° to 180° from the main beam direction, and concluded that the band width did not vary

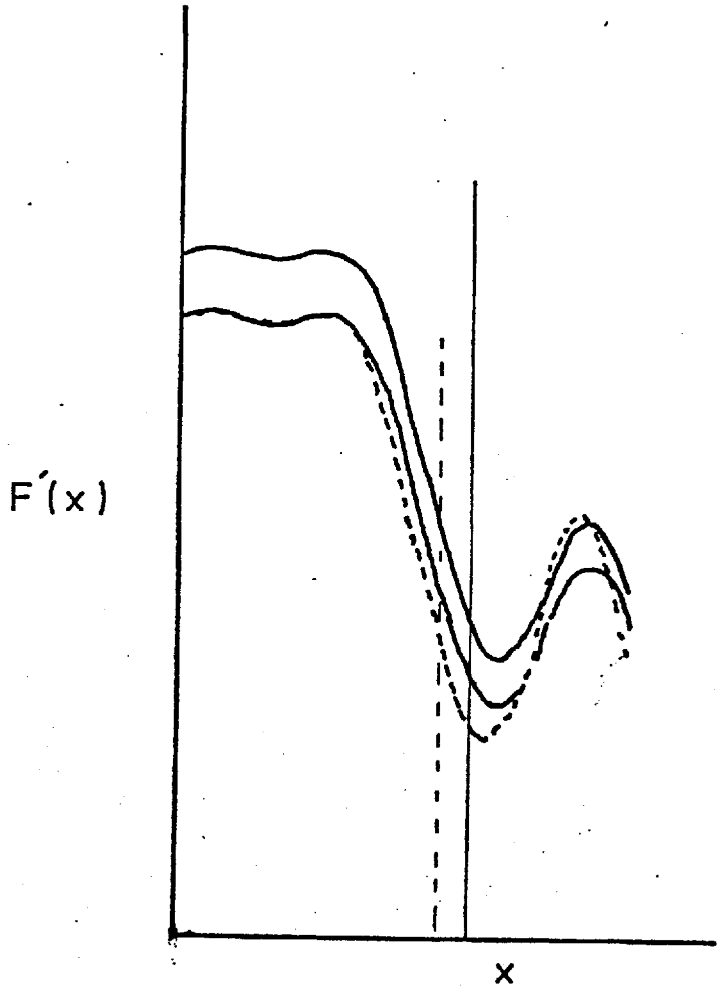

Fig.8.8 Kikuchi band shape in the backscattered direction for Gold at 30 kV primary energy.

Lower solid curve: Band shape including photographic response.
Upper solid curve: Band shape ignoring photographic response.
Pecked curve: $F(x)$
Solid vertical line : Bragg position on $F(x)$
Pecked vertical line : Steepest point on lower solid curve

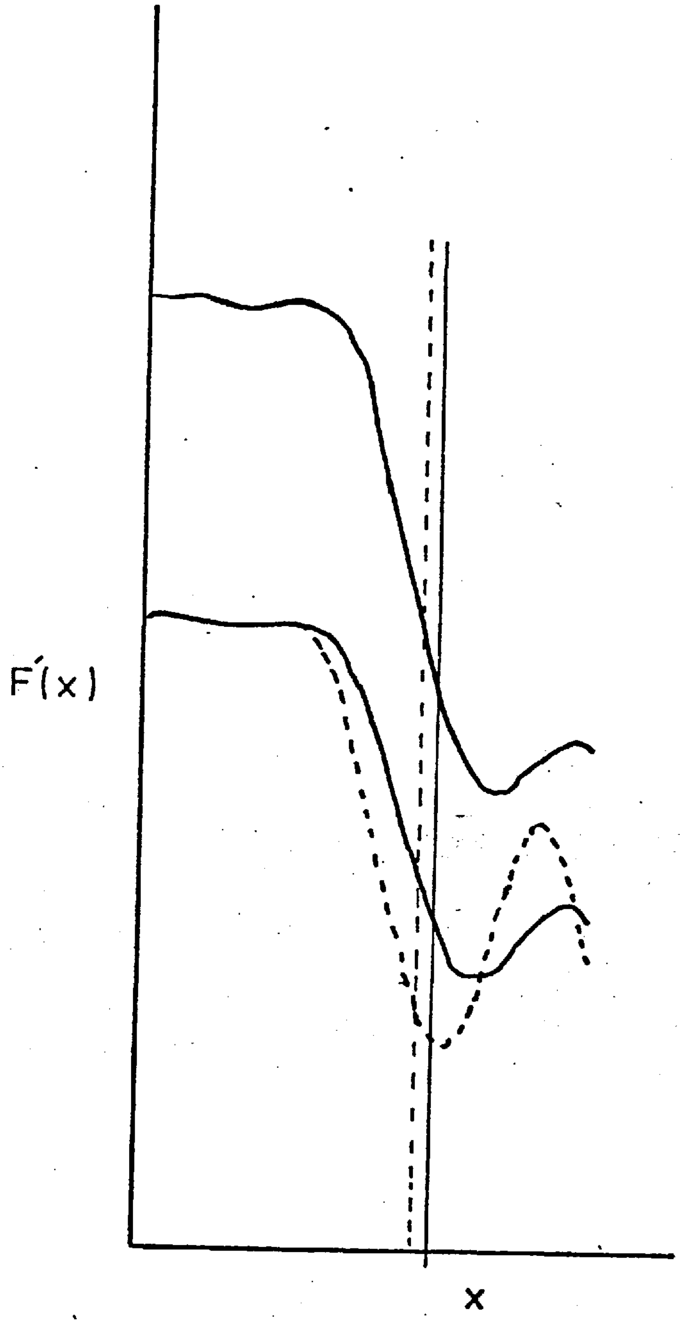

Fig.8.9 As 8.8, Aluminium at 30 keV.

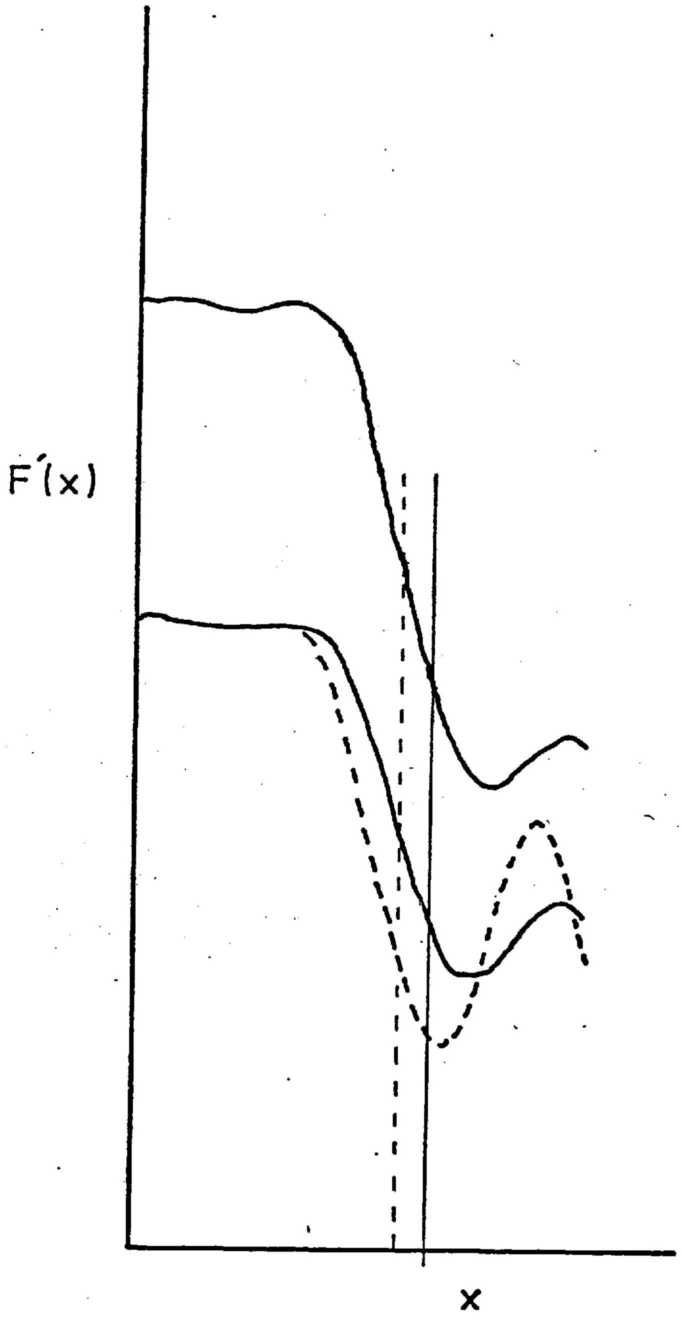

Fig.8.10 As 8.8 Aluminium at 10 keV

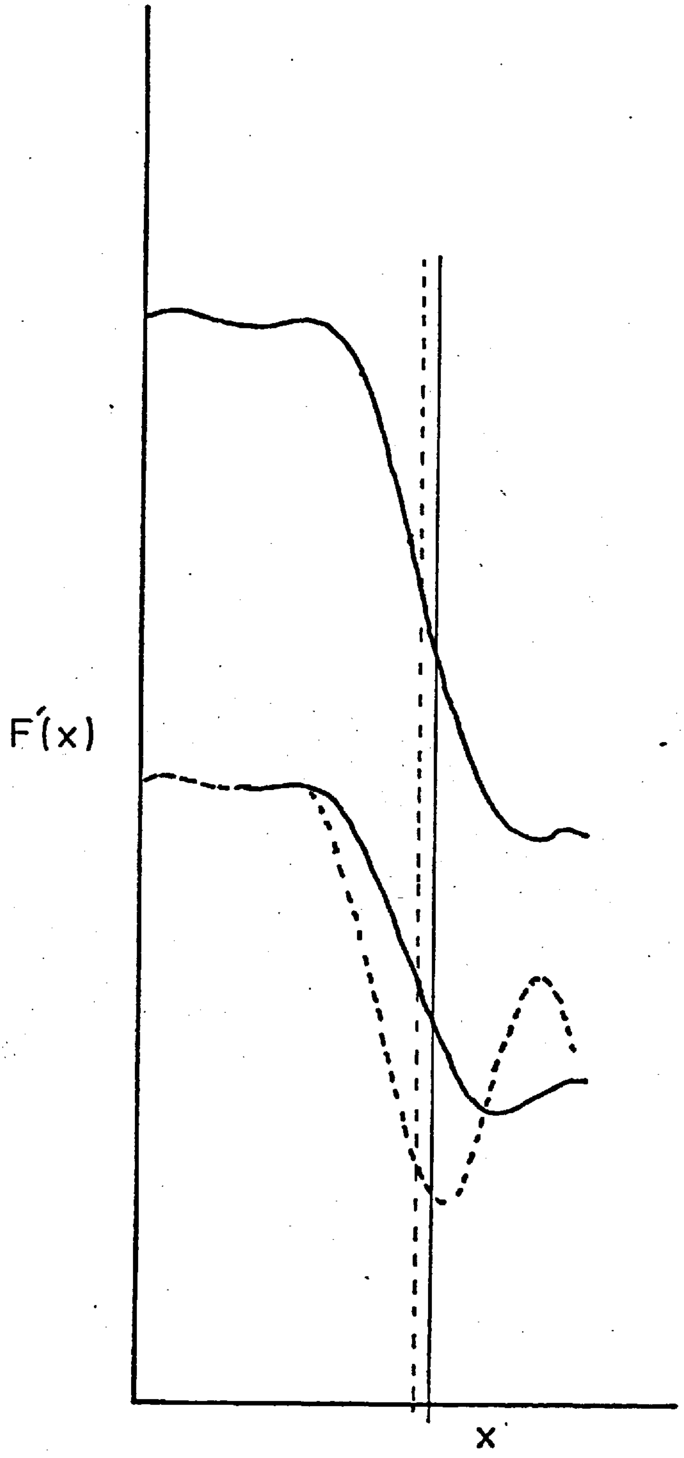

Fig.8.11 As 8.8 Carbon at 30 keV

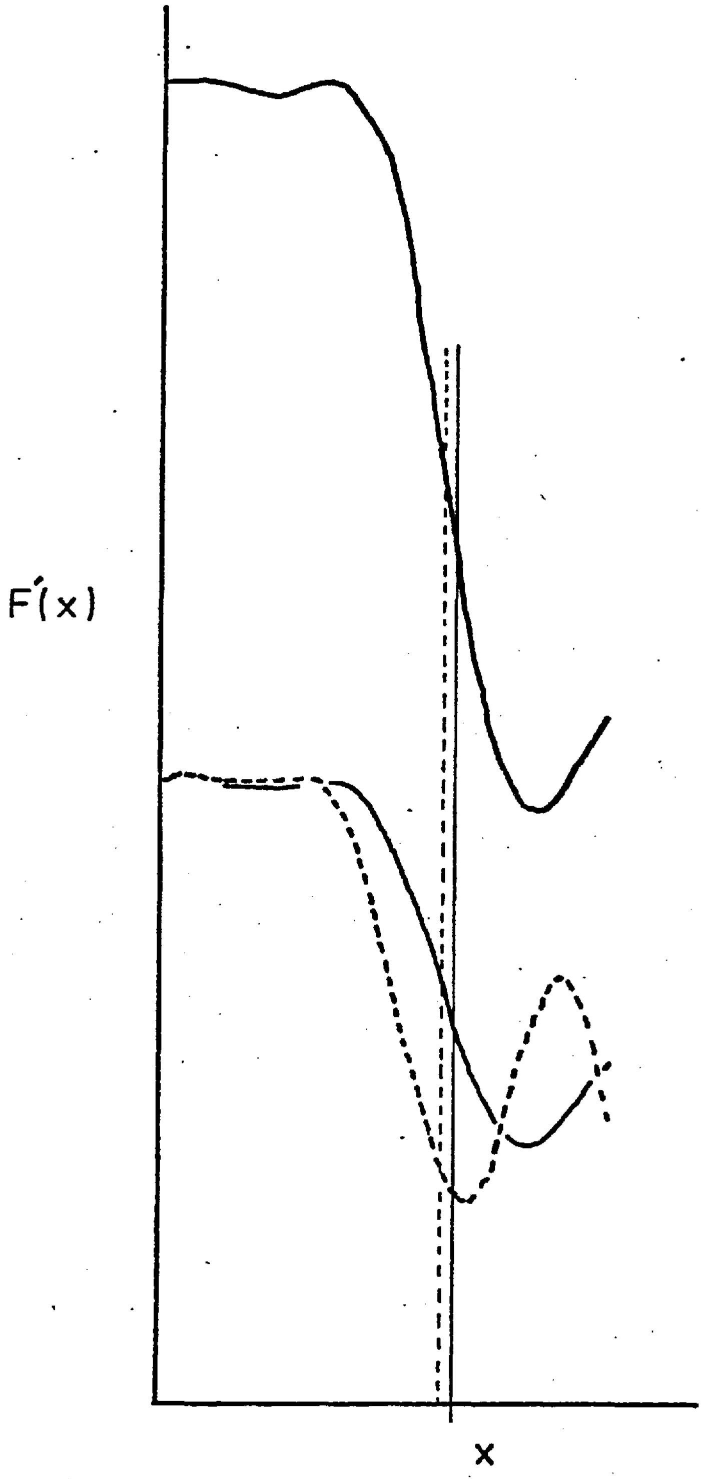

Fig.8.12 As 8.8 Carbon at 20 keV

despite strong variation in the spectra. He was, however, unable to measure band widths at angles of scatter less than 5°, and it is only in this region that the appreciable difference in the band shape might be expected to occur.

8.9 Conclusions

The curves presented show the largest possible change in shape due to energy spread and film response. They do not take into account all the effects produced by the finite energy spectrum, and in particular they ignore the change from excess to defect type band that might be expected as the energy of the scattered electrons is reduced. This effect would, however, tend to sharpen up the bands rather than make them more diffuse.

The curves predict a widening as compared with the elastic band, measured at the steepest point. Only for carbon does this amount to greater than 2%, and even for carbon it is under 10%.

The intensity of the centre of the band relative to the edge is reduced by the convolution of energies; however, there is no theory that can predict the contrast of a perfectly elastic band, so without detailed experimental evidence no relevant information can be gained from this.

These results show that the appearance of bands corresponding to the principal crystal directions is not contrary to expectations, and that it does not indicate a scattered spectrum strongly peaked in the high energy region.

Although not specifically considered here, Fig. 8.8 and 8.12 indicate that in light materials the high order bands will be washed out by overlap of individual patterns, whereas heavy materials will show several high order bands. This is consistent with Alam's observations.

CHAPTER 9

CONCLUSIONS

The main body of this thesis has been concerned with a critical account of the building of an electron spectrometer for high resolution work.

Spectrometer choice

The work has shown that the simple retarding field spectrometer is suitable for high resolution work on the no loss region of the spectrum. There are clearly considerable problems, in particular the noise produced by the ionization of the residual gas and the field emission near the retarding electrode. This type of analyser offers the simplest method of construction, though its range is limited and design parameters, particularly of the electrode, are a matter for trial and error.

Electron focusing

The main shortcoming of the analyser is the necessity for the entrance aperture to be small to maintain the collimation of the electrons as they enter the region of high electrostatic field. There is considerable scope for design of what is effectively a two tube lens, so that the parallelism of the beam can be maintained. This would allow the number of electrons entering the chamber to be increased, thus reducing either noise or recording time.

Recording

There is considerable scope for improvement in the detection of electrons. It was not possible to produce good light coupling between the phosphor and the photomultiplier. If this could be improved the collection efficiency could be up to 70% from an estimated 45%. Replacement of the P11 phosphor by a P47 phosphor would make detection easier, as would replacement of the photomultiplier with one with higher gain.

It would be tempting to replace the photomultiplier/phosphor combination with one of the many forms of electron multiplier. However, this would, without very careful design of the analyser, place the external electronics at risk from the almost inevitable discharges from the analyser. Therefore, the optically coupled system is probably superior and should be adhered to.

Experimental work

The main experimental work in this thesis has been to confirm the basic shape of the energy distribution of electrons backscattered from a range of surfaces. This has followed the pattern of previous work (Darlington, 1971) and produced similar results. The region of the backscattered spectrum which still deserves investigation is the quasi elastic peak. The proportion of electrons elastically scattered by Pb, Au and Ag (Chapter 6) were much larger than might be expected, and though a simple analysis does indicate that an elastic peak might be expected, it is not fully explained.

An investigation which should prove productive would be to adapt a high resolution analyser to work in U.H.V. and to use it to investigate the spectrum of electrons at one angle of scatter from a range of clean metal surfaces prepared in situ in the vacuum chamber. Such an investigation could well be extended to crystalline surfaces where it is almost certain that the spectrum would depend on the angles of incidence and collection relative to the specimen.

Calculations

In tandem with the above investigation a theoretical model of elastic scattering based on a Monte Carlo approach should be constructed, as outlined in Chapter 1. This should consider only elastic (quasi elastic) scattering and thus reduce calculation difficulties.

Kikuchi bands

The mechanism for the formation of Kikuchi bands has been simply explained

(Chapters 7 and 8) and until a far greater understanding of the scattered electron spectrum is obtained, little detail can be added to this model. The exception to this is a discussion of the transformation of bands from excess to defect type, which does not arise naturally from the discussion. This has, however, been discussed at length by Hall (1970). Hall's discussion could be extended to backscattered electrons and a convolution similar to that applied in Chapter 8 used, once a relationship between depth and energy distribution of backscattered electrons has been obtained.

APPENDIX 1

Comments on the solutions for the fractional penetration f, of an electric field through a wire mesh used as a retarding filter, due to Denbigh (1964) and Sheppard (1973).

In recent discussions of simple retarding field energy analysers (Denbigh, 1964; Sheppard, 1973; Ward, 1976) analytic expressions based on Verster (1963) have been invoked to predict the potential at the centre and edge of a mesh hole. The difference between the two potentials has been taken as the basic analyser resolution, assuming that monochromatic electrons initially stopped by the potential of the mesh bars would be completely rejected by the filter when the potential at the centre of the mesh reached the accelerating potential of the electrons.

It is shown in Chapter 5 that the above argument is untrue; however, an analytic expression for the potential around a mesh would still be useful. This appendix serves to show that the expressions produced by Denbigh and Sheppard are not sufficiently accurate for the required purpose.

A1.1 The basic expression :

Verster (1963) showed that the potential $\varphi(x,z)$ around a set of uniformly charged lines is given by :

$$\varphi(x,z) = \ln[2\cosh(2\pi z/s) - 2\cos(2\pi x/s)] \qquad \text{A1.1}$$

where x, z and s are defined in Fig. (A1.1). A more general expression which allows for a superimposed potential gradient also given by Verster is

$$\varphi(x,z) = V_1 z/s + V_2[\ln[2\cosh(2\pi z/s) - 2\cos(2\pi x/s)]] + V_{eff} \qquad \text{A1.2}$$

where V_1, V_2, V_{eff} are constants dependent on the boundary conditions of the particular system.

Boundary conditions :

In the usual retarding filter a mesh is placed between two earthed planes (Fig. A1.2). The boundary conditions at these planes, $z = p$ and $z = -q$ are :

$$\varphi(x, p) = 0 \qquad \text{A1.3}$$

$$\varphi(x, -q) = 0 \qquad \text{A1.4}$$

The lines of charge can be replaced by rods of finite radius r and potential V_g.

Thus,

$$\varphi(r, 0) = Vg \qquad \text{A1.5}$$

(Strictly,

$$\varphi(a, \sqrt{r^2 + a^2}) = Vg \qquad \text{A1.6}$$

where $a \leqslant r$. This condition is difficult to apply. It can be shown that A1.5 produces an error of 0.002% in the predicted value of the potential at (o, r), as compared with A1.6 for the mesh under consideration. Considering the practical errors in non uniformity of the mesh, etc., this is acceptable and simplifies the analysis considerably).

In most practical cases,

(i) $p \approx q$

(ii) $p \gg s$ A1.7

(iii) $s \approx 6r$

Substituting A1.3, A1.4 and A1.5 in A1.2, we obtain

$$V_1(p/s) + V_2(2\pi p/s) + V_{eff} = 0 \qquad \text{A1.8}$$

$$V_1(-q/s) + V_2(2\pi q/s) + V_{eff} = 0 \qquad \text{A1.9}$$

$$V_2(\ln(2 - 2\cos(2\ \ r/s))) + V_{eff} = 0 \qquad \text{A1.10}$$

From A1.8, A1.9 and A1.10

$$V_1 = Vg \cdot \frac{s}{2} \cdot \left(\frac{1}{q} - \frac{1}{p}\right) \qquad \text{A1.11}$$

$$V = -Vg \cdot \frac{s}{4\pi} \cdot \left(\frac{1}{p} + \frac{1}{q}\right) \qquad \text{A1.12}$$

$$V = Vg\left(1 + \frac{s}{4\pi} \cdot \left(\frac{1}{p} + \frac{1}{q}\right) \cdot \ln(2 - 2\cos(2\ \ r/s))\right) \qquad \text{A1.13}$$

Substituting for these constants in A1.2 gives the general equation for the potential in the x-z plane.

$$\varphi(x,z) = Vg\left[1 + \frac{z}{2}\left(\frac{1}{q} - \frac{1}{p}\right) - \frac{s}{4\pi}\left(\frac{1}{p} + \frac{1}{q}\right)\ln(2(\cosh(2\pi z/s) - \cos(2\pi x/s)))\right.$$

$$\left. + \frac{s}{4\pi}\left(\frac{1}{p} + \frac{1}{q}\right)\ln(2 - 2\cos(2\pi\, r/s)\right] \qquad \text{A1.14}$$

which can be simplified to

$$\varphi(x,z) = Vg\left[1 + \frac{z}{2}\left(\frac{1}{q} - \frac{1}{p}\right)\right.$$

$$\left. + \frac{s}{4\pi}\left(\frac{1}{p} + \frac{1}{q}\right)\ln((1 - \cos(2\ \ r/s)) / (\cosh(2\ \ z/s) - \cos(2\ \ x/s)))\right] \qquad \text{A1.15}$$

This is the general expression for the potential at any point in the (x, z) plane subject to the given boundary conditions (Eqns. A1.3-A1.7).

The potential midway between mesh rods, $\varphi(\frac{s}{2}, 0)$ is then given directly from A1.15

$$\varphi(\tfrac{s}{2}, 0) = Vg\left[1 - \frac{s}{4\pi}\left(\frac{1}{p} + \frac{1}{q}\right)\ln(2/(1 - \cos(2\pi r/s)))\right] \qquad \text{A1.16}$$

This potential is necessarily lower than the mesh because of the influence of the earthed planes. The difference between this and V_g is taken as the resolution of the mesh filter.

$$Vg - \varphi(\tfrac{s}{2}, 0) = Vg . \frac{s}{4\pi}\left(\frac{1}{p} + \frac{1}{q}\right) \ln(2/(1-\cos(2\pi r/s))) \qquad A1.17$$

It is useful to define the fractional field penetration f

$$f = \frac{Vg - \varphi(\tfrac{s}{2}, 0)}{Vg} \qquad A1.18$$

Substituting A1.16 in A1.18

$$f = \frac{s}{4\pi}\left(\frac{1}{p} + \frac{1}{q}\right) \ln(2/(1-\cos(2\pi r/s))) \qquad A1.19$$

The value of f in A1.19 is the fractional penetration of the field through a set of equally spaced rods of radius r. This expression has been used by both Denbigh (1964) and Sheppard (1973) on the basis of the calculation of the fractional field penetration through a square mesh.

Square mesh :

Denbigh and Sheppard both considered a square mesh to be made up of a set of vertical rods of spacing s overlaid by a coplanar set of horizontal rods with the same spacing (Fig. A1.1b). In order to obtain the correct potential on the bars, Denbigh and Sheppard regarded the charge on each set of rods as half that required to produce V_g if only one set of rods were present. The total potential of the two sets of rods at their intersection is thus V_g.

Both workers calculated the potential at the centre of the square mesh and

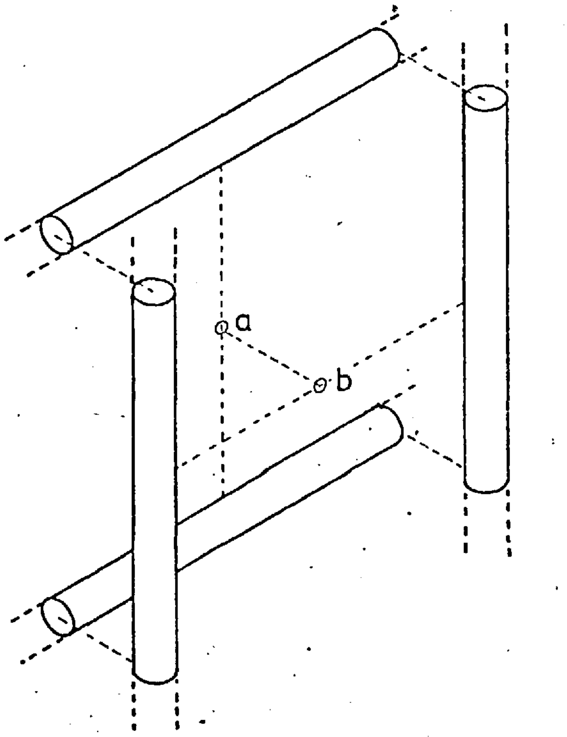

Fig.A1.1 Two sets of bars used to form the mesh.

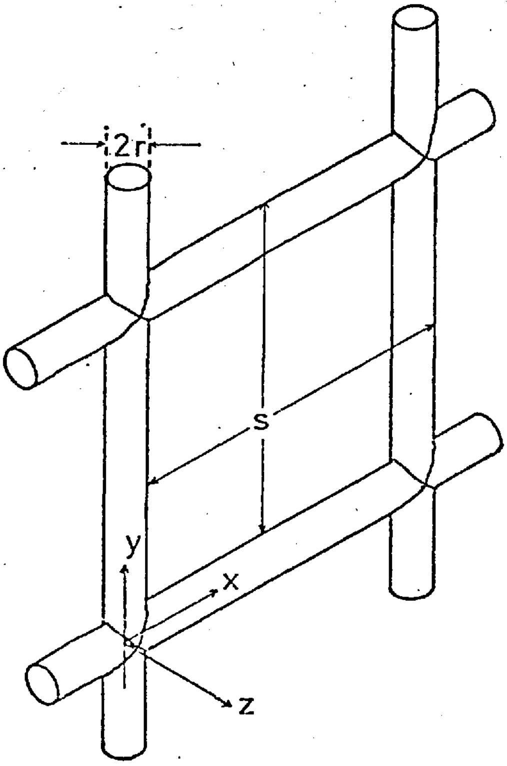

Fig.A1.2 Mesh bars - definitions of r, S, X,Y,Z.

defined the fractional field penetration in the same manner as they had for a single set of rods.

The fractional field penetration obtained by Sheppard was :

$$f = \frac{s}{4\pi}\left(\frac{1}{p} + \frac{1}{q}\right) \ln \left(2 / (1 - \cos (2\pi r / s))\right) \qquad \text{A1.20}$$

This is the same as the expression A1.19 for a single set of rods. The reason for this discrepancy is that the model of the mesh is wrong in detail. In fact the rods should not have a uniform charge distribution but uniform potential. The use of the former model results in the potential distribution shown in Fig. A1.3, which is obviously slightly incorrect.

A1.2 Comparison between Denbigh's and Sheppard's calculated values for f

Sheppard obtained the value for f given by A1.20 above, whereas Denbigh's expression for f was

$$f = \frac{s}{2p\pi} \ln 4 \left(\frac{2\pi r}{s}\right)^{-2} \qquad \text{A1.21}$$

The two expressions are equivalent, assuming, as Denbigh did, that

i) $p = q$

ii) $\cos (2\pi r/s) = 1 - \frac{1}{2}(2\pi r/s)^2$

Neither assumption is wrong for the system used by Denbigh which had a large coarse mesh ($r \ll s$) but Ward's application of it is wrong and results in a very different value from the more exact value obtained from A1.20.

Summary

i) The use of the model of the mesh described above is useful in obtaining an order of magnitude expression for the field distribution around a mesh. Verster was interested in coarse Videcon meshes, and for such the expressions obtained were very satisfactory.

The more general expression of Sheppard's should always be used as its only

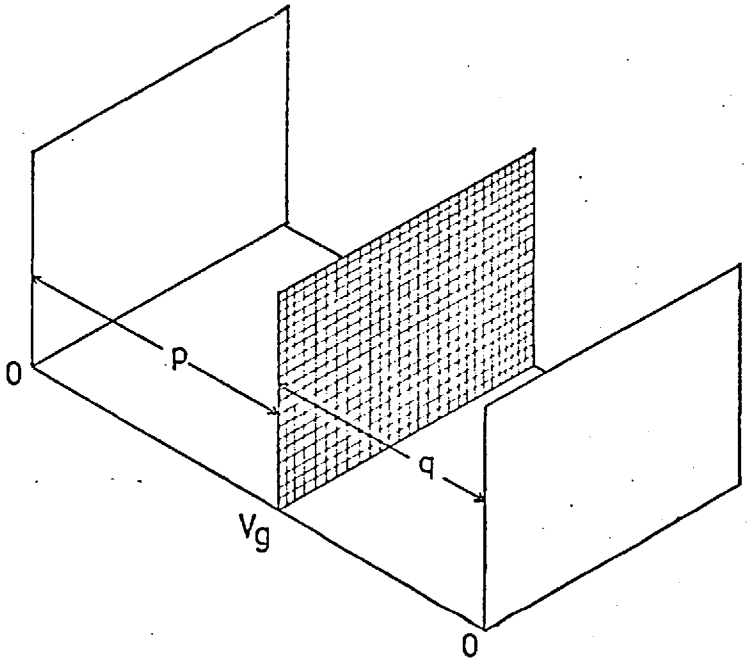

Fig.A1.3 Typical retarding field analyser configuration. Mesh, at a potential V_g ,is placed between two earthed planes at distances p and q from them.

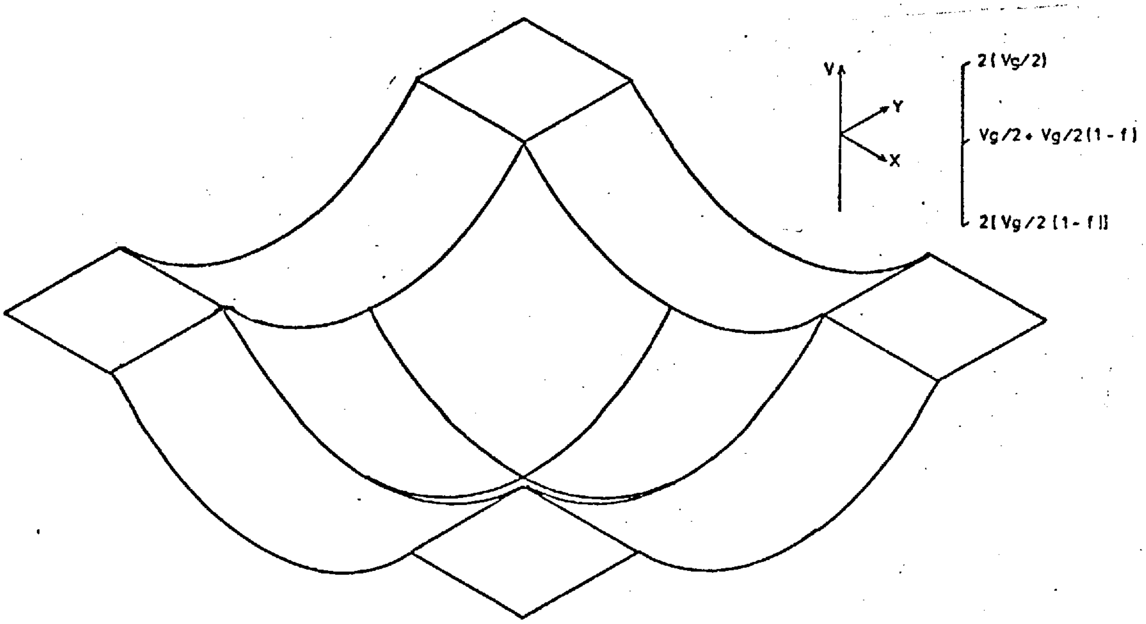

Fig.A1.4 Potential around a square mesh modeled using the analytic expression due to Verster (1963).

major restriction is that $6r < S$.

ii) The assumption that resolution = $1/f$ is incorrect (Chapter 5), and thus the analysis is only useful in finding the approximate potential distribution around a mesh.

iii) The analysis of the potential around any more complex structure is best done by the relaxation methods described in Chapter 5.

APPENDIX 2

The energy spread in a thermionic electron beam

The energy spread in an electron beam produced by a hot cathode has two separate causes. Firstly, there is a Maxwellian spread of velocities produced by the temperature of the electrons, and secondly the electrons in the beam interact with one another to produce an increase in energy of some electrons and a decrease in energy of others.

The subject of energy spread in an electron beam has been the subject of considerable discussion for over twenty years (Boersch, 1954; Dietrich, 1958; Hartwig and Ulmer, 1963; Zimmermann, 1970; Franzen and Porter, 1975).

These discussions have necessarily been confined to closely matched electron guns and electron velocity analysers, in order that one will not adversely affect the other. This means that the interpretation of reported data and its application to an arbitrary gun are often difficult.

Neglecting for a moment space charge, the distribution of velocity of thermionic electrons is Maxwellian, which, when expressed in terms of energy is

$$N(E)dE = \frac{8\pi E}{m} \exp\left(\frac{-E}{kT}\right) dE \qquad \text{(A2.1)}$$

(Fig. A2.1)

where E is the energy of the electron referred to the filament as zero. The integral of N(E)dE over all E is normalized to unity.

The function A2.1 has a maximum at $E = kT$ and a width at half height of $2.5kT$ where T is the filament temperature, k is Boltzmann's constant and m electron mass.

The typical operating temperature of an uncoated tungsten filament electron gun is 2500 K, which gives an energy width at half maximum of 0.54 eV. (The values of m and k are taken from Taylor, Parker and Langenberg, 1969).

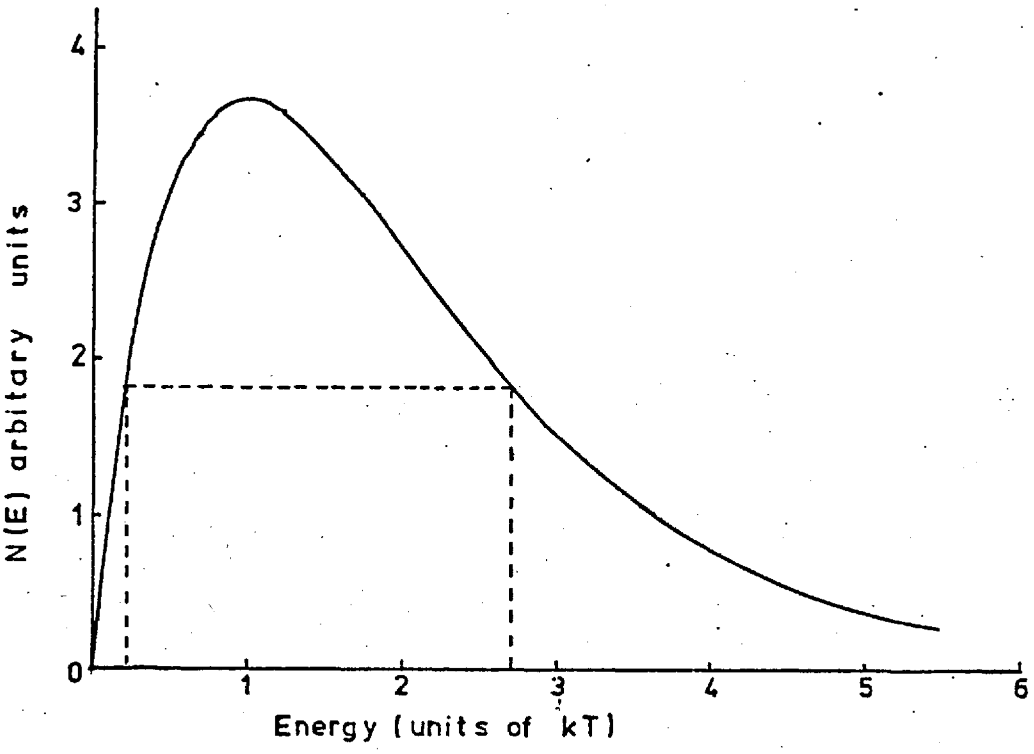

<u>Fig.A2.1</u> Maxwellian velocity distribution of thermal electrons.

This is a minimum value for the energy width at half height. A more detailed discussion, including the effect of work function, leads to a slightly higher value for the width at half height (Franzen and Porter, 1975).

Space charge

The energy spread derived above is only applicable to low current density beams (Harting and Ulmer's work indicates an upper limit of 4×10^{-3} A m^{-2}). In a typical electron gun the beam passes the grid with a density of $10^{3} - 10^{6}$ A m^{-2}, depending on the grid potential and position. These high current densities result in space charge interactions in the beam. Electron-electron interactions allow some electrons to gain energy at the expense of others. These effects operate in any density of beam current but as the number of electrons in any part of the beam increases the influence of the electrons on each other increases.

Hartwig and Ulmer suggest that the total energy width at half maximum, ΔE, is given by :

$$\Delta E = \Delta E_o + k_1 J^{1/3} E^{1/6} \qquad \text{(A2.2)}$$

where ΔE_o is the thermal width described above, J is the maximum current density at any point in the system, and E is the energy of the beam after acceleration from the gun, k_1 is a constant for the system.

On the other hand, Simpson and Kuyatt (1966) give an expression for ΔE derived from experiment

$$\Delta E = \Delta E_o + 1{\cdot}4 \times 10^{-3} J E^{2/3} \qquad \text{(A2.3)}$$

where J and E_o have the same meaning as above.

No exhaustive study has been made of the energy spread, and it is unclear if useful results could be obtained analytically for any arbitrary system. The main reason for this is that the current density J is difficult to obtain at all points in any system and is dependent on E. The dependence of J on E varies from system to system and probably explains the discrepancy between the two expressions (A2.2), (A2.3).

It may be suggested that the energy spread is only indirectly governed by E and is, in fact, a function of the energy of the beam at the point where J is a maximum. This point usually occurs in the gun at a point where the electrons are still being accelerated. There is, however, insufficient published information to interpret the results of either Simpson and Kuyatt or Hartwig and Ulmer on this basis.

Hartwig and Ulmer give experimental results indicating that the total energy spread at half maximum for a triode gun similar to that described in Chapter 4 was 1 eV. They also showed that the velocity distribution changed from the Maxwellian (thermal) distribution to a Gaussian form as the space charge effect increased.

Using these results and assuming a Gaussian form, both for the energy distribution of the electrons and the transfer function of the analyser (Chapter 4), the resolution of the analyser was calculated (Chapter 5).

APPENDIX 3

Calibration of Scintillators and Phosphors

The scintillator and phosphors used in the analyser were calibrated in order to find the current output at the photomultiplier or the pulse rate recorded for a given beam current. In all cases the photomultiplier (Chapter 4) was run at an operating potential of 1.1 kV.

A3.1 Scintillator calibration

The scintillator was calibrated directly by comparison of the output of the photomultiplier tube with the beam current measured by a Faraday cup in the apparatus.

The window holding the scintillator was removed from the analyser (Chapter 4) and placed opposite to the electron gun on the main chamber. The beam current was varied from 10^{-12}A to 10^{-8}A using a 10mm diameter spot, and the output of the photomultiplier recorded for various accelerating potentials. The output of the photomultiplier I_o was found to follow the relationship $I_o = k\ I_i\ (V - C)$, where I_i is the beam current, V the accelerating potential and k & C constants dependent on the age and condition of the scintillator surface (cf. Fig. A3.1).

The value of C governs the limit of low energy detection and gives an indication of the thickness of the layer at the surface of the scintillator, which is insensitive either because of contamination or radiation damage. Radiation damage caused a steady increase of C with operating time, but the response was restored by regular polishing of the surface. Under normal conditions of operation (current densities less than 10^{-6}A m^{-2}), the scintillator response fell by 20% in 20 hr. use. Where possible the scintillator was repolished after 5 - 10 hr. use.

The response curve was checked at regular intervals, but was found to vary by only about 3% for a newly polished scintillator. This was within experimental error of the accelerating potential setting.

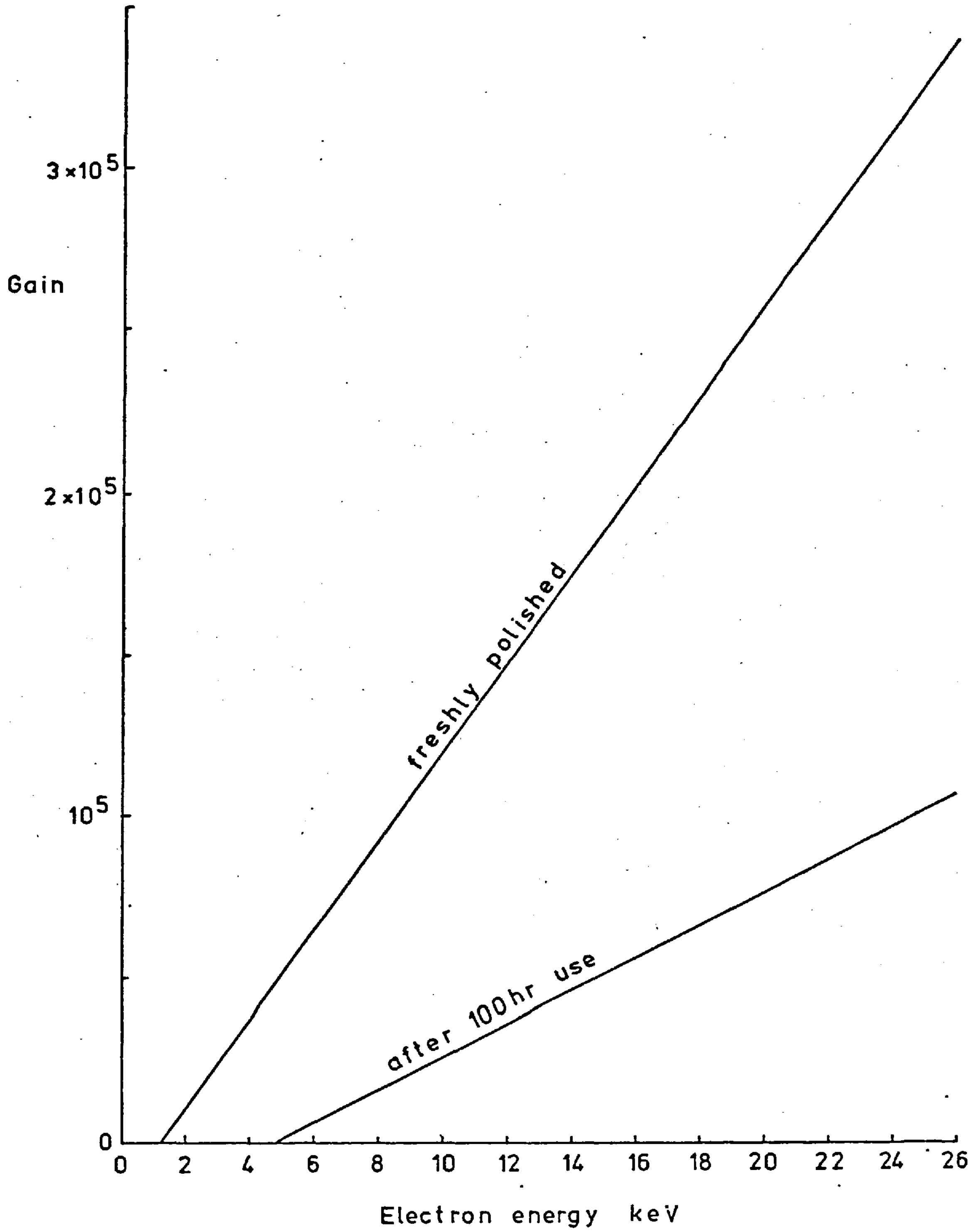

Fig.A3.1 Scintillator / photomultiplier gain plotted as a function of electron energy. Photomultiplier operating potential 1.1kV.

The effect of varying the position of a small spot on the screen was tried, but with a 0.5 mm diameter spot no variation in response with position could be found. This is consistent with Bunting's findings (Bunting, 1971).

The power densities used did not appear to cause any saturation of emission before permanent damage to the scintillator occurred.

A3.2 Phosphor calibration

The phosphors were initially calibrated in the same way as the scintillators by comparing their light output with the intensity and energy of the electron beam. The total light output of the phosphors was found to vary strongly with the position of the electron beam on the phosphor. The response of the phosphors was found to vary by up to 50% in a distance of 2 mm using a 0.5 mm spot. A more complete investigation has been carried out by Bunting (1971), who found similar effects in the thin phosphors he used.

A pulse height analyser showed that the number of pulses produced by the phosphors was nearly constant, but their height varied as the spot was moved. Thus, when pulse rate rather than current analysis was required at beam currents of less than 10^{-14}A, the phosphor was still suitable for use. The average height of pulses produced by the phosphor was 3- 5 times greater than background pulses produced by the photomultiplier, whereas the pulses produced by the scintillator in combination with the photomultiplier were only 1 - 1½ times greater than background. It was possible to discriminate between background and electrons using a phosphor, but not using the scintillator. The phosphors were thus used for pulse counting.

A3.3 Pulse counting

The pulse counting mode was used when the current produced by the scintillator/ photomultiplier combination fell below the dark current, 10^{-10}A of the tube. This corresponded to a beam current of 10^{-14}A. In order to calibrate the phosphors in this mode, a beam current of between 10^{-16}A and 10^{-14}A was required, but the electrometer used could only record currents down to 10^{-14}A, thus a neutral density filter was used to reduce the beam current by a fixed proportion after it had been measured in order to provide both a measurable current and a suitably small number of electrons at the phosphor.

The system adopted was to pass the beam through a series of micro-meshes (Fig. A3.2) set at a small positive potential (60V) relative to ground. The meshes were connected to an electrometer used to measure the beam current.

The meshes screened out a known proportion of the beam, the exact amount being found by using a high beam current (10^{-8}A) and measuring the beam current, transmitted current and collected current separately (Fig. A3.3).

The proportion of current in the beam to current transmitted was constant for all beam energies and for spot sizes above 0.5 mm diameter. The ratio I_T/I_B was 0.058 for the 5 element mesh used. It would have been better to measure the beam current directly, but this was not practical during calibration experiments, so the beam current was deduced by measuring the collected current and using a correction curve drawn up when the filter was investigated (Fig. A3.4). The rise in the ratio of main beam to collected current at the energies is consistent with increased production of secondary electrons at the filter.

It was of concern that the filtered beam should have only a small proportion of electrons that had lost energy. (Secondaries did not matter as their energy meant that they were mostly attracted back to the filter after production and could not affect the phosphors).

A3.4 Proportion of "lossy" electrons in filtered beam

The proportion of electrons with energy loss in the filtered beam can be estimated roughly as follows :-

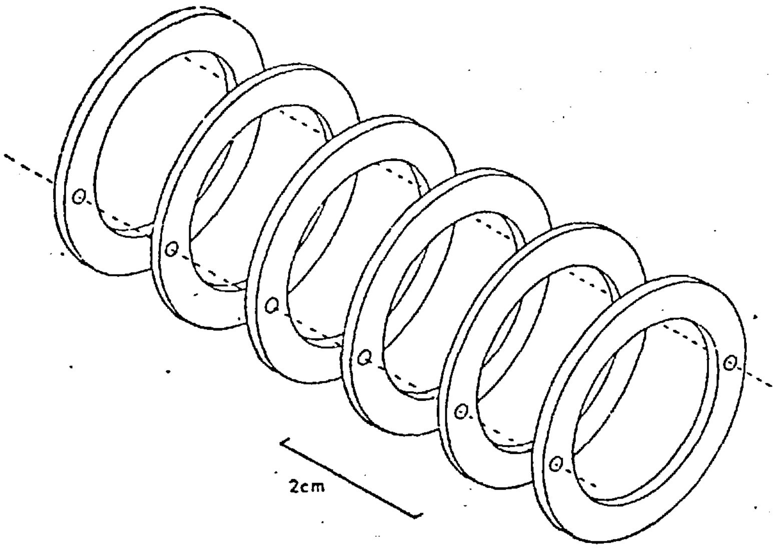

Fig.A3.2 Method of stacking meshes for use as a filter to reduce the beam intensity.

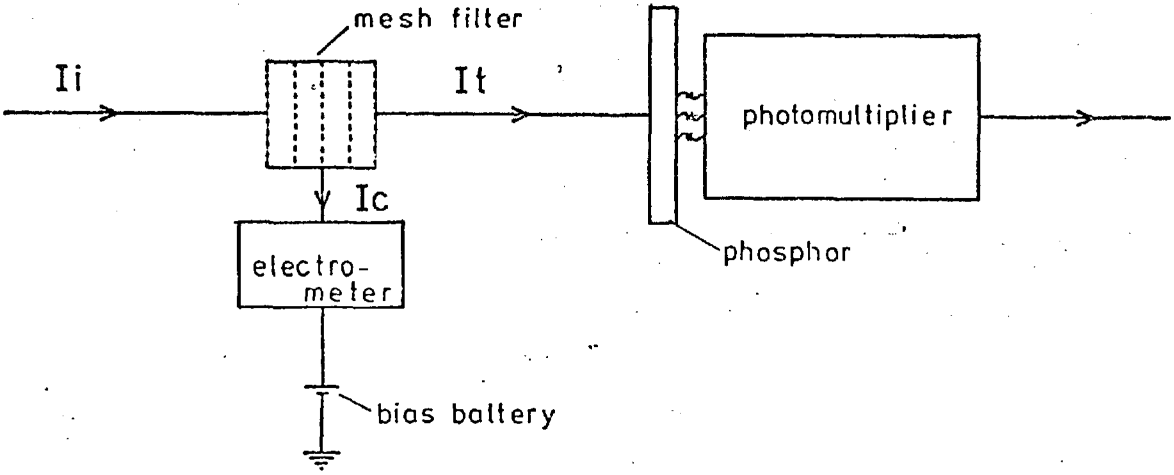

Fig.A3.3 Use of mesh filter for calibration of phosphors in the pulse counting mode.

Each mesh has a geometric transmission coefficient of 0.56, obtained by measurement from a scanning electron micrograph and confirmed by measurements in construction of the energy analyser.

There were fine meshes in the filter, thus $(0.56)^5 = 0.055$ of the main beam passed through without energy loss. Of the remainder some of the electrons are reflected twice and thus transmitted without further energy loss (Fig. A3.5). The amount reflected from each mesh at 20 kV, $R = (1 - T)\,\eta = 0.13$ (η is the back-scattering coefficient at 20 keV for Copper taken from Bishop, 1965).

Considering the first and second meshes only, the proportion of the original beam reflected from the second mesh back to the first is T(R). Some of these electrons are reflected back from the first mesh. The total proportion travelling towards the second mesh having been reflected twice is $T\,R^2$ of the initial beam. Thus, substituting for T and R, 0.325 of the initial beam is transmitted with no loss, and 0.0053 transmitted with some loss through the meshes. Extending the argument to five meshes, $T^5 = 0.055$ of the beam is transmitted with no loss and $R^2(4T^5 + 3T^7 + 2T^9 + T^{11}) =$ 0.005 of the beam is transitted with two or more collisions and thus some loss of energy. In practice, many of the scattered electrons are lost to the walls of the filter and as a result only about 4% of the beam emerging from the filter showed energy loss when checked with the energy analyser. The analysis is thus justified in ignoring electrons scattered more than twice.

This was satisfactory for the accuracy required; however, this could have been improved on by reducing R by coating the mesh with carbon. This would reduce the transmitted fraction with energy loss to 0.0002. The error in calibration produced by this means was small, though it would have been significant at energies above 25 keV, where the phosphor response was falling with energy.

This method was used to calibrate the two phosphor/photomultiplier counter

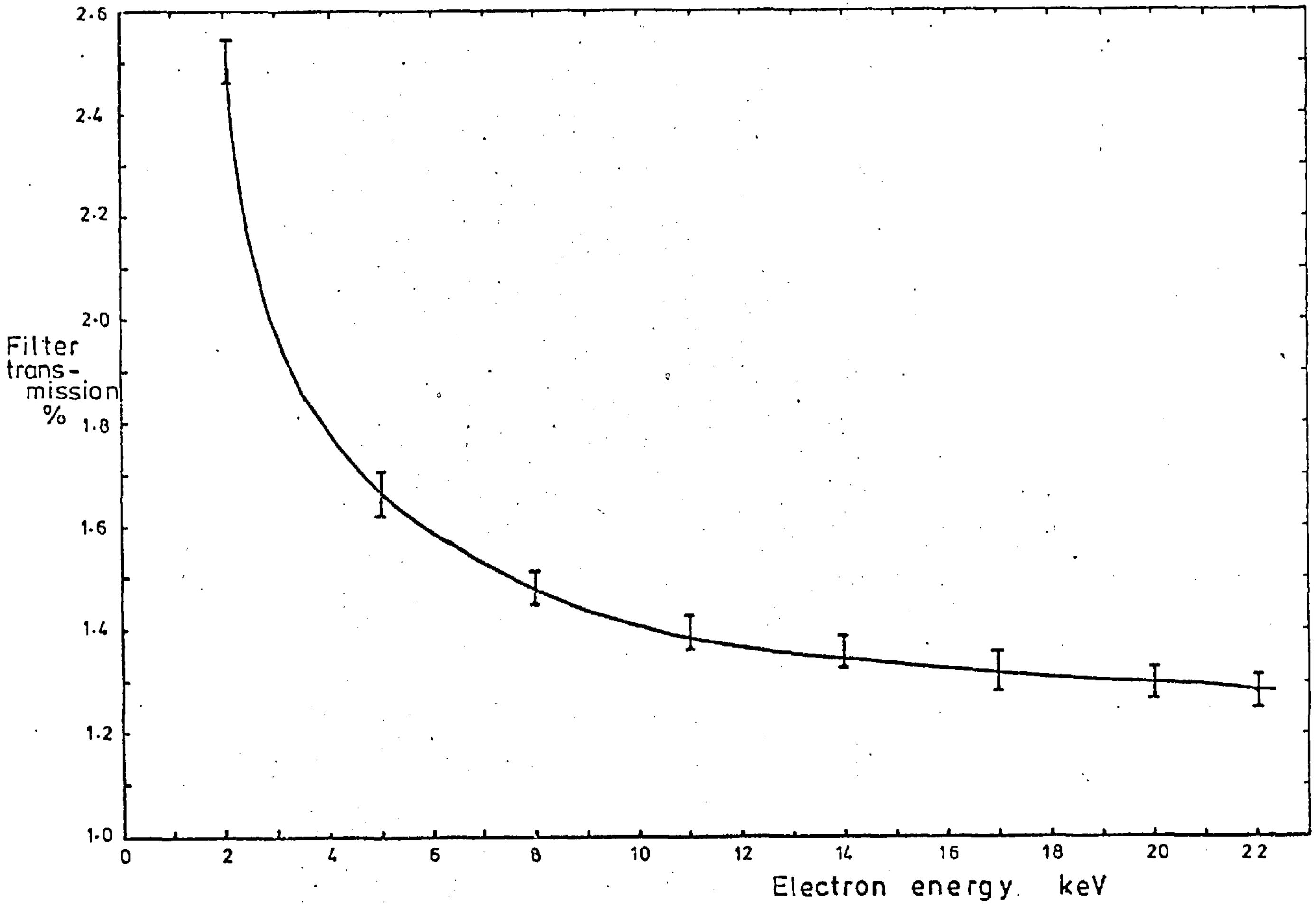

Fig.A3.4 Transmission of mesh filter as a function of beam energy.

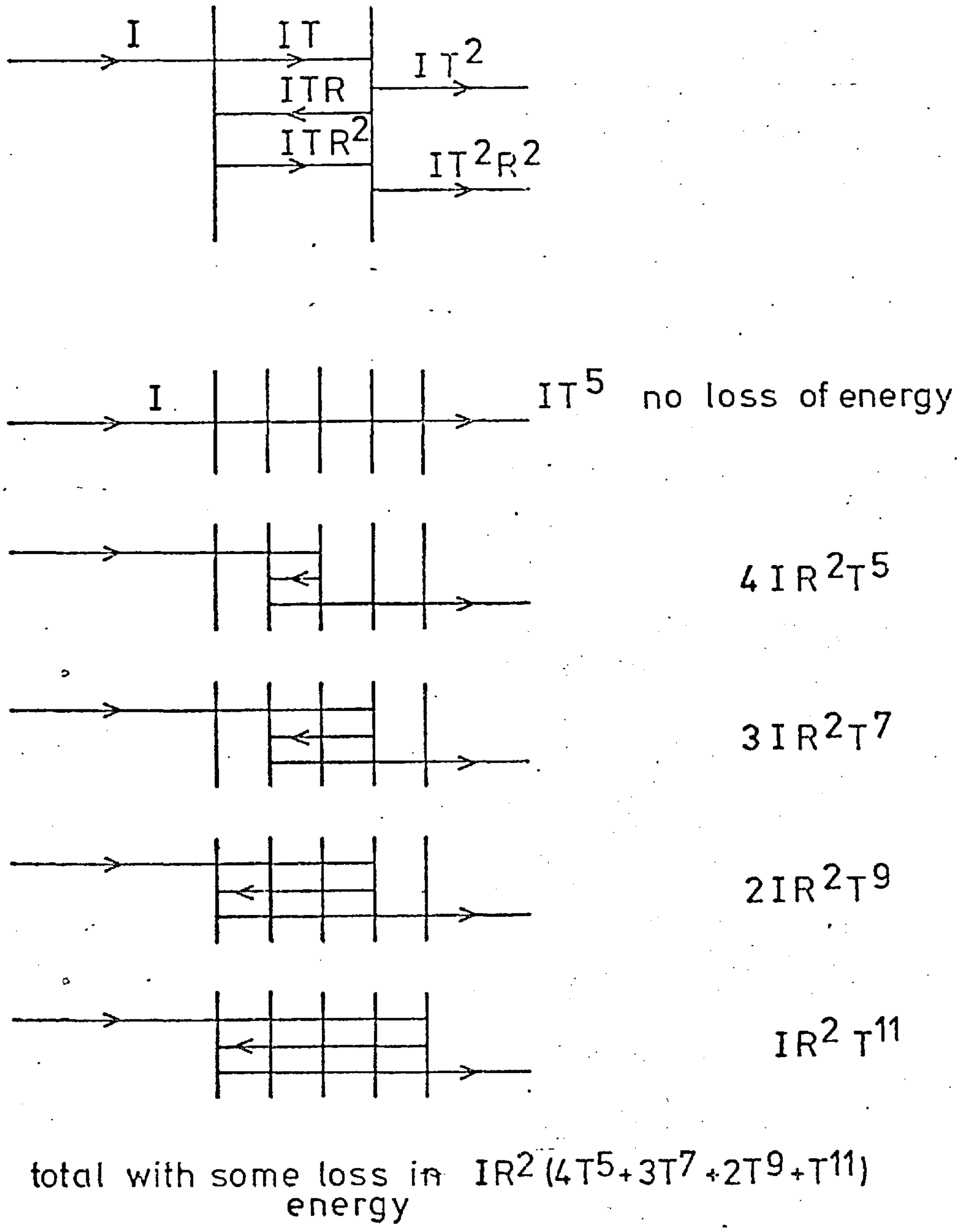

Fig.A3.5 Proportion of no loss electrons in the transmitted beam from the mesh filter.

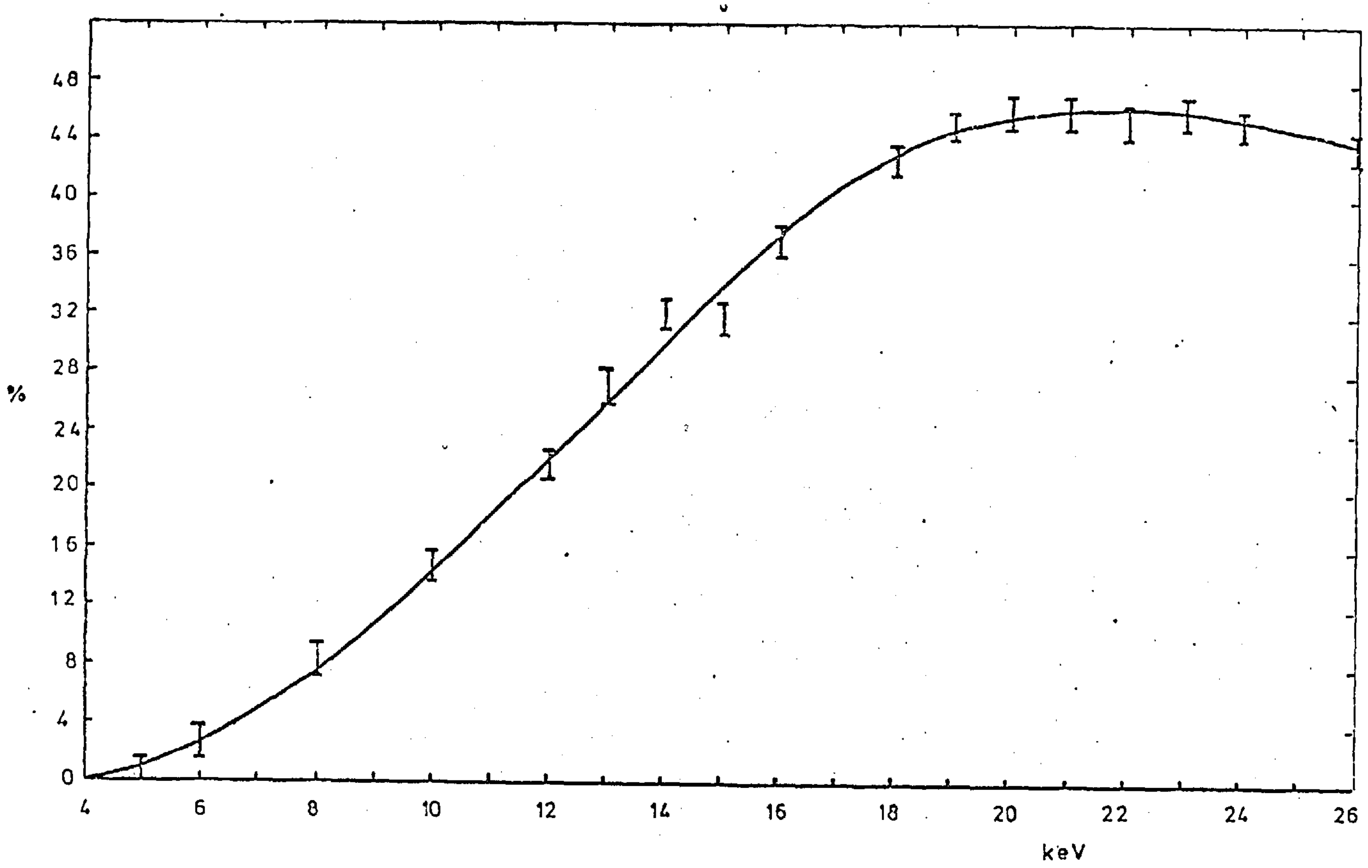

Fig.A3.6 Phosphor output as a function of beam energy. The output is expressed as the percentage ratio of the number of recorded pulses to the number of incident electrons. Phosphor in use to April '77.

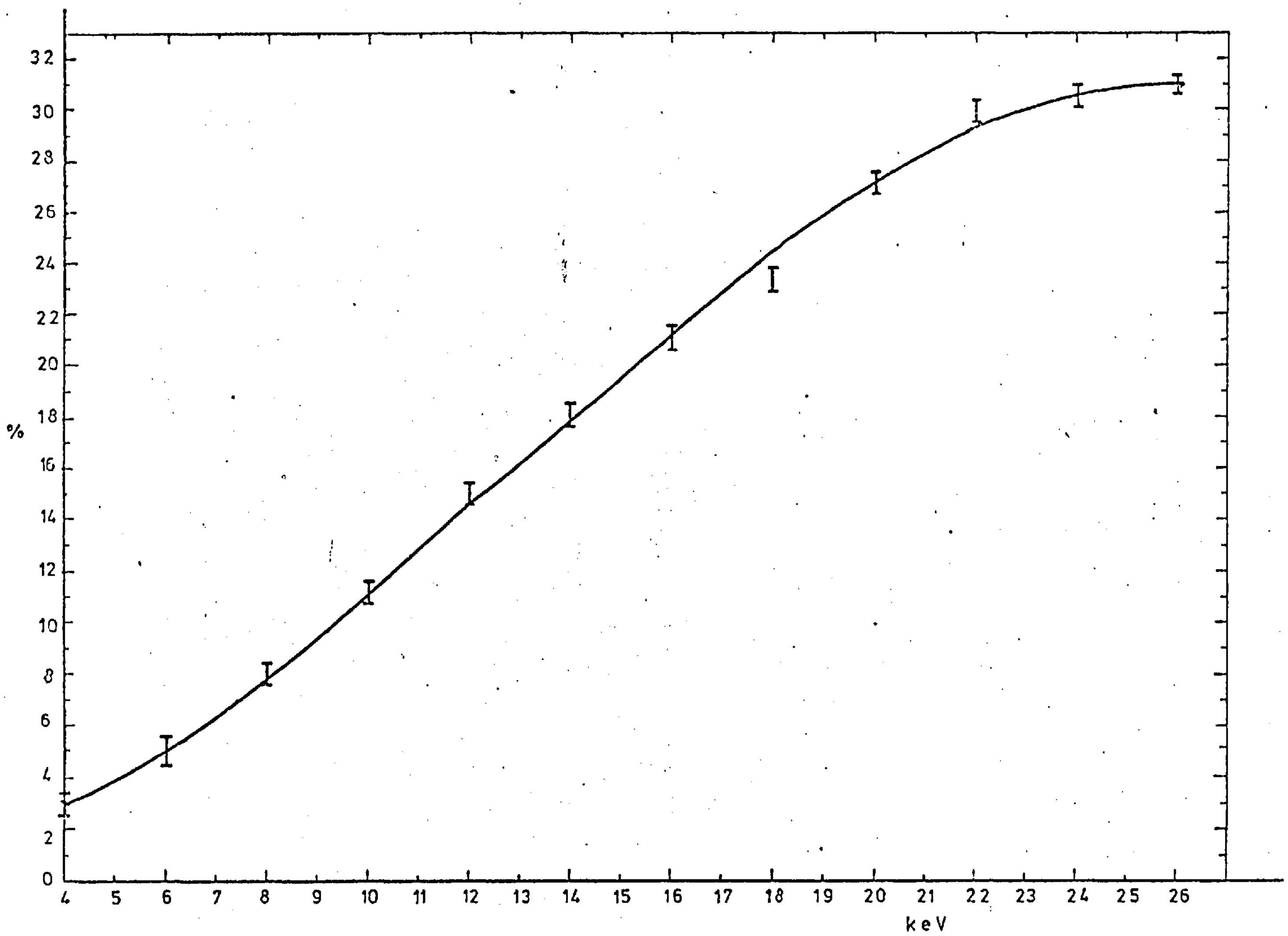

Fig.A3.7 As Fig.A3.6. Phosphor in use after April '77.

systems used (Figs. A3.6 and A3.7). (The first phosphor used lost its backing due to field stress and regular vacuum cycling after about six months use).

The phosphors were both fine grain P 11 prepared by electrophonetic deposition and backed by a 40 nm layer of Aluminium.

The calibration curves show that response in the system was never greater than 50%. This may be due to electrons passing through or between phosphor particles, or light loss between the phosphor and photomultiplier. The curves for each phosphor were different, but each produced self consistent and reproducible calibration to within 10%.

APPENDIX 4

ELECTRICAL DIFFERENTIATION

A4.1 Phase sensitive detection

The technique of phase sensitive detection (PSD) has been widely used for the electrical differentiation of the $\int_{E_0}^{\infty} N(E)\,dE$ output obtained from retarding potential energy analysers. (Spicer and Berglund, 1964, low energies, Curtis and Ferrier, 1970, high energies). $N(E)\,dE$ represents the number of electrons with energy between E and $E + dE$. A retarding potential analyser allows transmission of all electrons with energy greater than a fixed value E_o, hence its output is $\int_{E_0}^{\infty} N(E)\,dE$. A differential analyser (dispersive analyser) produces an output $N(E)\,\delta E$, where δE represents the finite energy window allowed by the analyser.

The most frequently documented use for PSD is in the detection of Auger electrons in hemispherical LEED/Auger systems (Taylor, 1969, Chang, 1971, O'Harer, 1972a and b). The technique was used in the experiments reported in Chapters 5 and 6 for both current and pulse rate differentiation. The latter application has not been extensively discussed, and it is therefore appropriate to examine the suitability of such a detector for the study of rate changes in pulsed systems.

Operation

The electrical differentiation of the output of the analyser is achieved by modulating its potential, E_o, with a sinusoidal signal, $\Delta E = k \sin \omega t$. The output then has a time varying component with an amplitude proportional to the number of electrons with energy between $E_o - k$ and $E_o + k$ (Fig. A4.1). The signal is chopped and inverted in phase with the modulating signal (Fig. A4.2) and time averaged (Fig. A4.3) using a suitable R.C. network. Only signals with a frequency ω will give an output, all others will be averaged out if a suitably long time constant is used (Chang, 1971). (Fig. A4.4).

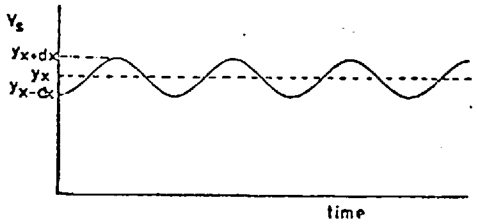

Fig.A4.1 The signal y_x is modulated by a time varying function x_t.

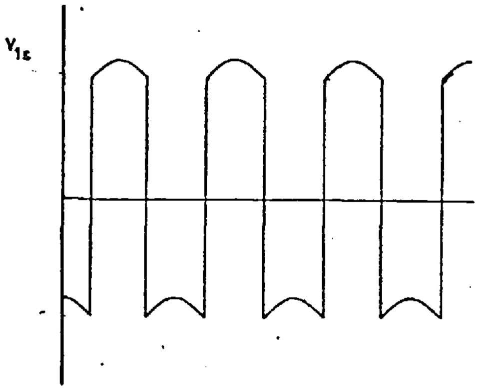

Fig.A4.2 The P.S.D. chops and inverts y_x in phase with its time variation.

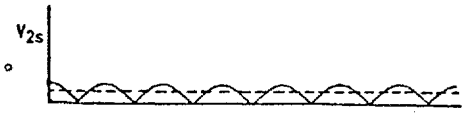

Fig.A4.3 The signal is time averaged to remove time independent noise.

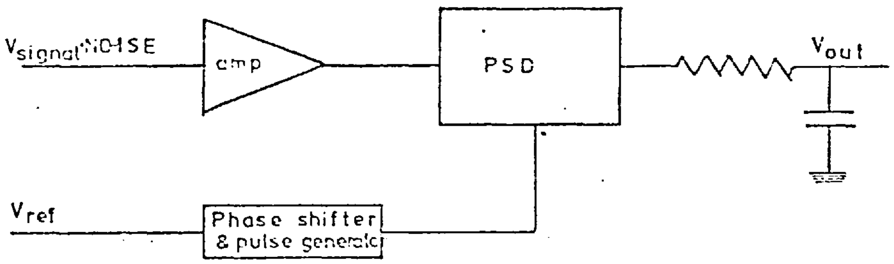

Fig.A4.4 Phase sensitive detector.

The output of a retarding field analyser is $\int_{E_0}^{\infty} N(E)\,dE$ when E_o is fixed. Modulation produces a signal $\int_{E_0+k\sin\omega t}^{\infty} N(E)\,dE$. This can be expanded in the form of a Taylor's series :-

$$\int_{E+k\sin\omega t}^{\infty} N(E)\,dE = \int_{E_0}^{\infty} N(E)\,dE + N(E_0)\,k\sin\omega t + \frac{N'(E_0)\,k^2\sin^2\omega t}{2!}$$

$$+ \frac{N''(E_0)\,k^3\sin^3\omega t}{3!} + \ldots\ldots\ldots\ldots \qquad \text{A4.1}$$

rearranging :-

$$\int_{E_0+k\sin\omega t}^{\infty} N(E)\,dE = \int_{E_0}^{\infty} N(E)\,dE$$

$$+ \left[N(E_0)k + \frac{N''(E_0)k^3}{8} + \frac{N''''(E_0)k^5}{192} + \ldots\ldots \right] \sin\omega t$$

$$- \left[\frac{N'(E_0)k^2}{4} + \frac{N'''(E_0)k^4}{48} + \ldots\ldots\ldots\ldots \right] \cos 2\omega t$$

$$- \left[\frac{N''(E_0)k^3}{24} + \ldots\ldots\ldots\ldots \right] \sin 3\omega t \qquad \text{A4.2}$$

$$+ \ldots\ldots\ldots\ldots\ldots\ldots$$

where $N^n(E_o)$ is the n^{th} derivative of $N(E_o)$ with respect to t at the energy E_o.

If k is sufficiently small k^3 and higher powers can be ignored, thus the output can be expressed simply as follows :-

$$\int_{E_0+k\sin\omega t}^{\infty} N(E)\,dE = \int_{E_0}^{\infty} N(E)\,dE + N(E_0)\,k\sin\omega t - \frac{N'(E_0)\,k^2}{4}\cos 2\omega t \qquad \text{A4.3}$$

Thus, if k is small, the signal detected at a frequency ω is proportional to $N(E_o)$ and the signal at the frequency 2ω is proportional to $N'(E_o)$. These are the first and second derivatives of the original output of the analyser.

Noise reduction

There are three main considerations in the production of any signal processor :-

i) The maximum amount of noise is removed from the signal

ii) No noise is added to the signal

iii) The signal is not distorted

The PSD achieves the first aim in different ways, depending on the noise type :

a) White noise :- The intensity of the noise spectrum is uniform, and thus noise reduction is governed by the bandwidth detected. The larger the bandwidth used by the detector, the more noise will be included.

The bandwidth, B, of the output filter of a PSD can typically be varied between 25 Hz and 0.0025 Hz (Brookdeal Model 401 A). ($B = \frac{1}{4\tau}$ where τ is the time constant, variable between 10 ms and 100 s).

A reasonable upper limit to the input is 100 k Hz and the minimum bandwidth is 2.5×10^{-3} Hz, thus maximum noise reduction for white noise is :-

$$\text{Noise power reduction} = \frac{\text{Input bandwidth}}{\text{Output bandwidth}} \qquad \text{A4.4}$$

$$= \frac{10^5}{2.5 \times 10^{-3}} = 4 \times 10^7$$

This is equivalent to a reduction in noise power of 76 d B, or of a reduction of output noise voltage by a factor of 6×10^3.

This assumes that the noise is 'white', i.e. that there is constant power per unit bandwidth in the range 0 - 100 K Hz. Much noise is, however, confined to narrow bands.

b) Narrow band noise :- Mains pickup, radio interference and very low frequency changes in the signal level are all confined to narrow frequency bands. By choosing a modulating frequency far removed from any such interference, the signal of interest can be shifted into a much quieter region of the noise spectrum for detection.

In this way, signal to noise ratio can be improved by up to 100 dB, using relatively fast output time constants (wide bandwidths) and hence using fast slew rates. The gain in signal to noise ratio is usually then only limited by the dynamic range of the PSD (the ratio of the input signal including noise to any signal derived from it) in this case 120 dB, and by Shot noise.

c) Shot noise :- The limit of noise reduction in any electrical filter is governed by Shot noise. It can be shown (Goodyear, 1971) that for independent processes in a thermionic current (i.e. where space charge is not important) the noise current, I_N, due to random fluctuations, is given by :-

$$I_N = (2e\,I\,B)^{\frac{1}{2}} \qquad \text{A4.5}$$

where B = bandwidth at which observations are made

I = input current

e = electron charge

In a typical situation where both signal and noise are large, Shot noise will be of minor concern. The situation often arises where the input of the PSD ($10^7\Omega$) is saturated (3 V). The lowest detection limit is then governed by the dynamic range of the PSD (120 dB) as the Shot noise limit is 150 dB and is well outside this range.

[Minimum detectable signal = Shot noise

$$= (2\,e\,I\,B)^{\frac{1}{2}}$$

Taking $B = 0.0025$ Hz

$I = 3 \times 10^{-7}$ A

$e = 1.6 \times 10^{-19}$ C

I_N (Shot) $= 1.5 \times 10^{-14}$ A

$$\text{Power ratio} = (\text{current ratio})^2$$

$$\text{Power ratio of signal/noise} = 10 \log \left(\frac{3 \times 10^{-7}}{1.5 \times 10^{-14}}\right)^2 \text{ d B}$$

$$= 146 \text{ d B}$$

This is well outside the dynamic range of the amplifier]

If the total current entering the PSD is lower than 3×10^{-7} A the Shot noise limit can come inside the dynamic range, and thus the Shot noise will set the lower limit of signal detection.

These considerations are dealt with by Chang (1971) for the case of Auger electrons detected using a LEED/Auger hemispherical analyser. In the present application, Shot noise became the limiting factor in the recording of backscattered spectra at low currents (Chapter 6).

Discussion

The noise reduction produced by a PSD is dependent on the type of noise and for both white and shot noise could equally well be done with an R.C. differentiating filter. However, in almost every application there is some narrow band noise, usually in the very low frequency region (i.e. shifting D.C. levels), which is most suitably removed by phase sensitive detection.

A4.2

The frequency spectrum and inherent distortion produced by phase sensitive detection

In the preceding section it was assumed that the modulating voltage amplitude, k, was sufficiently small that k^3 and higher powers could be ignored. In practice, the PSD user often tries to sacrifice resolution in energy by increasing k beyond what can be considered as small. It is of interest to see what effect this increase has on the output of the PSD.

In the following discussion a Gaussian peak of the type

$$N(E) = \frac{N_0}{\sigma(2\pi)^{1/2}} \exp \frac{-(E_1 - E)^2}{2\sigma^2} \qquad \text{A4.6}$$

(E_1 = energy of the maximum of the peak)

is considered as a typical peak shape. Noise has been ignored and so the output can be as small or as large as required, and the time constant as short (bandwidth as large) as is needed to reproduce the signal slew rate accurately.

Equation A4.2 gives the amplitude of the signal at a frequency ω as

$$A(\omega) = N(E)k + \frac{N''(E)k^3}{8} + \frac{N''''(E)k^5}{192} \qquad \text{A4.7}$$

where E is the potential to which the analyser is set.

Substituting for N(E), $N''(E)$ and $N''''(E)$ from A4.6 gives the set of functions A (ω , E, k) for values of different values of k shown in Fig. A4.5. It can be seen from these figures that as k increases the distortion of the peak increases. The main point to notice in these curves is that up to $k = \sigma$ the peak height is nearly proportional to k. When $k > \sigma$ the peak shape becomes badly distorted. The extent of the distortion can be seen for $k = \sigma$ in Fig. A4.6. The functions are

N(E) and A $(\omega, E, k = \sigma)$. The areas enclosed are the same, but the peak height of A $(\omega, k = \sigma)$ is depressed by 11% compared with N (E).

The areas under the curves (fig. A4.5) are all $k\int_{-\infty}^{\infty} N(E)\,dE$ as $\int_{-\infty}^{\infty} N''(E)\,dE = 0$ and despite the distortion of the peak height this can provide useful information. The signal to noise ratio however cannot be improved much by increasing k above .

Fig. A4.7 shows the amplitude of the 2ω frequency component of Eqn. A4.7 from $k = \frac{1}{2}\sigma$ to $k = 2\sigma$

$$A(2\omega) = \frac{N'(E)}{4}k^2 + \frac{N'''(E)}{48}k^4 + \ldots\ldots\ldots \qquad \text{A4.8}$$

The effect of the increase in k is less marked, as the shape of the curves remains similar to N (E) until k increases to 2.1σ. However, with $k > 2.1\sigma$ severe distortion results (Fig. A4.8). The peak separation has increased by a factor of 2 between $k = \sigma$ and $k = 2\sigma$ with a corresponding drop in resolution. (Fig. A4.7).

The effect of increasing the modulating amplitude on the N(E) d E curve was investigated using the analyser (Chapter 5). Fig. A4.9 shows the effect of increasing the modulating voltage on the peak width at half height. The predicted resolution of the analyser, allowing for the energy spread in the beam, was ~ 2 eV, thus the marked increase in width occurs as expected when the modulating voltage is equal to the resolution.

These calculations are for the simplest curve available which has all derivatives finite at every point. In practice, the curve shapes encountered will be more complex and thus the amplitude of the derivatives will be greater. The effect on the expected curve shapes will thus be more marked, even when k is restricted to values less than .

Effect of time constant

In practice k/σ is often increased to 2 or 3 (i.e. peak to peak modulating

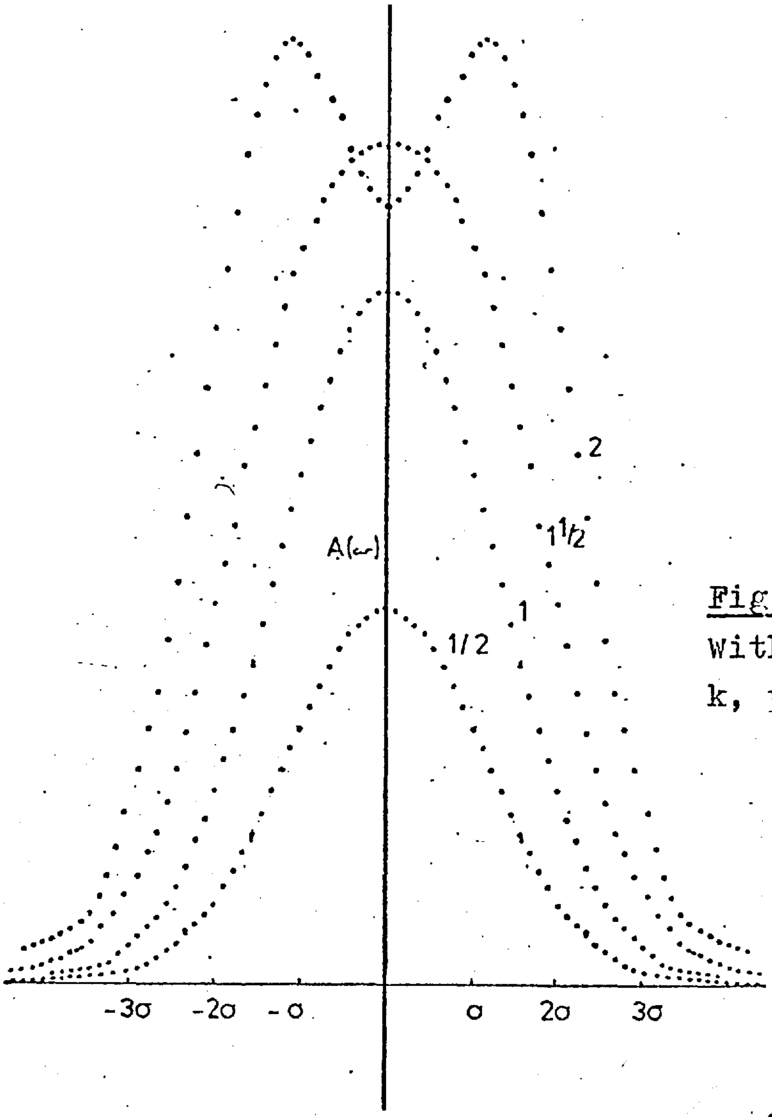

Fig.A4.5 Variation of $A(\omega)$ with modulating amplitude k, plotted for k= ½,1,1½,2. =1.

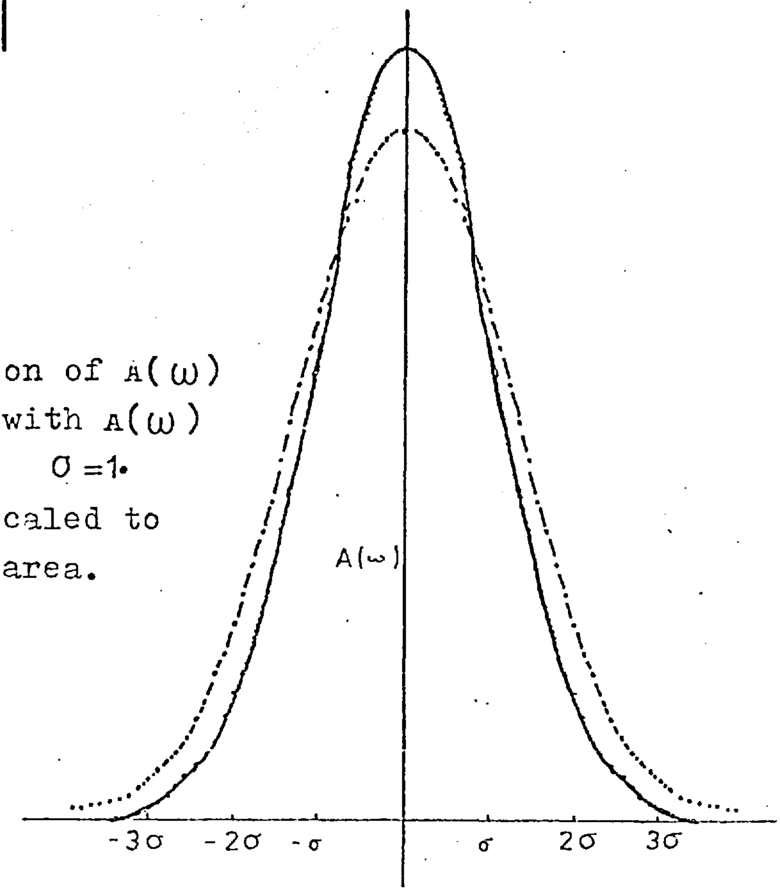

Fig.A4.6 Comparison of $A(\omega)$ k=0, solid line, with $A(\omega)$ k=1, dotted line. $\sigma=1$. Both curves are scaled to contain the same area.

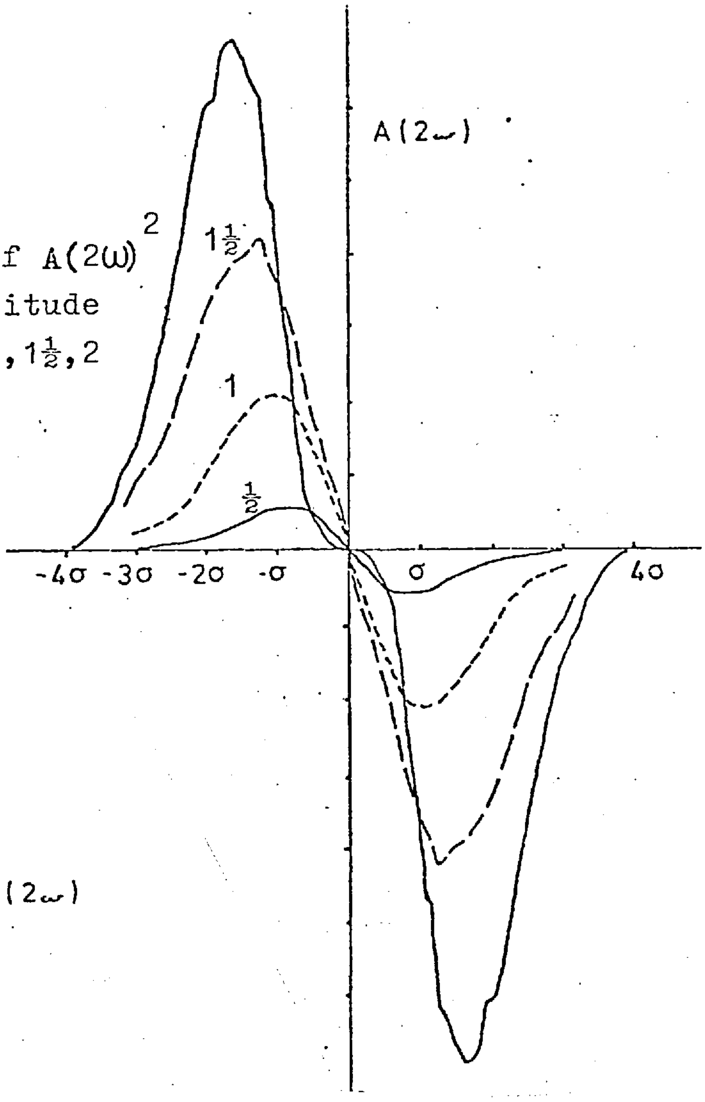

Fig.A4.7 Variation of A(2ω) with modulation amplitude k, plotted for $k=\frac{1}{2},1,1\frac{1}{2},2$ in units of .

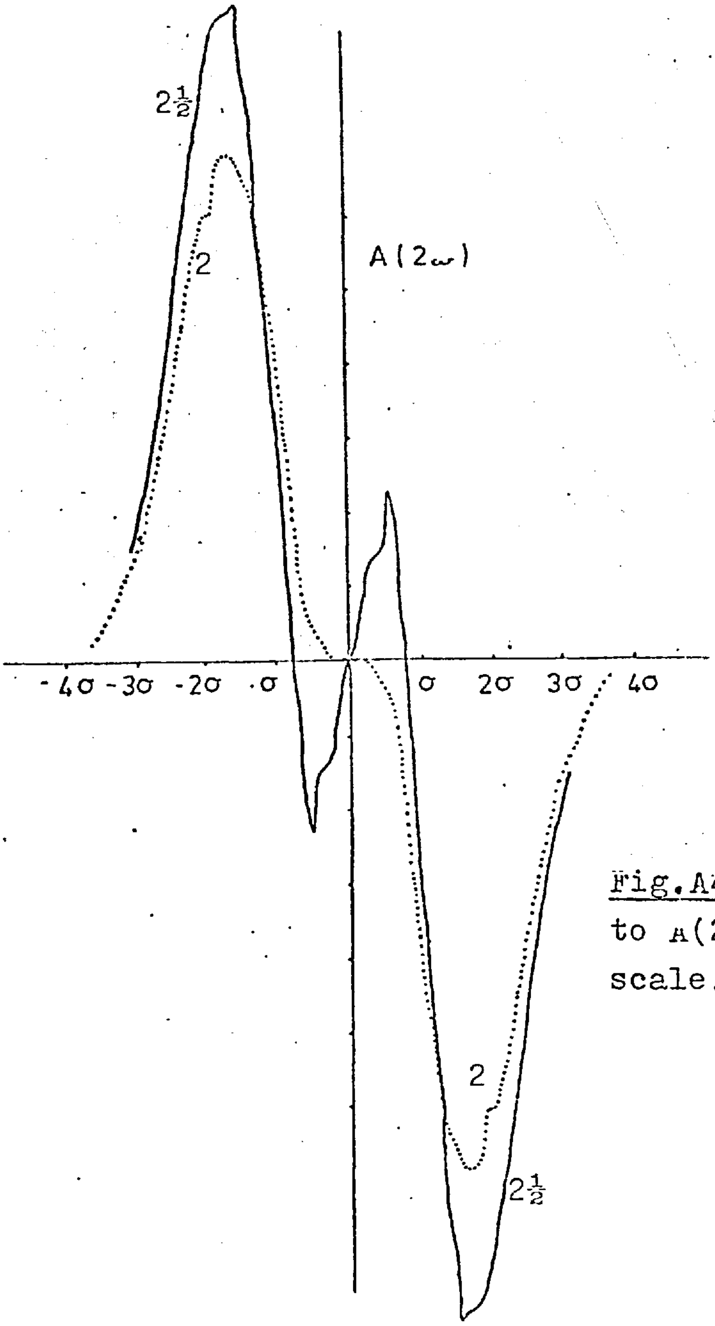

Fig.A4.8 A(2ω), k=2 compared to A(2ω), $k=2\frac{1}{2}$ on the same scale.

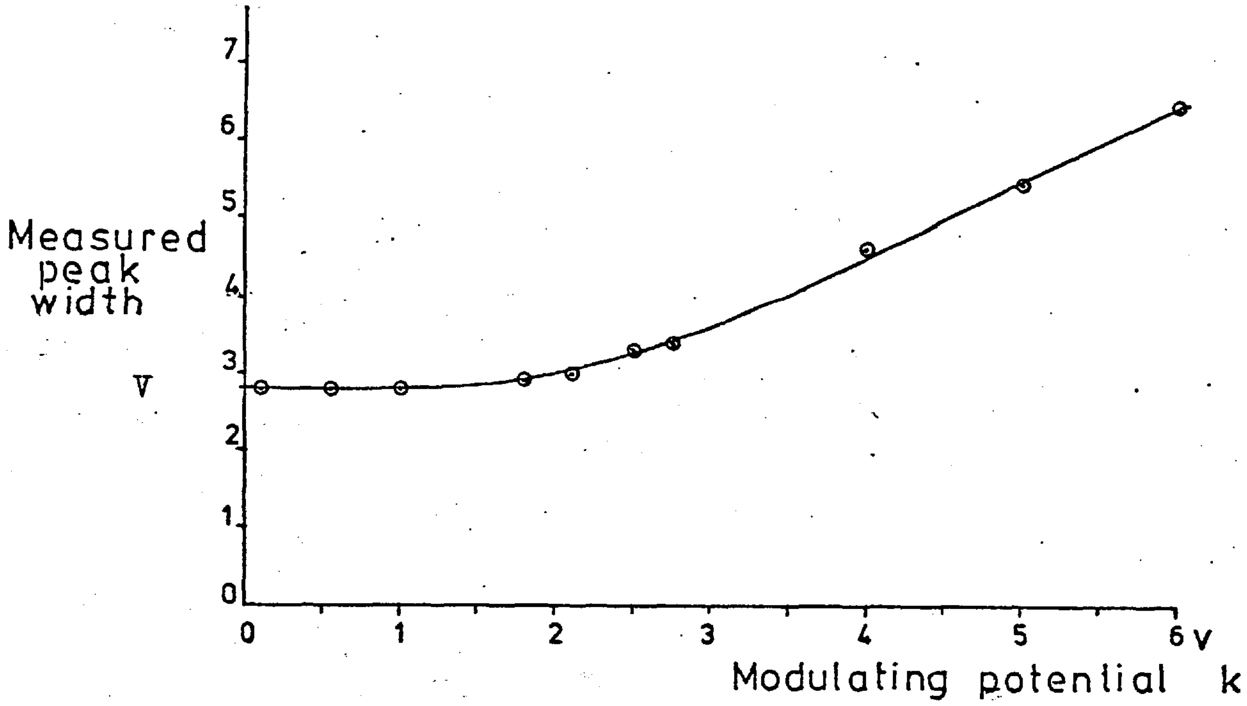

Fig.A4.9 Peak width of the analyser differential transfer function plotted as a function the modulating potential k.
Major distortion does not result until $k/\sigma = 1$.

voltage is up to 2.5 times larger than the full width at half height of the peak), yet the curve, $A(\omega)$ vs E, resulting, still appears as a broad Gaussian without the dip predicted in Fig. A4.5.

The reason for this is that the peak shape is smoothed by a long time constant. In practice, k is increased in order to obtain a better signal to noise ratio. This implies the use of the longest possible time constant consistent with the expected slew rate at the output of the PSD.

Whilst a particular slew rate may be suitable for detecting the original Gaussian curve, it may not be fast enough to detect the change at the peak produced by $N''(E)$. Thus, the peak will not show the expected dip.

The effect is illustrated in Fig. A4.10, which shows the amplitude $A(\omega)$ both for a ratio of filter time constant/scan rate of 0 and 2 in units of $1/\sigma$. These were calculated by averaging the signal over the time constant, rather than including an exponential decay, and therefore the latter curve does not show the shift in position that would normally be expected.

The effect of averaging produced by the time constant will obviously be more marked in the case of the first harmonic ($A(2\omega)$) where the slew rates are correspondingly faster.

Summary

An increase in the modulating amplitude k, together with use of a long time constant, can produce an improvement in signal to noise ratio without apparent change in the peak shape or position.

As has been pointed out, this common practice can be misleading, as it results in great distortion of the peak heights, and, if too long a time constant is used, peak areas.

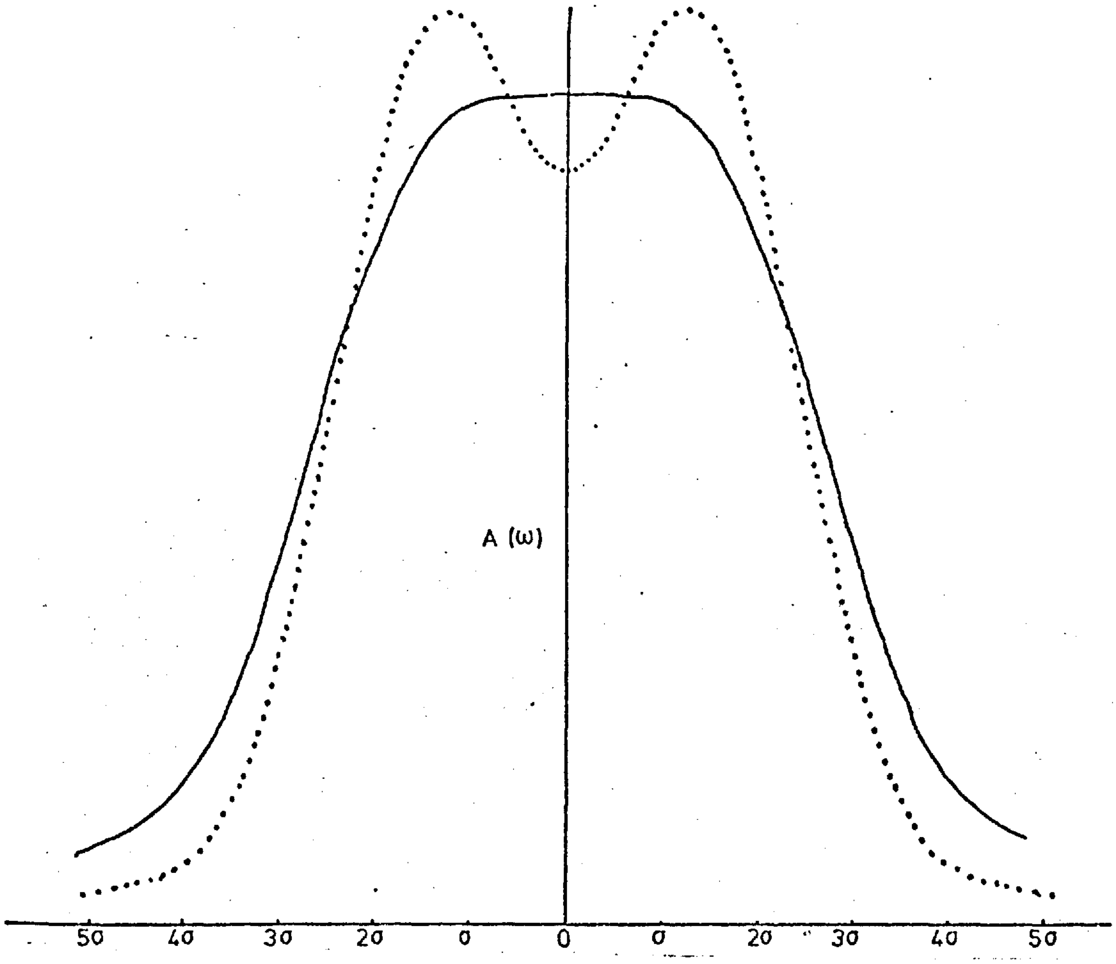

Fig.A4.10 The differential amplitude of the function $\int N(E)dE$ for k/σ =2 using different scan rates. Ratio of filter time constant to scan rate of 0, dotted and 2, solid line, in units of 1/σ are shown.

If consistent results are to be obtained using a PSD, the amplitude k must be restricted to σ, where this is interpreted as the half width at half height of the narrowest peak of interest.

The time constant should be kept below half the time required to cross between the half height points of the narrowest peak.

If these conditions cannot be met the results may be seriously distorted.

A4.3

The uses of higher order differential spectra

Several workers have suggested the use of $-d^2N(E)/dE^2$, $(-N''(E))$ for increasing the visibility, and therefore the accuracy of determination of peak positions in N(E) spectra. In particular this has been applied to low energy spectra. (Ibach and Rowe 1974, Rowe and Ibach, 1974). The use is such a context deserves some comment.

The main argument against using the second derivative of N(E) with respect to E to determine peak positions is that the positive going parts of the former curve may obscure or shift other smaller peaks in a rather unpredictable fashion.

Consider a Gaussian peak

$$N(E) = \frac{1}{\sigma(2\pi)^{1/2}} \exp \frac{-E^2}{2\sigma^2} \qquad \text{A4.9}$$

normalised to unit area and centered at E = 0.

It is straightforward to examine the effect on the peak height and position of a small peak of area a < 1 when a second peak of area unity is placed at a distance b from it. To simplify the calculation, σ is taken as 1. The two peaks are represented by the function

$$N(E) = \frac{1}{(2\pi)^{1/2}} \left[a \exp \frac{-E^2}{2} + \exp \frac{-(E-b)^2}{2} \right] \qquad \text{A4.10}$$

Similarly, N (E) can be examined.

$$N''(E) = \frac{1}{(2\pi)^{1/2}} \left[a(E^2-1) \exp \frac{-E^2}{2} + ((E-b)^2-1) \exp \frac{-(E-b)^2}{2} \right] \qquad \text{A4.11}$$

The results of doing this for $0.1 \leqslant a \leqslant 1$ are summarised in Fig. A4.11 for N(E) and Fig. A4.2 for N''(E), which show the peak separations at which two separate peaks can just be resolved on the N (E) curve. It is clear that once a peak

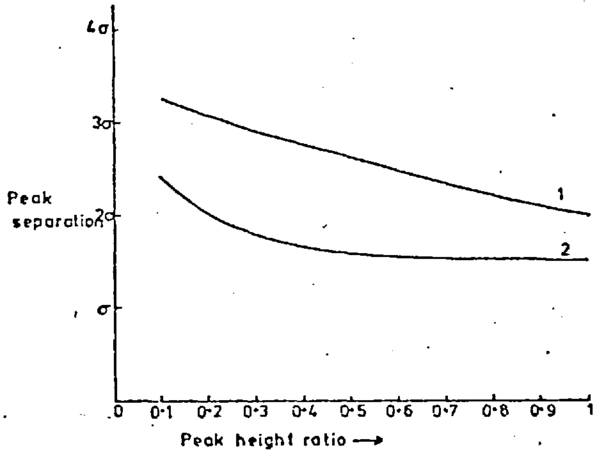

Fig.A4.11 Resolution of two Gaussian peaks of differing height.

The plot shows the peak separation at which the peaks are resolved (1) and the apparent separation when they are just resolved, (2).

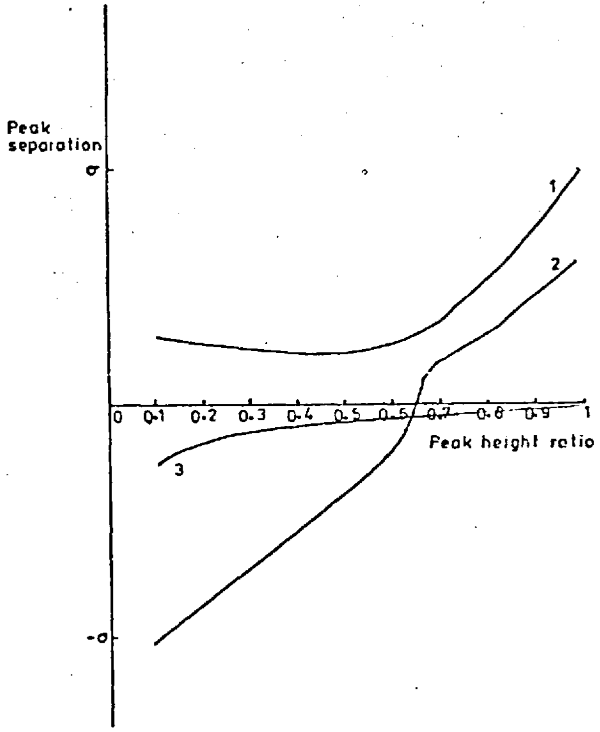

Fig.A4.12 Resolution of two Gaussian peaks of differing height by detection of the differential. 1), 2) as Fig.A4.11

3) difference between true and apparent position of smaller peak.

has been resolved using the N(E) curve, its position is best found using N ''(E). This is shown in Figs. A4.13 and A4.14.

Several conclusions can be drawn from these results :

1) It is a mistake to assume (as did Ibach and Rowe) that the resolution of an analyser for two Gaussian peaks is equal to the full width at half height of the second derivative minimum (the maximum of - N '' (E)) ie 1.2σ. Peaks can be resolved down to 0.4σ but unambiguous determination of peak position is only given when separation is at least 1.6σ. Exact determination of both positions (from N '' (E)) and height (from N(E) and N '' (E)) can only be achieved when the separation exceeds 2.4σ. This corresponds to full width at half height of the N(E) curve.

2) There is considerable difficulty in determination of the exact position of a small peak less than 2σ from a larger one. Only two peaks with σ the same have been considered, and if widely differing values were expected, the resolution of position would be ambiguous using even N ''(E). This would be particularly evident when σ for the small peak was larger.

3) The second derivative of a Gaussian is well defined. This is not true of any arbitrary curve, and care must be exercised in interpretation of an unknown system.

4) The use of the second derivative does reduce any background of the form $B(E) = g_1 + g_2 E + g_3 E^2$ to $B(E) = 2g_3$ is independent of energy.

It is often the case that background due to multiple inelastic scattering is of this form, and can strongly influence the resolution obtained from an N(E) curve. It is for this reason that N '(E) is so often used in Auger spectroscopy.

Relative availability of N ' (E), N '' (E)

In the discussion so far, it has been assumed that N(E), N '(E) and N '' (E) can all be obtained with equal ease from any particular system, and their relative merits

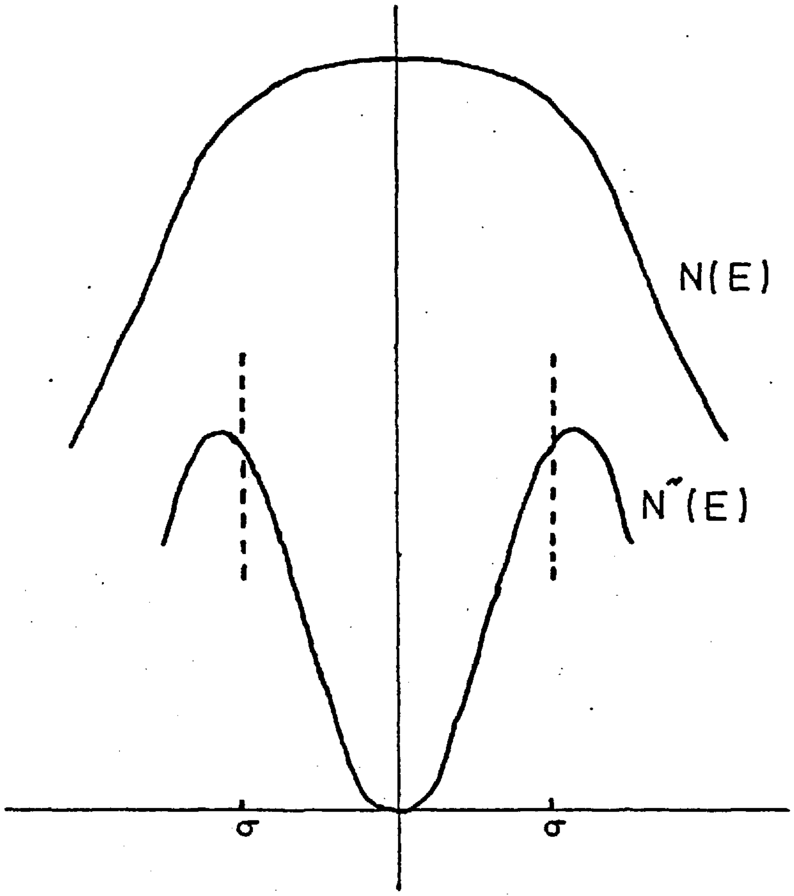

Fig.A4.13 N(E) and N (E) for two Gaussian peaks separated by 2σ. The N(E) curve does not resolve the two peaks while the N (E) curve does, though it shows a displaced peak position (dotted). The peaks are of equal size.

have been discussed on this assumption.

In practice, signal to noise ratio is of prime importance.

There are two possible ways of obtaining $N''(E)$:

i) by taking the third derivative in a non-dispersive analyser

or ii) by taking the second derivative in a dispersive analyser. In either case, these are obtained using the phase sensitive detection methods already described.

In the former case, the ratio $N''(E_o)/N(E_o)$ will be $k^2/24$, where k is the modulating amplitude, with the noise remaining constant.

$$I_{noise} = [2eB\int_{E_0}^{\infty} N(E)\,dE]^{1/2}$$

In the latter case, the ratio of $N''(E_o)/N(E_o)$ is $k^2/4$ and the noise current is

$$I_{noise} = [2eB\,N(E_0)\Delta E_0]^{1/2}$$

where E is the energy window of the analyser.

The maximum amplitude of N(E) and N''(E) of a Gaussian are equal, thus, taking $k/\sigma = 1$ there is a loss of signal of a factor of 4 in the dispersive analyser and 24 in the non-dispersive analyser. The time constant of the PSD should also be decreased to cope with the increased slew rate of the higher derivatives. Including this results in a total drop in signal to noise ratio of 8, for dispersive, and 48, for non-dispersive analysers.

While a fall of 18 dB in the dispersive curve where the signal to noise ratio is good is acceptable, a drop of 34 dB in the already poor signal to noise ratio of a non-dispersive analyser would be impractical.

Auger spectroscopy

In Auger spectroscopy N (E) is often used with both dispersive and non-dispersive analysers to obtain peak positions. If N'' (E) was used the signal to noise ratio would

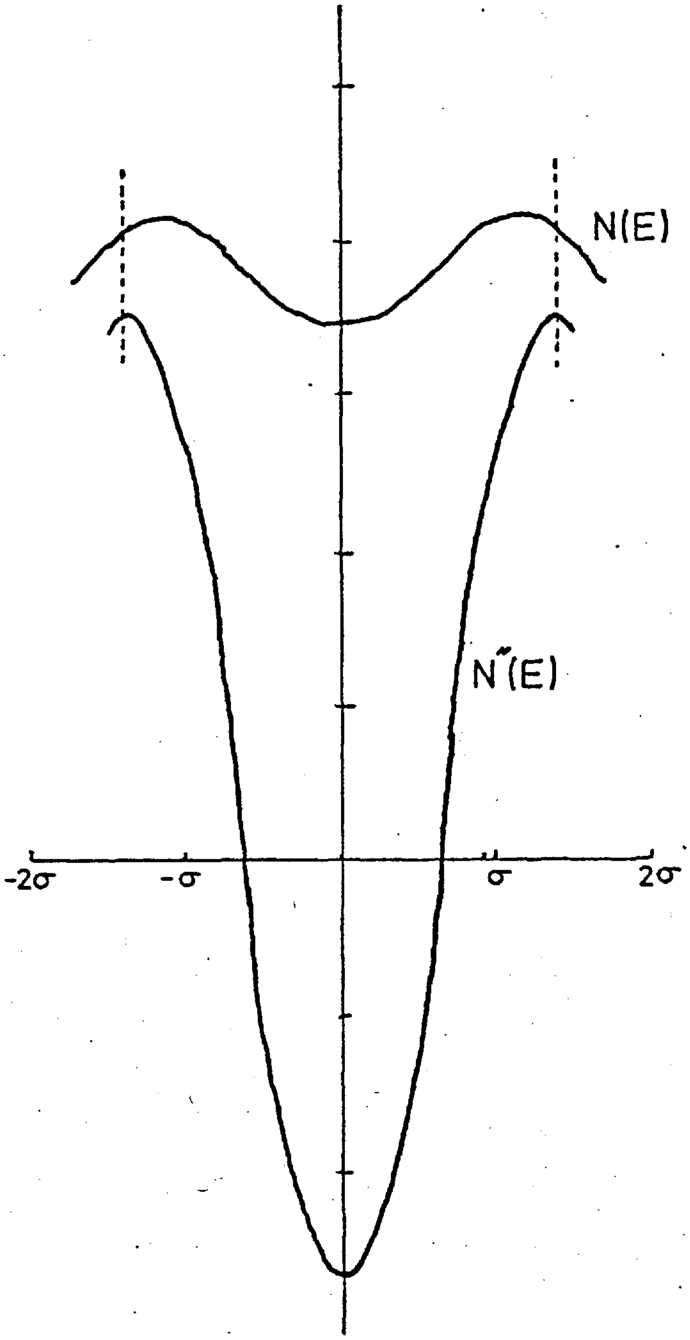

<u>Fig.A4.14</u> N(E) and N (E) for two similar Gaussian peaks separated by 2.8σ. The peaks are resolved by both functions. N (E) predicts the position correctly whereas N(E) shifts them towards each other.

fall by 10 dB and 14 dB respectively, again assuming $k/\sigma \approx 1$ and a Gaussian peak shape.

Summary

The use of the second differential $N''(E)$ of $N(E)$ to determine peak positions is a very reliable method, as long as it is remembered to treat apparent separations of less than 2σ with suspicion. Greater accuracy can be obtained if $N(E)$ and $N''(E)$ can be used in conjunction (cf. Figs. A4.13 and A4.14) with each other, so that the presence of two peaks is shown by $N(E)$, but their position is given by $N''(E)$.

The use of $N''(E)$ as opposed to $N'(E)$ for the detection of Auger electrons should allow better peak position determination, but at the cost of a drop in signal current.

In conclusion, it would seem that the routine use of $N''(E)$ would be practical with a dispersive analyser, but that the problem of signal to noise ratio and generation of a suitable reference frequency would preclude its use in a non-dispersive analyser in all but a few high signal applications.

All calculations were done using a programmable calculator (Texas T158).

APPENDIX 5

Ray tracing

Ray tracing was used for two separate purposes. Firstly, simple ray tracing was employed to obtain a suitable shape for the mesh mount, and, in particular, what depth it should have in relation to its diameter. Secondly, to explain the enhanced transmission that occurred through the mesh when the potential of the mesh was made equal to the energy of the beam with the beam incident normally on the mesh.

Two different methods were employed to obtain the field plots, but in both cases the same method was used for ray tracing.

A5.1 Conducting paper

The method used to obtain the field plots around the mesh mount was to use conducting (Teledeltos) paper. This conducting paper has a uniform resistivity, and thus by painting on the boundaries of the field region with highly conducting paint, the paper can be used in the same way as an electrolytic tank (Klemperer and Barnett, 1971). The field boundaries were painted, using thick silver paint, and their relative potentials fixed, using a dry battery.

The resistance of the painted boundaries was about 40 000 Ωm^{-1} when dry. Because of this, the equipotential boundaries were connected to the battery in several places. This was done to avoid non-uniformity of the potentials.

The field plotting was done using a potentiometer and digital voltmeter, as shown in Fig. A5.1. The potentiometer was set to a particular voltage, and then connected via the voltmeter to a pencil lead. A 2B pencil sharpened at both ends was found to work well. The pencil was touched lightly on the paper, and when a null reading was found a mark was made by pressing harder. With practice, the fields

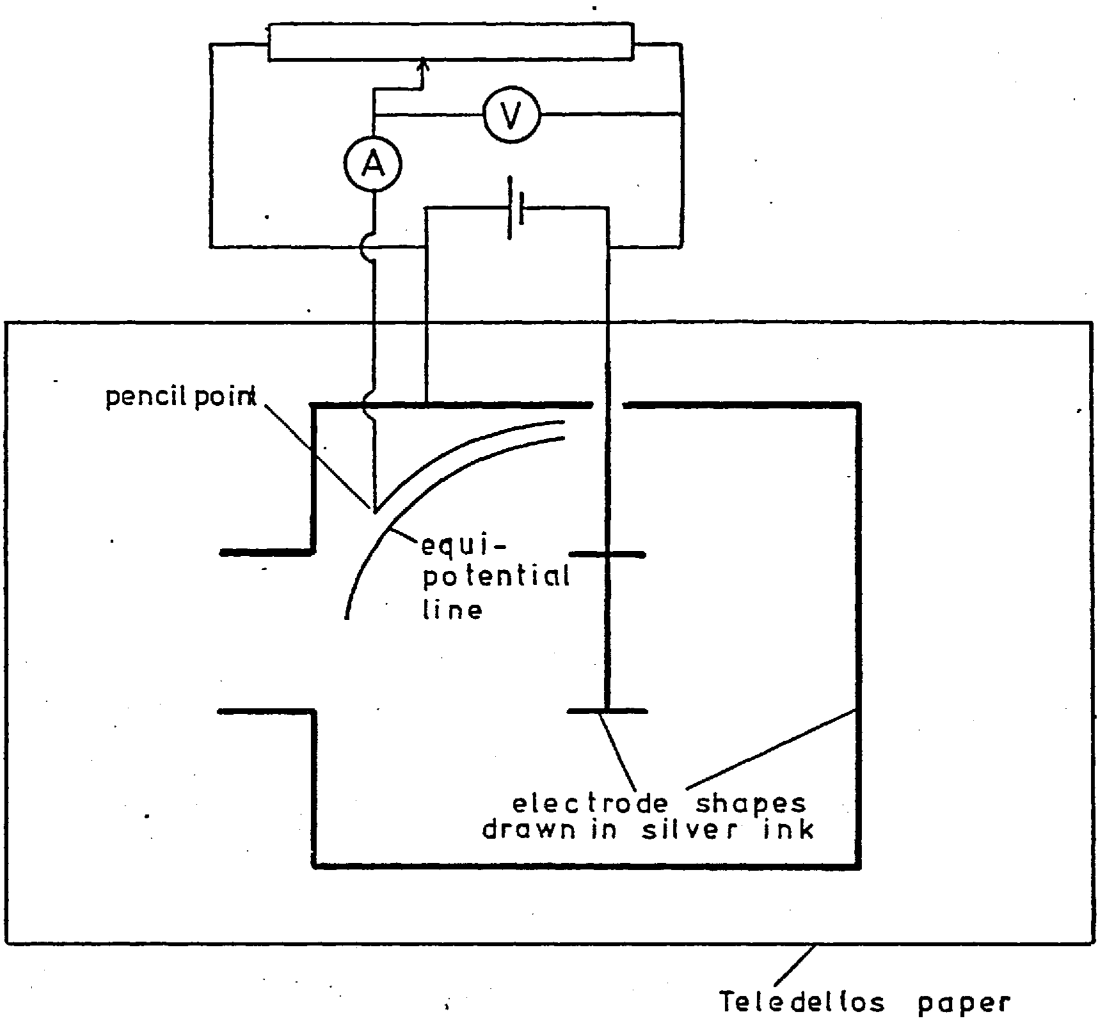

Fig.A5.1 Field plotting using Teledeltos, conducting, paper.

could be plotted very quickly, though accuracy was obviously limited by the sensitivity of the voltmeter and the resistance of the paper (Allen, 1968).

A5.2 Computer plots

The system of field plotting using Teledeltos paper could not be used for the fields around the mesh for two reasons : firstly, greater accuracy was required of the mesh shape and of the field plot, and secondly, the mesh had to show a repeat, i.e. there had to be two boundaries along which the potential was undefined and the field would be perpendicular to the boundary. These boundaries could be constructed using conducting paper, but would not be accurate because of other adjacent surfaces.

The plots were made using a program developed by K.W. Jones for his work on electron streak cameras (Jones, (private communication) ~~1980~~). His help in obtaining these plots was most valuable and I am very pleased to acknowledge it. The mesh was measured using a scanning electron micrograph, from which it was found that one face was nearly flat. This was then represented as a set of matrix points, as was the earthed plane. The intervening matrix potentials were calculated by an iterative solution of Laplace's equation in two dimensions, similar in concept to that given by Klemperer and Barnett (1971) and based on the methods of Buckingham (1962). This method allowed the inclusion of boundary conditions representing lines of force rather than equipotentials. The mesh repeat was thus taken into account, whilst only computing the field in front of half a mesh width, i.e. between the mesh bar and the centre of the mesh.

Initially, the whole region in front of one mesh was considered, and this was gradually cut down until the potentials in a region of only one mesh spacing on either side of the mesh were calculated. The potential at the plane boundary was not given by

$$V' = \frac{d\,V}{D} \tag{A5.1}$$

where d = distance from mesh to plane boundary

V = potential of ground relative to analyser

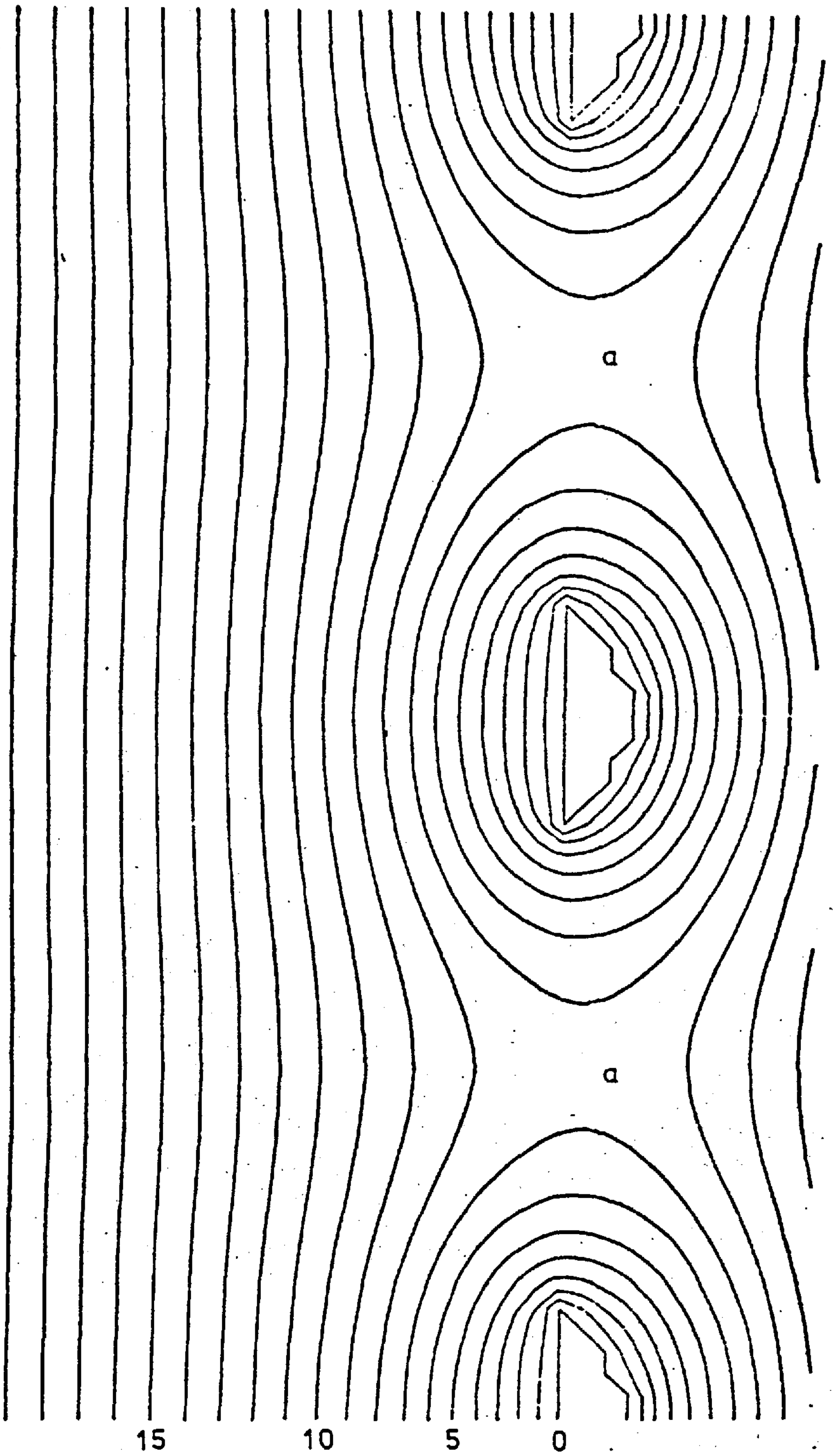

Fig.A5.2 Field near to a mesh with D section bars. The field shown corresponds with the analyser operated at 20keV. The marked potentials are in volts below mesh potential.

D = distance between mesh and anode.

The reason for this is that the field around the mesh was greater than the average field and thus the potential at a point close to the mesh is higher than would be predicted by simple proportion. The exact potential was found by considering the potential gradient at several mesh spacings and adjusting it so that the gradient there had the average value V/D.

A typical field plot is shown in Fig. A5.2. The potentials were calculated on both sides of the mesh but only plotted on one side because of the limitations of the graphics printer. The repetition was done by photocopying.

A5.3 Ray tracing

The ray tracing was done by hand, as no suitable program was available to do it. The technique used was to plot trajectories, using the electron equivalent of Snell's law. (Klemperer and Barnett, 1971).

$$\frac{\sin \vartheta_1}{\sin \vartheta_2} = \sqrt{\frac{V_2}{V_1}} \qquad \text{A5.2}$$

where ϑ_1 = angle between normal to equipotential and electron path in potential region V_1

ϑ_2 = angle between normal to equipotential and electron path in potential region V_2

V_1, V_2 are potentials on either side of an equipotential line. The potentials are expressed in Volts relative to the stationary electron as zero and thus are equal in magnitude to the electron energy at those points.

In practice, ϑ_1 and ϑ_2 were not measured directly. The method adopted was to align the field plot on a draining board and to measure the angles ϑ, α_1 and α_2 (Fig. A5.3). The angle between the normal and the beam is thus ($\alpha_1 - \vartheta$) in the region of potential V_1 and ($\alpha_2 - \vartheta$) in the region of potential V_2.

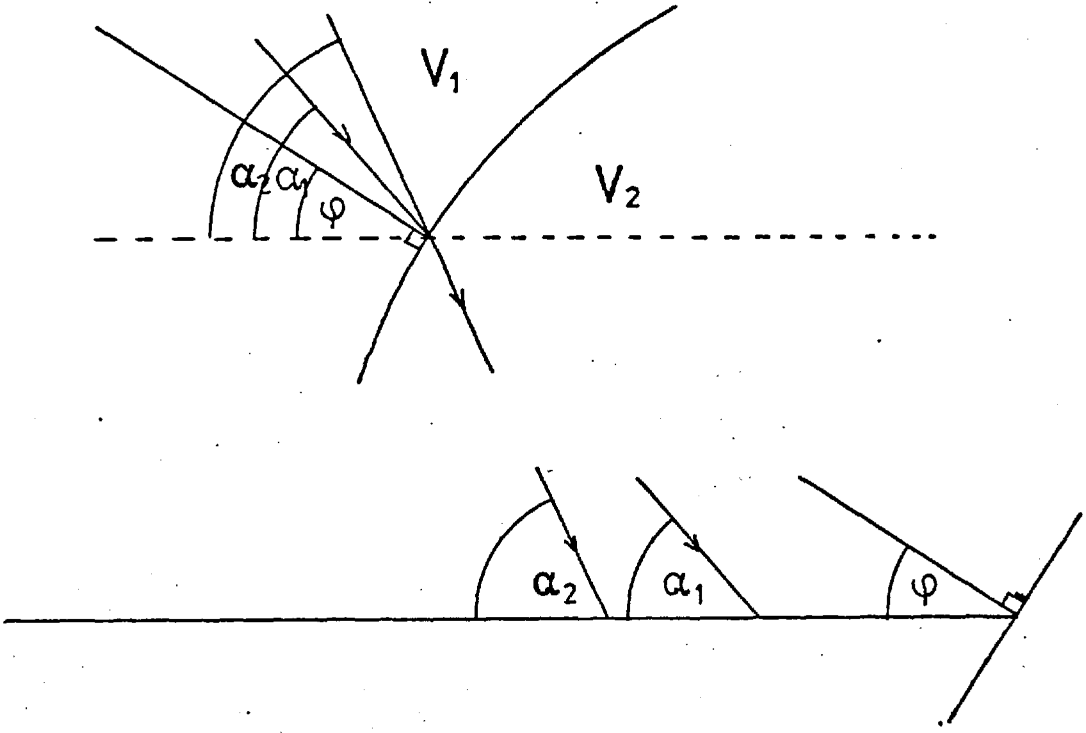

A53

Fig.A5.3 Angles used in ray tracing

α_1 = angle between incident beam and horizontal.

α_2 = angle between refracted ray and horizontal.

φ = angle between normal to the equipotential and horizontal.

Thus,

$$\alpha_2 = \sin^{-1} (\sin (\alpha_1 - \vartheta) \sqrt{V_1 / V_2}) + \vartheta \qquad \text{A5.3}$$

The reason for this apparently complex method is that once α_1 has been measured, a complete trajectory calculation can be done simply by measuring ϑ at each intersection of the beam with an equipotential. The calculations were done using a programmable calculator initially fed with α_1 and V_1 . The equipotentials are plotted at one volt intervals, thus $V_2 = V_1 - 1$, and successive values of ϑ were all that were required. This avoids a cumulative error in the beam angle for if a slight error is made in plotting a particular value of ϑ it does not carry forward. As the equipotentials do not change slope very quickly a small error in the points where the electrons meet them does not make a significant difference to the angles between them.

A5.4 Initial trajectories

Only part of the path of the electrons through the retarding field was calculated, thus the angle of the electron beam relative to the mesh as it enters the calculated region must be found from the angle at which it enters the retarding field. It was known that when a good cut off characteristic was obtained, the apparent energy shift of the elastic beam was 15 eV below the true primary beam energy. The transverse component of the electron velocity would be proportional to the square root of this energy difference. The total energy of the electron entering the region is numerically equal to the potential at the leftmost edge of the field (Figs. A5.3, A5.4, A5.5). The angle of entry, ϑ , is thus given by $\vartheta = \sin^{-1}$ (energy difference/total energy)$^{\frac{1}{2}}$. Having established the trajectories of the electrons, the effective aperture of the mesh for a given beam energy and angle of entry could be determined.

Fig. A5.4 shows the geometrical aperture 2a, and the effective aperture 2a' for

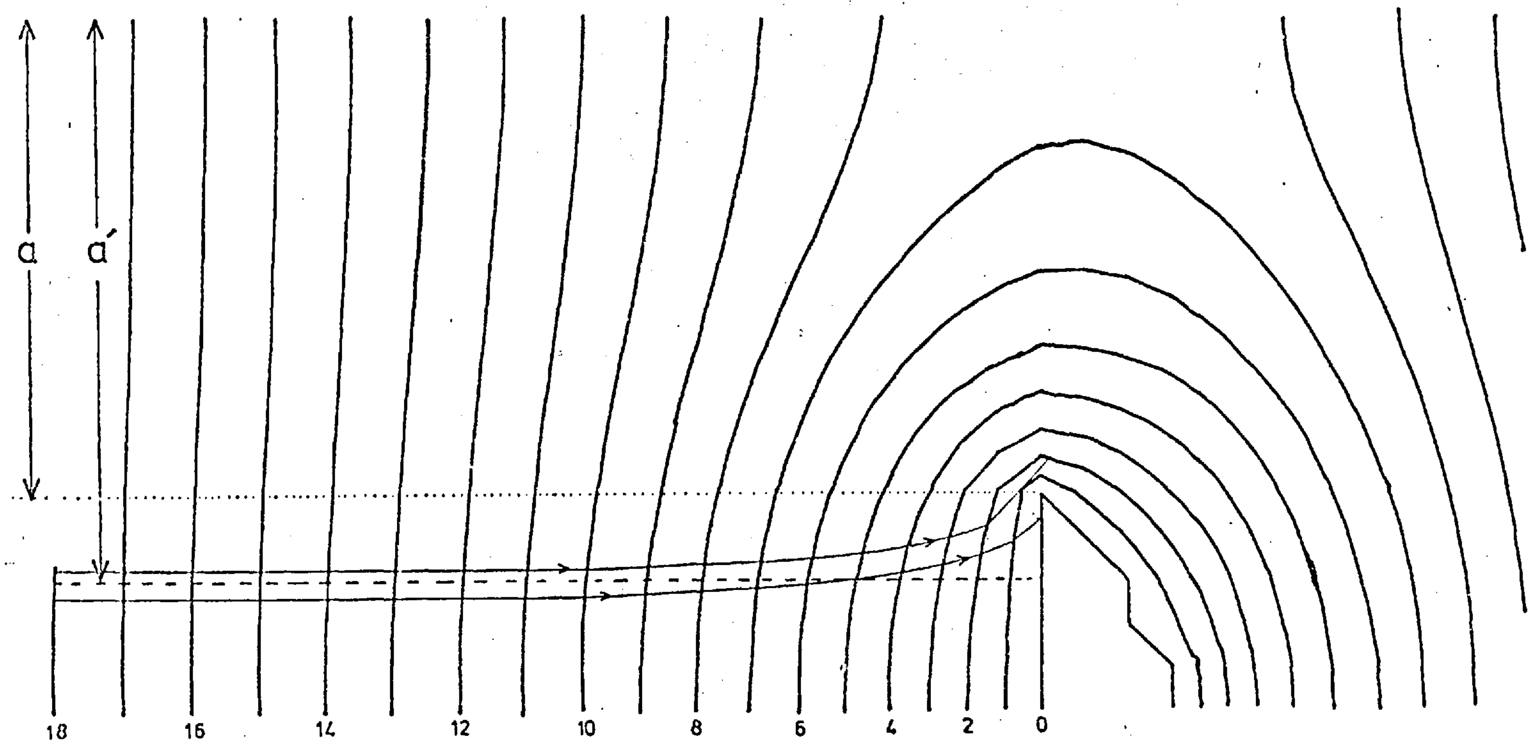

Fig.A5.4 Trajectories of electrons near to the mesh. The electrons are incident normally to the mesh and have zero potential energy with respect to the bars.
The effective aperture of the mesh, a', is much larger than the geometric aperture, a.

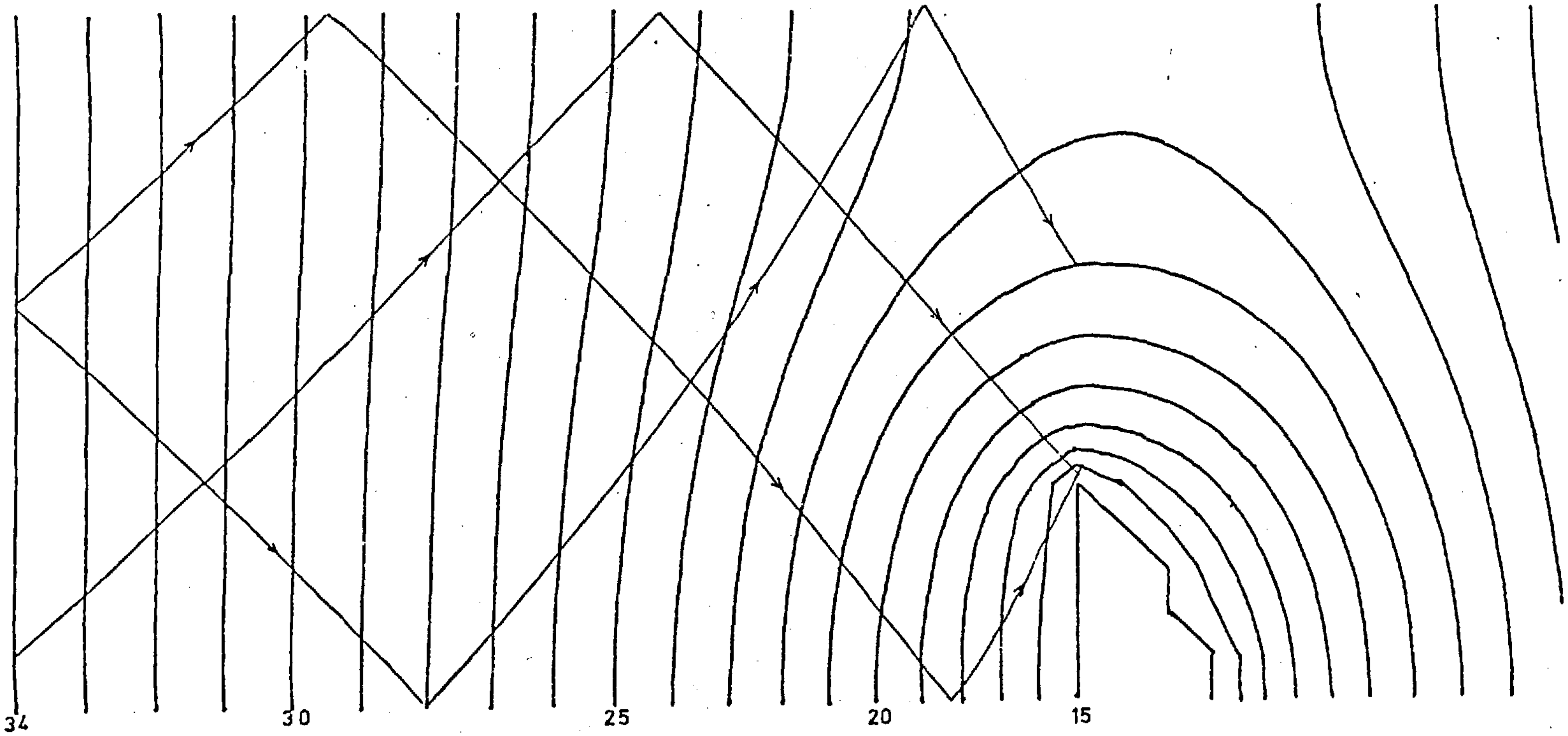

Fig.A5.5 Trajectories near the mesh of electrons entering the field at an angle of 0.040 rad to the normal.
The effective aperture is very similar to to geometric aperture.

electrons entering normal to the mesh surface. The effective transmission of the mesh is thus $4a'^2$, as opposed to the expected value of $4a^2$.

Electrons of a higher kinetic energy entering the mesh region will not be deviated so much by the field when they pass the mesh and thus the effective aperture will be smaller. This diagram alone is sufficient to explain the enhanced transmission observed experimentally.

A5.5 Mesh symmetry

Electrons which travel at a large angle to the mesh often leave the edge of the field. The symmetry of the system allowed the electron path to be continued by reflecting it from the boundary of the field (Fig. A5.5).

The initial angles between the normal to the mesh and the beam are surprisingly high before enhanced transmission is entirely eliminated. Fig. A5.5 shows the path of electrons through the mesh set at an angle of 0.045 rad. to the beam just before the beam is cut off. The effective aperture a is the same as the geometrical aperture a_o and thus no enhanced transmission occurs. This is similar to the experimentally established angle required for an ideal cut off characteristic (Chapter 5).

A5.6 Analyser transfer function

The analyser transfer function was determined by finding the effective aperture as the mesh potential was lowered from the accelerating potential. This involved plotting a large number of trajectories by hand; however, the method used above, together with a programmable calculator, reduced the time to about 5 minutes per trajectory.

The effective apertures were plotted against analyser potential for various angles of beam incidence. Figs. 5.13 and 5.14 show two such curves which are further discussed in Chapter 5.

A5.7 Accuracy

The method of ray tracing cannot be regarded as very accurate; however, its accuracy is sufficient to demonstrate the effects that were observed experimentally. The method was found to give reproducible trajectories. Several sets of trajectories were repeated and led to the conclusion that the effective aperture could be estimated to within 5%.

APPENDIX 6

Program used to calculate cut-off potential for electrons entering a wedge shaped potential system

The program is based on the assumption that the angle of one equipotential relative to the next, α, is given by :

$$\alpha = \gamma / n \qquad \text{A6.1}$$

where γ = angle between normal to mesh and normal to entrance aperture

n = no. of equipotentials

The relation between the angle of incidence, ϑ_1, of the beam on an equipotential and the refracted angle, ϑ_2, is

$$\frac{\sin \vartheta_1}{\sin \vartheta_2} = \sqrt{\frac{V_2}{V_1}} \qquad \text{A6.2}$$

where V_1 and V_2 are the potentials on each side of the equipotential (cf. A5.2)

On movement from one equipotential to the next the previous refracted angle, ϑ_2, is related to the new angle of incidence, ϑ_1',

$$\vartheta_1' = \vartheta_2 + \alpha \qquad \text{A6.3}$$

The program, Fig. A6.1, was run with initial conditions $\vartheta_1 = 0$, $n = 20,000$ for various values of γ. In each case the program was checked for cumulative errors by putting $\vartheta_1 = \gamma$, $n = 20,000$. This always gave the expected cut off potential $V = 20,000 \sin^2 \gamma$.

The interval between equipotentials was taken as 1eV.

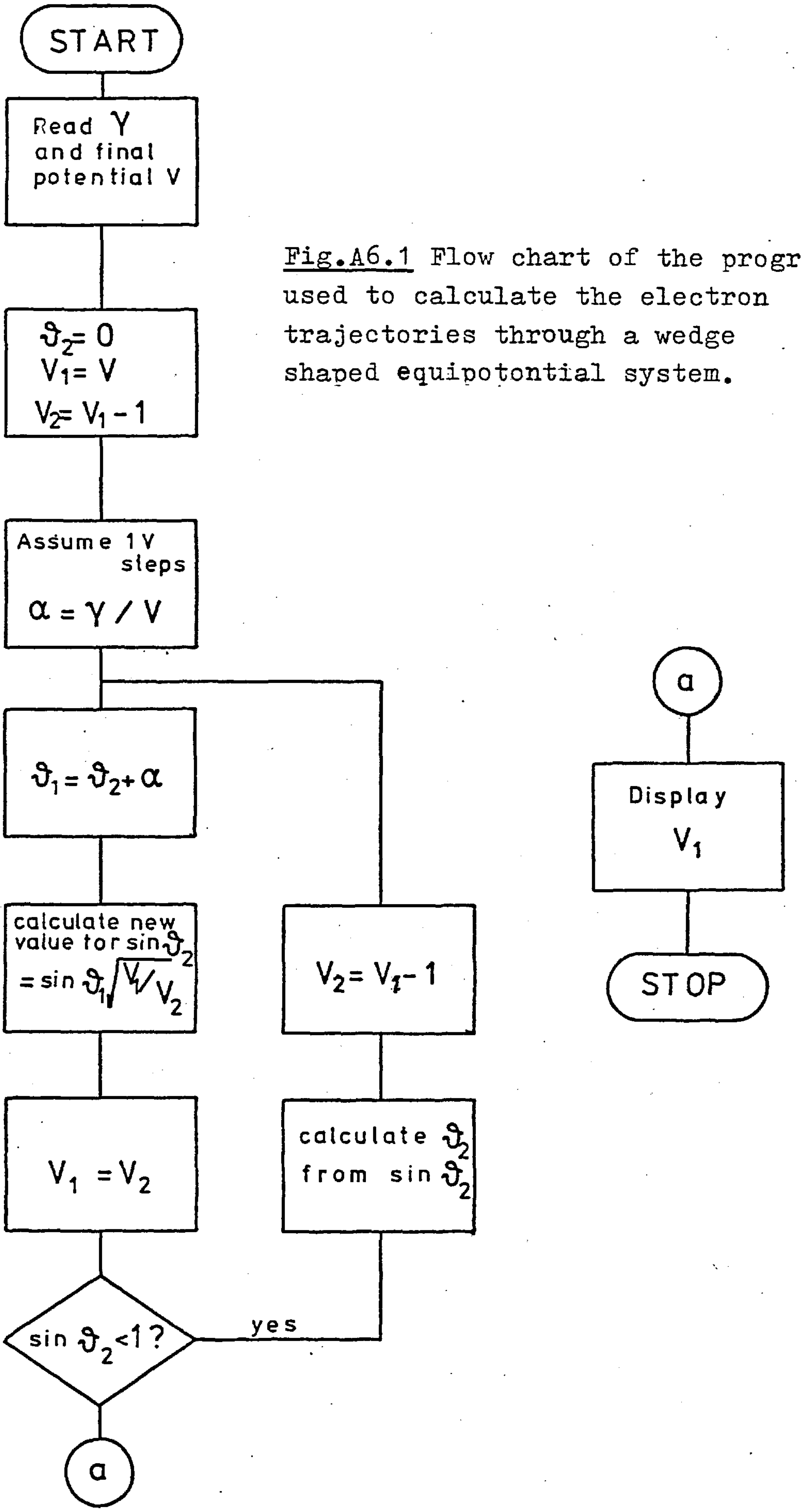

Fig.A6.1 Flow chart of the program used to calculate the electron trajectories through a wedge shaped equipotontial system.

APPENDIX 7

Calculation of the intensity expected at the analyser of 20 keV electrons backscattered through 150° by a gold surface normal to the incident beam

The intensity per unit solid angle of electrons scattered from a flat sample placed normally with respect to the incident beam is approximately proportional to the cosine of the scattering angle. The intensity di scattered into area da at an angle φ to the incident beam is

$$di = | \, i_0 \cos \varphi \;\; da \, | \qquad \text{A7.1}$$

i_o is the intensity per unit solid angle of the electrons backscattered along the reciprocal direction to that of the incident beam.

The total scattered current I is given by the integral over the backscattered hemisphere (Fig. A7.1) of di. Thus

$$I = \int_{\text{hemisphere}} | \, i_0 \cos \varphi \, | \, da \qquad \text{A7.2}$$

$$I = \int_{90}^{180} | i_0 \cos \varphi \,.\, 2\pi r^2 . | \sin \varphi . d \qquad \text{A7.3}$$

$$I = i_0 \pi r^2 \qquad \text{A7.4}$$

Thus given the total backscattered current the intensity per unit solid angle, i, at any scattering angle, φ, to the beam is given by

$$\begin{aligned} i &= i_0 \, | \cos \varphi \, | \\ &= I/\pi \,.\, | \cos \varphi \, | \end{aligned} \qquad \text{A7.5}$$

Thus the current scattered into an aperture of radius a at a distance r from the sample will be :

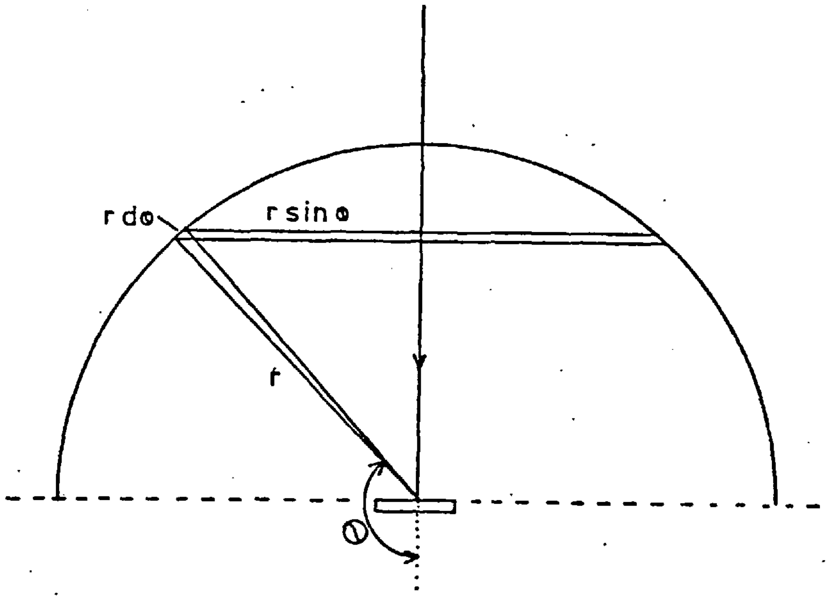

Fig.A7.1 Scattering geometry.

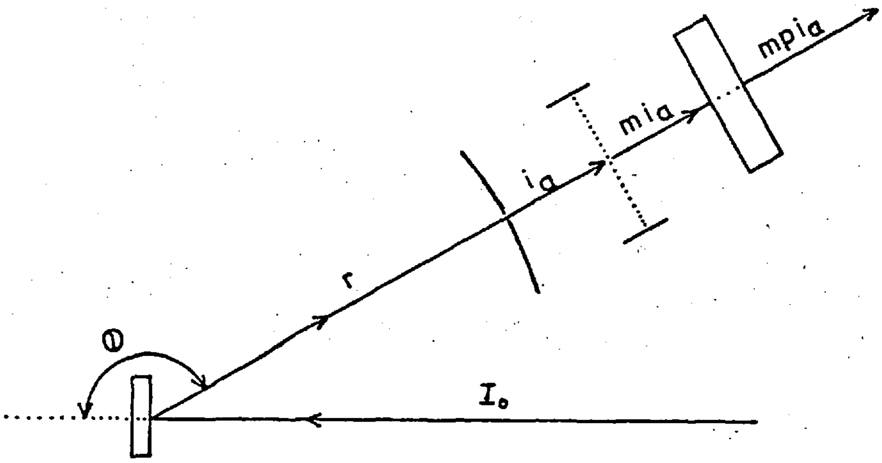

Fig.A7.2 Scattering parameters,see text.

$$i_a = I\,|\cos\varphi|\,a^2/r^2 \qquad \text{A7.6}$$

Assuming $\varphi \geqslant 90^\circ$

$$I = \eta\, I_o \qquad \text{A7.7}$$

where η is the backscattered fraction and I_o the beam incident on the specimen.

$$\therefore \quad i_a = \eta\, I_o|\cos\varphi|\,a^2/r^2 \qquad \text{A7.8}$$

This is the current entering the analyser. Only a fraction, m, of these electrons pass through the analyser, and of these only a fraction, p, produce a scintillation at the phosphor large enough to be registered above background (Fig. A7.2).

In the present work, one sample set of data was :

Material Au: $\eta = 0.5$ (Fig. A7.3)

$a = 1.4 \times 10^{-4}$ m

$r = 1.5 \times 10^{-1}$ m

$\varphi = 150^\circ$

$m = 0.57$

$p = 0.27$

i_φ measured $= 1.0 \times 10^4$ electrons/second

$I_o = 3 \times 10^{-8}$A

i_φ calculated $= 1.7 \times 10^{-15}$A

$\equiv 1.06 \times 10^4$ electrons/second

Values of η were taken from Bishop (1965)

The value of i_φ measured compared to that calculated is consistent within experimental error. Similar calculations were done to compare the expected and measured total currents received by the analyser for the other elements used (see Chapter 6), and all were found to be consistent within 10%. (Fig. A7.4).

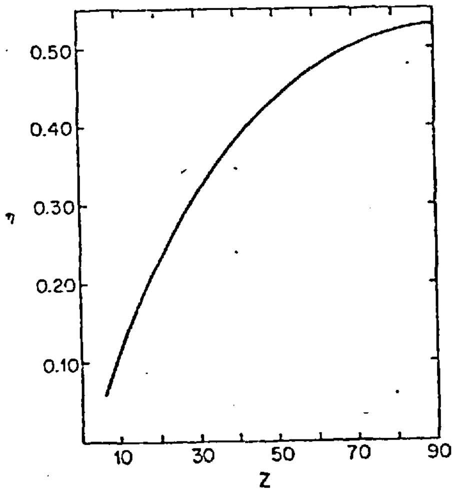

FIG. 3.8 Electron backscattering coefficient η as a function of Z at normal incidence at 30 kv. (*Data from Bishop 1966.*)

Fig.A7.3 Electron backscattering coefficients (Wells et al, 1974)

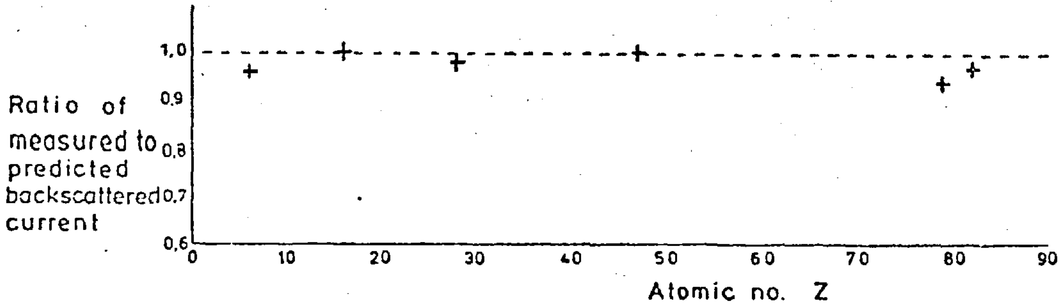

Fig.A7.4 Variation of the ratio of measured to predicted backscattered current with atomic number, Z.

ACKNOWLEDGEMENTS

I would like to thank Professor M. Blackman, F.R.S., and Dr. P.J. Dobson both for their suggestion of this project and for their help and encouragement throughout. I also thank the members of the Electron Diffraction Group with whom I had many helpful discussions.

I am pleased to acknowledge the help I received from Mr. K.W. Jones (Physics Department, I.C.S.T.) in calculating the fields within the spectrometer.

I am indebted to the Science Research Council for the provision of a maintenance grant, and to Miss Deanne Eastwood for typing and also correcting much of the punctuatio of this thesis.

Lastly I must thank my wife, Anne, for the time and help she has given, and the holidays she has lost to see this thesis finished.

R.S. SHORTER

September 1979

REFERENCES

1. A.P.T. Electronic Industries Ltd., Chertsey Rd., Byfleet, Sy.
2. AFANES'EV, V.P., YAVOR, S.Ya., 1975. Sov. Phys. - Tech. Phys. (20) 6 715
3. AKSELA, S., 1971. Rev. Sci. Inst. 42, 810
4. AKSELA, S., KARRAS, M., PESSA, M., SUONINEN, E., 1970. Rev. Sci. Inst. 41, 351
5. ALAM, M.N., 1952. Ph.D. Thesis, University of London (Imperial College)
6. ALAM, M.N., BLACKMAN, M., PASHLEY, D.W., 1954. Proc. Roy. Soc. Lond. A. 221, 224 - 242
7. ALLEN, J.D., WOLFE, J.P., SCHWEITZER, G.K., 1972. J. Mass Spect. & Ion Phys. 8, 81
8. ALLEN, J.D., DURHAM, J.D., SCHWEITZER, G.K., DEEDS, W.E., 1976. J.E.S.R.P. 8, 395 - 410
9. ALLEN, P.H.G., 1968. Phys. Education 3, 266
10. ANDERSON, W.H.J., LE POOLE, J.B., 1970. J. Sci. Inst. 3, 2, 121-6
11. ARCHARD, G.D., 1961. J. Appl. Phys. 32, 1505
12. ARNAL, F., VERDIER, P., VINCENSINI, P.D., 1969. C.r. hebd. Seanc. Acad. Sci., Paris 268, 1526
13. ARNOW, M.M., 1974. Phys. Rev. A 10, 1223 : 1976, J. Phys. E 9, 372
14. ARNOW, M.M., JONES, D.R., 1972. Rev. Sci. Inst. 43, 72
15. AVERY, N.R., 1976. J. Phys. E 9, 8, 676 - 9
16. BAKER, J.H., WILLIAMS, E.M., 1976. Vacuum 25, 409
17. BARNETT, M.E., 1973. Optik 38, 585
18. BASSETT, P.J., 1974. J. Phys. E 7, 461
19. BASSETT, P.J., GALLON, T.E., PRUTTON, M., 1972. J. Phys. E 5, 1008

20. BECK, A.H., ROBBIE, J.C., 1972. Int. J. Electron 33, 361

21. BETHE, H.A., ROSE, M.E., SMITH, L.P., 1938. Proc. Amer. Phil. Soc. 78, 573-585

22. BISHOP, H.E., 1965a. Proc. Phys. Soc. 85, 855-66 ; b. Proc. 4th Int. Conf. on x-ray Optics & Microanalysis, Paris.
1965, Brit. J. App. Phy. 18, 703

23. BISHOP, H.E., COAD, J.P., RIVIERE, J.C., 1972. JESRP 1, 389

24. BLACKSTOCK, A.W., RITCHIE, R.H., BIRKHOFF, R.D., 1955. Phys. Rev. 100, 1078

25. BLOCH, F., 1928. Zeit. Phys. 52, 555

26. BOERSCH, H., 1937. Zeit. Phys. 38, 1000 ; 1953, Zeit. Phys. 134, 156; 1954, Zeit. Phys. 139. 115; 1971, Proc. 25th Anniversary meeting of E.M.A.G. Inst. Phys. p.50

27. BOERSCH, H., GEIGER, J., STICKEL, W., 1964. Z. Phys. 180, 415

28. BOERSCH, H., MIESSNER, H., 1962. Zeit. Phys. 168, 298-304

29. BOERSCH, H., SCHWEDA, S., 1962. Z. Phys. 167, 1

30. BOLIN, P., TSE, F., BELL, W., MULCHAY, M., 1970. Insulation Circuits 16, 59

31. BORRMANN, G., 1941. Phys. Z. 42, 157 ; 1950, Z. Phys. 127, 297; 1955 a) Naturwiss. 42, 67 b) Naturwiss. 42, 68

32. BRACK, K., 1962. Z. Naturf. 17a, 1066

33. BRILLOUIN, L., 1946. Wave Propagation in Periodic Structures, 1946 McGraw-Hill, 1953 Dover

34. Brookdeal Electronics Ltd, Bracknell, Berkshire

35. Bryans Ltd., Willow Lane, Mitcham, Sy.

36. BUCKINGHAM, R.A., 1962. Numerical Methods in Computational Physics (London Pitman) p. 570

37. BUDAL, K., 1970. Report of University of Trondheim, Trondheim, Norway

38. BUNTING, C.D., 1971 a. Ph.D. Thesis, University of Cambridge ;
1971 b. Proc. 25th Anniversary meeting of EMAG Inst. Phys. ;
1972 Proc. 5th Euro. Conf. on Electron Microscopy

39. BURGE, R.E., GARRARD, D.F., 1968. J. Phys. E. Sci. Inst. 1, 715

40. BURGE, R.E., GARRARD, D.F., BROWNE, M.T., 1968. J. Phys. E. Sci. Inst. 1, 707

41. BURGEGRAF, C., GOLDSTRAUB, S., MOSSER, A., 1971. Rev. Phys. Appl. 6 319

42. BURKSTRAND, J.M., 1971. Ph.D. Thesis, University of Illinois

43. CASTAING, R., HENRY, L., 1962. Comptes rendus 255, 76;
1964 Journal de Microscopie 3, 133

44. CHANG, C.C., 1971. Surface Science 25, 53

45. CHUKHOVSKII, F.N., ALEXANJAN, L.A., PINSKER, Z.G., 1973. Acta. Cryst. A 29, 38

46. CITRIN, R.H., SHAW, R.W. Jnr., THOMAS, T.D., 1972. Int. Conf. on Electron Spectroscopy, Ed. D.A. Shirley, N. Holland

47. COATES, D.G., 1967 Phil. Mag. 16, 1179; 1969 I.I.T.R.I. 69, 27 - 40

48. COLE, R.S., JENNINGS, J.C.E., 1971. J. Phy. D. 4, 54 - 63

49. CONSIDINE, K.T., 1970. Ph.D. Thesis, University of Cambridge

50. COSSLETT, V.E., THOMAS, R.N., 1964 a) J. App. Phys. 15, 235 - 248
b) Brit. J. App. Phys. 15, 883 - 907 ; c) Brit. J. Appl. Phys. 15, 1283 - 1300

51. CREWE, A.V., 1977. Optik 47, 3, 299

52. CUNDY, S.L., METHERELL, A.J.F., WHELAN, M.J., 1965. J. Sci. Inst. 43, 712

53. CURTIS, G.H., FERRIER, R.P., 1970. J. Phys. E 3, 881

54. DANYSY, J., 1912. Le Radium 9, 1; 1913 Le Radium 10, 4

55. DARLINGTON, E.H., 1971. Ph.D. Thesis, University of Cambridge; 1975 J. Phys. D : Appl. Phys. 8, 85

56. DARLINGTON, E.H. and COSSLETT, V.E., 1972. J. Phys. D. App. Phys. 5, 1969

57. DARLINGTON, E.H., SPARROW, T.G., 1977. J. Phys. E 8, 596 - 600

58. DASHEN, R.F., 1964. Phys. Rev. 134 A, 1025 - 32

59. DAVISON, C.J., CALBICK, C.J., 1931. Phys. Rev. 38, 585

60. DENBIGH, P.N., 1964. Ph.D. Thesis, University of Cambridge

61. DENBIGH, P.N., GRIGSON, C.W.B., 1965. J. Sci. Instr. 42, 305-311

62. DIETRICH, W., 1958 a) Z. Phys. 151, 519 ; b) Z. Phys. 152, 306

63. DOLBY, R.M., SWIFT, D.W., 1960. Proc. European Conf. on Electron Microscopy, Delft, Vol. 1, 114 - 118

64. DUNCUMB, P., 1962. Phil. Mag. 7, 2101 - 2105

65. Edwards High Vacuum, Manor Royal, Crawley, Sy.

66. EGERTON, R.F., PHILIP, J.G., TURNER, P.S., WHELAN, M.J., 1975. J. Phys. E 8, 12, 1033

67. EL KAREH, A.B. and EL KAREH, J.C.S., 1970. Electron Beams, Lenses and Optics, Vol.1, Academic Press, N.Y.

68. EVANS, R.D., 1955. The atomic nucleus. McGraw Hill, N.Y.

69. EVERHART, T.E., 1960. J. Appl. Phys. 31, 1483

70. FORST, G., 1958. Z. Aginew Phys. 10, 546

71. FRANK, L., 1976. J. Phys. E 9, 670

72. FRANZEN, W., PORTER, J.H., 1975. Ad. E. E. Phys. 39, 73

73. FROITZHEIM, H., IBACH, H., LEHWALD, S., 1975. Rev. Sci. Inst. 46, 1325

74. GARDNER, J.L., SAMSON, J.A.R., 1975. J.E.S.R.P. 6, 53

75. GAUKLER, K.H., 1963. Naturwiss. 50, 438

76. GIBSON, M.J., 1973. Ph.D. Thesis, University of London

77. GJONNES, J., 1966. Acta. Cryst. 20, 240

78. GJONNES, J., WATANABE, D., 1966. Acta. Cryst. 21, 267

79. GOODYEAR, C.C., 1971. Signals and Information, Butterworths Lond.

80. GRACZYK, J.F., MOSS, S.C., 1968. Rev. Sci. Inst. 40, 3

81. GREEN, A.J., LECKEY, R.C.G., 1976. J. Phys. D : Appl. Phys. 9, 2123

82. GREEN, G.W., 1968. The design and construction of small vacuum systems. Chapman & Hall, London

83. GREEN, T.S., PROCA, G.A., 1970. Rev. Sci. Instr. 41, 1409

84. HABERSTROH , G., 1956. Z. Phys. 145, 20

85. HAFNER, H.,,SIMPSON, J.A., KUYATT, C.E., 1968. Rev. Sci. Inst. 39, 33

86. HALL, C.R., 1965 Phil Mag. 12, 815 ; 1966 Proc. Roy. Soc. A 295, 140 ; 1970 Phil. Mag. 21, 1075

87. HARTOP, H., HUBER, G., 1977. J.E.S.R.P. 11, 101 - 121

88. HARTWIG, D., ULMER, K., 1963. Zeit. Phys. 173, 294

89. HASHIMOTO, H., HOWIE, A., WHELAN, M.J., 1962. Proc. Roy. Soc. A 269, 80

90. HENKELMAN, R.M., OTTENSMEYER, F.P., 1974. J. Phys. E 7, 176

91. HENRY, L., 1964 a) Ph.D. Thesis, University of Paris ; 1964 b) Bull. Soc. Frans. Miner. Crist. 88, 172

92. HENRY, L., DUVAL, P,, HOAN, N., 1969. C.R. Acad. Sci. Paris 269, 955

93. HERTZOG, R., 1935. Zeit. Phys. 97, 586

94. HIRSCH, P.B., HOWIE, A., NICHOLSON, R.B., PASHLEY, D.W., WHELAN, M.J., 1965. Electron Microscopy of Thin Crystals, Butterworths, London

95. HOWIE, A., 1978. Inst. Phys. Conf. Ser. No. 41, 1

96. HUCHITAL, D.A., RIGDEN, J.D., 1972. J. Appl. Phys. 43, 2291

97. HUGHES, A.L., McMILLEN, J.H., 1929. Phys. Rev. 34, 291

98. HUGHES, A.L., ROJANSKY, V., 1929. Phys. Rev. 34, 286

99. IBACH, H., ROWE, J.E., 1974. Phys. Rev. 9, 1951

100. ICHINOKAWA, T., 1968. Jap. J. App. Phys. 7, 799

101. ISHIGURE, N., MORI, C., WATANABE, T., 1978. J. Phys. Soc. Japan 44, 1196

102. J & P Engineering Ltd., Portman House, Cardiff Rd., Reading (private communication)

103. JONES, K.W., 1980. Ph.D. Thesis, University of London. To be published

104. JULL, G., 1956. Proc. Phys. Soc. 69, 1237

105. KAINUMA, Y., 1953 J. Phys. Soc. Japan 8, 685 - 686 ; 1955 Acta. Cryst. 7, 777 - 779

106. KANTER, H., 1957 Ann. Phys. 5, 43 - 58 ; 1961 Phys. Rev. 121, 461 ; 1970 Phys. Rev. B1, 2357

107. KESSLER, J., LINDER, H., 1964. Z. angew Phys. 18, 7

108. KIKUCHI, S., 1928 a) Proc. Imp. Acad. 4, 275 - 278
b) " " " " 354 - 356
c) " " " " 471 - 474
d) Jap. J. Phys. 5, 83 - 96

109. KLEMPERER, O., 1935. Phil. Mag. 20, 45 ; 1965 Rpts. Prog. Phys. 28, 75

110. KLEMPERER, O., BARNETT, M.E., 1971. Electron Optics 3rd Ed. Cambridge Univ. Press

111. KLEMPERER, O., SHEPHERD, J.P.G., 1963. Adv. Phys. 12, 355

112. KRYN'KO, Yu. N., MEL'NIK, P.V., NAKHODKIN, N.G., 1965. Bull. Acad. Sci. U.S.S.R. Phys. Ser. 33 - 44B

113. KULENKAMPFF, H., SPYRA, W., 1954. Zeit. Phys. 137, 416

114. KUNZ, C., 1963. Zeit. Phys. 167, 53

115. KUYATT, C.E., SIMPSON, J.A., 1967. Rev. Sci. Inst. 38, 103

116. LAPONSKY, A.B., WHETTEN, N.R., 1960. Phys. Rev. 120, 801 - 806

117. LEDER, L.B., SIMPSON, J.A., 1958. Rev. Sci. Inst. 29, 571

118. LENARD, P., 1902. Ann. Phy. Lpz. 15, 283

119. LEONHARD, F., 1954. Z. Naturforsch. 9a, 727

120. LINDAU, I., HELMER, J.C., UEBBING, J., 1973. Rev. Sci. Inst. 44, 265

121. McDONALD, I.R., LAMKI, A.M., DELANEY, C.F.G., 1971. J. Phys. D. Appl. Phys. 4, 1210

122. MALOFF, I.G., EPSTEIN, P.W., 1938. Electron Optics in Television. McGraw Hill

123. MARTON, L., SIMPSON, J.A., FOWLER, H.A. and SWANSON, N., 1962. Phys. Rev. 126, 182

124. MATSUKAWA, T., SHIMIZU, R., HASHIMOTO, H., 1974. J. Phys. D 7, 695

125. METHERELL, A.J.F., WHELAN, M.J., 1966. J. App. Phys. 37, 1737

126. MIYAKE, S., HAYAKAWA, K., KAWAMURA, T., OHTSUKI, Y.H., 1975. Acta. Cryst. A31, 32

127. MOLLENSTEDT, G., 1949. Optik 5, 499

128. MOODEY, H.C., NEUHAUSER, R.G., RICHARDS, P.A., HEADRICK, L.B., 1957. T.V. Engineering Handbook. Ed. Fink McGraw Hill

129. MOSSER, A., BURGGRAF, Ch., GOLDSTRAUB, S., OHTSUKI, Y.H., 1976. Surf. Sci. 54, 580 - 592

130. MOTZ, J.W., OLSEN, H., KOCH, H.W., 1964. Rev. mod. Phys. 36, 881 - 928

131. MULLER, H.O., 1937. Zeit. Phys. 104, 475 - 486

132. MURAKAMI, S., MURATA, Y., 1978. Inst. Phys. Conf. Ser. No.41, 228

133. NAKAI, Y., 1978. Inst. Phys. Conf. Ser. No.41, 79

134. NISHIKAWA, S., KIKUCHI, S., 1928. Nature, Lond. 121, 1019-1020

135. NOLLER, H.G., POLASCHEGY, H.D., SCHILLALIES, H., 1975. Jap. J. App. Phys. Supp.2, pt.1, 343

136. O'HARER, T.C., 1972 a) J. Chem. Ed. 49, A131 ; 1972b) J. Chem. Ed. 49, A211

137. OKAMOTO, K., ICHINOKAWA, T., OHTSUKI, Y., 1971. J. Phys. Soc. Japan 30, 1690 - 1701

138. PALMBERG, P.W., 1967. J. Appl. Phys. 38, 2137

139. PIANETTA, P., LINDAU, I., 1977. JESRP 11, 13

140. PLIES, E., ROSE, H., 1977. Optik 47, 365

141. PORTEUS, J.O., 1969. The Structure and Chemistry of Solid Surfaces, Ed. Somorjai (Wiley N.Y.)

142. PURCELL, E.M., 1938. Phys. Rev. 54, 818

143. QUINN, J.J., 1962. Phys. Rev. 126, 1453

144. R.C.A. Ltd., Sunbury-on-Thames, Mx.

145. READHEAD, P.A., HOBSON, J.P., KONANELSON, E.V., 1968. The physical basis of ultra-high vacuum. Chapman & Hall, London

146. REZ, P., 1978. Inst. Phys. Conf. Ser. No.41, 61

147. REZ, P., HUMPHREYS, C.J., WHELAN, M.J., 1977. Phil. Mag. 35, 81

148. RISLEY, J.S., 1972. Rev. Sci. Inst. 43, 95-103

149. ROBINSON, N.W., 1968. The physical principles of ultra-high vacuum systems and equipment. Chapman & Hall, London

150. ROSE, H., PLIES, E., 1974. Optik 40, 336

151. ROWE, J.E., IBACH, H., 1974. Phys. Rev. Letters, 32, 421

152. ROY, D., BURROW, P.D., 1975. J. Phys. E 8, 273

153. ROY, D., DELAGE, A., CARETTE, J-D., 1975. J. Phys. E 8, 109

154. RUDD, M.E., 1962. Ph.D. Thesis, University of Nebraska ; 1972 Low energy electron spectrometry, Ed. Sevier, Wiley N.Y.

155. RUTHERFORD, E., 1911. Phil. Mag. 21, 669-88

156. SALDIN, D.K., WHELAN, M.J., ROSSOUW, C.J., 1978. Inst. Phys. Conf. Ser. No.41, 50

157. SANDSTROM, R., SPENCER, J.P., HUMPHREYS, C., 1974. J. Phys. D. Appl. Phys. 7, 1030-46

158. SAR-EL, H.Z., 1967. Rev. Sci. Inst. 38, 1210

159. SCHMITZ, W., MELHORN, W., 1972. J. Phys. E 5, 64

160. SEVIER, K.D., 1972. Low energy electron spectrometry, Wiley N.Y.

161. SHEPPARD, C.J.R., 1973. Ph.D. Thesis, University of Cambridge

162. SHIMAMOTO, N., FUKAMACHI, T., OHTSUKI, Y.H., 1972. J. Phys. Soc. Japan 33, 459

163. SHIMIZU, R., KATAOKA, Y., IKUTA, T., KOSHIKAWA, T., HASHIMOTO, H. 1976, J. Phys. D. App. Phys. 9, 101

164. SHIMIZU, R., KATAOKA, Y., MATSUKAWA, T., IKUTA, T., MURATA, K., HASHIMOTO, H., 1975. J. Phys. D. App. Phys. 8, 695

165. SHINOHARA, K., MATSUKAWA, K., 1933. Sci. Pap. Inst. Phys. Chem. Res. Japan 21, 21 - 25

166. SICKAFUS, E.N., HOLLOWAY, D.M., 1975. Surf. Sci. 51, 131

167. SIEGBAHN, K., 1965. "α, β and γ ray spectroscopy" Vol. 1, North Holland

168. SIMPSON, J.A., 1961. Rev. Sci. Inst. 32, 1283

169. SIMPSON, J.A., KUYATT, C.E., 1966. J. App. Phys. 37, 3805

170. SIMPSON, J.A., MARTON, L., 1961. Rev. Sci. Inst. 32, 802

171. SPICER, W.E., BERGLUND, C.N., 1964. Rev. Sci. Inst. 35, 1665

172. STAMATOVIC, A., SCHULZ, G.J., 1970. Rev. Sci. Inst. 41, 423

173. STILLE, U., 1949. Zeit. Phys. 125, 174

174. TAKAGI, S., 1958 a) J. Phys. Soc. Japan 13, 278 - 286 ; b) J. Phys. Soc. Japan 13, 287 - 296

175. TAYLOR, B.N., PARKER, W.H., LANGENBERG, D.N., 1969. Rev. Mod. Phys. 41, 375

176. TAYLOR, N.J., 1969. Rev. Sci. Inst. 40, 792 ; 1972 Techniques in Metals Research Vol. VIII, Ed. R.F. Bunshan, Interscience, N.Y.

177. Teledeltos (Anaplot) paper, Sensitised Coatings Ltd., 108 Church St., Croydon

178. THOMSON, G.P., 1931. Proc. Roy. Soc. 133, 1.

179. THOMSON, G.P., COCHRANE, W., 1939. Theory and Practice of Electron Diffraction, MacMillan

180. THOMSON, J.J., 1897. Phil. Mag. 44, 293

181. TOBURN, L.H., 1974. Phys. Rev. A9, 2505

182. TOMLIN, S.G., 1963. Proc. Phys. Soc. 82, 465

183. TOMPSETT, M.F., 1966. Ph.D. Thesis, University of Cambridge

184. UNVALA, B.A., MARIES, A., 1974. J. Phys. E 7, 349

185. UYEDA, R., 1974. J. Appl. Cryst. 7, 1

186. UYEDA, R., NONOYAMA, M., 1968. Jap. J. Appl. Phys. 7, 200-208

187. Vacuum Generators Ltd., East Grinstead, Sy.

188. Vaughn and Cameron Ltd., Wandle Trading Estate, Mitcham Junction, Sy.

189. VENABLES, J.A., HARLAND, C.J., 1973. Phil. Mag. 27, 1193-1200

190. VERDIER, P., 1974. Vide 28, 164, 83 - 85

191. VERDIER, P., ARNAL, F., 1969. C.r. hebd. Seanc. Acad. Sci. Paris 268, 1101

192. VERSTER, J.L., 1963. Philips Res. Repts. 18, 465-605

193. WANNBERG, B., GELIUS, U., SIEGBAHN, K., 1974. J. Phys. E. Sci. Inst. 7, 149

194. WARD, D.M., 1976. Ph.D. Thesis, University of Cambridge

195. WARD, L., BUNN, J.P., 1967. Introduction to the theory and practice of high vacuum technology. Butterworths, London

196. WELLINGTON, H.F., 1974. J. App. Phys. 44, 3669

197. WELLS, O.C., BOYDE, A., LIFSHIN, E., REZANOWICH, A., 1974. Scanning Electron Microscopy. McGraw Hill, N.Y.

198. WENDELKEN, J.F., PROPST, F.M., 1976. Rev. Sci. Inst. 47, 1069

199. WHELAN, M.J., 1965a) J. Appl. Phys. 36, 2099; b) J. Appl. Phys. 36, 2103

200. WIEN, W., 1897. Verh. Dt. Phys. Ges. 16, 165

201. Wier Instrumentation Ltd., Durban Rd., Bognor Regis, Sx.

202. WILLIAMSON, C.A., 1966. M.Sc. Thesis, University of London

203. WILMAN, H., 1948a) Proc. Phys. Soc. 60, 341; b) Proc. Phys. Soc. 61, 416

204. WOLLNIK, H., 1967. "Electrostatic Prisms" in Focusing of Charged Particles, Ed. Septier, Acad. Press, N.Y.

205. WOLLNIK, H., MATSUO, T., KASSECKERT, E.A., 1976. Optik 46, 255

206. YARNOLD, G.D., BOLTON, H.C., 1949. J. Sci. Inst. 26, 38

207. ZIMMERMANN, B., 1970. Adv. Electron Phys. 29, 257.